

Generation Scheme of Effective Models Based on Symmetry-Adapted Multipole Basis and Clarification for Universal Properties of Chiral Materials

メタデータ	言語: eng 出版者: 公開日: 2023-05-31 キーワード (Ja): キーワード (En): 作成者: OIWA, RIKUTO メールアドレス: 所属:
URL	http://hdl.handle.net/10291/00023144

Meiji University
Graduate School of Science and Technology

Academic Year 2022

Doctoral Dissertation

Generation Scheme of Effective Models

Based on Symmetry-Adapted Multipole Basis

and

Clarification for Universal Properties of Chiral Materials

Physics Program

Rikuto Oiwa

Acknowledgments

I would like to express my sincere gratitude to my supervisor Prof. Hiroaki Kusunose for his generous guidance and continuous support during my bachelor's, master's, and doctoral courses. His invaluable advice based on immense knowledge and abundant experience has always encouraged me in my research and daily life. I would be deeply grateful to Profs. Jun Kikuchi, Yukio Yasui, and Kazumasa Hattori for their valuable comments in reviewing my thesis. Likewise, I would like to offer my special thanks to Profs. Yuki Yanagi, Satoru Hayami, and Dr. Megumi Yatsushiro for the collaboration and the fruitful discussions.

I appreciate Profs. Michito Suzuki, Hiroaki Ikeda, Ryotaro Arita, and Yusuke Nomura for the fruitful discussions and the crucial advices as for the density-functional theory, Wannier functions, and our methodology discussed in Chap. 4. I am deeply grateful to Prof. Yuki Yanagi for providing us the data of the DFT calculation in Chap. 5. I would also like to thank Profs. Yoshihiko Togawa, Hiroshi Yamamoto, Koichi Izawa, Takahiro Onimaru, Hiroshi Amitsuka, Tatsuya Yanagisawa, Hiroyuki Hidaka for giving us crucial experimental information, and Prof. Junichiro Kishine, Dr. Akihito Kato, Shun Okumura, Mr. Yuta Suzuki, Eiji Kojima, Ryosuke Hirakida, Takayuki Ishitobi, and Ms. Tomomi Tateishi for the invaluable advice on theoretical and technical aspects. In addition, I appreciate Prof. Yukitoshi Motome and his students for giving us opportunities for fruitful discussions of the systematic analysis method for nonlinear response tensors [1].

I would also like to thank all of the former and present members of Condensed Matter Theory Laboratory in Meiji University who always supported my study and daily life. Lastly, I would like to express my deep gratitude to my family for their continuous encouragement and support all through my studies.

List of Publications

Papers related to the dissertation

1. R. Oiwa and H. Kusunose,
“Rotation, Electric-Field Responses, and Absolute Enantioselection in Chiral Crystals”,
Physical Review Letters **129**, 116401 (2022),
© 2022 American Physical Society
2. R. Oiwa and H. Kusunose,
“Systematic Analysis Method for Nonlinear Response Tensors”,
Journal of the Physical Society of Japan **91**, 014701 (2022),
© 2022 The Physical Society of Japan
3. H. Kusunose, R. Oiwa, and S. Hayami,
“Complete Multipole Basis Set for Single-Centered Electron Systems”,
Journal of the Physical Society of Japan **89**, 104704 (2020),
© 2020 The Physical Society of Japan

Papers not included in the dissertation

1. S. Hayami, R. Oiwa and H. Kusunose,
“Electric Ferro-Axial Moment as Nanometric Rotator and Source of Longitudinal Spin Current”,
Journal of the Physical Society of Japan **91**, 113702 (2022),
© 2022 The Physical Society of Japan
2. M. Yatsushiro, R. Oiwa, H. Kusunose, and S. Hayami,
“Analysis of model parameter dependences on the second-order nonlinear conductivity in PT-symmetric collinear antiferromagnetic metals with magnetic toroidal moment on zigzag chains”,
Physical Review B **105**, 155157 (2022),
© 2022 American Physical Society

Abstract

Various theoretical approaches have been developed to elucidate the hidden order parameters characterizing unusual physical phenomena in solids, such as the group theoretical arguments, electronic multipole theory, and density functional theory (DFT). Although these approaches have been successful in some aspects, they still need to be improved to reveal the microscopic representation of the order parameter and the microscopic understanding of its related physical phenomena. From these circumstances, it is highly desirable to develop a systematic prescription for clarifying the quantum-mechanical operator corresponding to the order parameter and quantitatively evaluating it. In particular, the order parameter for molecule and crystal chirality, i.e., the electric toroidal monopole, G_0 , has not fully been understood at the microscopic level. Clarifying the microscopic description of chirality, i.e., G_0 , is essential for unveiling the heart of chirality and achieving absolute enantioselection in chiral materials.

In this thesis, we develop a systematic generation scheme of a DFT-based tight-binding (TB) model based on the symmetry-adapted multipole theory. First, we construct a complete orthonormal symmetry-adapted multipole basis (SAMB) that enables us to express any electronic degrees of freedom in molecules and crystals. The Hamiltonian is expressed as the linear combination of SAMB, in which the weights correspond to the model parameters. We construct the DFT-based TB model by optimizing the weights to reproduce the DFT band dispersion. Using this systematic generation scheme, we can unveil hidden electronic multipole degrees of freedom and their quantum-mechanical operator expressions explicitly in molecules and crystals. Moreover, by optimizing the weights, we can also evaluate their contributions quantitatively. Using the generation scheme, we investigate the microscopic description of chirality and its related responses.

In Chap. 1, we give an introduction, outline, and organization of this thesis.

In Chap. 2, we clarify the advantages and disadvantages of using a de facto standard DFT-based tight-binding model based on the Wannier functions and atomic orbitals. In particular, the Wannier TB model is superior in its quantification, whereas the required symmetry is not taken into account in the model construction process. On the other hand, the Slater-Koster approach based on the atomic orbitals partially considers the symmetry, however, essential parameters would often be lost in the TB model owing to the lack of the effect from the surrounding environment around the bond of the electron hopping.

In Chap. 3, we develop the systematic generation scheme of SAMB. First, we decompose the electronic degrees of freedom into orbital/spin and the sublattice parts which are described by the atomic and site/bond-cluster multipole bases, respectively. By combining the atomic and site/bond-cluster multipole bases, we construct complete orthonormal SAMB set in the given Hilbert space. Using SAMB, we can describe any electronic degrees of freedom in the isolated and periodic multi-site systems, such as molecules and crystals.

In Chap. 4, we demonstrate a systematic generation scheme of the DFT-based symmetry-adapted TB model given by the linear combination of SAMB. We optimize the model parameters, i.e., the weights of each SAMB, so as to reproduce a given DFT band dispersion. To efficiently optimize the weights, we utilize machine learning techniques and introduce a deep neural network (DNN) where the SAMB plays a role of a neuron in the network, which we call DNN-SAMB. Using DNN-SAMB, we can perform highly efficient and accurate optimization with less initial guess dependence of the model parameters. We demonstrate our method for graphene, SrVO₃, and monolayer MoS₂. We achieve accuracy of less than 10^{-4} of the mean squared error between the normalized energy eigenvalues of the optimized TB model and that of the DFT or DFT-based Wannier calculation. Most remarkably, we obtain highly accurate optimized TB model although our TB model contains fewer model parameters

than the Wannier TB model. Since the proposed method refers only to the energy eigenvalues, there is no guarantee to reproduce the orbital dependence of the electronic states in the reference bands. Nevertheless, the optimized TB Hamiltonian well reproduces the orbital dependence of the electronic states of SrVO_3 because of the use of the SAMB, which imposes strong constraints by symmetry. It should be emphasized that our method is applicable to any crystallographic structure within 230 space group. Furthermore, DNN-SAMB could be useful in various fields such as materials informatics.

In Chap. 5, we elucidate the microscopic description of chirality, i.e., G_0 , by taking elemental Te crystal as the simplest example of chiral crystals. Based on the systematic generation scheme introduced in Chap. 4, we construct the DFT-based realistic tight-binding Hamiltonian of Te and elucidate that the local and itinerant G_0 are the most dominant contributions in the Hamiltonian. Furthermore, we clarify that the itinerant G_0 is the crucial element to realize the possible electric-field induced static rotational lattice deformation.

Lastly, we propose a possible experimental approach to realize the absolute enantioselection in chiral materials by means of the conjugate field of chirality, such as simultaneously applying electric and rotation fields, or a magnetic field and electric current, and so on. The sign of the combined field controls the preferred handedness during the crystallization process. It should be emphasized that this generic approach is applicable to any chiral material. Since a larger coupling magnitude between G_0 and its conjugate field is favorable for achieving an absolute enantioselection, quantitative experimental observation of the responses related to the coupling is essential in future development.

Contents

1	Introduction	1
1.1	Hidden Electronic Degrees of Freedom	1
1.2	Purpose of This Thesis	2
1.3	Outline and Organization of This Thesis	2
2	Theoretical Background	5
2.1	Tight-Binding Model Based on Wannier Functions	5
2.1.1	Wannier Function	5
2.1.2	Advantages and Disadvantages	11
2.2	Tight-Binding Model Based on Atomic Orbitals	16
2.3	Summary	18
3	Symmetry-Adapted Multipole Basis	21
3.1	Decomposition of Electronic Degrees of Freedom	21
3.2	Concept of Multipole Basis	23
3.3	Multipole Basis for Single-Centered Electron Systems	25
3.3.1	Four Types of Multipoles	25
3.3.2	Quantum-Mechanical Operator Expressions	28
3.3.3	Atomic Multipole Basis in Crystallographic Systems	36
3.4	Multipole Basis for Isolated Multi-Site Systems	39
3.4.1	Site/Bond-Cluster	39
3.4.2	Site/Bond-Cluster Multipole Basis	40
3.4.3	Symmetry-Adapted Multipole Basis	44
3.4.4	Final Matrix Form	46
3.5	Multipole Basis for Periodic Multi-Site Systems	47
3.5.1	Symmetry-Adapted Multipole Basis	47
3.5.2	Final Matrix Form	49
3.6	Summary	51
4	DFT-Based Symmetry-Adapted Tight-Binding Model	53
4.1	Introduction	53
4.2	Symmetry-Adapted Tight-Binding Model	55
4.3	DFT-Based Symmetry-Adapted TB Model	56
4.3.1	Outline	56
4.3.2	Workflow of the DNN-SAMB	57
4.4	Usage Examples	61
4.4.1	Graphene	61
4.4.2	SrVO ₃	71

4.4.3	MoS ₂	81
4.5	Summary	97
5	Microscopic Description of Chirality	99
5.1	Introduction	99
5.2	Tight-Binding Model for Te	102
5.2.1	DFT Calculation for Te	102
5.2.2	Symmetry-Adapted TB Hamiltonian for Te	103
5.3	Parameter Optimization	109
5.4	Electric-Field Induced Rotation	114
5.5	Absolute Enantioselection by Rotation and Electric Fields	117
5.6	Summary	118
6	Summary	119
A	Density Functional Theory	121
A.1	Born-Oppenheimer Approximation	121
A.2	Density Functional Theory	122
A.2.1	Hohenberg-Kohn Theorems	122
A.2.2	Kohn-Sham Approach	123
A.3	Proof of Hohenberg-Kohn Theorem I	127
A.4	Proof of Hohenberg-Kohn Theorem II	127
A.5	Various Approximations for Exchange-Correlation Energy	127
A.5.1	Local Density Approximation	128
A.5.2	Generalized Gradient Approximation	129
B	Atomic Orbitals	131
B.1	Radial Part	131
B.2	Angular Part	131
B.3	Slater-Koster Parameters	133
C	Multipole	135
C.1	Vector Spherical Harmonics	135
C.2	Cubic and Hexagonal Harmonics	136
C.3	Projection-Based Clebsch-Gordan Coefficients	137
C.3.1	Projection Operators	137
C.3.2	Clebsch-Gordan Coefficients	138
D	Graphene	139
D.1	Multipole Basis for Graphene	139
D.2	Comparison of Band Dispersion	140
E	SrVO₃	141
E.1	Multipole Basis for SrVO ₃	141
E.2	Comparison of Band Dispersion	143

F	MoS₂	145
F.1	Momentum Multipole Basis	145
F.1.1	Nearest-Neighbor Mo–Mo Bond-Cluster	145
F.1.2	Nearest-Neighbor S–S Bond-Cluster	145
F.1.3	Nearest-Neighbor Mo–S Bond-Cluster	146
F.2	Momentum Space Representation of the SAMB	147

Chapter 1

Introduction

1.1 Hidden Electronic Degrees of Freedom

Unusual physics governed by hidden electronic degrees of freedom has been extensively studied, and various theoretical approaches to elucidate them have been developed concurrently. The anomalous Hall effect (AHE) [2–4], Kerr effect [5–8], and Nernst effect [9–12] under collinear [13–17] and non-collinear [18–24] antiferromagnetic (AFM) orderings are typical examples. Since the AHE is usually characterized by a coupling between a magnetic dipole moment M_z and electronic motion through the spin-orbit coupling (SOC), the mechanism of AHE in antiferromagnets with $M_z = 0$ is nontrivial. In the series of study for the gigantic AHE observed in the non-collinear AFM Mn_3Sn [20], methodologies combining the density functional theory (DFT) with the symmetry-adapted multipole theory [25–28] have been developed [29] as well as the Berry curvature mechanism [30–33]. Then, it has been pointed out that there is a strong correlation between the AHE and a cluster magnetic octupole consisting of non-collinear magnetic structures [29].

In contrast to magnetic order, electric ferro-axial (lattice rotational) order, a consequence of broken mirror symmetries with preserving both spatial inversion and time reversal symmetries, has recently attracted much attention as one of the ferroic orders. Although the electric ferro-axial order has been less studied because of the absence of its conjugate electromagnetic fields and its quantum-mechanical operator, it has been observed in several materials, such as $\text{RbFe}(\text{MoO}_4)_2$ [34–39], NiTiO_3 [40–42], $\text{Ca}_5\text{Ir}_3\text{O}_{12}$ [39], superlattices of $\text{PbTiO}_3/\text{SrTiO}_3$ [43], and so on. Moreover, the quantum-mechanical operator corresponding to the electric ferro-axial order, so-called the electric toroidal dipole, was obtained quite recently [25, 26, 28]. Then, it has been elucidated that the electric toroidal dipole is the order parameter for the electric ferro-axial orderings [44]. In addition, an antiferroaxial ordering of the anti-polar units has been observed in $\text{Ba}(\text{TiO})\text{Cu}_4(\text{PO}_4)_4$ [45]. Remarkably the emergence of the antiferroaxial order accompanied with the anti-polar units induces the spontaneous ferro-chiral structural transition.

Chirality is a consequence of broken spatial inversion and mirror symmetries and has been paid much attention in various fields of science due to its diverse applications. CISS (Chirality Induced Spin Selectivity), a spin polarization caused by passing through chiral systems, is a typical chirality induced phenomenon discussed in both molecules [46–50] and inorganic crystals, such as CrNb_3S_6 [51, 52] and MSi_2 ($M = \text{Nb}, \text{Ta}$) [53]. Additionally, much variety of chirality induced phenomena has been extensively studied, such as the kinetic magnetoelectric (Edelstein) effect [54–58], heat-current/electric-field induced phonon angular momentum [59, 60], truly chiral phonons rotating in a plane perpendicular to the direction of propagation [61–63], and so on. Notably, recent studies elucidated that the electric toroidal monopole G_0 corresponds to the order parameter for chirality [26, 64] based on the electronic

multipole theory [25, 26, 28]. However, it has yet to be understood at the microscopic level.

1.2 Purpose of This Thesis

As mentioned above, there is a one-to-one correspondence between the symmetry breaking and the order parameter, such as the electric ferro-axial orderings characterized by the electric toroidal dipole, molecular and crystal chirality characterized by the electric toroidal monopole, G_0 , and so on. In theoretical studies, such order parameters have been investigated mainly based on the group theoretical arguments, electronic multipole theory, and DFT calculations. Although these approaches have been successful in some aspects, they still need to be improved to reveal the microscopic representation of the order parameter and the microscopic picture of its related physics. To elucidate them, it is highly desirable to develop a systematic prescription for clarifying the quantum-mechanical operator corresponding to the order parameter and quantitatively evaluating it. In particular, the order parameter for molecule and crystal chirality, G_0 , has not fully been understood at the microscopic level. Thus, clarifying the microscopic origin of G_0 inherent in chiral materials is essential for unveiling the heart of chirality and achieving absolute enantioselection in chiral materials.

The main purpose of this thesis is to develop a systematic generation scheme of a DFT-based tight-binding (TB) model based on the symmetry-adapted multipole theory. To achieve this purpose, we first construct a complete orthonormal symmetry-adapted multipole basis that enables us to express any electronic degrees of freedom in materials. The Hamiltonian is expressed as the linear combination of the symmetry-adapted multipole basis, where the weights of each basis correspond to the model parameters. Then, we construct the DFT-based TB model by optimizing the weights to reproduce the DFT band dispersion. Note that we utilize the machine-learning technique in the optimization process to efficiently optimize the weights. Using the systematic generation scheme, we can unveil hidden electronic multipole degrees of freedom in the Hamiltonian and their quantum-mechanical operator expressions explicitly. Moreover, by optimizing the weights, we can also evaluate their contributions numerically. We demonstrate the method by applying to graphene, SrVO₃, and monolayer MoS₂. We show that the optimized TB model well reproduce the DFT band dispersions, density of states, and Fermi surfaces. Moreover, using the method, we construct a realistic TB model for chiral Tellurium crystal. We find the dominant electric toroidal monopole G_0 terms in both the local and itinerant parts of the Hamiltonian. Then, we elucidate the microscopic origin of the possible electric-field induced static rotational lattice deformation and its inverse response, rotation-field induced electric polarization in Tellurium. Based on these responses, we propose a possible experimental approach to realize the absolute enantioselection in chiral crystals.

1.3 Outline and Organization of This Thesis

In order to make this thesis self-contained, thesis is organized as follows. In Chap. 2, we give a short summary of the de facto standard DFT-based Wannier TB model, and then we clarify their advantages and disadvantages. In Chap. 3, we introduce the symmetry-adapted multipole basis. In Chap. 4, we present a systematic generation scheme of a DFT-based TB model based on the symmetry-adapted multipole basis. We also show prime examples of the method to some typical crystals: graphene, SrVO₃, and monolayer MoS₂. Using the present systematic method, we elucidate the microscopic origin of chirality in elemental Tellurium in Chap. 5. We also show the explicit definitions of the dominant G_0 terms in both the local and itinerant parts of the Hamiltonian. We also discuss a possible electric-field induced static rotational lattice deformation and experimental approach to

achieve absolute enantioselection in chiral crystals. Chapter 6 summarizes thesis. There are six Appendices. We give a brief outline of DFT in Appendix A. In Appendix B, the atomic orbitals and the Slater-Koster parameters are given. Appendix C presents the vector spherical harmonics, cubic and hexagonal harmonics, and the projection-based Clebsch-Gorden coefficients. In Appendices D, E, and F, the detail of the multipole basis for graphene, SrVO₃, and monolayer MoS₂ are given, respectively.

Chapter 2

Theoretical Background

In this chapter, we show a theoretical background behind the present study. First, some advantages and disadvantages of the DFT-based Wannier TB model are given in Sec. 2.1. Then, we show the characteristic properties of the TB model based on the atomic orbitals in Sec. 2.2.

2.1 Tight-Binding Model Based on Wannier Functions

To analyze the material property, constructing a realistic theoretical model is essential. DFT-based electronic structure analysis is a de facto standard approach, which enables us to incorporate electronic states in materials in detail and to evaluate a wide range of physical quantities. There are several software packages to implement the DFT-based electronic structure calculations, such as VASP [65], QUANTUM ESPRESSO [66], WIEN2K [67], OpenMX [68], ABINIT5 [69], Gaussian [70], and so on. We briefly outline the concept of DFT in Appendix A. Once the Kohn-Sham (KS) energies and orbitals are obtained by solving the KS equation, one can analyze the electronic band structure and various physics quantitatively. However, since the KS Hamiltonian is defined in an auxiliary system, the microscopic mechanism of related physics tends to be opaque. In addition, only several bands, consisting of the electronic degrees of freedom near the Fermi level, are usually significant for analyzing the low-energy physics of interest. From these circumstances, recent studies have developed a generation scheme of a DFT-based TB model with the use of the Wannier function (WF) [71]. Depending on the model parameters, the effective model can describe a wide range of physical phenomena in the fields, such as ferromagnetism, antiferromagnetic, superconductivity, and so on. To perform realistic calculations based on actual materials, deriving the model parameters from the DFT calculations is required. In this section, we briefly show a methodology to create a DFT-based TB model based on the WF, which is implemented in the Wannier90 software package [72–74].

2.1.1 Wannier Function

The crystal potential satisfies the periodicity:

$$V(\mathbf{r} + \mathbf{R}) = V(\mathbf{r}) \quad (2.1.1)$$

where \mathbf{R} is any lattice vector in real space. Therefore, in a typical DFT calculation for crystals, the Bloch function (BF), periodically spreading through crystals according to Bloch's theorem, is adopted as the KS orbitals. The BF of the n th band at a crystal momentum \mathbf{k} is defined by

$$\psi_{n\mathbf{k}}(\mathbf{r}) = u_{n\mathbf{k}}(\mathbf{r})e^{i\mathbf{k}\cdot\mathbf{r}} \quad (2.1.2)$$

where $u_{n\mathbf{k}}(\mathbf{r})$ is the periodic part, $u_{n\mathbf{k}}(\mathbf{r} + \mathbf{R}) = u_{n\mathbf{k}}(\mathbf{r})$, and $|\psi_{n\mathbf{k}}\rangle$ is an eigenstate of the periodic Hamiltonian, H with an eigenvalue $\epsilon_{n\mathbf{k}}$:

$$H |\psi_{n\mathbf{k}}\rangle = \epsilon_{n\mathbf{k}} |\psi_{n\mathbf{k}}\rangle \quad (2.1.3)$$

Although the BF spreads through a crystal, one can construct a localized orbital in real space as a superposition of the BFs, called the Wannier function (WF).

Isolated Band

For simplicity, let us first consider a situation in that each band is isolated from the other bands, i.e., each band is separated by a gap from the others in the entire Brillouin zone (BZ). In this case, BFs are chosen as smooth periodic functions in the BZ. Thus, the WF of the n th band localized at a unit cell \mathbf{R} , $|w_{n\mathbf{R}}\rangle$, is defined by the Fourier transform of the BF [75]:

$$|\psi_{n\mathbf{k}}\rangle = \frac{1}{\sqrt{N}} \sum_{\mathbf{R}} |w_{n\mathbf{R}}\rangle e^{i\mathbf{k}\cdot\mathbf{R}} \quad (2.1.4)$$

$$|w_{n\mathbf{R}}\rangle = \frac{1}{\sqrt{N}} \sum_{\mathbf{k}} |\psi_{n\mathbf{k}}\rangle e^{-i\mathbf{k}\cdot\mathbf{R}} \quad (2.1.5)$$

where N is the number of unit cells.

Manifold of Bands

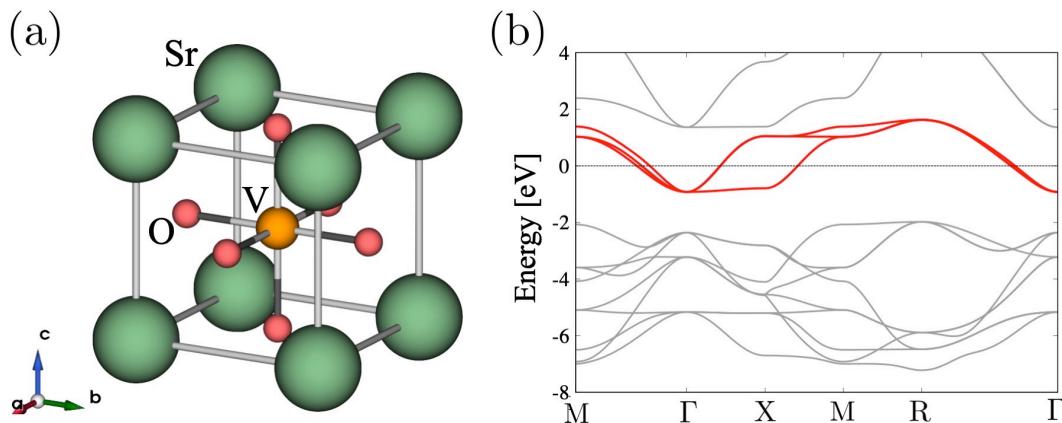


Figure 2.1: (a) Crystal structure of bulk crystalline SrVO₃. (b) Band dispersion obtained from a DFT calculation. The Fermi energy is taken as the origin. The red solid lines constitute a manifold of three t_{2g} orbitals isolated from the other bands.

Let us consider a more general situation where the J bands constitute a manifold separated from the others. Note that there can be band crossings at high symmetry points or degeneracies along high symmetry lines. As a simplest example, we show the band structure of SrVO₃ that is often chosen as the benchmark for developing the methodology associated with DFT calculation. As shown in Fig. 2.1(a), SrVO₃ has a cubic crystal structure with the space group $Pm\bar{3}m$ (#221, O_h^1). By using QUANTUM ESPRESSO [66], we calculate the electronic band structure of SrVO₃ as shown in Fig. 2.1(b). The three bands near the Fermi level depicted by the solid red lines, which correspond to the t_{2g} orbitals of V atom, constitute an isolated manifold. Since there are band degeneracies at the high symmetry points, and along high symmetry lines, the BFs of these bands are no longer analytic

functions in the BZ. Consequently, Eq. (2.1.5) is not capable of constructing well-localized WFs. In order to make well-localized WFs in such a situation, the unitary transformation of the J bands in the manifold is indispensable:

$$|\tilde{\psi}_{n\mathbf{k}}\rangle = \sum_{m=1}^J U_{mn\mathbf{k}} |\psi_{m\mathbf{k}}\rangle \quad (2.1.6)$$

$$|\tilde{u}_{n\mathbf{k}}\rangle = \sum_{m=1}^J U_{mn\mathbf{k}} |u_{m\mathbf{k}}\rangle \quad (2.1.7)$$

where $U_{\mathbf{k}}$ is a $J \times J$ unitary matrix defined in the manifold and $|u_{m\mathbf{k}}\rangle$ is the periodic part of $|\psi_{m\mathbf{k}}\rangle$, $|\psi_{m\mathbf{k}}\rangle = |u_{m\mathbf{k}}\rangle e^{i\mathbf{k}\cdot\mathbf{r}}$. The procedure of Eq. (2.1.6) eliminates the discontinuities of $|\psi_{m\mathbf{k}}\rangle$, and the obtained $|\tilde{\psi}_{n\mathbf{k}}\rangle$ becomes analytic in the BZ. Since the BFs with different eigenvalues are mixed in Eq. (2.1.6), $|\tilde{\psi}_{n\mathbf{k}}\rangle$ is no longer an energy eigenstate and n is not a band index. Using $|\tilde{\psi}_{n\mathbf{k}}\rangle$, the localized WF, $|\tilde{w}_{n\mathbf{R}}\rangle$, is obtain by

$$|\tilde{\psi}_{n\mathbf{k}}\rangle = \frac{1}{\sqrt{N}} \sum_{\mathbf{R}} |\tilde{w}_{n\mathbf{R}}\rangle e^{i\mathbf{k}\cdot\mathbf{R}} = \sum_{n=1}^J U_{mn\mathbf{k}} |\psi_{m\mathbf{k}}\rangle \quad (2.1.8)$$

$$|\tilde{w}_{n\mathbf{R}}\rangle = \frac{1}{\sqrt{N}} \sum_{\mathbf{k}} |\tilde{\psi}_{n\mathbf{k}}\rangle e^{-i\mathbf{k}\cdot\mathbf{R}} = \sum_{n=1}^J U_{mn\mathbf{k}} |w_{m\mathbf{R}}\rangle \quad (2.1.9)$$

The WFs have some characteristic properties as follows:

- (1) BFs and WFs are complete orthonormal basis functions

$$\langle \tilde{\psi}_{n\mathbf{k}} | \tilde{\psi}_{m\mathbf{k}'} \rangle = \int d\mathbf{r} \tilde{\psi}_{n\mathbf{k}}^*(\mathbf{r}) \tilde{\psi}_{m\mathbf{k}'}(\mathbf{r}) = \delta_{nm} \delta_{\mathbf{k}\mathbf{k}'} \quad (2.1.10)$$

$$\langle \tilde{w}_{n\mathbf{R}} | \tilde{w}_{m\mathbf{R}'} \rangle = \int d\mathbf{r} \tilde{w}_{n\mathbf{R}}^*(\mathbf{r}) \tilde{w}_{m\mathbf{R}'}(\mathbf{r}) = \delta_{nm} \delta_{\mathbf{R}\mathbf{R}'} \quad (2.1.11)$$

The n th band projection operator in both representations are equivalently defined by

$$P_n = \sum_{\mathbf{k}} |\tilde{\psi}_{n\mathbf{k}}\rangle \langle \tilde{\psi}_{n\mathbf{k}}| = \sum_{\mathbf{R}} |\tilde{w}_{n\mathbf{R}}\rangle \langle \tilde{w}_{n\mathbf{R}}| \quad (2.1.12)$$

- (2) WFs are translational images of each other

$$\tilde{w}_{n\mathbf{R}}(\mathbf{r}) = \tilde{w}_{n\mathbf{0}}(\mathbf{r} - \mathbf{R}) \quad (2.1.13)$$

- (3) WF is localized function in real space

Usually, $\tilde{w}_{n\mathbf{R}}(\mathbf{r})$ becomes a localized function in real space whose peak is located at a unit cell \mathbf{R} . As $|\mathbf{r} - \mathbf{R}|$ increases, the amplitude of $\tilde{w}_{n\mathbf{R}}(\mathbf{r})$ rapidly decreases.

- (4) DFT band dispersion can be reproduced by using the WFs

The matrix elements of the Hamiltonian against WFs and BFs are given by

$$\tilde{H}_{nm\mathbf{R}} = \langle \tilde{w}_{n\mathbf{R}} | H | \tilde{w}_{m\mathbf{0}} \rangle = \frac{1}{N} \sum_{\mathbf{k}} \langle \tilde{\psi}_{n\mathbf{k}} | H | \tilde{\psi}_{m\mathbf{k}} \rangle e^{i\mathbf{k}\cdot\mathbf{R}} = \frac{1}{N} \sum_{\mathbf{k}} \tilde{H}_{nm\mathbf{k}} e^{i\mathbf{k}\cdot\mathbf{R}} \quad (2.1.14)$$

$$\tilde{H}_{nm\mathbf{k}} = \langle \tilde{\psi}_{n\mathbf{k}} | H | \tilde{\psi}_{m\mathbf{k}} \rangle = \sum_{\mathbf{R}} \tilde{H}_{nm\mathbf{R}} e^{-i\mathbf{k}\cdot\mathbf{R}} \quad (2.1.15)$$

Here, $\tilde{H}_{nm\mathbf{R}}$ corresponds to the hopping between a pair of two WFs, and it decays rapidly with $|\mathbf{R}|$ as long as $U_{\mathbf{k}}$ is appropriately defined to make the WFs well-localized. The band dispersion $\epsilon_{n\mathbf{k}}$ is obtained by solving the eigenvalue problem:

$$\left| \tilde{H}_{\mathbf{k}} - \epsilon_{n\mathbf{k}} I \right| = 0 \quad (2.1.16)$$

where I is a $J \times J$ identity matrix.

(5) Gauge indeterminacy

Since $U_{\mathbf{k}}$ in Eq. (2.1.8) is not defined uniquely up to its phase factor, WF is gauge dependent.

(6) The matrix element of the position operator is related to the Berry connection

The matrix element of the position operator is given by

$$\tilde{\mathbf{a}}_{nm\mathbf{R}} \equiv \langle \tilde{w}_{n\mathbf{R}} | \mathbf{r} | \tilde{w}_{m\mathbf{0}} \rangle = \frac{1}{N} \sum_{\mathbf{k}} \tilde{\mathbf{a}}_{nm\mathbf{k}} e^{i\mathbf{k} \cdot \mathbf{R}} \quad (2.1.17)$$

$$\tilde{\mathbf{a}}_{nm\mathbf{k}} = i \langle \tilde{u}_{n\mathbf{k}} | \nabla_{\mathbf{k}} | \tilde{u}_{m\mathbf{k}} \rangle = \sum_{\mathbf{R}} \tilde{\mathbf{a}}_{nm\mathbf{R}} e^{-i\mathbf{k} \cdot \mathbf{R}} \quad (2.1.18)$$

where Eq. (2.1.18) is the Berry connection. The Wannier center of n th band is defined by

$$\bar{\mathbf{r}}_n = \langle \tilde{w}_{n\mathbf{R}} | \mathbf{r} | \tilde{w}_{n\mathbf{R}} \rangle = \frac{1}{N} \sum_{\mathbf{k}} \tilde{\mathbf{a}}_{nn\mathbf{k}} + \mathbf{R} \quad (2.1.19)$$

Note that $\bar{\mathbf{r}}_n$ is the gauge invariant quantity modulo a lattice vector \mathbf{R} .

The property (4) provides us the Wannier interpolation technique [76] that is similar to the Fourier interpolation. In the practical calculation, the KS equation is solved at coarse $N = N_1 \times N_2 \times N_3$ grid points $\{\mathbf{k}_j\}$ in the BZ. The matrix element of the Hamiltonian at each \mathbf{k}_j is given by

$$\tilde{H}_{nm\mathbf{k}_j} = \langle \tilde{\psi}_{n\mathbf{k}_j} | H | \tilde{\psi}_{m\mathbf{k}_j} \rangle \quad (2.1.20)$$

Using Eq. (2.1.14), $\tilde{H}_{nm\mathbf{k}_j}$ is mapped onto the Wannier representation as

$$\tilde{H}_{nm\mathbf{R}} = \frac{1}{N} \sum_{j=1}^N \tilde{H}_{nm\mathbf{k}_j} e^{i\mathbf{k}_j \cdot \mathbf{R}} \quad (2.1.21)$$

Then, using Eq. (2.1.15), $\tilde{H}_{nm\mathbf{k}_j}$ is interpolated onto an arbitrary \mathbf{k} as

$$\tilde{H}_{nm\mathbf{k}} = \sum_{\mathbf{R}} \tilde{H}_{nm\mathbf{R}} e^{-i\mathbf{k} \cdot \mathbf{R}} \quad (2.1.22)$$

The property (4) also indicates that the Wannier TB model can be constructed by the site energies $\epsilon_{n\mathbf{0}} = \tilde{H}_{nn\mathbf{0}}$ and hopping parameters $\tilde{H}_{nm\mathbf{R}}$ in real space. The amplitude of the hopping parameters decays rapidly with $|\mathbf{R}|$ because of the property (3). As a consequence, a few numbers of hopping parameters dominantly contribute to the Hamiltonian. By solving Eq. (2.1.16), one can reproduce the DFT band dispersion.

As mentioned in the property (5), since there is no unique way to construct the WFs up to the phase factor, the remaining question is how to define the unitary transformation matrix $U_{\mathbf{k}}$. A well-known method to overcome this difficulty is the maximal localization procedure [77, 78] as shown

below. Let us introduce the sum of variance of all WFs:

$$\Omega = \sum_{n=1}^J \left[\langle \tilde{w}_{n\mathbf{0}} | r^2 | \tilde{w}_{n\mathbf{0}} \rangle - |\langle \tilde{w}_{n\mathbf{0}} | \mathbf{r} | \tilde{w}_{n\mathbf{0}} \rangle|^2 \right] \quad (2.1.23)$$

A maximally-localized Wannier function (MLWF) is obtained by minimizing Ω . Ω is decomposed into a gauge invariant term Ω_{I} and a variant term $\tilde{\Omega}$,

$$\Omega = \Omega_{\text{I}} + \tilde{\Omega} = \Omega_{\text{I}} + \Omega_{\text{D}} + \Omega_{\text{OD}} \quad (2.1.24)$$

$$\Omega_{\text{I}} = \sum_{n=1}^J \left[\langle \tilde{w}_{n\mathbf{0}} | r^2 | \tilde{w}_{n\mathbf{0}} \rangle - \sum_{m\mathbf{R}} |\langle \tilde{w}_{m\mathbf{R}} | \mathbf{r} | \tilde{w}_{n\mathbf{0}} \rangle|^2 \right] \quad (2.1.25)$$

$$\Omega_{\text{D}} = \sum_{n=1}^J \sum_{\mathbf{R} \neq \mathbf{0}} |\langle \tilde{w}_{n\mathbf{R}} | \mathbf{r} | \tilde{w}_{n\mathbf{0}} \rangle|^2 \quad (2.1.26)$$

$$\Omega_{\text{OD}} = \sum_{m \neq n} \sum_{\mathbf{R}} |\langle \tilde{w}_{m\mathbf{R}} | \mathbf{r} | \tilde{w}_{n\mathbf{0}} \rangle|^2 \quad (2.1.27)$$

By using the projection operator $P = \sum_{n\mathbf{R}} |\tilde{w}_{n\mathbf{R}}\rangle \langle \tilde{w}_{n\mathbf{R}}|$ and its complement $Q = I - P$, Ω_{I} recasts as

$$\Omega_{\text{I}} = \sum_{\alpha} \sum_n \langle \tilde{w}_{n\mathbf{0}} | r_{\alpha} Q r_{\alpha} | \tilde{w}_{n\mathbf{0}} \rangle = \sum_{\alpha} \text{Tr} [P r_{\alpha} Q r_{\alpha}] \quad (2.1.28)$$

Using the relations $PP^{\dagger} = P$ and $QQ^{\dagger} = Q$, Ω_{I} can be further transformed as

$$\Omega_{\text{I}} = \sum_{\alpha} \text{Tr} \left[(P r_{\alpha} Q) (P r_{\alpha} Q)^{\dagger} \right] = \sum_{\alpha} \|P r_{\alpha} Q\|^2 \geq 0 \quad (2.1.29)$$

As a result, Ω_{I} is gauge invariant positive definite, and Ω_{D} and Ω_{OD} are also positive definite. Thus, minimizing Ω corresponds to minimizing $\tilde{\Omega} = \Omega_{\text{D}} + \Omega_{\text{OD}} \geq 0$.

To obtain well-localized WFs, a better choice of the initial guess for the iterative calculation of $U_{\mathbf{k}}$ is crucial. The projection procedure is a widely used method to construct an initial guess systematically [77]. Let us start with the J trial orbitals $|\varphi_n\rangle$ ($n = 1, \dots, J$) that are localized in the home unit cell, such as atomic-like s , p , d , and f orbitals (See Appendix B in detail). $|\varphi_n\rangle$ is projected onto the Bloch manifold at \mathbf{k} as

$$|\phi_{n\mathbf{k}}\rangle = \sum_{m=1}^J |\psi_{m\mathbf{k}}\rangle \langle \psi_{m\mathbf{k}} | \varphi_n \rangle = \sum_{m=1}^J A_{mn\mathbf{k}} |\psi_{m\mathbf{k}}\rangle \quad (2.1.30)$$

Note that $(A_{\mathbf{k}})_{mn} = A_{mn\mathbf{k}} = \langle \psi_{m\mathbf{k}} | \varphi_n \rangle$ is not a unitary matrix. By using the overlap matrix $S_{nm\mathbf{k}} = \langle \phi_{n\mathbf{k}} | \phi_{m\mathbf{k}} \rangle = \left(A_{\mathbf{k}}^{\dagger} A_{\mathbf{k}} \right)_{nm}$, $|\phi_{n\mathbf{k}}\rangle$ is transformed as

$$|\tilde{\psi}_{n\mathbf{k}}\rangle = \sum_{m=1}^J \left(S_{\mathbf{k}}^{-1/2} \right)_{mn} |\phi_{m\mathbf{k}}\rangle = \sum_{m=1}^J \left[A_{\mathbf{k}} (A_{\mathbf{k}}^{\dagger} A_{\mathbf{k}})^{-1/2} \right]_{mn} |\psi_{m\mathbf{k}}\rangle \quad (2.1.31)$$

Since the transformation matrix $S_{\mathbf{k}}^{-1/2} = A_{\mathbf{k}} (A_{\mathbf{k}}^{\dagger} A_{\mathbf{k}})^{-1/2}$ is unitary, it can be chosen as the initial guess of $U_{\mathbf{k}}$. Notably, when the maximal localization procedure is neglected, the obtained WFs roughly preserve the symmetry of the trial orbitals $|\varphi_n\rangle$.

Figure 2.2(a) shows the comparison of the band dispersion of SrVO₃ between the DFT calculation

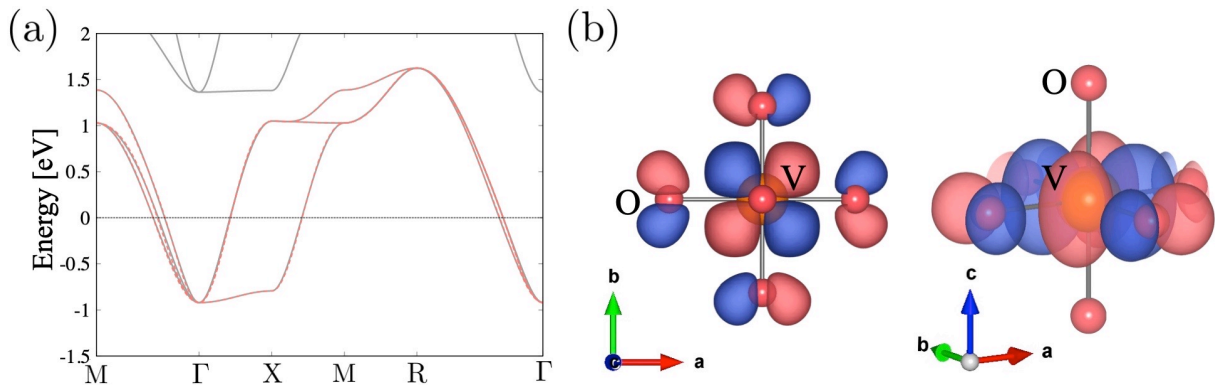


Figure 2.2: (a) The comparison of the band dispersion of SrVO₃ between the DFT calculation and the Wannier TB model. The Fermi energy is taken as the origin. The solid grey lines are band dispersion of the DFT calculation, while the dashed red lines are that of the Wannier TB model. (b) One of the MLWFs with d_{xy} orbital-like symmetry. It has weights around O atoms with p orbital-like symmetry.

and the Wannier TB model. The following atomic t_{2g} orbitals are adopted as the trial functions to construct the MLWFs,

$$\varphi_{yz}(\mathbf{r}) = 2e^{-r} \sqrt{\frac{15}{4\pi}} \frac{yz}{r^2}, \quad \varphi_{zx}(\mathbf{r}) = 2e^{-r} \sqrt{\frac{15}{4\pi}} \frac{zx}{r^2}, \quad \varphi_{xy}(\mathbf{r}) = 2e^{-r} \sqrt{\frac{15}{4\pi}} \frac{xy}{r^2} \quad (2.1.32)$$

As shown in Fig. 2.2(a), the band dispersion obtained from the DFT calculation is accurately reproduced by the obtained Wannier TB model.

As shown in Fig. 2.2(b), although the MLWFs have similar symmetry properties with that of the trial t_{2g} orbitals near V atom, they have weights around O atoms with p orbital-like symmetry. This is because the three electronic states near the Fermi level are the anti-bonding orbitals composed of the t_{2g} orbitals at the V atom and the p orbitals at the O atoms. In order to obtain well-localized WFs at the V atom, the p orbital of the O atoms must be involved. On the other hand, doing so would increase the size of the Hamiltonian matrix, resulting in a more complicated TB model.

Entangled Bands

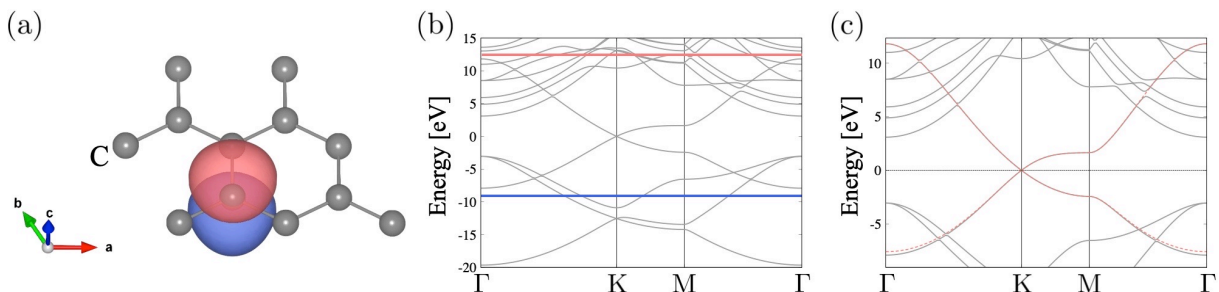


Figure 2.3: (a) Crystal structure of two-dimensional graphene and the one of the MLWFs with p_z orbital-like symmetry. (b) Band dispersion obtained from a DFT calculation. The Fermi energy is taken as the origin. The energy window between the red and blue lines consists of entangled bands. (c) The comparison of the band dispersion near the Fermi level between the DFT calculation (solid grey lines) and the Wannier TB model (dashed red lines).

Usually, the bands of interest are not isolated from others, such as metals or the empty bands of

insulators. In this case, the procedure given in the previous section is not applicable. Graphene is one such example. Graphene has a hexagonal crystal structure with the space group $P6/mmm$ (#191, D_{6h}^1) as shown in Fig. 2.3(a). Figure 2.3(b) shows the non-isolated groups of bands near the Fermi level obtained from the DFT calculation using QUANTUM ESPRESSO [66]. Within the energy window between the red and blue lines, the bands are entangled and mixed with others outside the energy window. Since the number of bands in the energy window can be different at each \mathbf{k} point, $N^{(\mathbf{k})}$, the N Bloch states of interest is obtained by performing a unitary transformation among $N^{(\mathbf{k})} > N$ Bloch states in the energy window [78]:

$$|\tilde{\psi}_{n\mathbf{k}}\rangle = \sum_{m=1}^{N^{(\mathbf{k})}} U_{mn\mathbf{k}} |\psi_{m\mathbf{k}}\rangle \quad (2.1.33)$$

$$|\tilde{u}_{n\mathbf{k}}\rangle = \sum_{m=1}^{N^{(\mathbf{k})}} U_{mn\mathbf{k}} |u_{m\mathbf{k}}\rangle \quad (2.1.34)$$

The fixed number J in Eq. (2.1.6) is replaced by the \mathbf{k} dependent number $N^{(\mathbf{k})}$. Note that $U_{mn\mathbf{k}}$ is a rectangular $N^{(\mathbf{k})} \times N$ matrix and Eq. (2.1.33) is still a unitary transformation in the sense that $U_{\mathbf{k}}^\dagger U_{\mathbf{k}} = 1_N$ where 1_N is a $N \times N$ identity matrix. $U_{mn\mathbf{k}}$ is determined by minimizing Ω_{I} and the MLWFs are obtained by minimizing $\tilde{\Omega}$. In addition, choosing appropriate energy windows and initial trial orbitals is significant to reproduce the original DFT band dispersion accurately. The detailed procedure to obtain $U_{\mathbf{k}}$ is found in Ref. [78].

We construct a minimum Wannier TB model for graphene. By choosing the p_z orbital as a trial orbital, we obtain a MLWF as shown in Fig. 2.3(a). As shown in Fig. 2.3(c), the obtained TB model well reproduces the DFT band dispersion near the Dirac point at K point. Thus, following the above technique, we can generate a Wannier TB model even when the bands of interest are entangled.

2.1.2 Advantages and Disadvantages

In this section, we present some advantages and disadvantages of using the Wannier TB model.

Advantages

The most remarkable advantage of using the Wannier TB model is that it allows quantitative calculations. The Wannier TB model reproduces the DFT band dispersion accurately, and the model parameters are systematically derived from the DFT calculation. Therefore, the systematic scheme based on the WFs has been widely used to analyze various properties quantitatively. For example, by incorporating electron-phonon interactions into the Wannier TB model in a perturbative manner, various phonon-related physics, such as superconductivity and electric/heat transport phenomena have been analyzed quantitatively [79]. Furthermore, the WFs enable us to evaluate the coupling constants of the local Coulomb interaction U , Hund's coupling J , and then the multi-orbital Hubbard model can be generated systematically to take account of electron correlations beyond the DFT scheme [80, 81].

In addition, the interpolation procedure by means of the MLWFs is also powerful tool to create a compact TB Hamiltonian. Since the MLWFs is well-localized in real space, the hopping parameters rapidly decay with the distance between a pair of two WFs, leading the Hamiltonian matrix sparse. Moreover, MLWFs provide intuitive understanding in real-space properties especially chemical bonding and electric polarization. There has been a long discussion about the definition of the electric polarization in crystal, $\mathbf{P} = \int d\mathbf{r} \mathbf{r} \rho(\mathbf{r})$, because \mathbf{r} is ill defined, i.e., $|\mathbf{P}|$ diverges at $|\mathbf{r}| \rightarrow \infty$. The

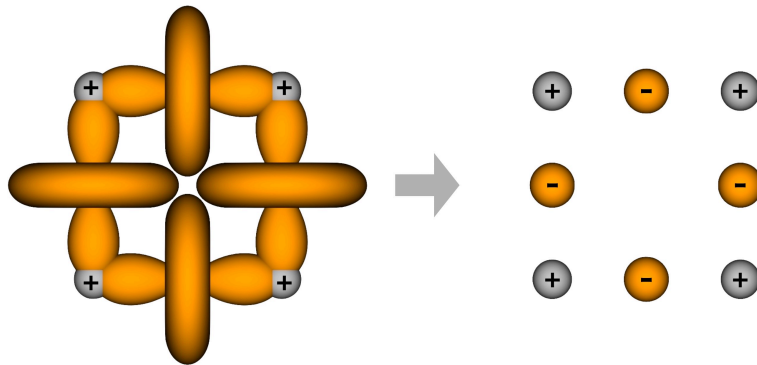


Figure 2.4: Mapping of the actual complicated electronic charge clouds (left) to a simple point charge located at the Wannier centers (right). The grey (orange) points represent the (ion) Wannier center with “+” (“-”) symbol that denotes the nuclei charge (electronic charge located at the Wannier center).

paradigm shift has been brought about by the establishment of so-called modern theory of polarization, based on the works of Resta [82–84], King-Smith and Vanderbilt [85–87]. Following theory, the electric polarization in the periodic crystal is defined by using the Berry connection as

$$\mathbf{P} = -\frac{e}{\Omega_0 N} \sum_n^{\text{occ.}} \sum_{\mathbf{k}} \mathbf{a}_{n\mathbf{k}} + \mathbf{P}^{(0)} = -\frac{e}{\Omega_0} \sum_n^{\text{occ.}} \bar{\mathbf{r}}_n, \quad \mathbf{P}^{(0)} = -\frac{e}{\Omega_0} N_b \mathbf{R} \quad (2.1.35)$$

where Ω_0 is the unit-cell volume and occ. means that the summation is taken over N_b occupied bands below the Fermi energy in the band gap. Thus, \mathbf{P} is defined as gauge invariant modulo $\mathbf{P}^{(0)}$ same as the Berry phase. As shown in the second equation in Eq. (2.1.35), the electric polarization is determined by using the Wannier centers $\bar{\mathbf{r}}_n$ of the occupied bands. In other words, the realistic complicated charge distribution can be replaced by $-e$ point charges located at the Wannier centers as depicted in Fig. 2.4. The Bloch and Wannier representations of polarization given in the first and second equations in Eq. (2.1.35) enable us to quantitatively evaluate the polarization in insulators based on DFT-based Wannier TB model.

On the other hand, recent studies have developed some evaluation schemes of the hidden electronic degrees of freedom and their related physics based on DFT calculation and Berry curvature physics. For example, a systematic formalism to numerically evaluate the macroscopic magnetic monopole $M_0 = \int d\mathbf{r} \mathbf{r} \cdot \boldsymbol{\mu}(\mathbf{r})$ ($\boldsymbol{\mu}$ is the magnetization density) based on DFT framework has been developed [88–90]. M_0 is one of the order parameters that give rise to the ME effect. For collinear spin systems, the Bloch and Wannier representations of M_0 are defined by analogy to the electric polarization [90]:

$$M_0 = \frac{\mu_B}{3\Omega_0 N} \sum_{\mathbf{k}} \sum_{\sigma}^{\uparrow\downarrow} \sum_{n^\sigma}^{\text{occ.}} \sigma a_{n^\sigma n^\sigma \mathbf{k}}^z + M_0^{(0)} = \frac{\mu_B}{3\Omega_0} \sum_{\sigma}^{\uparrow\downarrow} \sum_{n^\sigma}^{\text{occ.}} \sigma \bar{r}_{n^\sigma}^z, \quad M_0^{(0)} = \frac{\mu_B}{\Omega_0} (N_b^\uparrow - N_b^\downarrow) R^z \quad (2.1.36)$$

where n^σ is the band index of the spin $\sigma = \uparrow, \downarrow$ state and N^σ is the number of the occupied states with spin σ . Similar to the electric polarization given in Eq. (2.1.35), M_0 is defined as gauge invariant modulo $M_0^{(0)}$. Based on Eq. (2.1.36), M_0 for collinear magnetic insulator can be quantitatively evaluated by using the Berry connection obtained from DFT calculation or by calculating the difference of the Wannier center between spin-up and spin-down states.

The another example is the study for the gigantic AHE observed in the non-collinear AFM Mn_3Sn based on the Wannier TB model by M.-T. Suzuki *et al.* [29]. The anomalous Hall conductivity (AHC)

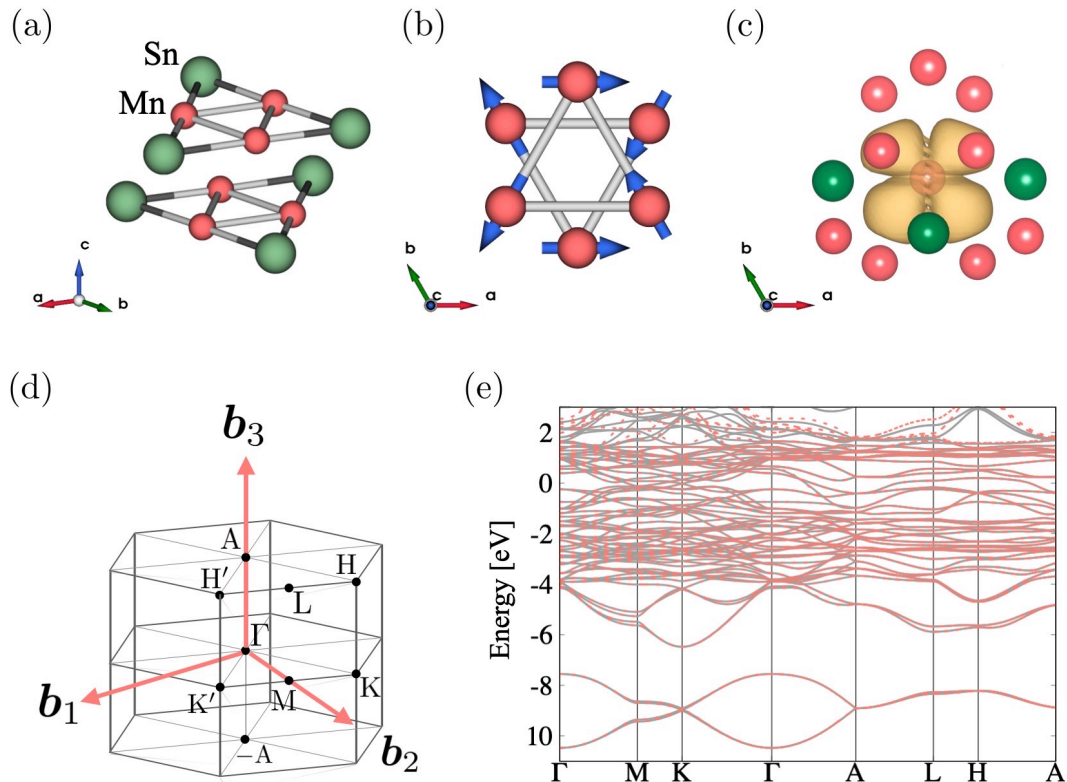


Figure 2.5: (a) Crystal and (b) AFM structures of Mn_3Sn . (c) One of the WFs with d_{xy} like symmetry (the phase is not shown). (d) Brillouin zone and (e) the comparison of the band dispersion between the DFT calculation (solid grey lines) and the Wannier TB model (dashed red lines).

is generally obtained by

$$\sigma_{\alpha\beta}^{\text{AHC}} = -\frac{e^2}{\hbar V} \sum_{\gamma} \epsilon_{\alpha\beta\gamma} \sum_{\mathbf{k}} \Omega_{\mathbf{k}}^{\gamma} \quad (2.1.37)$$

$$\Omega_{\mathbf{k}}^{\gamma} = \sum_n f_{n\mathbf{k}} \Omega_{n\mathbf{k}}^{\gamma} \quad (2.1.38)$$

where $\epsilon_{\alpha\beta\gamma}$ is the Levi-Civita symbol, $f_{n\mathbf{k}} = [1 + \exp(\beta\epsilon_{n\mathbf{k}})]^{-1}$ is the Fermi-Dirac distribution function, and V is the system volume. $\Omega_{\mathbf{k}}^{\gamma}$ is the sum of the Berry curvature of each band $\Omega_{n\mathbf{k}}$ that is defined as the rotation of the Berry connection:

$$\Omega_{n\mathbf{k}} = \nabla_{\mathbf{k}} \times \mathbf{a}_{n\mathbf{k}} = i \sum_{m \neq n} \mathbf{a}_{m\mathbf{k}} \times \mathbf{a}_{n\mathbf{k}} \quad (2.1.39)$$

Thus, by using Eqs. (2.1.38) and (2.1.39), the AHC can be quantitatively evaluated by calculating the Berry curvature/connection based on the Wannier TB model. In addition, from Eq. (2.1.37), one can realize that the origin of the AHE is different from a net magnetization which is given by the integration of spin moment over the entire BZ. In other words, the existence of the net magnetization is not necessary for the emergence of AHE.

Figure 2.5 (a) represents the crystal structure of bulk crystalline Mn_3Sn , which belongs to the space group $P6_3/mmc$ (#194, D_{6h}^4) [91, 92]. In Mn_3Sn , AFM phase with inverse triangular spin structure emerges below the Neel temperature of $T_N \simeq 420$ K [93, 94] as shown in Fig. 2.5(b). We construct the Wannier TB model of Mn_3Sn with Mn s, d and Sn s, p initial orbitals. One of the obtained WFs without the maximal localization procedure is shown in Fig. 2.5(c). Although the

shape of the WF is similar to d_{xy} orbital, it is distorted because of the surrounding environment. As shown in Fig. 2.5(e), the DFT band dispersion is well reproduced by the Wannier TB model. Since $\Omega_{\mathbf{k}}^x$ is negative in most region of the BZ, the AHC becomes positive finite according to Eq. (2.1.37) [29]. The AHC evaluated by M.-T. Suzuki *et al.* in Ref. [29] is $\sigma_{yz}^{\text{AHC}} = 129$ S/cm with Mn magnetic moment $3.39 \mu_B$, which are consistent with the experiment, $\sigma_{yz}^{\text{AHC}} 100$ S/cm and $3 \mu_B$ [20]. Thus, the analysis based on the Wannier TB model clarifies that the AHE occurs even in the non-collinear AFM Mn_3Sn .

The advantages of using the Wannier TB model are summarized below.

- (1) The Wannier TB model reproduces the band dispersion obtained from the DFT calculation.
- (2) The model parameters are derived from the DFT calculation.
- (3) Since the MLWFs are well-localized in real space, the hopping parameters rapidly decay with the distance between a pair of two WFs, leading to the Hamiltonian matrix sparse.
- (4) MLWFs have the advantage of providing intuitive understanding in real-space discussions especially chemical bonding and electric polarization.
- (5) Berry connection and curvature, and their related quantities, such as electric polarization, bulk magnetic monopole, and AHC can be evaluated quantitatively.
- (6) There is a variety of open-source software packages that provides an interface to the Wannier90 code and a tool to systematically construct or analyze the Wannier TB Hamiltonian, such as PythTB (see <http://www.physics.rutgers.edu/pythtb/>), WannierBerri [95], TBM [96].

Disadvantages

Using the DFT-based Wannier TB model, we can quantitatively analyze various physical properties of interest. In addition, the MLWFs give us an intuitive and deeper understanding of the Berry phase physics, such as electric polarization. On the other hand, there might be some disadvantages or problems summarized below:

- (1) The symmetry of the given material would be broken by numerical error in
- (2) The microscopic expression of the order parameter and the microscopic mechanism of their related physics often remain obscure.
- (3) Although the hopping parameters of small magnitude for sufficiently far bonds seem to be neglected safely, the removal of such hoppings results in the difficulty to reproduce the original DFT band dispersion.

Let us first focus on the problem (1). As shown in Sec. 2.1.1, since the bands are entangled in most cases, the disentanglement procedure is necessary. In this case, some eigenstates are discarded in the disentanglement procedure, leading to the loss of accuracy of the band structure of the given system. D. Gresch *et al.* mentions the detail of this problem in Ref. [97]. Owing to this problem, the obtained Wannier band dispersion includes the unexpected slight lifting of the degeneracies in the DFT band dispersion as shown in Fig. 1(b) in Ref. [97]. This seemingly trivial issue can lead to unexpected behavior of some properties that are sensitive to symmetry and topology of the electronic states. In addition, the problem also results in the superfluous hopping parameters that must be zero

because of the symmetry. D. Gresch *et al.* have proposed a solution to the problem by recreating the symmetrized Hamiltonian as

$$H^{(\text{sym})}(\mathbf{k}) = \frac{1}{N_g} \sum_{\mathcal{G} \in G} D_{\mathbf{k}}(\mathcal{G}) H(\mathbf{k}) D_{\mathbf{k}}(\mathcal{G}^{-1}) \quad (2.1.40)$$

where G is the space group, $D_{\mathbf{k}}(\mathcal{G})$ is the \mathbf{k} -dependent representation matrix of the symmetry operation \mathcal{G} , and N_g is the total number of symmetry operations. To use this method, the WFs must have the same symmetry properties as the initial atomic orbitals. However, the disentanglement procedure mixes multiple atomic orbitals and the symmetry of the obtained WFs is often lower than that of the initial atomic orbitals as shown in Fig. 2.5(c). In addition, the maximal localization procedure must be omitted as well, because the initial atomic orbitals are mixed in this process. Meanwhile, the maximal localization procedure itself has another problem in that the symmetry is not considered as well as the disentanglement procedure. R. Sakuma mentioned this problem and proposed the algorithm to create symmetry-adapted WFs [98]. However, note that this method is not always applicable.

Next, let us discuss the problem (2). As shown in the previous section, the Wannier TB model is indeed superior in the quantitative analysis of material properties. However, the microscopic expression of the order parameter and the microscopic mechanism of its related physics often remain obscure. For example, as for the AHE in non-collinear AFM Mn_3Sn , the microscopic mechanism of the AHE, such as the implicit couplings among AFM ordering, electron hopping, and SOC, have remained unclear. In addition, non-trivial physical phenomena driven by unfamiliar electronic multipole orders, such as the electric toroidal dipole \mathbf{G} and monopole G_0 , which are closely related to the lattice rotation and crystal chirality respectively, have yet to be understood at the microscopic level.

It should be emphasized that the WFs typically contain no useful information except for their location and geometric shape, hampering such analysis from a microscopic point of view. Since the WFs are not characterized by the atomic orbital and magnetic quantum numbers (l, m) or irreducible representation and its component of a given symmetry, (Γ, γ) , the symmetry argument is more difficult than a description using the atomic orbital that is characterized by (l, m) or (Γ, γ) . In addition, it is also difficult to exactly define the matrix form of the basic atomic operators, such as the electric quadrupole $Q_{xy} \propto xy$, atomic angular momentum $\mathbf{l} = \mathbf{r} \times \mathbf{p}$ (\mathbf{r} is a position operator of an electron belongs to one nucleus), electric toroidal dipole $\mathbf{G} = \mathbf{l} \times \boldsymbol{\sigma}$, and so on. For example, as shown in Fig. 2.5(c), the WFs located at Mn atom in Mn_3Sn clearly different from the initial d orbitals, because of the disentanglement procedure. Thus, the atomic orbital angular momentum operator l_z at a Mn atom can not be defined by a simple 5×5 matrix with the basis functions, $(d_u, d_v, d_{yz}, d_{zx}, d_{xy})$ (See Appendix B in detail):

$$\langle \text{WFs} | l_z | \text{WFs} \rangle \neq \begin{pmatrix} 0 & 0 & 0 & 0 & 0 \\ 0 & 0 & 0 & 0 & -2i \\ 0 & 0 & 0 & i & 0 \\ 0 & 0 & -i & 0 & 0 \\ 0 & 2i & 0 & 0 & 0 \end{pmatrix} \quad (2.1.41)$$

In order to systematically investigate various electronic multipoles such as \mathbf{G} and G_0 , it is highly desirable to define their corresponding quantum-mechanical operator as analytic form of matrix. To realize this, the atomic orbitals are more appropriate than WFs as the basis function of the TB model.

The last problem (3) increases computational cost, e.g., calculating the electron-phonon couplings. Moreover, it is difficult to identify which model parameter plays a crucial role in the physics of interest, hampering an intuitive and deeper understanding of it.

2.2 Tight-Binding Model Based on Atomic Orbitals

In this section, we briefly show the another approach to construct the effective TB model based on the atomic orbitals.

The atomic orbital is defined by the multiplication of the radial function and spherical harmonics:

$$\varphi_a(\mathbf{r}) \equiv \varphi_{nlm}(\mathbf{r}) = R_{nl}(r)Y_{lm}(\hat{\mathbf{r}}) \quad (2.2.1)$$

where an abbreviation $a = (n, l, m)$ is introduced (m is a magnetic quantum number or a subscript of the orbitals in real representation). The real representation of the angular part of the atomic orbitals are defined by arbitrary linear combinations of Y_{lm} within the same l (See Appendix B). The atomic orbital located at a sublattice s in the unit-cell \mathbf{R} is given by

$$\varphi_{as\mathbf{R}}(\mathbf{r}) \equiv \varphi_a(\mathbf{r} - (\mathbf{R} + \mathbf{s})) \quad (2.2.2)$$

where \mathbf{s} is the position of the sublattice s within the home unit cell, $\mathbf{R} = \mathbf{0}$. Similar to Eqs. (2.1.4) and (2.1.5), the BF is defined by using the atomic orbitals as

$$|\psi_{as\mathbf{k}}\rangle = \frac{1}{\sqrt{N}} \sum_{\mathbf{R}} |\varphi_{as\mathbf{R}}\rangle e^{i\mathbf{k}\cdot(\mathbf{R}+\mathbf{s})} \quad (2.2.3)$$

$$|\varphi_{as\mathbf{R}}\rangle = \frac{1}{\sqrt{N}} \sum_{\mathbf{k}} |\psi_{as\mathbf{k}}\rangle e^{-i\mathbf{k}\cdot(\mathbf{R}+\mathbf{s})} \quad (2.2.4)$$

Note that the atomic orbitals are not orthogonal basis:

$$S_{ss'}^{aa'}(\mathbf{R}) = \langle \varphi_{as\mathbf{R}} | \varphi_{a's'\mathbf{0}} \rangle = \frac{1}{N} \sum_{\mathbf{k}} \langle \psi_{as\mathbf{k}} | \psi_{a's'\mathbf{k}} \rangle e^{i\mathbf{k}\cdot((\mathbf{R}+\mathbf{s})-\mathbf{s}')} = \frac{1}{N} \sum_{\mathbf{k}} S_{ss'}^{aa'}(\mathbf{k}) e^{i\mathbf{k}\cdot((\mathbf{R}+\mathbf{s})-\mathbf{s}')} \quad (2.2.5)$$

$$S_{ss'}^{aa'}(\mathbf{k}) = \langle \psi_{as\mathbf{k}} | \psi_{a's'\mathbf{k}} \rangle = \sum_{\mathbf{R}} S_{ss'}^{aa'}(\mathbf{R}) e^{-i\mathbf{k}\cdot((\mathbf{R}+\mathbf{s})-\mathbf{s}')} \quad (2.2.6)$$

$S_{ss'}^{aa'}(\mathbf{R})$ is the overlap matrix. The matrix elements of the Hamiltonian are given by

$$H_{ss'}^{aa'}(\mathbf{R}) = \langle \varphi_{as\mathbf{R}} | H | \varphi_{a's'\mathbf{0}} \rangle = \frac{1}{N} \sum_{\mathbf{k}} \langle \psi_{as\mathbf{k}} | H | \psi_{a's'\mathbf{k}} \rangle e^{i\mathbf{k}\cdot((\mathbf{R}+\mathbf{s})-\mathbf{s}')} = \frac{1}{N} \sum_{\mathbf{k}} H_{ss'}^{aa'}(\mathbf{k}) e^{i\mathbf{k}\cdot((\mathbf{R}+\mathbf{s})-\mathbf{s}')} \quad (2.2.7)$$

$$H_{ss'}^{aa'}(\mathbf{k}) = \langle \psi_{as\mathbf{k}} | H | \psi_{a's'\mathbf{k}} \rangle = \sum_{\mathbf{R}} H_{ss'}^{aa'}(\mathbf{R}) e^{-i\mathbf{k}\cdot((\mathbf{R}+\mathbf{s})-\mathbf{s}')} \quad (2.2.8)$$

The eigenstates $|\psi_{n\mathbf{k}}\rangle$ and eigenvalues $\epsilon_{n\mathbf{k}}$ of Eq. (2.2.8) are obtained by solving the secular equations:

$$\sum_{a's'} \left[H_{ss'}^{aa'}(\mathbf{k}) - \epsilon_{n\mathbf{k}} S_{ss'}^{aa'}(\mathbf{k}) \right] U_{n,a's'}(\mathbf{k}) = 0 \quad (2.2.9)$$

$$|\psi_{n\mathbf{k}}\rangle = \sum_{as} U_{n,as}(\mathbf{k}) |\psi_{as\mathbf{k}}\rangle \quad (2.2.10)$$

We summarize the most significant differences between the Wannier TB model and the TB model based on the atomic orbitals.

(1) Orthogonality

While the WFs are orthogonal basis, the atomic orbitals are non-orthogonal, $S_{ss'}^{aa'}(\mathbf{R}) \neq 0$. However, the atomic orbitals are often treated as orthogonal basis approximately, i.e., $S_{ss'}^{aa'}(\mathbf{R}) \simeq N^{-1} \delta_{\mathbf{R}\mathbf{0}} \delta_{aa'} \delta_{ss'}$, $S_{ss'}^{aa'}(\mathbf{k}) \simeq \delta_{aa'} \delta_{ss'}$. Hereafter, we follow this approximation.

(2) Gauge indeterminacy

Similar to the WFs, atomic orbitals depend on gauge (phase). Nevertheless, the gauge in atomic orbitals are easier to control than the WFs. The phase $e^{-i\mathbf{k}\cdot\mathbf{s}}$ added in Eq. (2.2.4) is suitable choice for symmetry arguments. Hereafter, we adopt this gauge.

(3) Model building process

The DFT-based WFs are derived from the BFs obtained from the DFT band calculation and the DFT band dispersion is automatically reproduced. On the other hand, the atomic orbitals are introduced manually unless DFT solver is based on the atomic orbitals.

(4) Flexibility of the model

$H_{ss'}^{aa'}(\mathbf{R})$ is a controllable parameter. $\epsilon^{aa'}(s) = H_{ss}^{aa'}(\mathbf{0})$ corresponds to the crystal field parameter at \mathbf{s} site in the unit-cell and $t_{ss'}^{aa'}(\mathbf{R}) = H_{ss'}^{aa'}(\mathbf{R})$ is the hopping parameter, and they must satisfy the symmetry of the given system. When building a TB model using atomic orbitals, we can choose a small number of orbitals of interest and freely control the model parameters and system size, enabling us to analyze the physics of interest flexibly. Since the atomic orbitals are characterized by (l, m) or (Γ, γ) , the symmetry arguments are more straightforward than the WFs. Moreover, any atomic operator matrices can be defined universally.

(5) Optimization of the model

As shown above, the Wannier TB model is derived from the DFT calculation directly, whereas the TB model based on the atomic orbitals includes empirical model parameters, $\epsilon^{aa'}(s)$ and $t_{ss'}^{aa'}(\mathbf{R})$. One way to determine the TB model parameters is to reproduce the DFT band dispersion.

As shown in (5), to reproduce the DFT band dispersion, we need to optimize the model parameters, $\epsilon^{aa'}(s)$ and $t_{ss'}^{aa'}(\mathbf{R})$, appropriately. Since $\epsilon^{aa'}(s)$ and $t_{ss'}^{aa'}(\mathbf{R})$ must satisfy the symmetry of the system, they are determined by the atomic orbitals $\varphi_{as\mathbf{R}}, \varphi_{a's'\mathbf{0}}$, bond vector $\mathbf{R}_{ss'} \equiv (\mathbf{R} + \mathbf{s}) - \mathbf{s}'$, and surrounding environment. The Slater-Koster approach is a well-known method to determine independent hopping parameters according to the symmetry of the atomic orbitals and bond vector [99]. When $\mathbf{R}_{ss'}$ is chosen as the z axis, the atomic orbitals $\varphi_{n_s l_s m_s s \mathbf{R}}, \varphi_{n_{s'} l_{s'} m_{s'} s' \mathbf{0}}$ are proportional to $e^{im_s \phi}, e^{im_{s'} \phi}$ where ϕ is the azimuthal angle measured from the x axis. In the Slater-Koster approach, the Hamiltonian is approximated to have axial symmetry along the z axis, and then hopping matrix elements vanish when $m_s \neq m_{s'}$:

$$t_{ss'}^{aa'}(\mathbf{R}) \propto \int_0^{2\pi} \frac{d\phi}{2\pi} e^{-i(m_s - m_{s'})\phi} = \delta_{m_s m_{s'}} \quad (2.2.11)$$

As a consequence, there are only ten independent Slater-Koster parameters for s, p, d orbitals [99]:

$$\begin{aligned}
V_{ss\sigma} &= \langle \varphi_s | H | \varphi_s \rangle, & V_{sp\sigma} &= \langle \varphi_s | H | \varphi_{p0} \rangle, & V_{sd\sigma} &= \langle \varphi_s | H | \varphi_{d0} \rangle \\
V_{pp\sigma} &= \langle \varphi_{p0} | H | \varphi_{p0} \rangle, & V_{pd\sigma} &= \langle \varphi_{p0} | H | \varphi_{d0} \rangle, & V_{dd\sigma} &= \langle \varphi_{d0} | H | \varphi_{d0} \rangle \\
V_{pp\pi} &= \langle \varphi_{p\pm 1} | H | \varphi_{p\pm 1} \rangle, & V_{pd\pi} &= \langle \varphi_{p\pm 1} | H | \varphi_{d\pm 1} \rangle, & V_{dd\pi} &= \langle \varphi_{d\pm 1} | H | \varphi_{d\pm 1} \rangle \\
V_{dd\delta} &= \langle \varphi_{d\pm 2} | H | \varphi_{d\pm 2} \rangle
\end{aligned} \tag{2.2.12}$$

where σ, π, δ denote $|m| = 0, 1, 2$. In general, when the quantization axis of the atomic orbitals is different from the bond direction, the hopping matrix elements can be obtained by using the direction cosine, $\mathbf{R}_{ss'}/|\mathbf{R}_{ss'}| = (l, m, n)$, as shown in Table B.1. Note that the matrix elements that are not included in Table B.1 can be obtained by permutation of indices and cosine directions of the other matrix elements in Table B.1. To our knowledge, there are some open-source software packages that enable us to automatically generate the TB Hamiltonian based on the Slater-Koster approach, such as Tight-Binding Studio [100].

Following the Slater-Koster approach, we can implement the electronic structure calculation by using the Slater-Koster parameters with low computational cost. However, since it assumes the axial symmetry along the bond direction and neglects the surrounding environment, some essential parameters could be lost.

2.3 Summary

As discussed above, the WFs and the atomic orbitals are widely used to construct the DFT-based TB model, both of which have advantages and disadvantages.

The Wannier TB model is superior in terms of quantitative calculation, since it well reproduces the DFT calculations. However, while the WF is well localized in real space, it exhibits low symmetry and is not characterized by any quantum number, such as the atomic orbital and magnetic quantum numbers or irreducible representation of relevant point group. Consequently, the WF is unsuitable for symmetry arguments and for defining the matrix form of the atomic operators universally, such as the atomic angular momentum \mathbf{l} , thus hindering the analysis of unconventional order parameters, e.g., the electric toroidal dipole $\mathbf{G} = \mathbf{l} \times \mathbf{s}$ and the electric toroidal monopole G_0 .

On the other hand, the TB model based on the atomic orbitals with a small number of model parameters is a suitable choice for symmetry arguments and electronic structure calculations with low computational costs. In particular, following the Slater-Koster approach, we can construct a TB model satisfying partially the symmetry of a given system, which provides an intuitive understanding of the electronic band structure and various physics of interest. Nonetheless, some essential hopping parameters could be lost owing to the assumption of the axial symmetry along the bond direction. Furthermore, to construct the DFT-based TB model using the atomic orbitals, we must optimize the model parameters to reproduce the DFT band dispersion. However, this process is not straightforward. One of the difficulties is that the accuracy of the optimization strongly depends on the initial guess of the optimization parameters. From these circumstances, it is highly desirable to develop a systematic generation scheme to build TB models satisfying the symmetry of a given system and overcome these difficulties.

To realize this, we first introduce the symmetry-adapted multipole basis in Chap. 3, which enable us to describe any electronic degrees of freedom in materials. Then, in Chap. 4, we show a systematic generation scheme of a DFT-based TB model based on the symmetry-adapted multipole basis with the help of the machine learning techniques. The obtained TB model not only satisfies the symmetry of a given system precisely but also reproduces the DFT band dispersion with high accuracy. From the

result of parameter optimization, we can identify which multipole basis has a dominant contribution in the Hamiltonian. Additionally, since the atomic orbitals are used as basis functions, we can easily obtain the matrix form of any atomic operator in terms of these bases.

Chapter 3

Symmetry-Adapted Multipole Basis

In this chapter, we introduce the symmetry-adapted multipole basis (SAMB) [25, 26, 28, 101, 102], which enable us to describe any electronic degrees of freedom in materials.

To generate the SAMB systematically, we first decompose the electronic degrees of freedom in materials into orbital/spin and sublattice parts in Sec. 3.1, and then we introduce the definition of the SAMB. Next, in Sec. 3.2, we demonstrate a fundamental concept of multipole basis and review recent development of the multipole basis theory [25, 26, 28, 101, 102]. In Sec. 3.3, we present the definition of the atomic multipole basis for both spinless and spinful single-centered electron systems. In Sec. 3.4, we introduce the site-cluster and bond-cluster multipole basis that describes the intra and inter sublattice degrees of freedom in the isolated multi-site systems. Then, we define the SAMB as the linear combination of the direct product of the atomic and site/bond-cluster multipole basis. Furthermore, we extend the definition of the SAMB to the periodic crystals in Sec. 3.5.

3.1 Decomposition of Electronic Degrees of Freedom

First, let us introduce the bra-ket notation for an operator \hat{A} since each operator plays a role of basis vector to expand any physical operator:

$$\begin{aligned} |\hat{A}\rangle_{aa'} &= [\hat{A}]_{aa'}, & \langle \hat{A}|_{aa'} &= [\hat{A}^\dagger]_{aa'} = [\hat{A}]_{a'a}^* \\ \langle \hat{A}|\hat{B}\rangle &= \text{Tr}[\hat{A}^\dagger \hat{B}] = \sum_{aa'} [\hat{A}^\dagger]_{aa'} [\hat{B}]_{a'a} \\ \left(|\hat{A}\rangle \langle \hat{B}| \right)_{aa',bb'} &= [\hat{A}]_{aa'} [\hat{B}^\dagger]_{b'b} = [\hat{A}]_{aa'} [\hat{B}^*]_{bb'} \end{aligned} \quad (3.1.1)$$

Next, suppose that we have a complete orthonormal basis set of matrices $\{\hat{Z}_j\}$ in a given Hilbert space satisfying the orthonormal and complete relations:

$$\langle \hat{Z}_i|\hat{Z}_j\rangle = \delta_{ij}, \quad \left(\sum_i |\hat{Z}_i\rangle \langle \hat{Z}_i| \right)_{aa',bb'} = \delta_{ab} \delta_{a'b'} \quad (3.1.2)$$

Then, we can expand any operator $|\hat{A}\rangle$ as the linear combination of \hat{Z}_j :

$$|\hat{A}\rangle = \sum_j \langle \hat{Z}_j|\hat{A}\rangle |\hat{Z}_j\rangle = \sum_j z_j |\hat{Z}_j\rangle \quad (3.1.3)$$

where $z_j = \langle \hat{Z}_j|\hat{A}\rangle$ is the weight of contribution of $|\hat{Z}_j\rangle$ to $|\hat{A}\rangle$. Note that $|\hat{Z}_j\rangle$ has two constraints:

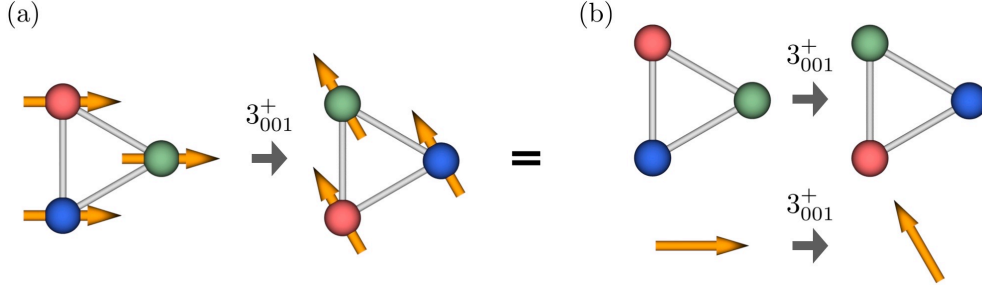


Figure 3.1: Decomposition of (a) the 3-fold rotation operation 3_{001}^+ into (b) site and atomic orbital parts.

- (1) Since \hat{A} is Hermitian, \hat{Z}_j must be also Hermitian provided that z_j is real.
- (2) Symmetry property of \hat{Z}_j must be same as that of \hat{A} .

In particular, when \hat{A} is the Hamiltonian, we can express it as the linear combination of \hat{Z}_j :

$$|\hat{H}\rangle = \sum_j z_j |\hat{Z}_j\rangle \quad (3.1.4)$$

where z_j corresponds to a model parameter. Since \hat{H} is fully symmetric for all the symmetry operations, $\mathcal{G}\hat{H}\mathcal{G}^{-1} = \hat{H}$, \hat{Z}_j must be also fully symmetric, $\mathcal{G}\hat{Z}_j\mathcal{G}^{-1} = \hat{Z}_j$. When the system preserves the time reversal symmetry, \hat{Z}_j must be time reversal even. Otherwise, \hat{Z}_j can be time reversal odd. We call such \hat{Z}_j as a symmetry-adapted basis that is characterized by the spatial inversion and time reversal parities \mathcal{P} and \mathcal{T} , and the irreducible representation of a given point group, Γ . One can realize that the crystal field Hamiltonian \hat{H}_{CEF} is an example that is obtained by the above idea:

$$|\hat{H}_{\text{CEF}}\rangle = \sum_j \phi_j |\hat{O}_j\rangle \quad (3.1.5)$$

where ϕ_j is the crystal field parameter and \hat{O}_j is the cubic or hexagonal harmonics or their Stevens' equivalent operators.

Thus, the remaining question is how to systematically generate the symmetry-adapted basis for various electron systems, such as single-centered electron systems, molecules, periodic crystals, and so on. To realize this, the SAMB, which is characterized by the irreducible representation and the time reversal and spatial inversion parities, is the most suitable choice for \hat{Z}_j .

In general, the electrons in crystallographic systems acquire site and bond degrees of freedom in addition to the atomic orbital (including spin) degrees of freedom, which hinders to obtain the explicit expression of \hat{Z}_j . Based on this circumstance, let us consider decomposing the electronic degrees of freedom into the site/bond and atomic orbital parts and treating them independently.

Let us consider a symmetry operation \mathcal{G} of the given system. \mathcal{G} can be separated into two parts; an operation moves a site (bond) to the other site (bond) and an operation that acts only on the atomic orbital. Figure 3.1 represents a simple example of separating the 3-fold rotation operation 3_{001}^+ into site and atomic orbital parts. Since the symmetry operation acts independently on the site/bond and atomic orbital degrees of freedom, \hat{Z}_j can be expressed as the linear combination of the direct products of the basis $|\hat{X}_\alpha\rangle$ of the atomic orbital part and the basis $|\hat{Y}_\beta\rangle$ of the site/bond parts:

$$|\hat{Z}_j\rangle = \sum_{\alpha\beta} \langle \hat{X}_\alpha \otimes \hat{Y}_\beta | \hat{Z}_j \rangle |\hat{X}_\alpha \otimes \hat{Y}_\beta\rangle = \sum_{\alpha\beta} C_{\alpha\beta}^j |\hat{X}_\alpha \otimes \hat{Y}_\beta\rangle \quad (3.1.6)$$

where we assume that $|\hat{X}_\alpha \otimes \hat{Y}_\beta\rangle$ is also complete orthonormal basis. To define \hat{Z}_j as fully symmetric, the irreducible representation of \hat{X}_α and \hat{Y}_β must be same. In addition, when \hat{Z}_j is time reversal even (odd), the time reversal parities of \hat{X}_α and \hat{Y}_β must be same (different). Thus, if we have $\{\hat{X}_\alpha\}$ and $\{\hat{Y}_\beta\}$, we can obtain $\{\hat{Z}_j\}$ by implementing the irreducible decomposition of the product of them with appropriate coefficients $C_{\alpha\beta}^j$ as shown in Eq. (3.1.6). This construction procedure is much easier than directly constructing $\{\hat{Z}_j\}$. According to the electronic multipole theory, \hat{X}_α and \hat{Y}_β correspond to the atomic multipole basis and the site/bond multipole basis as discussed below.

In Sec. 3.2, we briefly outline the concept of multipole basis. Then, we show the explicit definition of the atomic multipole basis in Sec. 3.3. We introduce the site/bond multipole basis and define the SAMB for isolated multi-site systems in Sec. 3.4. In Sec. 3.5, we extend the definition of the SAMB to periodic crystals.

3.2 Concept of Multipole Basis

From a mathematical point of view, a multipole expansion is a series expansion of a function depending on the polar and azimuth angles in the spherical coordinate system for three dimensional Cartesian space. A multipole basis is a complete orthonormal basis used in a multipole expansion and its expansion coefficient corresponds to the multipole moment. Usually, the spherical harmonics $Y_{lm}(\hat{\mathbf{r}})$ is used as the multipole basis that satisfies the orthogonal and complete relations:

$$\langle lm|l'm'\rangle \equiv \int d\hat{\mathbf{r}} Y_{lm}^*(\hat{\mathbf{r}})Y_{l'm'}(\hat{\mathbf{r}}) = \delta_{ll'}\delta_{mm'}, \quad \sum_{l=0}^{\infty} \sum_{m=-l}^l |lm\rangle \langle lm| = 1 \quad (3.2.1)$$

Using $Y_{lm}(\hat{\mathbf{r}})$, an arbitrary angular dependent function $f(\hat{\mathbf{r}})$ is expanded as

$$|f\rangle = \sum_{lm} \langle lm|f\rangle |lm\rangle = \sum_{lm} y_{lm} |lm\rangle \quad (3.2.2)$$

where $y_{lm} = \langle lm|f\rangle$ is the multipole moment depending on f . Equation (3.2.2) is a linear combination that can express finer anisotropic structure with use of the higher rank- l spherical harmonics. $|lm\rangle$ is called 2^l multipole basis or monopole ($l = 0$), dipole ($l = 1$), quadrupole ($l = 2$), octupole ($l = 3$), hexadecapole ($l = 4$), triakontadipole ($l = 5$), hexacontatetrapole ($l = 6$), octacosahetapole ($l = 7$) bases, and so on. Some notable advantages of using multipole expansion are summarized below.

- (1) Using complete orthonormal multipole basis, any angular dependent function can be expressed by Eq. (3.2.2) systematically.
- (2) Only a few multipole basis are often important to reproduce the original function, similar to the Taylor and Fourier series expansions.
- (3) The most dominant multipole contribution is elucidated by performing the multipole expansion.

Due to these advantages, the concept of multipole basis is widely utilized in various fields of physics such as classical electromagnetism [103–105], nuclear physics [106–108], solid-state physics [25–28, 88–90, 109–114], meta-materials [115–117], and so on.

The concept of multipole basis is also applied to describe atomic-scale electromagnetic distribution of the wave function of electrons bound to a single-centered atom, so-called atomic multipole basis. The well-known examples are the electric and magnetic multipoles as shown in Figs. 3.2(a) and (b), respectively. Remarkably, it has been clarified that the four types of atomic multipoles, well-known electric and magnetic multipoles and lesser-known magnetic toroidal and electric toroidal multipoles,

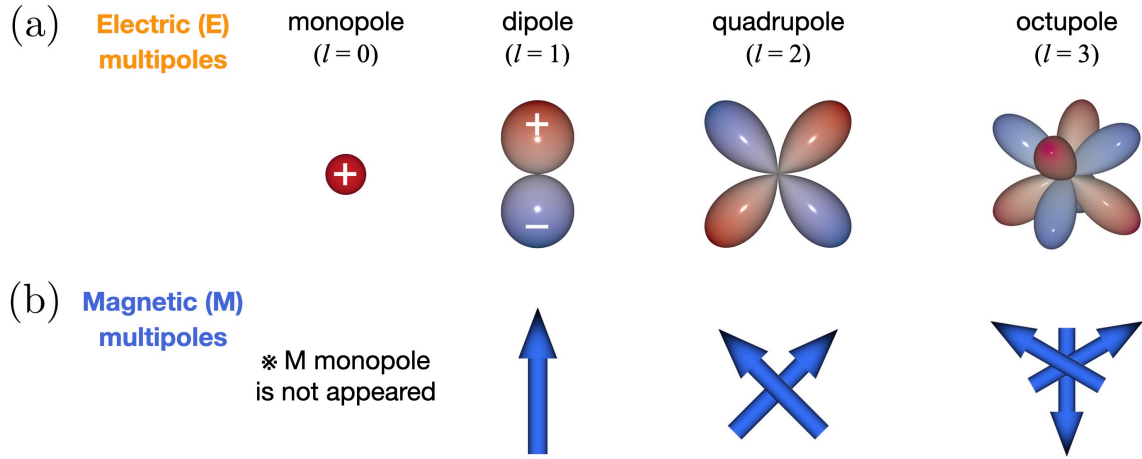


Figure 3.2: Schematic figures of (a) electric (E) and (b) magnetic (M) multipoles.

constitute the complete orthogonal basis set in the Hilbert space for s , p , d , and f electrons [25,26,28]. In addition, the quantum-mechanical operators of the atomic multipole basis were obtained and a compact formula to calculate their matrix elements are also derived quite recently [28]. Thus, the atomic multipole basis is a powerful tool to describe electronic internal degrees of freedom, such as charge, spin, and orbital and their combinations. Indeed, various electric and magnetic atomic multipole ordered states have been studied mainly in d - and f -electron systems, such as the electric quadrupole ordering in CeB_6 [109,118–124] and PrT_2X_{20} ($T = \text{Ir, Rh, V, Ti, Nb}$ and $X = \text{Al, Zn}$) [125–133], electric hexadecapole ordering in $\text{PrRu}_4\text{P}_{12}$ [134,135], magnetic octupole ordering in $\text{Ce}_{1-x}\text{La}_x\text{B}_6$ [136–139] and NpO_2 [140–145], magnetic octacosahexapole ordering in $\text{Yb}_2\text{Pt}_2\text{Pb}$ [146,147], and so on. These atomic multipoles, being active in the orbitals with the same orbital angular momenta, are called conventional atomic multipoles. On the other hand, recent studies have pointed out that the magnetic toroidal and electric toroidal atomic multipoles also become active in multiple hybrid orbitals with different orbital angular momenta [25,26,148]. Such multipoles that are activated only in hybrid orbitals are called hybrid atomic multipoles. In particular, it has been elucidated that magnetic toroidal dipole in d - f hybrid orbitals can be a microscopic origin of the ME effect [148].

Moreover, recent studies extend the scope of the concept of multipole from a single-centered electron systems to isolated multi-site systems such as molecules and periodic crystals, which provides helpful insights for complicated electric/magnetic orderings over a site-cluster and bond-cluster in the system. This concept is well-known as a molecular orbital in quantum chemistry. For example, the complicated non-collinear AFM ordering in Mn_3Sn is regarded as the site-cluster magnetic octupole composed of the six Mn sites in the unit-cell [29,101]. In addition, a recent study has discussed that the odd parity electric toroidal quadrupoles induced by anisotropic bond modulation can be a candidate order parameter for the unusual phase transition in the pyrochlore spin-orbital coupled metal $\text{Cd}_2\text{Re}_2\text{O}_7$ [149].

3.3 Multipole Basis for Single-Centered Electron Systems

This section presents the explicit definition of the atomic multipole basis as the complete orthonormal basis for both the spinless and spinful single-centered electron systems [25, 26, 28].

3.3.1 Four Types of Multipoles

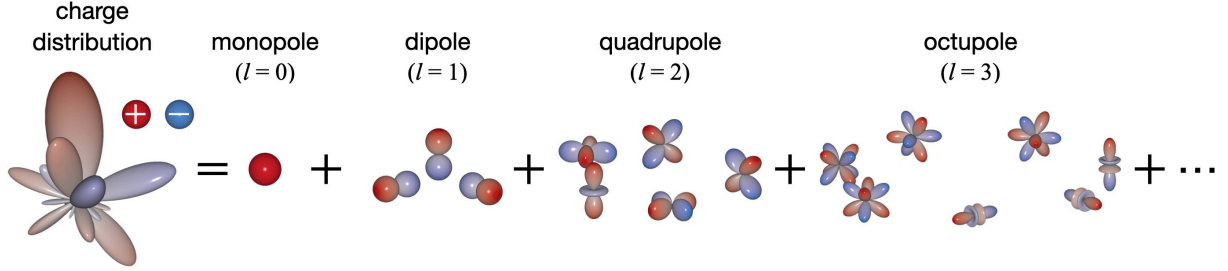


Figure 3.3: Multipole expansion of scalar potential with complex charge distribution.

In classical electromagnetism, the multipole expansion is utilized to describe the angle dependence of charge and current distributions [25, 103, 105, 150] as shown in Fig. 3.3. Let us consider the static electric and magnetic fields with Coulomb gauge $\nabla \cdot \mathbf{A}(\mathbf{r}) = 0$. The Poisson equations of the scalar and vector potentials, $\phi(\mathbf{r})$ and $\mathbf{A}(\mathbf{r})$, for Gaussian-cgs unit are given by

$$\nabla^2 \phi(\mathbf{r}) = -4\pi \rho_e(\mathbf{r}) \quad (3.3.1)$$

$$\nabla^2 \mathbf{A}(\mathbf{r}) = -\frac{4\pi}{c} \mathbf{j}_e(\mathbf{r}) \quad (3.3.2)$$

where c is the speed of light and $\rho_e(\mathbf{r})$ ($\mathbf{j}_e(\mathbf{r})$) represents a source electric charge (current) density. Based on the multipole expansion, $\phi(\mathbf{r})$ and $\mathbf{A}(\mathbf{r})$ are expanded by using the spherical harmonics $Y_{lm}(\hat{\mathbf{r}})$ and vector spherical harmonics $\mathbf{Y}_{lm}^{l+k}(\hat{\mathbf{r}})$ (see Appendix C.1 in detail):

$$\phi(\mathbf{r}) = \sum_{l=0}^{\infty} \sum_{m=-l}^l \sqrt{\frac{4\pi}{2l+1}} Q_{lm} \frac{Y_{lm}^*(\hat{\mathbf{r}})}{r^{l+1}} \quad (3.3.3)$$

$$\mathbf{A}(\mathbf{r}) = \sum_{l=0}^{\infty} \sum_{m=-l}^l \left[\sqrt{\frac{4\pi(l+1)}{(2l+1)l}} M_{lm} \frac{\mathbf{Y}_{lm}^{(l)*}(\hat{\mathbf{r}})}{ir^{l+1}} - \sqrt{4\pi(l+1)} T_{lm} \frac{\mathbf{Y}_{lm}^{(l+1)*}(\hat{\mathbf{r}})}{r^{l+2}} \right] \quad (3.3.4)$$

The expansion coefficients Q_{lm} , M_{lm} , and T_{lm} represent the rank- l electric (E), magnetic (M), and magnetic toroidal (MT) multipole moments, respectively. They are defined by

$$Q_{lm} = \int d\mathbf{r} \rho_e(\mathbf{r}) O_{lm}(\mathbf{r}) = \int d\mathbf{r} \mathbf{P}(\mathbf{r}) \cdot \nabla O_{lm}(\mathbf{r}) \quad (3.3.5)$$

$$M_{lm} = \frac{1}{c(l+1)} \int d\mathbf{r} [\mathbf{r} \times \mathbf{j}_e(\mathbf{r})] \cdot \nabla O_{lm}(\mathbf{r}) = \int d\mathbf{r} \mathbf{M}(\mathbf{r}) \cdot \nabla O_{lm}(\mathbf{r}) \quad (3.3.6)$$

$$T_{lm} = \frac{1}{c(l+1)} \int d\mathbf{r} [\mathbf{r} \cdot \mathbf{j}_e(\mathbf{r})] O_{lm}(\mathbf{r}) = \int d\mathbf{r} \mathbf{T}(\mathbf{r}) \cdot \nabla O_{lm}(\mathbf{r}) \quad (3.3.7)$$

where $O_{lm}(\mathbf{r}) = \sqrt{4\pi/(2l+1)} r^l Y_{lm}(\hat{\mathbf{r}})$, $\rho_e(\mathbf{r}) = -\nabla \cdot \mathbf{P}(\mathbf{r})$, $\mathbf{j}_e(\mathbf{r}) = c[\nabla \times \mathbf{M}(\mathbf{r})]$, and $\mathbf{M}(\mathbf{r}) = c[\nabla \times \mathbf{T}(\mathbf{r})]$.

type	notation	spatial inversion (\mathcal{P})	time reversal (\mathcal{T})	polar/axial	source	monopole	dipole	quadrupole
E	Q_{lm}	$(-1)^l$	+	Polar	$\rho_e(\mathbf{r})$ $\mathbf{j}_m(\mathbf{r})$			
M	M_{lm}	$(-1)^{l+1}$	-	Axial	$\mathbf{j}_e(\mathbf{r})$			
MT	T_{lm}	$(-1)^l$	-	Polar	$\mathbf{j}_e(\mathbf{r})$			
ET	G_{lm}	$(-1)^{l+1}$	+	Axial	$\mathbf{j}_m(\mathbf{r})$			

Figure 3.4: Four types of multipoles and their \mathcal{P} and \mathcal{T} parities. Their sources and schematic images up to rank-2 are also shown.

The second expressions are given by using identity for an arbitrary vector field X [25]:

$$\frac{1}{l+1} \int d\mathbf{r} \mathbf{r} \times (\nabla \times \mathbf{X}) \cdot \nabla O_{lm} = \int d\mathbf{r} \mathbf{X} \cdot \nabla O_{lm} \quad (3.3.8)$$

Note that M_{00} and T_{00} vanish in the classical multipole expansion, because $\nabla O_{00}(\mathbf{r}) = 0$ and $\int d\mathbf{r} \mathbf{r} \cdot \mathbf{j}_e(\mathbf{r}) = 0$, respectively.

Using Eqs. (3.3.3) and (3.3.4), the electric and magnetic fields are expanded in the same way,

$$\mathbf{E}(\mathbf{r}) = -\nabla\phi(\mathbf{r}) = -\sum_{lm} \sqrt{4\pi(l+1)} Q_{lm} \frac{\mathbf{Y}_{lm}^{(l+1)*}(\hat{\mathbf{r}})}{r^{l+2}} \quad (3.3.9)$$

$$\mathbf{B}(\mathbf{r}) = \nabla \times \mathbf{A}(\mathbf{r}) = -\sum_{lm} \sqrt{4\pi(l+1)} M_{lm} \frac{\mathbf{Y}_{lm}^{(l+1)*}(\hat{\mathbf{r}})}{r^{l+2}} \quad (3.3.10)$$

As shown in Eq. (3.3.10), T_{lm} does not contribute to $\mathbf{B}(\mathbf{r})$, and then it is often neglected in Eq. (3.3.4). From the quantum mechanical point of view, however, T_{lm} makes an appearance on the phase of the electron wave function via the vector potential $\mathbf{A}(\mathbf{r})$ as shown in Eq. (3.3.4).

Since $O_{lm}(\mathbf{r})$, $\rho_e(\mathbf{r})$, and $\mathbf{j}_e(\mathbf{r})$ have spatial inversion \mathcal{P} and time reversal \mathcal{T} parities $(\mathcal{P}, \mathcal{T}) = [(-1)^l, +1]$, $[+1, +1]$, and $[-1, -1]$, respectively, $Q_{lm}(\mathbf{r})$, $M_{lm}(\mathbf{r})$, and $T_{lm}(\mathbf{r})$ are characterized by $(\mathcal{P}, \mathcal{T}) = [(-1)^l, +1]$, $[(-1)^{l+1}, -1]$, and $[(-1)^l, -1]$, respectively. In other words, Q_{lm} is the \mathcal{T} -even polar tensor, M_{lm} is the \mathcal{T} -odd axial tensor, and T_{lm} is the \mathcal{T} -odd polar tensor, respectively. It is clear that the \mathcal{T} -even axial tensor with $(\mathcal{P}, \mathcal{T}) = [(-1)^{l+1}, +1]$ is missing in the multipole expansion of classical electromagnetic potentials, which is essential multipole degree of freedom for completeness.

The missing fourth multipole is called an electric toroidal (ET) multipole and is naturally derived by considering the magnetic current density as the vorticity of the electric polarization, $\mathbf{j}_m(\mathbf{r})$ [25, 151, 152]. The expression of the magnetic current density, $\mathbf{j}_m(\mathbf{r}) = c[\nabla \times \mathbf{P}(\mathbf{r})]$ is similar to the electric current density, $\mathbf{j}_e(\mathbf{r}) = c[\nabla \times \mathbf{M}(\mathbf{r})]$. Since $\mathbf{j}_e(\mathbf{r})$ ($\mathbf{j}_m(\mathbf{r})$) is polar (axial) and \mathcal{T} -odd (even), the transformation $\mathbf{j}_e(\mathbf{r}) \rightarrow \mathbf{j}_m(\mathbf{r})$ reverses both the \mathcal{P} and \mathcal{T} parities. For example, by replacing $\mathbf{j}_e(\mathbf{r})$ with $\mathbf{j}_m(\mathbf{r})$ in the first expression of M_{lm} given in Eq. (3.3.6), the first expression of Q_{lm} given in Eq. (3.3.5) is obtained. Thus, the \mathcal{T} -even axial ET multipole moment G_{lm} can be defined by

replacing $\mathbf{j}_e(\mathbf{r})$ with $\mathbf{j}_m(\mathbf{r})$ in the first expression of T_{lm} given in Eq. (3.3.7):

$$G_{lm} = \frac{1}{c(l+1)} \int d\mathbf{r} [\mathbf{r} \cdot \mathbf{j}_m(\mathbf{r})] O_{lm}(\mathbf{r}) = \int d\mathbf{r} \mathbf{G}(\mathbf{r}) \cdot \nabla O_{lm}(\mathbf{r}) \quad (3.3.11)$$

where $\mathbf{P}(\mathbf{r}) = \nabla \times \mathbf{G}(\mathbf{r})$ and $\mathbf{G}(\mathbf{r})$ represents the electric toroidarization.

Figure 3.4 summarizes the \mathcal{P} and \mathcal{T} parities of four types of multipoles, their sources, and their schematic images up to rank-2. These four types of multipoles, Q_{lm} , M_{lm} , T_{lm} , and G_{lm} , satisfy a completeness to describe any angle dependence of electromagnetic charge and current distributions in materials. For example, any scalar quantities, \mathcal{T} -even scalar, \mathcal{T} -odd pseudoscalar, \mathcal{T} -odd scalar, and \mathcal{T} -even pseudoscalar are described by Q_{00} , M_{00} , T_{00} , and G_{00} , respectively. Notably, G_{00} corresponds to the chirality from the symmetry point of view as discussed in Chap. 5. As we will show in the next section, G_{00} does not appear in spinless Hilbert space, indicating that spin degrees of freedom are essential to describe the chirality of electronic systems.

On the other hand, any vector quantities are described by \mathbf{Q} , \mathbf{M} , \mathbf{T} , and \mathbf{G} , respectively. As shown in “dipole” column in Fig. 3.4, the vorticity of the M (MT) dipole corresponds to the MT (M) dipole, while the vorticity of the E (ET) dipole corresponds to the ET (E) dipole. Since the E dipole has the same symmetry property of the lattice displacement vector, its vorticity, ET dipole, corresponds to the static lattice rotational deformation. Similarly, the higher rank tensor quantities more than $l = 2$ are also described by the corresponding multipole basis.

3.3.2 Quantum-Mechanical Operator Expressions

In this section, the quantum-mechanical operator expressions and the matrix elements of the atomic multipoles for both the spinless and spinful systems are given [26, 28].

For spinless systems

Based on Eqs. (3.3.5)-(3.3.7), and (3.3.11), the spinless atomic multipole operators are explicitly given by

$$\hat{Q}_{lm}^{(\text{orb})} = -eO_{lm} \quad (3.3.12)$$

$$\hat{M}_{lm}^{(\text{orb})} = -\mu_B \alpha_l^{(M)} \left[(\nabla O_{lm}) \cdot \hat{\mathbf{l}} + \hat{\mathbf{l}} \cdot (\nabla O_{lm}) \right] \quad (3.3.13)$$

$$\hat{T}_{lm}^{(\text{orb})} = -\mu_B \alpha_l^{(T)} \left[(\nabla O_{lm}) \cdot (\mathbf{r} \times \hat{\mathbf{l}}) - (\hat{\mathbf{l}} \times \mathbf{r}) \cdot (\nabla O_{lm}) \right] = i\alpha_l^{(T)} \left[O_{lm} \hat{\mathbf{l}}^2 - \hat{\mathbf{l}}^2 O_{lm} \right] \quad (3.3.14)$$

$$\hat{G}_{lm}^{(\text{orb})} = -e i \alpha_l^{(G)} \left[(\nabla O_{lm}) \cdot \hat{\mathbf{l}}^2 - \hat{\mathbf{l}}^2 \cdot (\nabla O_{lm}) \right] \quad (3.3.15)$$

where $-e$ and $-\mu_B$ are the electron charge and Bohr magneton, which are taken to be unity hereafter, $-e, -\mu_B \rightarrow 1$, and

$$\alpha_l^{(M)} = \frac{1}{2} \frac{2}{l+1}, \quad \alpha_l^{(T)} = \frac{1}{2} \frac{2}{(l+1)(l+2)}, \quad \alpha_l^{(G)} = \frac{1}{2} \frac{4}{(l+1)^2(l+2)} \quad (3.3.16)$$

Here, $\hat{\mathbf{l}} = -i(\mathbf{r} \times \nabla)$ is the dimensionless orbital angular momentum operator, and the parenthesis in (∇O_{lm}) denotes that ∇ acts only on O_{lm} . Note that the above operators are symmetrized to satisfy

$$[\hat{X}_{lm}^{(\text{orb})}]^\dagger = (-1)^m X_{l-m}^{(\text{orb})} \quad (3.3.17)$$

Hereafter, we omit the hat symbol ($\hat{}$) for notational simplicity.

The four spinless atomic multipole operators $X_{lm}^{(\text{orb})}$ ($X = Q, M, T, G$) can describe arbitrary electronic degrees of freedom in the Hilbert space of $|n, L, M\rangle$ with the angular momentum L , and its component M , and the other quantum number n , such as the principal quantum number. Notably, $X_{lm}^{(\text{orb})}$ transforms like Y_{lm} with respect to the spatial rotation. Therefore, following the Wigner-Eckart theorem, the matrix elements of $X_{lm}^{(\text{orb})}$ are given by

$$\langle n_1 L_1 M_1 | X_{lm}^{(\text{orb})} | n_2 L_2 M_2 \rangle = (-1)^{L_1 + M_1} \begin{pmatrix} L_1 & L_2 & l \\ -M_1 & M_2 & m \end{pmatrix} \langle n_1 L_1 || X_l^{(\text{orb})} || n_2 L_2 \rangle \quad (3.3.18)$$

where the parenthesis represents the Wigner's $3j$ symbol, and $\langle n_1 L_1 || X_l^{(\text{orb})} || n_2 L_2 \rangle$ represents the reduced matrix elements given by

$$\langle n_1 L_1 || Q_l^{(\text{orb})} || n_2 L_2 \rangle = (-1)^{L_1} \sqrt{(2L_1 + 1)(2L_2 + 1)} \begin{pmatrix} L_1 & L_2 & l \\ 0 & 0 & 0 \end{pmatrix} \langle r^l \rangle_{12} \quad (3.3.19)$$

$$\begin{aligned} \langle n_1 L_1 || M_l^{(\text{orb})} || n_2 L_2 \rangle &= (-1)^{L_1} \sqrt{l(2l+1)(2l-1)(2L_1+1)L_2(L_2+1)} \times \\ &\times \frac{2(2L_2+1)}{l+1} \begin{pmatrix} L_1 & L_2 & l-1 \\ 0 & 0 & 0 \end{pmatrix} \begin{Bmatrix} l-1 & l & 1 \\ L_2 & L_2 & L_1 \end{Bmatrix} \langle r^{l-1} \rangle_{12} \end{aligned} \quad (3.3.20)$$

$$\langle n_1 L_1 || T_l^{(\text{orb})} || n_2 L_2 \rangle = i R_l(L_1, L_2) \langle n_1 L_1 || Q_l^{(\text{orb})} || n_2 L_2 \rangle \quad (3.3.21)$$

$$\langle n_1 L_1 || G_l^{(\text{orb})} || n_2 L_2 \rangle = i R_l(L_1, L_2) \langle n_1 L_1 || M_l^{(\text{orb})} || n_2 L_2 \rangle \quad (3.3.22)$$

where the curly bracket denotes the Wigner's $6j$ symbol, and

$$\langle r^k \rangle_{12} = \int_0^\infty dr r^{k+2} R_{n_1 L_1}(r) R_{n_2 L_2}(r) \quad (3.3.23)$$

is the matrix element in the radial part. Here, we introduced the common proportional coefficient as

$$R_l(L_1, L_2) = -\frac{L_1(L_1 + 1) - L_2(L_2 + 1)}{(l + 1)(l + 2)} \quad (3.3.24)$$

The reduced matrices with same rank- l are orthogonal in the fixed (L_1, L_2) subspace:

$$\sum_{n_1 L_1 \leftrightarrow n_2 L_2} \langle n_1 L_1 || X_l^{(\text{orb})} || n_2 L_2 \rangle^* \langle n_1 L_1 || Y_l^{(\text{orb})} || n_2 L_2 \rangle = \delta_{XY} X(l, n_1, L_1, n_2, L_2) \quad (3.3.25)$$

$$X(l, n_1, L_1, n_2, L_2) = \sum_{n_1 L_1 \leftrightarrow n_2 L_2} | \langle n_1 L_1 || X_l^{(\text{orb})} || n_2 L_2 \rangle |^2 \quad (3.3.26)$$

where $\sum_{n_1 L_1 \leftrightarrow n_2 L_2}$ denotes to sum $(n_1 L_1, n_2 L_2)$ and $(n_2 L_2, n_1 L_1)$ terms.

The Wigner's $3j$ symbol satisfies the following selection rules:

$$\begin{aligned} \begin{pmatrix} j_1 & j_2 & j_3 \\ m_1 & m_2 & m_3 \end{pmatrix} &= \frac{(-1)^{j_1 - j_2 - m_3}}{\sqrt{2j_3 + 1}} \langle j_1 m_1 j_2 m_2 | j_3 (-m_3) \rangle \\ &= \begin{cases} \text{finite} & \begin{cases} m_i \in \{-j_i, -j_i + 1, -j_i + 2, \dots, j_i\} \ (i = 1, 2, 3) \\ m_1 + m_2 + m_3 = 0 \\ |j_1 - j_2| \leq j_3 \leq j_1 + j_2 \ (\text{addition rule of the angular momentum}) \\ j_1 + j_2 + j_3 \ \text{is an (even) integer (when } m_1 = m_2 = m_3 = 0) \end{cases} \\ 0 & \text{otherwise} \end{cases} \end{aligned} \quad (3.3.27)$$

We summarize some notable properties of $X_{lm}^{(\text{orb})}$ as follows:

- (1) From the addition rule of the angular momentum, only the rank- l multipoles satisfying $|L_1 - L_2| \leq l \leq L_1 + L_2$ can be active.
- (2) Since the spatial parities of $Q_{lm}(M_{lm})$ and $T_{lm}(G_{lm})$ are $(-1)^l ((-1)^{l+1})$, they are active only when $(-1)^{L_1+L_2} = (-1)^l ((-1)^{l+1})$.
- (3) $M_{00} = T_{00} = G_{00} = G_{1m} = 0$ because of the identities, $\nabla O_{00}(\mathbf{r}) = \mathbf{0}$ and $\nabla_\alpha \nabla_\beta O_{1m}(\mathbf{r}) = 0$.
- (4) From Eq. (3.3.24), T_{lm} and G_{lm} are inactive for $L_1 = L_2$, whereas they are activated when $L_1 \neq L_2$ and called hybrid multipoles.
- (5) Since the Wigner's $3j$ and $6j$ symbols and $\langle r^k \rangle_{12}$ are real, the matrix elements of Q_{lm} (T_{lm}) and M_{lm} (G_{lm}) are real (pure imaginary).
- (6) By normalizing $\{X_{lm}^{(\text{orb})}\}$ ($X = Q, M, T, G$), it constitutes a complete orthonormal basis set.

We here prove the property (6). Let us consider the Hilbert space of $|L, M\rangle$ up to $L = 3$, where there are independent 11 subspaces: 4 diagonal (non-hybrid) spaces, $L_1 = L_2 = 0(s), 1(p), 2(d), 3(f)$, and 6 off-diagonal (hybrid) spaces, $(L_1, L_2) = (s, p), (s, d), (s, f), (p, d), (p, f), (d, f)$. Since the dimension of the matrices defined in the total Hilbert space is 16, there should be $16 \times 16 = 256$ independent

Table 3.1: Activated atomic multipoles in each diagonal (non-hybrid) and off-diagonal (hybrid) subspaces.

	s	p	d	f
s	Q_0 (1)	Q_{1m} (3), T_{1m} (3)	Q_{2m} (5), T_{2m} (5)	Q_{3m} (7), T_{3m} (7)
p		Q_0 (1) M_{1m} (3) Q_{2m} (5)	Q_{1m} (3), T_{1m} (3) M_{2m} (5), G_{2m} (5) Q_{3m} (7), T_{3m} (7)	Q_{2m} (5), T_{2m} (5) M_{3m} (7), G_{3m} (7) Q_{4m} (9), T_{4m} (9)
d			Q_0 (1) M_{1m} (3) Q_{2m} (5) M_{3m} (7) Q_{4m} (9)	Q_{1m} (3), T_{1m} (3) M_{2m} (5), G_{2m} (5) Q_{3m} (7), T_{3m} (7) M_{4m} (9), G_{4m} (9) Q_{5m} (11), T_{5m} (11)
f				Q_0 (1) M_{1m} (3) Q_{2m} (5) M_{3m} (7) Q_{4m} (9) M_{5m} (11) Q_{6m} (13)

active multipoles, which are summarized in Table 3.1. Using the orthogonal relation of the Wigner's $3j$ symbols,

$$(2j+1) \sum_{m_1 m_2} \begin{pmatrix} j_1 & j_2 & j \\ m_1 & m_2 & m \end{pmatrix} \begin{pmatrix} j_1 & j_2 & j' \\ m_1 & m_2 & m' \end{pmatrix} = \delta_{jj'} \delta_{mm'} \quad (3.3.28)$$

we can confirm that $|X_{lm}^{(\text{orb})}\rangle$ is orthogonal in the fixed (L_1, L_2) subspace:

$$\begin{aligned}
\langle X_{lm}^{(\text{orb})} | X_{l'm'}^{(\text{orb})} \rangle_{L_1 L_2} &= \sum_{n_1 L_1 \leftrightarrow n_2 L_2} \sum_{M_1=-L_1}^{L_1} \sum_{M_2=-L_2}^{L_2} \langle n_1 L_1 M_1 | X_{lm}^{(\text{orb})} | n_2 L_2 M_2 \rangle^* \langle n_1 L_1 M_1 | X_{l'm'}^{(\text{orb})} | n_2 L_2 M_2 \rangle \\
&= \sum_{n_1 L_1 \leftrightarrow n_2 L_2} \left[\sum_{M_1=-L_1}^{L_1} \sum_{M_2=-L_2}^{L_2} \begin{pmatrix} L_1 & L_2 & l \\ -M_1 & M_2 & m \end{pmatrix} \begin{pmatrix} L_1 & L_2 & l' \\ -M_1 & M_2 & m' \end{pmatrix} \right] \\
&\times \langle n_1 L_1 || X_l^{(\text{orb})} || n_2 L_2 \rangle^* \langle n_1 L_1 || X_{l'}^{(\text{orb})} || n_2 L_2 \rangle \\
&= \frac{1}{2l+1} \delta_{ll'} \delta_{mm'} \sum_{n_1 L_1 \leftrightarrow n_2 L_2} \langle n_1 L_1 || X_l^{(\text{orb})} || n_2 L_2 \rangle^* \langle n_1 L_1 || X_{l'}^{(\text{orb})} || n_2 L_2 \rangle \\
&= \frac{X(l, n_1, L_1, n_2, L_2)}{2l+1} \delta_{ll'} \delta_{mm'} \delta_{XX'}
\end{aligned} \quad (3.3.29)$$

The last line is derived by using Eq. (3.3.25). Thus, $|X_{lm}^{(\text{orb})}\rangle$ is normalized as

$$|\tilde{X}_{lm}^{(\text{orb})}\rangle_{L_1 L_2} \equiv \frac{1}{\sqrt{\langle X_{lm}^{(\text{orb})} | X_{lm}^{(\text{orb})} \rangle_{L_1 L_2}}} |X_{lm}^{(\text{orb})}\rangle_{L_1 L_2} = \frac{\sqrt{2l+1}}{\sqrt{X(l, n_1, L_1, n_2, L_2)}_{L_1 L_2}} |X_{lm}^{(\text{orb})}\rangle_{L_1 L_2} \quad (3.3.30)$$

Similarly, using the another orthogonal relation of the Wigner's $3j$ symbols,

$$\sum_{jm} (2j+1) \begin{pmatrix} j_1 & j_2 & j \\ m_1 & m_2 & m \end{pmatrix} \begin{pmatrix} j_1 & j_2 & j \\ m'_1 & m'_2 & m \end{pmatrix} = \delta_{m_1 m'_1} \delta_{m_2 m'_2} \quad (3.3.31)$$

we can also confirm that $|\tilde{X}_{lm}^{(\text{orb})}\rangle$ satisfies the complete relation in the fixed (L_1, L_2) subspace:

$$\begin{aligned} \sum_{lm} \left(|\tilde{X}_{lm}^{(\text{orb})}\rangle \langle \tilde{X}_{lm}^{(\text{orb})}| \right)_{M_1 M_2, M'_1 M'_2}^{(L_1, L_2)} &= \sum_{lm} \sum_{n_1 L_1 \leftrightarrow n_2 L_2} \langle n_1 L_1 M_1 | \tilde{X}_{lm}^{(\text{orb})} | n_2 L_2 M_2 \rangle \langle n_1 L_1 M'_1 | \tilde{X}_{lm}^{(\text{orb})} | n_2 L_2 M'_2 \rangle^* \\ &= (-1)^{M_1 + M'_1} \sum_{lm} (2l+1) \begin{pmatrix} L_1 & L_2 & l \\ -M_1 & M_2 & m \end{pmatrix} \begin{pmatrix} L_1 & L_2 & l \\ -M'_1 & M'_2 & m \end{pmatrix} \\ &\quad \times \frac{1}{X(l, n_1, L_1, n_2, L_2)_{L_1 L_2}} \sum_{n_1 L_1 \leftrightarrow n_2 L_2} |\langle n_1 L_1 || X_l^{(\text{orb})} || n_2 L_2 \rangle|^2 \\ &= (-1)^{M_1 + M'_1} \sum_{lm} (2l+1) \begin{pmatrix} L_1 & L_2 & l \\ -M_1 & M_2 & m \end{pmatrix} \begin{pmatrix} L_1 & L_2 & l \\ -M'_1 & M'_2 & m \end{pmatrix} \\ &= \delta_{M_1 M'_1} \delta_{M_2 M'_2} \end{aligned} \quad (3.3.32)$$

We used Eq. (3.3.30) to obtain the third line.

The above considerations and Eqs. (3.3.29) and (3.3.32) indicate that $\{\tilde{X}_{lm}^{(\text{orb})}\}$ constitutes the complete orthonormal basis set in the Hilbert space of $|n, L, M\rangle$. In other words, it can describe arbitrary spinless operator $O^{(\text{orb})}$ in the fixed (L_1, L_2) space as the linear combination of $|\tilde{X}_{lm}^{(\text{orb})}\rangle$:

$$|O^{(\text{orb})}\rangle_{L_1 L_2} = \sum_X^{Q, M, T, G} \sum_{l=|L_1-L_2|}^{L_1+L_2} \sum_{m=-l}^l \langle \tilde{X}_{lm}^{(\text{orb})} | O^{(\text{orb})} \rangle_{L_1 L_2} |\tilde{X}_{lm}^{(\text{orb})}\rangle_{L_1 L_2} \quad (3.3.33)$$

For spinful systems

Table 3.2: Correspondence between $X_l(k)$ and $X_{l+k}^{(\text{orb})}$ in spin sector [28].

$X_l^{(1)}(k)$	$k = 0$	$k = \pm 1$
$Q_i^{(1)}(k)$	$T_i^{(\text{orb})}$	$M_{l\pm 1}^{(\text{orb})}$
$M_l^{(1)}(k)$	$G_l^{(\text{orb})}$	$Q_{l\pm 1}^{(\text{orb})}$
$T_l^{(1)}(k)$	$Q_l^{(\text{orb})}$	$G_{l\pm 1}^{(\text{orb})}$
$G_l^{(1)}(k)$	$M_l^{(\text{orb})}$	$T_{l\pm 1}^{(\text{orb})}$

Next, we briefly show the definition of the atomic multipole basis for spinful systems. The detail derivation is found in Ref. [28].

The spinful atomic multipole operators can be naturally constructed by composing the 2×2 identity matrix σ_0 (rank 0 tensor) and the Pauli matrices $\boldsymbol{\sigma}$ (rank 1 tensor) with $X_{lm}^{(\text{orb})}$ (rank- l tensor)

in accordance with the addition rule of angular momentum:

$$X_{lm}^{(s)}(k) = i^{s+k} (-1)^{l+m} \sqrt{2l+1} \sum_{n=-s}^s \begin{pmatrix} l+k & l & s \\ m-n & -m & n \end{pmatrix} X_{l+k, m-n}^{(\text{orb})} \sigma_{s,n} \quad (3.3.34)$$

$X_{lm}^{(0)}(0) = X_{lm}^{(\text{orb})} \sigma_0$ with $\sigma_{0,0} = \sigma_0$ is a multipole in charge sector, while $X_{lm}^{(1)}(k)$ ($k = 0, \pm 1$) is a multipole in spin sector, where three spin components ($n = 0, \pm 1$) are defined as $\sigma_{1,0} = \sigma_z$ and $\sigma_{1,\pm 1} = \mp(\sigma_x \pm i\sigma_y)/\sqrt{2}$. Similar to Eq. (3.3.17), thanks to the phase factor i^{s+k} , the spinful atomic multipole operator also satisfies

$$[X_{lm}^{(s)}(k)]^\dagger = (-1)^m X_{l-m}^{(s)}(k) \quad (3.3.35)$$

Since $\boldsymbol{\sigma}$ is the \mathcal{T} odd axial vector, the \mathcal{T} parity of $X_{lm}^{(1)}(k)$ is opposite to that of $X_{lm}^{(\text{orb})}$, and the \mathcal{P} parity is further reversed for $k = \pm 1$ components. The correspondence is summarized in Table 3.2.

By introducing the spinful spherical harmonics as

$$O_{lm}^{(s)}(k) = i^{s+k} (-1)^{l+m} \sqrt{2l+1} \sum_{n=-s}^s \begin{pmatrix} l+k & l & s \\ m-n & -m & n \end{pmatrix} O_{l+k, m-n} \sigma_{s,n} \quad (3.3.36)$$

and replacing O_{lm} in Eqs. (3.3.12)-(3.3.15) with $O_{lm}^{(s)}(k)$, the explicit expressions of the composed spinful atomic multipole operators are given by

$$Q_{lm}^{(1)}(0) = \alpha_l^{(T)} \left[\left(\nabla O_{lm}^{(1)}(0) \right) \cdot (\mathbf{r} \times \mathbf{l}) - (\mathbf{l} \times \mathbf{r}) \cdot \left(\nabla O_{lm}^{(1)}(0) \right) \right] = i\alpha_l^{(T)} \left[O_{lm}^{(1)}(0) \mathbf{l}^2 - \mathbf{l}^2 O_{lm}^{(1)}(0) \right] \quad (3.3.37)$$

$$M_{lm}^{(1)}(0) = i\alpha_l^{(G)} \left[\left(\nabla O_{lm}^{(1)}(0) \right) \cdot \mathbf{u}^2 - \mathbf{l}^2 \mathbf{l} \cdot \left(\nabla O_{lm}^{(1)}(0) \right) \right] \quad (3.3.38)$$

$$T_{lm}^{(1)}(0) = O_{lm}^{(1)}(0) \quad (3.3.39)$$

$$G_{lm}^{(1)}(0) = \alpha_l^{(M)} \left[\left(\nabla O_{lm}^{(1)}(0) \right) \cdot \mathbf{l} + \mathbf{l} \cdot \left(\nabla O_{lm}^{(1)}(0) \right) \right] \quad (3.3.40)$$

$$Q_{lm}^{(1)}(\pm 1) = \alpha_l^{(M)} \left[\left(\nabla O_{lm}^{(1)}(\pm 1) \right) \cdot \mathbf{l} + \mathbf{l} \cdot \left(\nabla O_{lm}^{(1)}(\pm 1) \right) \right] \quad (3.3.41)$$

$$M_{lm}^{(1)}(\pm 1) = O_{lm}^{(1)}(\pm 1) \quad (3.3.42)$$

$$T_{lm}^{(1)}(\pm 1) = i\alpha_l^{(G)} \left[\left(\nabla O_{lm}^{(1)}(\pm 1) \right) \cdot \mathbf{u}^2 - \mathbf{l}^2 \mathbf{l} \cdot \left(\nabla O_{lm}^{(1)}(\pm 1) \right) \right] \quad (3.3.43)$$

$$\begin{aligned} G_{lm}^{(1)}(\pm 1) &= i\alpha_l^{(T)} \left[\left(\nabla O_{lm}^{(1)}(\pm 1) \right) \cdot (\mathbf{r} \times \mathbf{l}) - (\mathbf{r} \times \mathbf{l}) \cdot \left(\nabla O_{lm}^{(1)}(\pm 1) \right) \right] \\ &= i\alpha_l^{(T)} \left[O_{lm}^{(1)}(\pm 1) \mathbf{l}^2 - \mathbf{l}^2 O_{lm}^{(1)}(\pm 1) \right] \end{aligned} \quad (3.3.44)$$

In the spinful basis of the direct product, $|nLM\sigma\rangle = |nLM\rangle \otimes |1/2\sigma\rangle$, the matrix elements of $X_{lm}^{(s)}(k)$ are given by

$$\begin{aligned} \langle n_1 L_1 M_1 \sigma_1 | X_{lm}^{(s)}(k) | n_2 L_2 M_2 \sigma_2 \rangle &= i^{s+k} (-1)^{l+m} \sqrt{2l+1} \sum_{n=-s}^s \begin{pmatrix} l+k & l & s \\ m-n & -m & n \end{pmatrix} \\ &\quad \times \langle n_1 L_1 M_1 | X_{l+k, m-n}^{(\text{orb})} | n_2 L_2 M_2 \rangle \langle 1/2\sigma_1 | \sigma_{s,n} | 1/2\sigma_2 \rangle \end{aligned} \quad (3.3.45)$$

where

$$\langle 1/2\sigma_1|\sigma_{1,0}|1/2\sigma_2\rangle = \delta_{\sigma_1\sigma_2}, \quad \langle 1/2\sigma_1|\sigma_{1,n}|1/2\sigma_2\rangle = (-1)^{\sigma_1-1/2}\sqrt{6} \begin{pmatrix} 1/2 & 1/2 & 1 \\ -\sigma_1 & \sigma_2 & n \end{pmatrix} \quad (3.3.46)$$

Notably, the matrix elements of the spinful atomic multipole operators $X_{lm}^{(s)}(k)$ are obtained simply by using the matrix elements of $X_{l+k}^{(\text{orb})}$, which are given by Eq. (3.3.18).

Let us next consider the eigenstates $|nJM; L\rangle$ of the total angular momentum operator $\mathbf{j} = \mathbf{l} + (1/2)\boldsymbol{\sigma}$:

$$|nJM; L\rangle = (-1)^{J+M}\sqrt{2J+1} \sum_{\sigma}^{\pm 1} \begin{pmatrix} L & J & 1/2 \\ M - \sigma/2 & -M & \sigma/2 \end{pmatrix} |nLM - \frac{\sigma}{2}\sigma\rangle \quad (3.3.47)$$

Since $X_{lm}^{(s)}(k)$ transforms like Y_{lm} under the spatial rotation, the matrix elements of $X_{lm}^{(s)}(k)$ under $|nJM; L\rangle$ is also given by following the Wigner-Eckart theorem:

$$\langle n_1J_1M_1; L_1|X_{lm}^{(s)}(k)|n_2J_2M_2; L_2\rangle = (-1)^{J_1+M_1} \begin{pmatrix} J_1 & J_2 & l \\ -M_1 & -M_2 & m \end{pmatrix} \langle n_1J_1; L_1|X_l^{(s)}(k)|n_2J_2; L_2\rangle \quad (3.3.48)$$

The reduced matrix elements $\langle n_1J_1; L_1|X_l^{(s)}(k)|n_2J_2; L_2\rangle$ are expressed by using $\langle n_1L_1|X_{l+k}^{(\text{orb})}|n_2L_2\rangle$ as

$$\langle n_1J_1; L_1|X_l^{(s)}(k)|n_2J_2; L_2\rangle = P_l(s, k; J_1, J_2; L_1, L_2) \langle n_1L_1|X_{l+k}^{(\text{orb})}|n_2L_2\rangle \quad (3.3.49)$$

$$P_l(s, k; J_1, J_2; L_1, L_2) = i^{s+k}(-1)^s \sqrt{(2l+1)(2J_1+1)(2J_2+1)(1-s)!(2+s)!} \begin{Bmatrix} L_1 & J_1 & 1/2 \\ L_2 & J_2 & 1/2 \\ l+k & l & s \end{Bmatrix} \quad (3.3.50)$$

where the curly bracket denotes the Wigner's $9j$ symbol. The explicit expressions of $\langle n_1J_1; L_1|X_l^{(s)}(k)|n_2J_2; L_2\rangle$ are given by

$$\begin{aligned} \langle n_1J_1; L_1|Q_l^{(1)}(0)|n_2J_2; L_2\rangle &= R_l(L_1, L_2)P_l(0, k; J_1, J_2; L_1, L_2) \langle n_1L_1|Q_l^{(\text{orb})}|n_2L_2\rangle \\ \langle n_1J_1; L_1|M_l^{(1)}(0)|n_2J_2; L_2\rangle &= R_l(L_1, L_2)P_l(0, k; J_1, J_2; L_1, L_2) \langle n_1L_1|M_l^{(\text{orb})}|n_2L_2\rangle \\ \langle n_1J_1; L_1|T_l^{(1)}(0)|n_2J_2; L_2\rangle &= -iP_l(0, k; J_1, J_2; L_1, L_2) \langle n_1L_1|Q_l^{(\text{orb})}|n_2L_2\rangle \\ \langle n_1J_1; L_1|G_l^{(1)}(0)|n_2J_2; L_2\rangle &= -iP_l(0, k; J_1, J_2; L_1, L_2) \langle n_1L_1|M_l^{(\text{orb})}|n_2L_2\rangle \\ \langle n_1J_1; L_1|Q_l^{(1)}(\pm 1)|n_2J_2; L_2\rangle &= \pm P_l(\pm 1, k; J_1, J_2; L_1, L_2) \langle n_1L_1|M_{l\pm 1}^{(\text{orb})}|n_2L_2\rangle \\ \langle n_1J_1; L_1|M_l^{(1)}(\pm 1)|n_2J_2; L_2\rangle &= \pm P_l(\pm 1, k; J_1, J_2; L_1, L_2) \langle n_1L_1|Q_{l\pm 1}^{(\text{orb})}|n_2L_2\rangle \\ \langle n_1J_1; L_1|T_l^{(1)}(\pm 1)|n_2J_2; L_2\rangle &= \pm iR_{l\pm 1}(L_1, L_2)P_l(\pm 1, k; J_1, J_2; L_1, L_2) \langle n_1L_1|M_{l\pm 1}^{(\text{orb})}|n_2L_2\rangle \\ \langle n_1J_1; L_1|G_l^{(1)}(\pm 1)|n_2J_2; L_2\rangle &= \pm iR_{l\pm 1}(L_1, L_2)P_l(\pm 1, k; J_1, J_2; L_1, L_2) \langle n_1L_1|Q_{l\pm 1}^{(\text{orb})}|n_2L_2\rangle \end{aligned} \quad (3.3.51)$$

$$(3.3.52)$$

We have confirmed that the reduced matrices with same rank- l are orthogonal in the fixed (L_1, L_2) subspace:

$$\begin{aligned} & \sum_{n_1 J_1 L_1 \leftrightarrow n_2 J_2 L_2} \sum_{J_1}^{L_1 \pm 1/2} \sum_{J_2}^{L_2 \pm 1/2} \langle n_1 J_1; L_1 | X_l^{(s)}(k) | n_2 J_2; L_2 \rangle^* \langle n_1 J_1; L_1 | X_l'^{(s')}(k') | n_2 J_2; L_2 \rangle \\ &= \delta_{X X'} \delta_{s s'} \delta_{k k'} X(l, s, k; n_1 L_1, n_2 L_2) \end{aligned} \quad (3.3.53)$$

$$X(l, s, k; n_1 L_1, n_2 L_2) = \sum_{n_1 J_1 L_1 \leftrightarrow n_2 J_2 L_2} \sum_{J_1}^{L_1 \pm 1/2} \sum_{J_2}^{L_2 \pm 1/2} |\langle n_1 J_1; L_1 | X_l^{(s)}(k) | n_2 J_2; L_2 \rangle|^2 \quad (3.3.54)$$

We summarize some notable properties of $X_{lm}^{(s)}(k)$ as follows:

- (1) From the addition rule of the angular momentum, only the rank- l multipoles satisfying $|J_1 - J_2| \leq l \leq J_1 + J_2$ can be active.
- (2) Since the spatial parities of $Q_l^{(s)}(k)$ ($M_l^{(s)}(k)$) and $T_l^{(s)}(k)$ ($G_l^{(s)}(k)$) are $(-1)^l$ ($(-1)^{l+1}$), $Q_{lm}^{(s)}(k)$ ($M_{lm}^{(s)}(k)$) and $T_{lm}^{(s)}(k)$ ($G_{lm}^{(s)}(k)$) are active only when $(-1)^{L_1+L_2} = (-1)^l$ ($(-1)^{l+1}$)
- (3) $T_{00}^{(s)}(k) = 0$.
- (4) From Eq. (3.3.24), $Q_{lm}^{(1)}(0)$, $M_{lm}^{(1)}(0)$, $T_{lm}^{(1)}(\pm 1)$, and $G_{lm}^{(1)}(\pm 1)$ are active only for $L_1 \neq L_2$, otherwise zero.
- (5) Since the Wigner's $3j$ and $6j$ symbols and $\langle r^k \rangle_{12}$ are real, the matrix elements of $Q_{lm}^{(s)}(k)$ ($T_{lm}^{(s)}(k)$) and $M_{lm}^{(s)}(k)$ ($G_{lm}^{(s)}(k)$) are real (pure imaginary).
- (6) By normalizing $\{X_{lm}^{(s)}(k)\}$ ($X = Q, M, T, G$), it constitutes complete orthonormal basis set.

The property (6) can be easily proven based on the orthogonal and complete relations of $X_{lm}^{(\text{orb})}$ given by Eqs. (3.3.29) and (3.3.32) and the orthogonal relations of Wigner's $3j$ symbols given by Eqs. (3.3.28) and (3.3.31).

$|X_{lm}^{(s)}(k)\rangle$ is orthogonal in the fixed (L_1, L_2) subspace:

$$\begin{aligned} & \langle X_{lm}^{(s)}(k) | X_{l'm'}'^{(s')}(k') \rangle_{L_1 L_2} \\ &= (-i)^{s+k} i^{s'+k'} (-1)^{l+m+l'+m'} \sqrt{(2l+1)(2l'+1)} \\ & \times \sum_{nn'} \begin{pmatrix} l+k & l & s \\ m-n & -m & n \end{pmatrix} \begin{pmatrix} l'+k' & l' & s' \\ m'-n' & -m' & n' \end{pmatrix} \langle X_{l+k, m-n}^{(\text{orb})} | X_{l'+k', m'-n'}'^{(\text{orb})} \rangle_{L_1 L_2} \langle \sigma_{s, n} | \sigma_{s', n'} \rangle \\ &= 2(-i)^k i^{k'} (-1)^{m+m'} \sqrt{(2l+1)(2l'+1)} \frac{X(l, n_1, L_1, n_2, L_2)}{2l+1} \delta_{X X'} \delta_{l+k, l'+k'} \delta_{s s'} \\ & \times \sum_n \begin{pmatrix} l+k & s & l \\ m-n & n & -m \end{pmatrix} \begin{pmatrix} l+k & s & l' \\ m-n & n & -m' \end{pmatrix} \\ &= 2 \frac{X(l, n_1, L_1, n_2, L_2)}{2l+1} \delta_{X X'} \delta_{l+l'} \delta_{m m'} \delta_{s s'} \delta_{k k'} \end{aligned} \quad (3.3.55)$$

To obtain the second line, we used Eq.(3.3.29) and the orthogonality of σ_{sn} , $\langle \sigma_{sn} | \sigma_{s'n'} \rangle = 2\delta_{ss'} \delta_{nn'}$. Then, $|X_{lm}^{(s)}(k)\rangle$ is normalized as

$$|\tilde{X}_{lm}^{(s)}(k)\rangle_{L_1 L_2} \equiv \frac{1}{\sqrt{\langle X_{lm}^{(s)}(k) | X_{lm}^{(s)}(k) \rangle_{L_1 L_2}}} |X_{lm}^{(s)}(k)\rangle_{L_1 L_2} \quad (3.3.56)$$

$$= \frac{\sqrt{2l+1}}{\sqrt{2X(l, n_1 L_1, n_2 L_2)}} |X_{lm}^{(s)}(k)\rangle_{L_1 L_2} \quad (3.3.57)$$

$$= i^{s+k} (-1)^{l+m} \sqrt{2l+1} \sum_{n=-s}^s \begin{pmatrix} l+k & l & s \\ m-n & -m & n \end{pmatrix} \tilde{X}_{l+k, m-n}^{(\text{orb})} \tilde{\sigma}_{s,n} \quad (3.3.58)$$

where $\tilde{\sigma}_{s,n} = \sigma_{s,n}/\sqrt{2}$ are the normalized spin tensors, $\langle \tilde{\sigma}_{s,n} | \tilde{\sigma}_{s',n'} \rangle = \delta_{ss'} \delta_{nn'}$.

In addition, the complete relation of $|\tilde{X}_{lm}^{(s)}(k)\rangle_{L_1 L_2}$ in the fixed (L_1, L_2) subspace is represented by

$$\begin{aligned} & \sum_{lmsk} |\tilde{X}_{lm}^{(s)}(k)\rangle \langle \tilde{X}_{lm}^{(s)}(k)| \\ &= \sum_{lmsk} \sum_{nn'} (2l+1) \begin{pmatrix} l+k & s & l \\ m-n & n & -m \end{pmatrix} \begin{pmatrix} l+k & s & l \\ m-n' & n' & -m \end{pmatrix} |\tilde{X}_{l+k, m-n}^{(\text{orb})}\rangle \langle \tilde{X}_{l+k, m-n'}^{(\text{orb})}| |\tilde{\sigma}_{s,n}\rangle \langle \tilde{\sigma}_{s,n'}| \\ &= \sum_{l'm_1 m_2 s n n'} \left[\sum_{lm} (2l+1) \begin{pmatrix} l' & s & l \\ m_1 & n & m \end{pmatrix} \begin{pmatrix} l' & s & l \\ m_2 & n' & m \end{pmatrix} \right] |\tilde{X}_{l', m_1}^{(\text{orb})}\rangle \langle \tilde{X}_{l', m_2}^{(\text{orb})}| |\tilde{\sigma}_{s,n}\rangle \langle \tilde{\sigma}_{s,n'}| \\ &= \sum_{lmsn} |\tilde{X}_{l,m}^{(\text{orb})} \otimes \tilde{\sigma}_{s,n}\rangle \langle \tilde{X}_{l,m}^{(\text{orb})} \otimes \tilde{\sigma}_{s,n}| \quad (3.3.59) \end{aligned}$$

We redefined the subscripts $l+k \rightarrow l'$, $m-n \rightarrow m_1$, $m-n' \rightarrow m_2$, $-m \rightarrow m$ in the second line and $l' \rightarrow l$, $m_1 \rightarrow m$ in the third line. Since $|\tilde{X}_{l,m}^{(\text{orb})} \otimes \tilde{\sigma}_{s,n}\rangle$ is a complete basis,

$$\begin{aligned} & \left(\sum_{lmsn} |\tilde{X}_{l,m}^{(\text{orb})} \otimes \tilde{\sigma}_{s,n}\rangle \langle \tilde{X}_{l,m}^{(\text{orb})} \otimes \tilde{\sigma}_{s,n}| \right)_{(M_1 \sigma_1 M_2 \sigma_2), (M'_1 \sigma'_1 M'_2 \sigma'_2)}{}^{L_1 L_2} \\ &= \left(\sum_{lm} |\tilde{X}_{l,m}^{(\text{orb})}\rangle \langle \tilde{X}_{l,m}^{(\text{orb})}| \right)_{(M_1 M_2), (M'_1 M'_2)}{}^{L_1 L_2} \left(\sum_{sn} |\tilde{\sigma}_{s,n}\rangle \langle \tilde{\sigma}_{s,n}| \right)_{(\sigma_1 \sigma_2), (\sigma'_1 \sigma'_2)} \\ &= \delta_{M_1 M'_1} \delta_{M_2 M'_2} \delta_{\sigma_1 \sigma'_1} \delta_{\sigma_2 \sigma'_2} \quad (3.3.60) \end{aligned}$$

$|\tilde{X}_{lm}^{(s)}(k)\rangle_{L_1 L_2}$ also satisfies the complete relation in the fixed (L_1, L_2) :

$$\left(\sum_{lmsk} |\tilde{X}_{lm}^{(s)}(k)\rangle \langle \tilde{X}_{lm}^{(s)}(k)| \right)_{(M_1 \sigma_1 M_2 \sigma_2), (M'_1 \sigma'_1 M'_2 \sigma'_2)}{}^{L_1 L_2} = \delta_{M_1 M'_1} \delta_{M_2 M'_2} \delta_{\sigma_1 \sigma'_1} \delta_{\sigma_2 \sigma'_2} \quad (3.3.61)$$

Using Eq. (3.3.47), $|\tilde{X}_{lm}^{(s)}(k)\rangle_{L_1 L_2}$ also satisfies the complete relation in the fixed (L_1, L_2) subspace of $|JM; L\rangle$ basis:

$$\begin{aligned} & \left(\sum_{lmsk} |\tilde{X}_{lm}^{(s)}(k)\rangle \langle \tilde{X}_{lm}^{(s)}(k)| \right)_{(J_1 M_1 J_2 M_2), (J'_1 M'_1 J'_2 M'_2)}{}^{L_1 L_2} \\ &= (-1)^{J_1 + M_1 + J_2 + M_2 + J'_1 + M'_1 + J'_2 + M'_2} \sqrt{(2J_1+1)(2J_2+1)(2J'_1+1)(2J'_2+1)} \\ & \times \sum_{\sigma_1 \sigma_2} \begin{pmatrix} L_1 & J_1 & 1/2 \\ M_1 - \sigma_1/2 & -M_1 & \sigma_1/2 \end{pmatrix} \begin{pmatrix} L_2 & J_2 & 1/2 \\ M_2 - \sigma_2/2 & -M_2 & \sigma_2/2 \end{pmatrix} \\ & \times \sum_{\sigma'_1 \sigma'_2} \begin{pmatrix} L_1 & J'_1 & 1/2 \\ M'_1 - \sigma'_1/2 & -M'_1 & \sigma'_1/2 \end{pmatrix} \begin{pmatrix} L_2 & J'_2 & 1/2 \\ M'_2 - \sigma'_2/2 & -M'_2 & \sigma'_2/2 \end{pmatrix} \end{aligned}$$

$$\begin{aligned}
& \times \left(\sum_{lmsk} |\tilde{X}_{lm}^{(s)}(k)\rangle \langle \tilde{X}_{lm}^{(s)}(k)| \right)_{(M_1-\sigma_1/2\sigma_1 M_2-\sigma_2/2\sigma_2), (M'_1-\sigma'_1/2\sigma'_1 M'_2-\sigma'_2/2\sigma'_2)}^{L_1 L_2} \\
& = (-1)^{J_1+M_1+J_2+M_2+J'_1+M'_1+J'_2+M'_2} \sqrt{(2J_1+1)(2J_2+1)(2J'_1+1)(2J'_2+1)} \\
& \times \sum_{\sigma_1\sigma_2} \begin{pmatrix} L_1 & J_1 & 1/2 \\ M_1-\sigma_1/2 & -M_1 & \sigma_1/2 \end{pmatrix} \begin{pmatrix} L_2 & J_2 & 1/2 \\ M_2-\sigma_2/2 & -M_2 & \sigma_2/2 \end{pmatrix} \\
& \times \sum_{\sigma'_1\sigma'_2} \begin{pmatrix} L_1 & J'_1 & 1/2 \\ M'_1-\sigma'_1/2 & -M'_1 & \sigma'_1/2 \end{pmatrix} \begin{pmatrix} L_2 & J'_2 & 1/2 \\ M'_2-\sigma'_2/2 & -M'_2 & \sigma'_2/2 \end{pmatrix} \\
& \times \delta_{M_1 M'_1} \delta_{M_2 M'_2} \delta_{\sigma_1 \sigma'_1} \delta_{\sigma_2 \sigma'_2} \\
& = (-1)^{J_1+M_1+J_2+M_2+J'_1+M'_1+J'_2+M'_2} \sqrt{(2J_1+1)(2J_2+1)(2J'_1+1)(2J'_2+1)} \\
& \times \sum_{\sigma_1} \begin{pmatrix} L_1 & J_1 & 1/2 \\ M_1-\sigma_1/2 & -M_1 & \sigma_1/2 \end{pmatrix} \begin{pmatrix} L_1 & J'_1 & 1/2 \\ M_1-\sigma_1/2 & -M_1 & \sigma_1/2 \end{pmatrix} \\
& \times \sum_{\sigma_2} \begin{pmatrix} L_2 & J_2 & 1/2 \\ M_2-\sigma_2/2 & -M_2 & \sigma_2/2 \end{pmatrix} \begin{pmatrix} L_2 & J'_2 & 1/2 \\ M_2-\sigma_2/2 & -M_2 & \sigma_2/2 \end{pmatrix} \\
& \times \delta_{M_1 M'_1} \delta_{M_2 M'_2} \\
& = (-1)^{J_1+M_1+J_2+M_2+J'_1+M'_1+J'_2+M'_2} \sqrt{(2J_1+1)(2J_2+1)(2J'_1+1)(2J'_2+1)} \\
& \times \frac{1}{2J_1+1} \frac{1}{2J'_1+1} \delta_{J_1 J'_1} \delta_{J_2 J'_2} \delta_{M_1 M'_1} \delta_{M_2 M'_2} \\
& = \delta_{J_1 J'_1} \delta_{J_2 J'_2} \delta_{M_1 M'_1} \delta_{M_2 M'_2} \tag{3.3.62}
\end{aligned}$$

The above consideration and Eqs. (3.3.55), (3.3.61), and (3.3.62) indicate that $\{\tilde{X}_{lm}^{(s)}(k)\}$ constitute the complete orthonormal basis set in the spinful Hilbert space of $|nLM\sigma\rangle$ or $|nJM;L\rangle$. In other words, it can describe arbitrary spinful operators O in the fixed (L_1, L_2) space:

$$|O\rangle_{L_1 L_2} = \sum_X^{Q,M,T,G} \sum_{l=|L_1-L_2|}^{L_1+L_2} \sum_{m=-l}^l \sum_{s=0,1} \sum_{k=-s}^s \langle \tilde{X}_{lm}^{(s)}(k)|O\rangle_{L_1 L_2} |\tilde{X}_{lm}^{(s)}(k)\rangle_{L_1 L_2} \tag{3.3.63}$$

Hereafter, we neglect $(\tilde{})$ in $\tilde{X}_{lm}^{(s)}(k)$ for notational simplicity unless otherwise stated.

3.3.3 Atomic Multipole Basis in Crystallographic Systems

For crystalline systems, the real representation $X_\alpha^{(a)}$, characterized by $\alpha = (l, \Gamma, m, \gamma; s, k)$ is suitable, where Γ, m, γ , are the irreducible representation of the point group, multiplicity, and component, respectively. The superscript (a) denotes the atomic multipole basis. Notably, since $X_{lm}^{(s)}(k)$ transforms like O_{lm} by the symmetry operation of the point group, the real representations of $X_{lm}^{(s)}(k)$ and O_{lm} can be obtained in the same way,

$$X_\alpha^{(a)} = \sum_m U_{m;\alpha} X_{lm}^{(s)}(k) \tag{3.3.64}$$

$$O_\alpha = \sum_m U_{m;\alpha} O_{lm} \tag{3.3.65}$$

We calculate all the matrix elements of $U_{m;\alpha}$ for O_h and D_{6h} point groups up to rank 11 [28]. The explicit expressions of atomic multipoles $X_\alpha^{(a)}$ up to rank 1 are shown in Table 3.3, and the explicit expressions of the cubic and hexagonal harmonics O_α up to rank 4 are shown in Table C.1. O_α for the other point groups can be also obtained by following the compatibility relation and redefining Γ , m , and γ without changing any matrix element of $U_{m;\alpha}$. Compatibility relation among irreducible representations of cubic and hexagonal point groups are shown in Tables XII and XXVIII in Ref. [26], respectively. Note that the multipoles with the fully symmetric irreducible representation, such as A_{1g} , A_1 , A_g , A in Tables XII and XXVIII in Ref. [26] can have finite expectation values and appear in the Hamiltonian. Meanwhile, the other multipoles are candidate order parameters of various phase transitions.

Table 3.3: Explicit expressions of the atomic multipole operators up to rank 1. \mathbf{l} , $\boldsymbol{\sigma}/2$, and $\mathbf{t} = (\mathbf{r} \times \mathbf{l} - \mathbf{l} \times \mathbf{r})/6$ represent the dimensionless orbital and spin angular-momentum operators and magnetic toroidal dipole operator. Here, $(A_i B_j) = (A_i B_j + A_j B_i + B_i A_j + B_j A_i)/4$. The upper and lower parts separated by double line represent the spinless and spinful multipoles, respectively.

rank	type	$(\mathcal{P}, \mathcal{T})$	notation	expression
0	E	(+, +)	$Q_0^{(a)}$	1
1	E	(-, +)	$\mathbf{Q}^{(a)}$	\mathbf{r}
	M	(+, -)	$\mathbf{M}^{(a)}$	\mathbf{l}
	MT	(-, -)	$\mathbf{T}^{(a)}$	\mathbf{t}
0	E	(+, +)	$Q_0^{(a)}(1)$	$\frac{1}{\sqrt{3}} \mathbf{l} \cdot \boldsymbol{\sigma}$
	M	(+, -)	$M_0^{(a)}(1)$	$\frac{1}{\sqrt{3}} \mathbf{r} \cdot \boldsymbol{\sigma}$
	ET	(-, +)	$G_0^{(a)}(1)$	$\frac{1}{\sqrt{3}} \mathbf{t} \cdot \boldsymbol{\sigma} \propto \mathbf{r} \cdot \mathbf{G}^{(a)}(0)$
1	E	(-, +)	$\mathbf{Q}^{(a)}(0)$	$\frac{1}{\sqrt{2}} (\boldsymbol{\sigma} \times \mathbf{t})$
	E	(-, +)	$Q_z^{(a)}(1)$	$\frac{2}{3\sqrt{10}} [3(lr)_{zx}\sigma_x + 3(lr)_{yz}\sigma_y + 2[2(lr)_{zz} - (lr)_{xx} - (lr)_{yy}]\sigma_z]$ (+cyclic)
	M	(+, -)	$\mathbf{M}^{(a)}(-1)$	$\boldsymbol{\sigma}$
	M	(+, -)	$\mathbf{M}^{(a)}(+1)$	$\frac{3}{\sqrt{10}} \left[(\mathbf{r} \cdot \boldsymbol{\sigma}) \mathbf{r} - \frac{r^2}{3} \boldsymbol{\sigma} \right]$
	MT	(-, -)	$\mathbf{T}^{(a)}(0)$	$\frac{1}{\sqrt{2}} (\mathbf{r} \times \boldsymbol{\sigma})$
	MT	(-, -)	$T_z^{(a)}(+1)$	$\frac{1}{2\sqrt{10}} [3(lt)_{zx}\sigma_x + 3(lt)_{yz}\sigma_y + 2[2(lt)_{zz} - (lt)_{xx} - (lt)_{yy}]\sigma_z]$ (+cyclic)
	ET	(+, +)	$\mathbf{G}^{(a)}(0)$	$\frac{1}{\sqrt{2}} (\mathbf{l} \times \boldsymbol{\sigma})$
	ET	(+, +)	$G_z^{(a)}(+1)$	$\frac{1}{2\sqrt{10}} [3(tr)_{zx}\sigma_x + 3(tr)_{yz}\sigma_y + 2[2(tr)_{zz} - (tr)_{xx} - (tr)_{yy}]\sigma_z]$ (+cyclic)

In a given Hilbert space $\langle \phi_e |$ and $|\psi_{e'} \rangle$ of interest, such as the atomic orbitals (See Appendix B in detail), any electronic degrees of freedom in this space can be described by the matrix representation of the atomic multipole basis $\langle \phi_e | X_\alpha^{(a)} | \psi_{e'} \rangle$. The actual calculation requires $\langle \phi_e | X_\alpha^{(a)} | \psi_{e'} \rangle$ for a limited Hilbert space, and $|\phi_e \rangle$ and $|\psi_{e'} \rangle$ can be represented by the unitary transformation of $|LM\rangle$ (spinless) or $|LM\sigma\rangle/|JM;L\rangle$ (spinful). Thus, $\langle \phi_e | X_\alpha^{(a)} | \psi_{e'} \rangle$ for spinless and spinful systems are explicitly given by

$$\text{spinless systems} \left\{ \begin{array}{l} \langle L_1 M_1 | X_\alpha^{(a)} | L_2 M_2 \rangle = \sum_m U_{m;\alpha} \langle L_1 M_1 | X_{lm}^{(0)}(0) | L_2 M_2 \rangle \\ \langle L_1 \phi_e | X_\alpha^{(a)} | L_2 \psi_{e'} \rangle = \sum_{m M_1 M_2} U_{m;\alpha} U_{M_1;e}^* U_{M_2;e'} \langle L_1 M_1 | X_{lm}^{(0)}(0) | L_2 M_2 \rangle \end{array} \right. \quad (3.3.66)$$

$$\text{spinful systems} \left\{ \begin{array}{l} \langle L_1 M_1 \sigma_1 | X_\alpha^{(a)} | L_2 M_2 \sigma_2 \rangle = \sum_m U_{m;\alpha} \langle L_1 M_1 \sigma_1 | X_{lm}^{(1)}(k) | L_2 M_2 \sigma_2 \rangle \\ \langle L_1 \phi_e \sigma_1 | X_\alpha^{(a)} | L_2 \psi_{e'} \sigma_2 \rangle = \sum_{m M_1 M_2} U_{m;\alpha} U_{M_1;e}^* U_{M_2;e'} \langle L_1 M_1 \sigma_1 | X_{lm}^{(1)}(k) | L_2 M_2 \sigma_2 \rangle \\ \langle J_1 M_1; L_1 | X_\alpha^{(a)} | J_2 M_2; L_2 \rangle = \sum_m U_{m;\alpha} \langle J_1 M_1; L_1 | X_{lm}^{(1)}(k) | J_2 M_2; L_2 \rangle \end{array} \right. \quad (3.3.67)$$

By storing the following matrix elements,

$$\langle L_1 M_1 | X_{lm}^{(0)}(0) | L_2 M_2 \rangle, \langle L_1 M_1 \sigma_1 | X_{lm}^{(1)}(k) | L_2 M_2 \sigma_2 \rangle, \langle J_1 M_1; L_1 | X_{lm}^{(1)}(k) | J_2 M_2; L_2 \rangle, U_{m;\alpha}, U_{M_1;e}, U_{M_2;e'}$$

as binary data once in advance, any matrix elements of the atomic multipole operator are calculable based on Eqs. (3.3.66) and (3.3.67).

Note that the obtained $\{X_\alpha^{(a)}\}$ becomes non-orthogonal in general when a given Hilbert space is the subspace of the rank block (L_1, L_2) , e.g., (p_x, p_y) which is the subspace of the rank block $(1, 1)$, (p_x, p_y, p_z) . Nevertheless, by using Gram-Schmidt orthonormalization, we can also construct the complete orthonormal basis set $\{\tilde{X}_\alpha^{(a)}\}$ expressed by the linear combination of $X_\alpha^{(a)}$. Furthermore, when given orbitals include several ranks, such as $\langle L_1 \oplus L_2 | X_\alpha^{(a)} | L \rangle$, by considering the radial parts of the matrix elements, the matrix elements are given by $\langle r^k \rangle_{L_1 L} \langle L_1 | X_\alpha^{(a)} | L \rangle \oplus \langle r^k \rangle_{L_2 L} \langle L_2 | X_\alpha^{(a)} | L \rangle$. As a result, $\langle L_1 | X_\alpha^{(a)} | L \rangle$ and $\langle L_2 | X_\alpha^{(a)} | L \rangle$ must be treated independently, and then the matrix elements for each rank block, (L_1, L) and (L_2, L) , must be orthogonalized in each block.

3.4 Multipole Basis for Isolated Multi-Site Systems

In this section, we present the SAMB for isolated multi-site systems such as molecules. As shown in Sec. 3.1, we treat the atomic orbital and site/bond degrees of freedom independently.

The definition of the site/bond-cluster is shown in Sec. 3.4.1. Then, we introduce the virtual-cluster in Sec. 3.4.2 that is used for generating the site/bond-cluster multipole basis in periodic crystals as shown in Sec. 3.4.2. Finally, by combining the atomic and site/bond-cluster multipole basis, we define the SAMB in Sec. 3.4.3. The matrix representation of the SAMB is shown in Sec. 3.4.4.

3.4.1 Site/Bond-Cluster

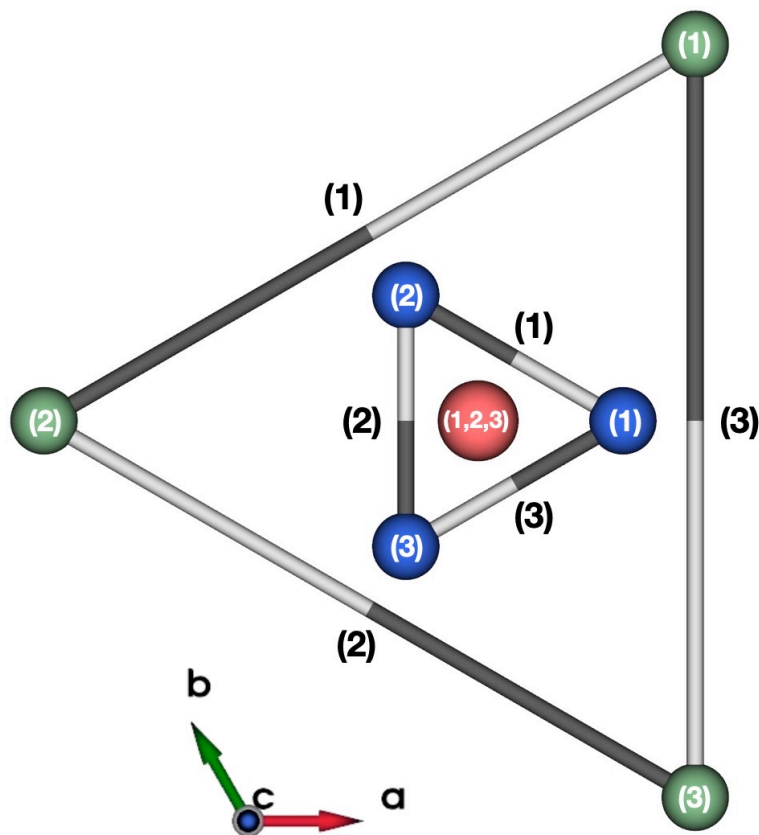


Figure 3.5: Site- and bond-clusters in point group C_3 . Sites with same color belong to the same site-cluster. The numbers in parentheses denote the serial numbers of the symmetry operations.

Let us consider how to generate a basis describing site and bond degrees of freedom for any isolated multi-site system belonging to a crystalline point group P . For this purpose, we classify all sites and bonds constituting the isolated multi-site system into a set of site-clusters and bond-clusters as follows. Figure 3.5 shows a simple example of the site-clusters and bond-clusters in a multi-site system belonging to a point group C_3 , $P = \{1, 3_{001}^+, 3_{001}^-\}$ (1 represents the identity operation).

Site-Cluster

Site-cluster is generated as follows. First, select a representative site \mathbf{R}_1 among the sites constituting the isolated multi-site system. Then, a set of sites $\{\mathbf{R}\} = (\mathbf{R}_1, \mathbf{R}_2, \dots, \mathbf{R}_{N_c})$, which are obtained by applying the symmetry operations $p \in P$ to \mathbf{R}_1 , is called a site-cluster that is characterized by a

Wyckoff position of N_c sites. As shown in Fig. 3.5, there are three independent site-clusters colored by red, blue, and green.

The site obtained by applying the symmetry operation p_g to \mathbf{R}_1 , $\mathbf{R}'_g = p_g \mathbf{R}_1 (p_g \in P)$ sometimes coincides with a site \mathbf{R}_s in the site-cluster. We denote this relationship by $s(g)$.

By selecting an another representative site that is not belonging to the site-cluster generated by \mathbf{R}_1 , and repeating the above procedure, the sites constituting the isolated multi-site system can be classified into a set of site-clusters.

Bond-Cluster

The same procedure is used for generating bond clusters. First, we select a representative bond $\mathbf{R}_n \rightarrow \mathbf{R}_m$ among the bonds in the isolated multi-site system and represent it as $\mathbf{b}_1 @ \mathbf{c}_1$ where $\mathbf{c}_1 = (\mathbf{R}_m + \mathbf{R}_n)/2$ and $\mathbf{b}_1 = \mathbf{R}_m - \mathbf{R}_n$ are the bond center and the bond vector. Then, a set of bond $\{\mathbf{b} @ \mathbf{c}\} = (\mathbf{b}_1 @ \mathbf{c}_1, \mathbf{b}_2 @ \mathbf{c}_2, \dots, \mathbf{b}_{N_c} @ \mathbf{c}_{N_c})$, which are obtained by applying the symmetry operations $p \in P$ to $\mathbf{b}_1 @ \mathbf{c}_1$, is called a bond-cluster that is characterized by a Wyckoff position of N_c bond centers. As shown in Fig. 3.5, there are two independent bond-clusters among the blue colored site-cluster and green colored site-cluster.

The bond obtained by applying the symmetry operation p_g to $\mathbf{b}_1 @ \mathbf{c}_1$, $\mathbf{b}'_g @ \mathbf{c}'_g = p_g \mathbf{b}_1 @ \mathbf{c}_1$ sometimes coincides with a bond $\mathbf{b}_s @ \mathbf{c}_s$ in the bond-cluster. We denote this relationship by $s(g)$. Note that when the bond direction is reversed, $\mathbf{b}'_g = -\mathbf{b}_s$, a negative sign is added to $s(g)$, i.e., $-s(g)$,

By selecting an another representative bond that is not belonging to the bond-cluster generated by $\mathbf{b}_1 @ \mathbf{c}_1$, and repeating the above procedure, the bonds within the isolated multi-site system can be classified into a set of bond-clusters.

3.4.2 Site/Bond-Cluster Multipole Basis

From the above considerations, the basis for each site/bond-cluster can be generated independently. Therefore, we focus on a single site/bond-cluster and present the method to generate a basis set describing the site/bond degrees of freedom within the site/bond-cluster.

A basis set describing the site/bond degrees of freedom is obtained by evaluating the electric multipole $Q_\beta(\mathbf{r})$ at each site $\mathbf{r} = \mathbf{R}_s$ or bond center $\mathbf{r} = \mathbf{c}_s$ within the given multi-site cluster. However, this simple method have two difficulties. First, when $\mathbf{c}_s = \mathbf{0}$, e.g., the diagonal bond in the square and honeycomb cluster, $Q_\beta(\mathbf{c}_s) = \mathbf{0}$ except for $Q_0(\mathbf{c}_s) = 1$. Second, as discussed in Sec. 3.5, since symmetry operations in nonsymmorphic space groups involve partial translations, the sites in a site-cluster are not equidistant from the origin. Consequently, a multipole basis cannot be constructed by the above simple method. To overcome these difficulties, we utilize the virtual-cluster method [101].

Virtual-Cluster

Let us introduce a virtual-cluster generated by operations of a point group or a corresponding point group by removing translation operations from the symmetry operation of a space group (called associated point group). Virtual-clusters for all 32 crystallographic point groups were constructed by selecting an arbitrary general point as $\tilde{\mathbf{R}}_1$ and applying symmetry operations to it to obtain all general points. The virtual-cluster of the D_{6h} point group is shown in Fig. 3.6, where 24 sites are labeled by the index of the corresponding symmetry operation p_g as shown in Table 3.4. Since the distances between the origin and each site are same in the virtual-cluster, we can construct a virtual-cluster E

Table 3.4: Symmetry operations of the point group D_{6h} .

sym. op.	EP	sym. op.	E	sym. op.	E
(1)	1	(x, y, z)	(9)	3_{001}^+	$(-y, x - y, z)$
(2)	2_{001}	$(-x, -y, z)$	(10)	3_{001}^-	$(-x + y, -x, z)$
(3)	2_{100}	$(x - y, -y, -z)$	(11)	6_{001}^+	$(x - y, x, z)$
(4)	2_{010}	$(-x, -x + y, -z)$	(12)	6_{001}^-	$(y, -x + y, z)$
(5)	2_{110}	$(y, x, -z)$	(13)	-1	$(-x, -y, -z)$
(6)	2_{120}	$(-x + y, y, -z)$	(14)	m_{100}	$(-x + y, y, z)$
(7)	2_{210}	$(x, x - y, -z)$	(15)	m_{010}	$(x, x - y, z)$
(8)	2_{1-10}	$(-y, -x, -z)$	(16)	m_{110}	$(-y, -x, z)$
(17)	m_{001}	$(x, y, -z)$	(17)	m_{001}	$(x, y, -z)$
(18)	m_{120}	$(x - y, -y, z)$	(18)	m_{120}	$(x - y, -y, z)$
(19)	m_{210}	$(-x, -x + y, z)$	(19)	m_{210}	$(-x, -x + y, z)$
(20)	m_{1-10}	(y, x, z)	(20)	m_{1-10}	(y, x, z)
(21)	-3_{001}^+	$(y, -x + y, -z)$	(21)	-3_{001}^+	$(y, -x + y, -z)$
(22)	-3_{001}^-	$(x - y, x, -z)$	(22)	-3_{001}^-	$(x - y, x, -z)$
(23)	-6_{001}^+	$(-x + y, -x, -z)$	(23)	-6_{001}^+	$(-x + y, -x, -z)$
(24)	-6_{001}^-	$(-y, x - y, -z)$	(24)	-6_{001}^-	$(-y, x - y, -z)$

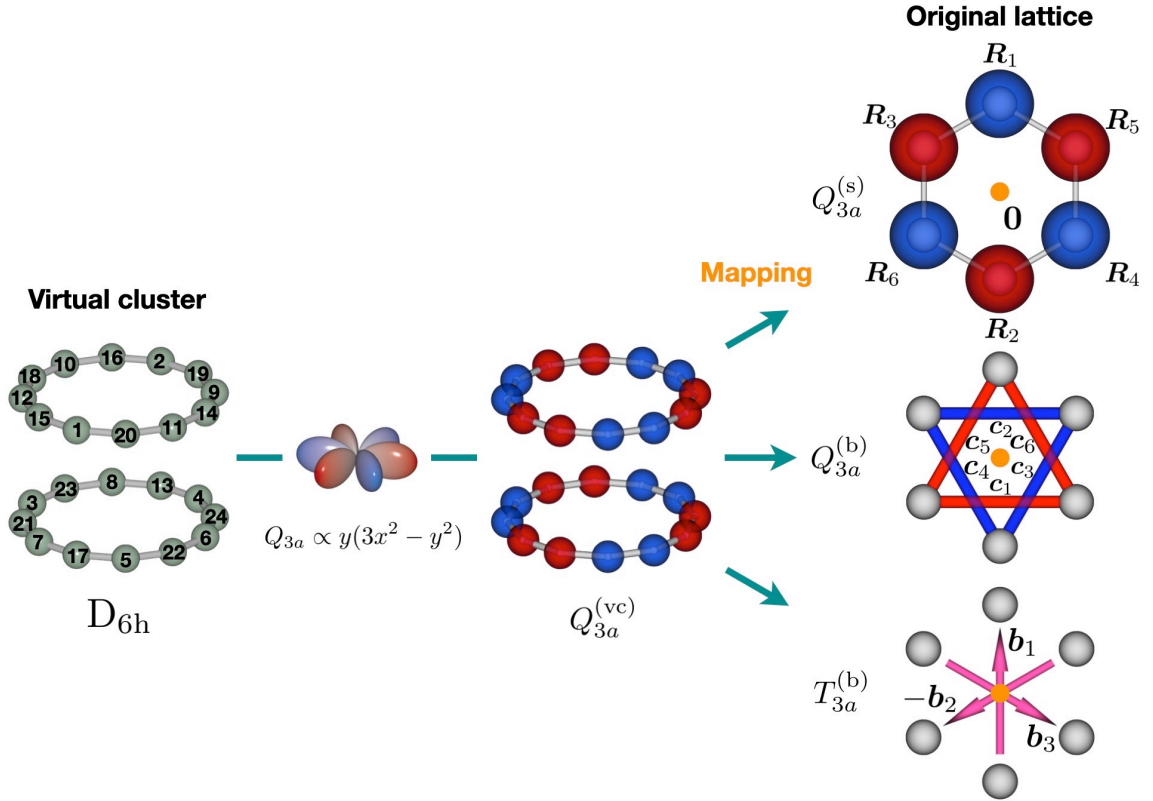


Figure 3.6: Schematic figure of the mapping from the virtual-cluster of D_{6h} point group onto the original honeycomb lattice. The virtual-cluster E octupole $Q_{3a}^{(vc)}$ is mapped to the site-cluster E octupole $Q_{3a}^{(s)}$, bond-cluster E octupole $Q_{3a}^{(b)}$, and bond-cluster MT octupole $T_{3a}^{(b)}$ on the original honeycomb lattice. Since the bond centers of the 3rd neighbor bond are located at the origin, $c_s = \mathbf{0}$, $Q_{3a}(c_s) = 0$.

multipole basis as N_g (number of symmetry operations) dimensional vector:

$$|Q_\beta^{(\text{vc})}\rangle = [Q_\beta(\tilde{\mathbf{R}}_1), Q_\beta(\tilde{\mathbf{R}}_2), \dots, Q_\beta(\tilde{\mathbf{R}}_{N_g})] \quad (3.4.1)$$

where $\tilde{\mathbf{R}}_s$ is the site position in the virtual-cluster. By generating from lower rank basis and following the Gram-Schmidt orthonormalization, we can obtain the complete orthonormal virtual-cluster basis set $\{\tilde{Q}_\beta^{(\text{vc})}\}$ satisfying

$$\langle \tilde{Q}_\beta^{(\text{vc})} | \tilde{Q}_{\beta'}^{(\text{vc})} \rangle = \delta_{\beta\beta'}, \quad \sum_\beta |\tilde{Q}_\beta^{(\text{vc})}\rangle \langle \tilde{Q}_\beta^{(\text{vc})}| = 1_{N_g \times N_g} \quad (3.4.2)$$

where $1_{N_g \times N_g}$ is the $N_g \times N_g$ identity matrix.

$Q_\beta(\tilde{\mathbf{R}})$ is transformed by a symmetry operation p of the point group P as

$$Q_\beta(p^{-1}\tilde{\mathbf{R}}) = \sum_{\beta'} Q_{\beta'}(\tilde{\mathbf{R}}) D_{\beta'\beta}^{\Gamma_\beta}(p) \quad (3.4.3)$$

where $\hat{D}^{\Gamma_\beta}(p)$ is the representation matrix within Γ_β subspace. Similarly, $|\tilde{Q}_\beta^{(\text{vc})}\rangle$ is also transformed by p as follows:

$$p |\tilde{Q}_\beta^{(\text{vc})}\rangle = [\tilde{Q}_\beta(p^{-1}\tilde{\mathbf{R}}_1), \tilde{Q}_\beta(p^{-1}\tilde{\mathbf{R}}_2), \dots, \tilde{Q}_\beta(p^{-1}\tilde{\mathbf{R}}_{N_g})] = \sum_{\beta'} |\tilde{Q}_{\beta'}^{(\text{vc})}\rangle D_{\beta'\beta}^{\Gamma_\beta}(p) \quad (3.4.4)$$

As shown in Fig. 3.6, the virtual-cluster E octupole $Q_{3a}^{(\text{vc})}$ ($Q_{3a} = \frac{\sqrt{10}}{4}y(3x^2 - y^2)$) in the D_{6h} point group is given by

$$|\tilde{Q}_{3a}^{(\text{vc})}\rangle = \frac{[+1, -1, -1, -1, -1, +1, +1, +1, +1, +1, -1, -1, -1, +1, +1, +1, +1, -1, -1, -1, -1, -1, +1, +1]}{\sqrt{24}} \quad (3.4.5)$$

Mapping

To construct the site/bond-cluster multipole basis for the original isolated multi-site system, we map the virtual-cluster E multipole basis, Eq. (3.4.1), onto the sites or bonds in the original cluster.

When we act the symmetry operation $p_g \in \mathcal{P}$ to the representative site \mathbf{R}_1 in the original cluster, some sites overlap at the same site unless \mathbf{R}_1 is a general point. Since the correspondence is given by $s(g)$ as described in Sec. 3.4.1, the site-cluster E multipole basis for the original cluster can be constructed by adding some components in Eq. (3.4.1) that belong to the same site:

$$|Q_\beta^{(s)}\rangle = [Q_\beta^{(s)}(\mathbf{R}_1), Q_\beta^{(s)}(\mathbf{R}_2), \dots, Q_\beta^{(s)}(\mathbf{R}_{N_c})], \quad Q_\beta^{(s)}(\mathbf{R}_j) = \sum_g^{s(g)=s_j} Q_\beta(\tilde{\mathbf{R}}_g) \quad (3.4.6)$$

The bond-cluster multipole basis can be obtained similarly. However, since the bond has directional information \mathbf{b}_s in addition to the bond center \mathbf{c}_s , there are symmetric and antisymmetric basis with respect to reversal of bond directions. The symmetric bond-cluster basis $S_\beta^{(b)}(-\mathbf{b}_s @ \mathbf{c}_s) = S_\beta^{(b)}(\mathbf{b}_s @ \mathbf{c}_s)$, which is independent of the bond direction, is given by

$$|S_\beta^{(b)}\rangle = [S_\beta^{(b)}(\mathbf{b}_1 @ \mathbf{c}_1), S_\beta^{(b)}(\mathbf{b}_2 @ \mathbf{c}_2), \dots, S_\beta^{(b)}(\mathbf{b}_{N_c} @ \mathbf{c}_{N_c})], \quad S_\beta^{(b)}(\mathbf{b}_j @ \mathbf{c}_j) = \sum_g^{|s(g)|=s_j} Q_\beta(\tilde{\mathbf{R}}_g) \quad (3.4.7)$$

While the antisymmetric bond-cluster basis $A_\beta^{(b)}(-\mathbf{b}_s @ \mathbf{c}_s) = -A_\beta^{(b)}(\mathbf{b}_s @ \mathbf{c}_s)$, which changes its sign by the reversal of bond directions, is defined by using $w_g \equiv \text{sgn}(s(g))$ as

$$|A_\beta^{(b)}\rangle = \left[A_\beta^{(b)}(\mathbf{b}_1 @ \mathbf{c}_1), A_\beta^{(b)}(\mathbf{b}_2 @ \mathbf{c}_2), \dots, A_\beta^{(b)}(\mathbf{b}_{N_c} @ \mathbf{c}_{N_c}) \right], \quad A_\beta^{(b)}(\mathbf{b}_j @ \mathbf{c}_j) = \sum_{g}^{|s(g)|=s_j} w_g Q_\beta(\tilde{\mathbf{R}}_g) \quad (3.4.8)$$

Since the real hopping, $t'(a_s^\dagger a_{s'} + \text{h.c.})$, is \mathcal{T} even and is symmetric against an exchange $s \leftrightarrow s'$, it can be described by the bond-cluster E multipole basis defined as the $2N_c$ dimensional vector as

$$|Q_\beta^{(b)}\rangle = \left[S_\beta^{(b)}(\mathbf{b}_1 @ \mathbf{c}_1), \dots, S_\beta^{(b)}(\mathbf{b}_{N_c} @ \mathbf{c}_{N_c}); S_\beta^{(b)}(-\mathbf{b}_1 @ \mathbf{c}_1), \dots, S_\beta^{(b)}(-\mathbf{b}_{N_c} @ \mathbf{c}_{N_c}) \right] \quad (3.4.9)$$

While the imaginary hopping, $it''(a_s^\dagger a_{s'} - \text{h.c.})$, is \mathcal{T} odd and is antisymmetric against an exchange $s \leftrightarrow s'$, it can be described by the bond-cluster MT multipole basis defined as the $2N_c$ dimensional vector as

$$|T_\beta^{(b)}\rangle = i \left[A_\beta^{(b)}(\mathbf{b}_1 @ \mathbf{c}_1), \dots, A_\beta^{(b)}(\mathbf{b}_{N_c} @ \mathbf{c}_{N_c}); A_\beta^{(b)}(-\mathbf{b}_1 @ \mathbf{c}_1), \dots, A_\beta^{(b)}(-\mathbf{b}_{N_c} @ \mathbf{c}_{N_c}) \right] \quad (3.4.10)$$

Thus, by generating from lower rank site-cluster basis and following the Gram-Schmidt orthonormalization, we can construct the complete orthonormal site-cluster multipole basis set $\{\tilde{Q}_\beta^{(s)}\}$ satisfying

$$\langle \tilde{Q}_\beta^{(s)} | \tilde{Q}_{\beta'}^{(s)} \rangle = \delta_{\beta\beta'}, \quad \sum_{\beta} |\tilde{Q}_\beta^{(s)}\rangle \langle \tilde{Q}_\beta^{(s)}| = \mathbf{1}_{N_c \times N_c} \quad (3.4.11)$$

where $\mathbf{1}_{N_c \times N_c}$ is the $N_c \times N_c$ identity matrix.

Similarly, we can also obtain the complete orthonormal bond-cluster multipole basis set $\{\tilde{Y}_\beta^{(b)}\}$ (β distinguishes between Q and T) satisfying

$$\langle \tilde{Y}_\beta^{(b)} | \tilde{Y}_{\beta'}^{(b)} \rangle = \delta_{\beta\beta'}, \quad \sum_{\beta} |\tilde{Y}_\beta^{(b)}\rangle \langle \tilde{Y}_\beta^{(b)}| = \mathbf{1}_{2N_c \times 2N_c} \quad (3.4.12)$$

where $\mathbf{1}_{2N_c \times 2N_c}$ is the $2N_c \times 2N_c$ identity matrix.

Using Eq. (3.4.3), $|\tilde{Q}_\beta^{(s)}\rangle$ and $|\tilde{Y}_\beta^{(b)}\rangle$ are transformed by a symmetry operation p of the point group P as follows:

$$p |\tilde{Q}_\beta^{(s)}\rangle = \sum_{\beta'} |\tilde{Q}_{\beta'}^{(s)}\rangle D_{\beta'\beta}^{\Gamma_\beta}(p) \quad (3.4.13)$$

$$p |\tilde{Y}_\beta^{(b)}\rangle = \sum_{\beta'} |\tilde{Y}_{\beta'}^{(b)}\rangle D_{\beta'\beta}^{\Gamma_\beta}(p) \quad (3.4.14)$$

Figure 3.6 shows an example of mapping from the virtual-cluster of D_{6h} point group onto the original honeycomb lattice. The site-cluster of the original honeycomb lattice consists of the six sites, $(\mathbf{R}_1, \dots, \mathbf{R}_6)$. The relationship between \mathbf{R}_s and $\tilde{\mathbf{R}}_g = p_g \mathbf{R}_1$ represented by $s(g)$ is given by

$$\begin{aligned} 1(g) &= [1, 6, 14, 17], & 4(g) &= [7, 10, 15, 23] \\ 2(g) &= [2, 3, 13, 18], & 5(g) &= [5, 12, 20, 21] \\ 3(g) &= [4, 11, 19, 22], & 6(g) &= [8, 9, 16, 24] \end{aligned} \quad (3.4.15)$$

Then, the site-cluster E octupole $Q_{3a}^{(s)}$ is obtained by using Eq. (3.4.6):

$$|\tilde{Q}_{3a}^{(s)}\rangle = \frac{1}{\sqrt{6}} (-1, +1, +1, -1, +1, -1) \quad (3.4.16)$$

It is depicted in Fig. 3.6.

The 2nd neighbor bond-cluster consists of the six bonds, $(\mathbf{b}_1 @ \mathbf{c}_1, \dots, \mathbf{b}_6 @ \mathbf{c}_6)$. The relationship between $\mathbf{b}_s @ \mathbf{c}_s$ and $\mathbf{b}'_g @ \mathbf{c}'_g = p_g \mathbf{b}_1 @ \mathbf{c}_1$ represented by $s(g)$ is given by

$$\begin{aligned} 1(g) &= [1, -6, -14, 17], & 4(g) &= [5, -12, 20, -21] \\ 2(g) &= [-2, 3, -13, 18], & 5(g) &= [7, -10, 15, -23] \\ 3(g) &= [-4, 11, -19, 22], & 6(g) &= [-8, 9, -16, 24] \end{aligned} \quad (3.4.17)$$

The 2nd neighbor bond-cluster E octupole $Q_{3a}^{(b)}$ is obtained by using Eq. (3.4.9):

$$|\tilde{Q}_{3a}^{(b)}\rangle = \frac{1}{\sqrt{12}} (+1, -1, -1, -1, +1, +1; +1, -1, -1, -1, +1, +1) \quad (3.4.18)$$

It is depicted in Fig. 3.6. Note that the bond-cluster E and MT octupoles $Q_{3a}^{(b)}$ and $T_{3a}^{(b)}$ are not active in the nearest neighbor bond-cluster. Similarly, the bond-cluster MT octupole $T_{3a}^{(b)}$ vanishes in the 2nd neighbor bond-cluster.

The 3rd neighbor bond-cluster consists of the six bonds, $(\mathbf{b}_1 @ \mathbf{c}_1, \dots, \mathbf{b}_6 @ \mathbf{c}_6)$. The relationship between $\mathbf{b}_s @ \mathbf{c}_s$ and $\mathbf{b}'_g @ \mathbf{c}'_g = p_g \mathbf{b}_1 @ \mathbf{c}_1$ represented by $s(g)$ is given by

$$\begin{aligned} 1(g) &= [1, -2, -3, 6, -13, 14, 17, -18] \\ 2(g) &= [5, -8, -9, 12, -16, 20, 21, -24] \\ 3(g) &= [-4, 7, 10, -11, 15, -19, -22, 23] \end{aligned} \quad (3.4.19)$$

The 3rd neighbor bond-cluster MT octupole $T_{3a}^{(b)}$ is obtained by using Eq. (3.4.10):

$$|\tilde{T}_{3a}^{(b)}\rangle = \frac{i}{\sqrt{6}} (+1, -1, +1; -1, +1, -1) \quad (3.4.20)$$

It is depicted in Fig. 3.6. Note that the bond-cluster E octupole $Q_{3a}^{(b)}$ is not active in the 3rd neighbor bond-cluster. It should be emphasized that the bond centers of the 3rd neighbor bond are located at the origin, $\mathbf{c}_s = \mathbf{0}$, $Q_{3a}(\mathbf{c}_s) = 0$. Therefore, the site/bond-cluster multipole basis can not be obtained without the use of the virtual-cluster and mapping method in this case.

As shown above, using the virtual-cluster and mapping method, we can systematically generate complete orthonormal site/bond-cluster multipole basis set.

3.4.3 Symmetry-Adapted Multipole Basis

Following the discussion in Sec. 3.1 and Eq. (3.1.6), the SAMB for isolated multi-site systems is obtained by combining the atomic multipole basis $X_\alpha^{(a)}$ and the site/bond-cluster multipole basis $Y_\beta^{(s/b)}$ as follows:

$$|Z_j\rangle = \sum_{\alpha\beta} \langle X_\alpha^{(a)} \otimes Y_\beta^{(s/b)} | Z_j \rangle |X_\alpha^{(a)} \otimes Y_\beta^{(s/b)}\rangle = \sum_{\alpha\beta} C_{\alpha\beta}^j |X_\alpha^{(a)} \otimes Y_\beta^{(s/b)}\rangle \quad (3.4.21)$$

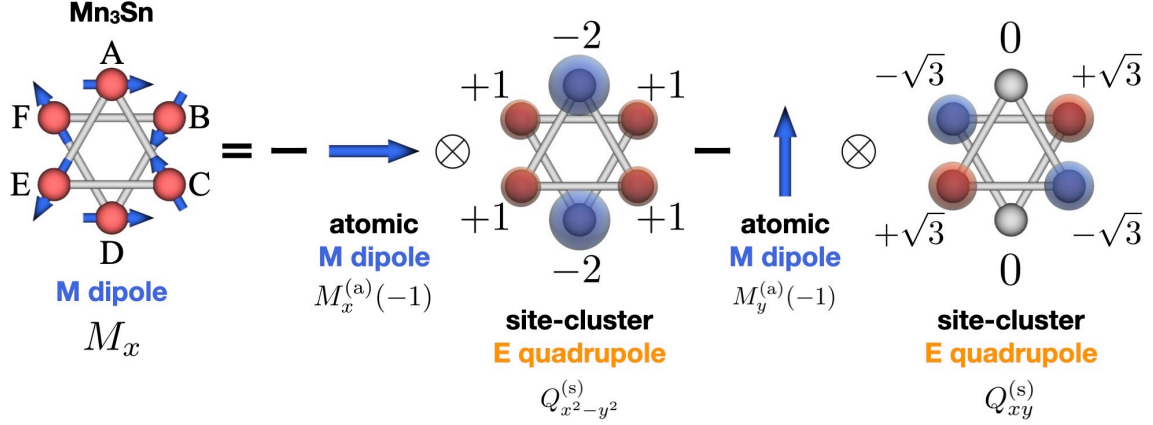


Figure 3.7: Schematic figure of decomposition of the non-collinear AFM ordering in Mn_3Sn into the linear combination of the product of the atomic M dipoles (M_x, M_y) and the site-cluster E quadrupoles ($Q_{x^2-y^2}^{(s)}, Q_{xy}^{(s)}$).

where $j = (\Gamma, m, \gamma)$ and Γ, m, γ , are the irreducible representation of the point group, multiplicity, and component, respectively. The multiplicity m is used to distinguish between multipole basis belonging to the same rank and irreducible representation.

A point group symmetry operation p acts on $|Z_j\rangle$ as follows:

$$p|Z_j\rangle = \sum_i D_{ij}^{\Gamma Z_j}(p)|Z_i\rangle \quad (3.4.22)$$

$$p|Z_j\rangle = \sum_{\alpha\beta} C_{\alpha\beta}^j |pX_\alpha^{(a)} \otimes pY_\beta^{(s/b)}\rangle = \sum_{\alpha\beta} C_{\alpha\beta}^j \sum_{\gamma\delta} D_{\gamma\alpha}^{\Gamma X_\alpha}(p) D_{\delta\beta}^{\Gamma Y_\beta}(p) |X_\gamma^{(a)} \otimes Y_\delta^{(s/b)}\rangle \quad (3.4.23)$$

where Γ_j, Γ_α , and Γ_β are the irreducible representations of $Z_j, X_\alpha^{(a)}$, and $Y_\beta^{(s/b)}$, respectively, and $\hat{D}^\Gamma(p)$ is the representation matrix within Γ subspace. $C_{\alpha\beta}^j = \langle X_\alpha^{(a)} \otimes Y_\beta^{(s/b)} | Z_j \rangle$ is the point-group version of the Clebsch-Gordan (CG) coefficient that appears in reducing the direct product of the irreducible representations Γ_α and Γ_β into Γ_j . See Appendix C.3 for a detailed derivation of $C_{\alpha\beta}^j$.

Since both $|\tilde{X}_\alpha^{(a)}\rangle$ and $|\tilde{Y}_\beta^{(s/b)}\rangle$ are orthonormal and complete in fixed rank block (L_1, L_2) and each site/bond-cluster, we can obtain the complete orthonormal SAMB by orthogonalizing the CG coefficients $\{C_{\alpha\beta}^j\} \rightarrow \{\tilde{C}_{\alpha\beta}^j\}$ according to the Gram-Schmidt orthonormalization:

$$|\tilde{Z}_j\rangle = \sum_{\alpha\beta} \tilde{C}_{\alpha\beta}^j |\tilde{X}_\alpha^{(a)} \otimes \tilde{Y}_\beta^{(s/b)}\rangle \quad (3.4.24)$$

$$\langle \tilde{Z}_i | \tilde{Z}_j \rangle = \delta_{ij}, \quad \left(\sum_j |\tilde{Z}_j\rangle \langle \tilde{Z}_j| \right)_{aa', bb'} = \delta_{ab} \delta_{a'b'} \quad (3.4.25)$$

Hereafter, we neglect ($\tilde{}$) in $\tilde{X}_\alpha^{(a)}, \tilde{Y}_\beta^{(s/b)}$, and \tilde{Z}_j for notational simplicity unless otherwise noticed. Following the above procedure, the complete orthonormal SAMB set $\{Z_j\}$ can be obtained for each pair of rank block and site/bond-cluster independently.

It should be emphasized that the CG coefficient $C_{\alpha\beta}^j$ can be generated with only the labels (α, β) of $X_\alpha^{(a)}$ and $Y_\beta^{(s/b)}$ that contribute to Z_j . In other words, the explicit matrix elements of $X_\alpha^{(a)}$ and $Y_\beta^{(s/b)}$ are not necessary. When the explicit matrix elements of Z_j are necessary, they can be obtained by the procedure described in Sec. 3.4.4.

As shown in Fig. 3.7, the non-collinear AFM ordering in Mn_3Sn can be described by the SAMB of M dipole:

$$|M_x\rangle = -\frac{1}{\sqrt{2}} \left(|M_x^{(a)}(-1)\rangle \otimes |Q_{x^2-y^2}^{(s)}\rangle + |M_y^{(a)}(-1)\rangle \otimes |Q_{xy}^{(s)}\rangle \right) \quad (3.4.26)$$

Equation (3.4.26) provides us an intuitive understanding for the occurrence of the AHE, $\sigma_{yz}^{\text{AHC}} \neq 0$, even under the AFM ordering in Mn_3Sn . Note that since only the parity of rank (even or odd) has a proper meaning in SAMB (see Appendix C.3 in detail), M_x is mixed with the M octupole M_{3u} in reality, which is consistent with the result previously reported by M.-T. Suzuki *et al.* in Ref. [29].

3.4.4 Final Matrix Form

In a practical calculation, the matrix form of Z_j is useful. However, since $Y_\beta^{(s/b)}$ is defined by a $N_c/2N_c$ -dimensional vector, its size depends on each cluster. Similarly, the orbital spaces $\langle\phi_e|$ and $|\psi_{e'}\rangle$ also depend on the site/bond-cluster. Consequently, the matrix elements $\langle\phi_e|X_\alpha^{(a)}|\psi_{e'}\rangle$ and $Y_\beta^{(s/b)}(s)$ have to be rearranged to the corresponding component (i, j) in the total Hilbert space of the site/bond-cluster, $\langle\phi_e \otimes s|$ and $|\psi_{e'} \otimes s'\rangle$. Assuming that each site/bond component consists of a block of atomic orbitals, each element of (s, s') space is a block matrix of $X_\alpha^{(a)}$. Therefore, only $Y_\beta^{(s/b)}$ needs to be rearranged.

In the case of a site-cluster, $Y_\beta^{(s)}(s)$ should be placed on the diagonal element (s, s) . While, in the case of a bond-cluster, $Y_\beta^{(b)}(\mathbf{b}_s @ \mathbf{c}_s)$ should be placed on the off-diagonal element based on the correspondence $\mathbf{b}_s @ \mathbf{c}_s \rightarrow (s, s')$, where $\mathbf{b}_s = \mathbf{R}_s - \mathbf{R}_{s'}$. These operations are denoted as follows:

$$Y_\beta^{(s/b)} \rightarrow M_\beta^{(t)} \quad (3.4.27)$$

If $Y_\beta^{(s/b)}$ is the complete orthonormal basis, $M_\beta^{(t)}$ also satisfies the orthonormal and complete relations

$$\langle M_\beta^{(t)} | M_{\beta'}^{(t)} \rangle = \delta_{\beta\beta'}, \quad \left(\sum_{\beta} |M_\beta^{(t)}\rangle \langle M_\beta^{(t)}| \right)_{(s_1 s_2), (s'_1 s'_2)} = \delta_{s_1 s'_1} \delta_{s_2 s'_2} \quad (3.4.28)$$

For example, the matrix forms of Eqs. (3.4.16), (3.4.18), and (3.4.20) are given by

$$\begin{aligned} \tilde{Q}_{3a}^{(s)} \rightarrow \tilde{Q}_{3a}^{(t,1)} &= \frac{1}{\sqrt{6}} \begin{pmatrix} -1 & 0 & 0 & 0 & 0 & 0 \\ 0 & 1 & 0 & 0 & 0 & 0 \\ 0 & 0 & 1 & 0 & 0 & 0 \\ 0 & 0 & 0 & -1 & 0 & 0 \\ 0 & 0 & 0 & 0 & 1 & 0 \\ 0 & 0 & 0 & 0 & 0 & -1 \end{pmatrix}, & \tilde{Q}_{3a}^{(b)} \rightarrow \tilde{Q}_{3a}^{(t,2)} &= \frac{1}{\sqrt{12}} \begin{pmatrix} 0 & 0 & 0 & 1 & 0 & 1 \\ 0 & 0 & -1 & 0 & -1 & 0 \\ 0 & -1 & 0 & 0 & -1 & 0 \\ 1 & 0 & 0 & 0 & 0 & 1 \\ 0 & -1 & -1 & 0 & 0 & 0 \\ 1 & 0 & 0 & 1 & 0 & 0 \end{pmatrix}, \\ \tilde{T}_{3a}^{(b)} \rightarrow \tilde{T}_{3a}^{(t)} &= \frac{1}{\sqrt{6}} \begin{pmatrix} 0 & i & 0 & 0 & 0 & 0 \\ -i & 0 & 0 & 0 & 0 & 0 \\ 0 & 0 & 0 & -i & 0 & 0 \\ 0 & 0 & i & 0 & 0 & 0 \\ 0 & 0 & 0 & 0 & 0 & -i \\ 0 & 0 & 0 & 0 & i & 0 \end{pmatrix} \end{aligned} \quad (3.4.29)$$

where the superscript (t, i) ($i = 1, 2$) distinguishes the diagonal and off-diagonal basis.

3.5 Multipole Basis for Periodic Multi-Site Systems

In this section, we present the SAMB for periodic multi-site systems such as crystals. The procedure to obtain the SAMB is exactly the same as for the isolated multi-site systems. On the other hand, some modification are essential to obtain the site/bond-cluster multipole basis for periodic multi-site systems as shown below.

3.5.1 Symmetry-Adapted Multipole Basis

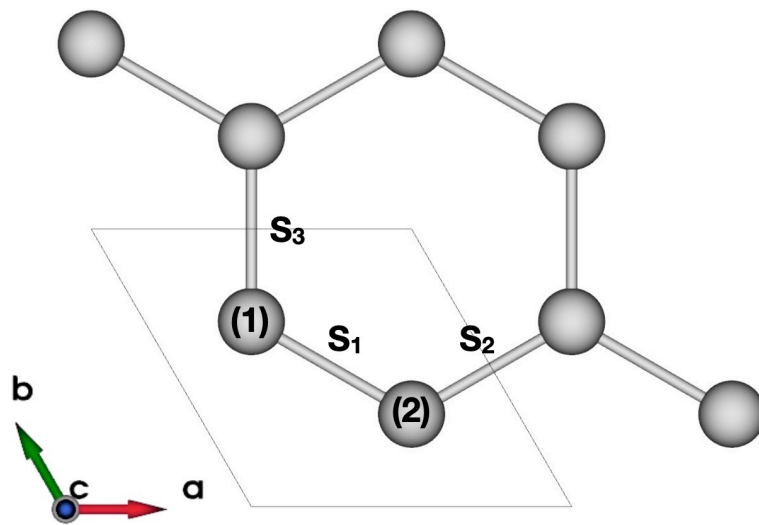


Figure 3.8: Site- and bond-clusters in the graphene. The black diamond represents the home unit cell. The site-cluster consists of two sublattices, while the nearest neighbor bond-cluster is composed of three bonds. The numbers in parentheses are the serial numbers of the symmetry operations.

Site/Bond-Cluster

Let us consider the site/bond-clusters constituting the periodic crystals belonging to a space group G :

$$G = \sum_{g=1}^{N_g} \mathcal{G}T \quad (3.5.1)$$

$$\mathcal{G} = \{p_g | \tau_g\} \quad (3.5.2)$$

where p_g is a point group symmetry operation, τ_g is a partial translation, and T denotes the lattice translations. When the generated site ($\mathbf{R}'_g = \mathcal{G}\mathbf{R}_1$) or bond ($\mathbf{b}'_g @ \mathbf{c}'_g = \mathcal{G}\mathbf{b}_1 @ \mathbf{c}_1$) is transferred outside the home unit cell, it must be shifted into the home unit cell by appropriate lattice translation.

Figure 3.8 shows an example of the site/bond-cluster in the graphene whose space group is $P6/mmm$ (#191, D_{6h}^1). The relationship between \mathbf{R}_s and $\mathbf{R}'_g = \mathcal{G}\mathbf{R}_1$ represented by $s(g)$ is given by

$$\begin{aligned} 1(g) &= [1, 6, 7, 8, 9, 10, 14, 15, 16, 17, 23, 24] \\ 2(g) &= [2, 3, 4, 5, 11, 12, 13, 18, 19, 20, 21, 22] \end{aligned} \quad (3.5.3)$$

While, the relationship between $s = \mathbf{b}_s @ \mathbf{c}_s$ and $\tilde{\mathbf{R}}_g = \mathcal{G} \mathbf{b}_1 @ \mathbf{c}_1$ represented by $s(g)$ is given by

$$1(g) = [1, -2, -5, 8, -13, 16, 17, -20] \quad (3.5.4)$$

$$2(g) = [3, -6, -10, 11, -14, 18, 22, -23] \quad (3.5.5)$$

$$3(g) = [-4, 7, 9, -12, 15, -19, -21, 24] \quad (3.5.6)$$

Virtual-Cluster

The virtual-cluster for space group G is generated as follows. In general, space group G can be expanded as the sum of the cosets:

$$G = \sum_{j=1}^{N_{\text{coset}}} \{p_j | \tau_j\} UT \quad (3.5.7)$$

where U denotes the set of point group symmetry operations $\{p | \mathbf{0}\}$ in G and N_{coset} is the number of the cosets. Note that $\{p_1 | \tau_1\} = \{E | \mathbf{0}\}$ and $\tau_j \neq \mathbf{0}$ for $j \geq 2$, and $N_{\text{coset}} = 1$ (> 1) for symmorphic (nonsymmorphic) space group. Then, the virtual-cluster for the space group G is generated by considering the associated point group P defined by

$$P = \sum_{j=1}^{N_{\text{coset}}} \{p_j | \mathbf{0}\} U \quad (3.5.8)$$

There is a one-to-one correspondence between a symmetry operation \mathcal{G} of the space group G and a symmetry operation p_g of the associated point group P , i.e., an operation \mathcal{G} in the actual periodic crystal corresponds to an operation p_g in the virtual cluster:

$$\mathcal{G} = \{p_g | \tau_g\} \longrightarrow \{p_g | \mathbf{0}\} = p_g \quad (3.5.9)$$

This is nothing but the mapping relation between the actual periodic crystal and the virtual cluster. Thus, using the associated point group symmetry operations p_g with neglecting the partial translation τ_g , we can generate a virtual-cluster for both the symmorphic ($\tau_g = \mathbf{0}$) and nonsymmorphic ($\tau_g \neq \mathbf{0}$) space groups in the same way.

With the above considerations, the complete orthonormal site/bond-cluster multipole basis set $\{\tilde{Q}_\beta^{(s)}\}$ and $\{\tilde{Y}_\beta^{(b)}\}$ can be generated based on the mapping given by Eqs. (3.4.6)-(3.4.12). Thanks to the mapping relation given by Eq. (3.5.9), we can define the irreducible representation matrix in the actual periodic crystal $\hat{D}^\Gamma(\mathcal{G})$ as

$$\hat{D}^\Gamma(\mathcal{G}) \equiv \hat{D}^\Gamma(p_g) \quad (3.5.10)$$

Thus, $|\tilde{Q}_\beta^{(s)}\rangle$ and $|\tilde{Y}_\beta^{(b)}\rangle$ are transformed by \mathcal{G} as follows:

$$\mathcal{G} |\tilde{Q}_\beta^{(s)}\rangle = \sum_{\beta'} |\tilde{Q}_{\beta'}^{(s)}\rangle D_{\beta'\beta}^{\Gamma_\beta}(\mathcal{G}) = \sum_{\beta'} |\tilde{Q}_{\beta'}^{(s)}\rangle D_{\beta'\beta}^{\Gamma_\beta}(p_g) \quad (3.5.11)$$

$$\mathcal{G} |\tilde{Y}_\beta^{(b)}\rangle = \sum_{\beta'} |\tilde{Y}_{\beta'}^{(b)}\rangle D_{\beta'\beta}^{\Gamma_\beta}(\mathcal{G}) = \sum_{\beta'} |\tilde{Y}_{\beta'}^{(b)}\rangle D_{\beta'\beta}^{\Gamma_\beta}(p_g) \quad (3.5.12)$$

As a result, $|\tilde{Q}_\beta^{(s)}\rangle$ and $|\tilde{Y}_\beta^{(b)}\rangle$ are characterized by the irreducible representation Γ_β of the associated point group P of the original space group G regardless of the symmorphic ($\tau_g = \mathbf{0}$) or nonsymmorphic ($\tau_g \neq \mathbf{0}$) groups.

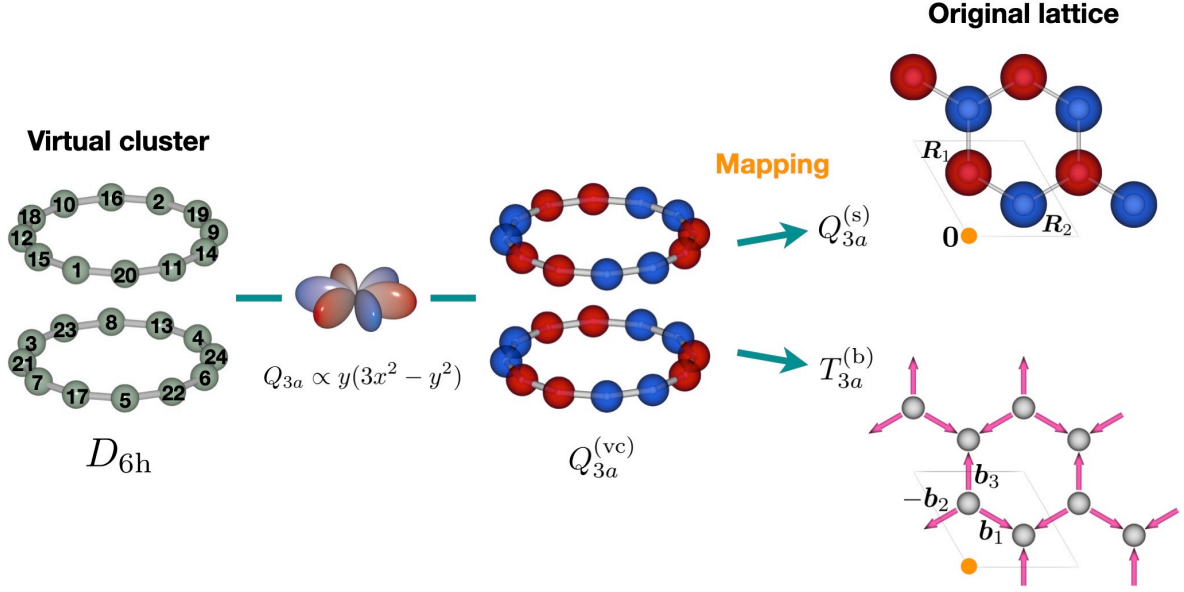


Figure 3.9: Schematic figure of the mapping from the virtual-cluster of D_{6h} point group onto the original graphene lattice. The virtual-cluster E octupole $Q_{3a}^{(vc)}$ is mapped to the site-cluster E octupole $Q_{3a}^{(s)}$ and bond-cluster MT octupole $T_{3a}^{(b)}$ on the original graphene lattice.

For example, the virtual-cluster of the graphene is that of the point group D_{6h} as shown in Fig. 3.9. The site-cluster E octupole $Q_{3a}^{(s)}$ and the nearest neighbor bond-cluster MT octupole $T_{3a}^{(b)}$ are obtained by using Eq. (3.4.6) and (3.4.10) as follows:

$$|Q_{3a}^{(s)}\rangle = \frac{1}{\sqrt{2}}(+1, -1) \quad (3.5.13)$$

$$|T_{3a}^{(b)}\rangle = \frac{1}{\sqrt{2}}(+i, -i, +i, -i, +i, -i) \quad (3.5.14)$$

The schematic figures of $Q_{3a}^{(s)}$ and $T_{3a}^{(b)}$ are shown in Fig. 3.9. The site/bond-cluster multipole basis for nonsymmorphic space group, i.e., elemental Tellurium, is shown in Chap. 5.

Thus, the SAMB of a periodic multi-site system is exactly same as that of an isolated multi-site system given by Eq. (3.4.21):

$$|Z_j\rangle = \sum_{\alpha\beta} \langle X_\alpha^{(a)} \otimes Y_\beta^{(s/b)} | Z_j \rangle | X_\alpha^{(a)} \otimes Y_\beta^{(s/b)} \rangle = \sum_{\alpha\beta} C_{\alpha\beta}^j | X_\alpha^{(a)} \otimes Y_\beta^{(s/b)} \rangle \quad (3.5.15)$$

A space group symmetry operation $\mathcal{G} = \{p_g | \tau_g\}$ acts on $|Z_j\rangle$ as follows:

$$\mathcal{G} |Z_j\rangle = \sum_i D_{ij}^{\Gamma_j} (p_g) |Z_i\rangle \quad (3.5.16)$$

$$\mathcal{G} |Z_j\rangle = \sum_{\alpha\beta} C_{\alpha\beta}^j | \mathcal{G} X_\alpha^{(a)} \otimes \mathcal{G} Y_\beta^{(s/b)} \rangle = \sum_{\alpha\beta} C_{\alpha\beta}^j \sum_{\gamma\delta} D_{\gamma\alpha}^{\Gamma_j} (p_g) D_{\delta\beta}^{\Gamma_j} (p_g) | X_\gamma^{(a)} \otimes Y_\delta^{(s/b)} \rangle \quad (3.5.17)$$

3.5.2 Final Matrix Form

The final matrix form of the site-cluster multipole basis $Y_\beta^{(s)}$ is obtained by the same way given in Sec. 3.4.4. Therefore, we only consider the matrix form of the bond-cluster multipole basis $Y_\beta^{(b)}$ as

follows.

Let us first define the E and MT momentum multipole basis $f_\beta(\mathbf{k})$ by the Fourier transform of the symmetric and antisymmetric bond-cluster basis, respectively:

$$Q_\beta(\mathbf{k}) = \frac{1}{\sqrt{2}} \sum_{s=1}^{N_c} S_\beta^{(b)}(s) (B_s + \text{c.c.}) = \sqrt{2} \sum_{s=1}^{N_c} S_\beta^{(b)}(s) C_s \quad (3.5.18)$$

$$T_\beta(\mathbf{k}) = \frac{1}{\sqrt{2}i} \sum_{s=1}^{N_c} A_\beta^{(b)}(s) (B_s - \text{c.c.}) = \sqrt{2} \sum_{s=1}^{N_c} A_\beta^{(b)}(s) S_s \quad (3.5.19)$$

where $B_s \equiv e^{-i\mathbf{k}\cdot\mathbf{b}_s}$, $C_s = \cos(\mathbf{k}\cdot\mathbf{b}_s)$, and $S_s = \sin(\mathbf{k}\cdot\mathbf{b}_s)$. Similar to Eq. (3.5.12), the obtained $f_\beta(\mathbf{k})$ is transformed in the same way as the irreducible representation Γ_β for the symmetric operation on the space group.

The matrix elements of the bond-cluster multipole basis $Y_\beta^{(b)}(s)$ is modified by the phase B_s as $Y_\beta^{(b)}(s)B_s$. Then, the final matrix form is denoted as $M_\beta^{(t)}(\mathbf{k})$. Note that $M_\beta^{(t)} = M_\beta^{(t)}(\mathbf{k} = \mathbf{0})$. $M_\beta^{(t)}(\mathbf{k})$ is expanded as the linear combination of the direct product of $M_\gamma^{(t)}$ and $f_\delta(\mathbf{k})$ as

$$M_\beta^{(t)}(\mathbf{k}) = \sum_{\gamma\delta} p_{\gamma\delta}^\beta M_\gamma^{(t)} f_\delta(\mathbf{k}) \quad (3.5.20)$$

The expansion coefficient $p_{\gamma\delta}^\beta$ can be obtained by solving a simultaneous linear equations for B_s given in Eq. (3.5.20).

Since $S_\beta^{(b)}$ and $A_\beta^{(b)}$ are orthonormal, $f_\beta(\mathbf{k})$ is also orthonormal:

$$\langle f_\beta(\mathbf{k}) | f_{\beta'}(\mathbf{k}) \rangle = \frac{V}{(2\pi)^d} \int_{\text{BZ}} f_\beta^*(\mathbf{k}) f_{\beta'}(\mathbf{k}) = \delta_{\beta\beta'} \quad (3.5.21)$$

Note that if all bond-clusters in the given system are considered, $f_\beta(\mathbf{k})$ (β includes the bond-cluster) satisfies the complete relation in the momentum space as

$$\sum_{\beta} f_\beta^*(\mathbf{k}) f_\beta(\mathbf{k}') = \delta_{\mathbf{k}\mathbf{k}'} \quad (3.5.22)$$

Thus, $M_\beta^{(t)}(\mathbf{k})$ also satisfies both the orthonormal and complete relations:

$$\langle M_\beta^{(t)}(\mathbf{k}) | M_{\beta'}^{(t)}(\mathbf{k}) \rangle = \frac{V}{(2\pi)^d} \int_{\text{BZ}} \text{Tr} [M_\beta^{(t)\dagger}(\mathbf{k}) M_{\beta'}^{(t)}(\mathbf{k})] = \delta_{\beta\beta'} \quad (3.5.23)$$

$$\left(\sum_{\beta} |M_\beta^{(t)}(\mathbf{k})\rangle \langle M_\beta^{(t)}(\mathbf{k}')| \right)_{(s_1 s_2), (s'_1 s'_2)} = \delta_{s_1 s'_1} \delta_{s_2 s'_2} \delta_{\mathbf{k}\mathbf{k}'} \quad (3.5.24)$$

Based on the above procedure, we obtain the SAMB of the momentum space representation as

$$|Z_j(\mathbf{k})\rangle = \sum_{\beta\gamma} C_{\alpha\beta}^j |X_\alpha^{(a)} \otimes M_\beta^{(t)}(\mathbf{k})\rangle \quad (3.5.25)$$

$$[Z_j(\mathbf{k})]_{ss'}^{aa'} = \sum_{\alpha\beta} C_{\alpha\beta}^j [X_\alpha^{(a)}]_{aa'} [M_\beta^{(t)}(\mathbf{k})]_{ss'} \quad (3.5.26)$$

$Z_j(\mathbf{k})$ satisfies both the orthonormal and complete relations:

$$\langle Z_i(\mathbf{k}) | Z_j(\mathbf{k}) \rangle = \frac{V}{(2\pi)^d} \int_{\text{BZ}} \text{Tr} \left[Z_i^\dagger(\mathbf{k}) Z_j(\mathbf{k}) \right] = \delta_{ij} \quad (3.5.27)$$

$$\sum_j (|Z_j(\mathbf{k})\rangle \langle Z_j(\mathbf{k}')|)_{aa',bb'} = \delta_{\mathbf{k}\mathbf{k}'} \delta_{ab} \delta_{a'b'} \quad (3.5.28)$$

Note that the complete relation is satisfied only if all bond-clusters are considered.

3.6 Summary

In this Chapter, we have introduced the symmetry-adapted multipole basis, which enable us to describe any electronic degrees of freedom in the isolated and periodic multi-site systems, such as molecules and crystals.

In Sec. 3.1, we have decomposed the electronic degrees of freedom into the orbital/spin and the sublattice parts. We have clarified the definition of the symmetry-adapted multipole basis that is given by the linear combination of the direct product of the atomic multipole basis and the site/bond-cluster multipole basis.

In Sec. 3.3, we have presented the definition of the atomic multipole basis for both spinless and spinful single-centered electron systems. We have confirmed that the atomic multipole basis constitutes the complete orthonormal basis set. Using the atomic multipole basis, any electronic degrees of freedom in the isolated single-centered electron systems can be described.

In Sec. 3.4, we have introduced the virtual-cluster defined by the general points produced by the symmetry operations of a point group, which enable us to systematically generate the site/bond-cluster multipole basis without difficulty of choosing the origin and cluster unit especially for non-centrosymmetric space group. Similar to the atomic multipole basis, the site/bond-cluster multipole basis constitutes the complete orthonormal basis set in the sublattice space. Then, by combining the atomic and site/bond-cluster multipole basis, we have defined the symmetry-adapted multipole basis. In Sec. 3.5, we have extended the definition of the symmetry-adapted multipole basis to the periodic crystals. Since both the atomic and site/bond-cluster multipole basis satisfy the complete and orthonormal relations, the obtained symmetry-adapted multipole basis also constitutes the complete orthonormal basis set in the given Hilbert space.

Using the symmetry-adapted multipole basis, we can describe any electronic degrees of freedom in the isolated and periodic multi-site systems, such as molecules and crystals. In particular, since the Hamiltonian must be fully-symmetric, it can be described by the sum of the fully-symmetric symmetry-adapted multipole basis:

$$|H\rangle = \sum_j \langle Z_j | H \rangle |Z_j\rangle = \sum_j z_j |Z_j\rangle \quad (3.6.1)$$

$$z_j = \langle Z_j | H \rangle \quad (3.6.2)$$

where z_j is the weight of the contribution of $|Z_j\rangle$ in $|H\rangle$. We summarize the advantages of using the above expression:

- (1) Since each Z_j is fully symmetric, the Hamiltonian satisfies the symmetry of a given system precisely.
- (2) By decomposing the Hamiltonian in the form of Eq. (3.6.1), we can unveil a hidden multipole basis, which corresponds to a candidate order parameter, in a given system.

- (3) When the matrix elements of the given Hamiltonian are described in terms of the atomic orbital basis, we can clarify the weight of each multipole basis by taking a matrix trace based on Eq. (3.6.2).
- (4) When we build up the Hamiltonian from scratch, z_j corresponds to a controllable parameter. In particular, given an energy band dispersion obtained from DFT calculations, we can also construct a DFT-based symmetry-adapted TB model by optimizing z_j to reproduce the DFT band dispersion.

In Chap. 4, we will show a systematic generation scheme of the DFT-based symmetry-adapted TB model based on the symmetry-adapted multipole basis.

Chapter 4

DFT-Based Symmetry-Adapted Tight-Binding Model

4.1 Introduction

Eccentric orderings and their related physical phenomena are determined from symmetry and material-specific microscopic properties such as electronic band structure. To understand them from a microscopic point of view, constructing a realistic model satisfying the symmetry of a given system is essential. The DFT-based electronic structure analysis is a powerful way to incorporate electronic states in materials in detail and to evaluate a wide range of physical quantities. There are several software packages to perform DFT calculations, such as VASP [65], QUANTUM ESPRESSO [66], WIEN2K [67], OpenMX [68], ABINIT5 [69], Gaussian [70], and so on.

On the other hand, to understand low-energy physics, only a few electronic states close to the Fermi level are crucial. The DFT-based Wannier TB model has been widely used for quantitative analysis of various physical properties of interest, and it can be constructed by using an open-source Wannier90 software package [72–74]. To our knowledge, there are also some open-source software packages that provide an interface to the Wannier90 code and a tool to construct or analyze the Wannier TB Hamiltonian systematically, such as PythTB (see <http://www.physics.rutgers.edu/pythtb/>), WannierBerri [95], TBM [96], and so on. However, as discussed in Chap. 2, the Wannier TB model has several disadvantages: (1) The symmetry of a given system is not rigorously satisfied during the construction of the Wannier TB Hamiltonian. (2) The Wannier function is unsuitable for symmetry arguments because it has no characteristic quantum number, such as the atomic orbital and magnetic quantum numbers. (3) Many hopping parameters associated with long-range bonds are involved in the Hamiltonian, which hampers the analysis of material properties from a microscopic point of view. (4) The microscopic expression of the order parameter and the microscopic mechanism of the physical properties of interest often remain unclear.

Meanwhile, the TB model based on the atomic orbitals with a small number of model parameters is a suitable choice for symmetry arguments and electronic structure calculations with low computational costs. In particular, adopting the Slater-Koster approach [99], we can construct a TB model which uses moderate number of model parameters and approximately satisfies the symmetry of a given system, which provides an intuitive and deeper understanding of the electronic band structure and various physical properties of interest. However, as mentioned in Chap. 2, some essential hopping parameters would be lost because of neglecting the exact symmetry around each bond.

In this regard, as shown in Chap. 3, the TB Hamiltonian constructed by the linear combination of the symmetry-adapted multipole basis (SAMB) is the most suitable prescription since the symmetry

of the system is considered rigorously. Henceforth, we refer to the TB Hamiltonian based on the SAMB as the symmetry-adapted TB model. In the symmetry-adapted TB model, the weight of each SAMB corresponds to the model parameter. Thus, the reliability of the calculations using this model strongly depends on the choice of the weight of each SAMB. In particular, to construct the DFT-based symmetry-adapted TB model, we must optimize the weights to reproduce the DFT band dispersion. However, the optimization process is not easy and has yet to be developed. One of the difficulties is that the accuracy of the optimization strongly depends on the initial guess of the model parameters. This problem is pronounced when there are more than a few hundred model parameters owing to many sublattices and orbital degrees of freedom. By these circumstances, developing a method to overcome these difficulties is highly desirable.

In the last decades, machine learning (ML) techniques and deep neural networks (DNN) [153] have developed rapidly with the improvement of computational resources. The ML techniques have been utilized in various fields of science [154], such as chemistry [155–160], materials science [161–164], and condensed matter physics, such as strongly correlated electron systems [165], identification of phase transitions [166], strain engineering [167], exploration of topological band structures [168], prediction of the electrical conductivity [169], thermal transport [170], and the band gap of materials [171–173], and so on. Notably, the ML techniques to construct DFT-based TB Hamiltonian [174, 175] and to systematically predict electronic band structures have been developed [168, 176, 177]. Although the TB models generated by Z. Wang *et al.* [175] reproduce the DFT band dispersions with high accuracy, the symmetry of the system is not considered because each matrix element of the Hamiltonian plays the role of a neuron in the neural networks (NN) without any constraint by symmetry. On the other hand, since the method proposed by M. Nakhaee *et al.* [175] adopted the Slater-Koster approach, the resultant model satisfies the symmetry of the system. Nevertheless, as mentioned above, some essential parameters would be lost in this Slater-Koster approach.

In the present study, we develop a systematic generation scheme of the DFT-based symmetry-adapted TB model with the help of the ML techniques. The weights of the SAMB are optimized by fitting the DFT band dispersion. To this end, we regard the symmetry-adapted TB model as a fully-connected DNN that connects nonlinearly between every weight of the SAMB and every energy eigenvalue obtained from the DFT calculation. It should be emphasized that since each SAMB is fully symmetric, the symmetry of a given system is maintained during the optimization process. In addition, the weight of each SAMB plays a role of the neuron, and the number of the model parameters is equal to that of the independent SAMBs. Thus, these features overcome the disadvantages of the methods proposed by M. Nakhaee *et al.* [174] and Z. Wang *et al.* [175]. Moreover, we have constructed the symmetry-adapted multipole DNN (DNN-SAMB) system by inserting the hidden layers between the SAMB and the DFT band dispersion layers. The DNN-SAMB shows high optimization accuracy and less dependence on the initial guess for the model parameters. Additionally, from the optimization results, we can unveil hidden characteristic multipole degrees of freedom in the system and evaluate their contribution to the Hamiltonian and various physical quantities. Note that our method is applicable to any crystallographic structure within 230 space group regardless of symmorphic or nonsymmorphic groups in cooperation with the reliable DFT band dispersion data. Moreover, since the SAMB can describe any electronic degrees of freedom, such as spin, orbital, and sublattice degrees of freedom, and contains enough information to investigate the physical properties of the material of interest, the DNN-SAMB could be useful to materials informatics.

The rest of this chapter is organized as follows. In Sec. 4.2, we briefly show the symmetry-adapted TB model. In Sec. 4.3, we present the workflow of the DNN-SAMB and how to systematically construct the DFT-based symmetry-adapted TB model. In Sec. 4.4, we show prime examples of the method for graphene, SrVO₃, and MoS₂. We summarize the results in Sec. 4.5.

4.2 Symmetry-Adapted Tight-Binding Model

Let us consider the general form of the TB Hamiltonian in the real space representation:

$$\mathcal{H} = \sum_{\mathbf{R}} \sum_{ss'} \sum_{aa'} [H(\mathbf{R})]_{ss'}^{aa'} c_{as\mathbf{R}}^\dagger c_{a's'\mathbf{0}} \quad (4.2.1)$$

$c_{as\mathbf{R}}^{(\dagger)}$ denotes the annihilation (creation) operator of the electron characterized by the atomic orbital $|\varphi_{as\mathbf{R}}\rangle$ (See Eq. 2.2.2), where $a(a')$ denotes both the orbital and spin labels, \mathbf{R} is a lattice vector, and $\mathbf{s}(s')$ is a position vector of the sublattice $s(s')$ in a unit cell. Note that H can describe any potentials and hoppings, such as off-site SOC and mean-field potentials. In Ref. [175], since $[H(\mathbf{R})]_{ss'}^{aa'}$ is treated as the model parameter, the optimized model without any symmetry restrictions does not satisfy the symmetry of a system. Meanwhile, following the Slater-Koster approach, although $[H(\mathbf{R})]_{ss'}^{aa'}$ can be viewed as approximate symmetry-adapted model parameters given by Eq. (2.2.12), essential parameters could be lost owing to the assumption of the axial symmetry along the bond direction.

On the other hand, as shown in Chap. 3, we introduced a complete orthonormal SAMB given by

$$Z_j = \sum_{\alpha\beta} C_{\alpha\beta}^j X_\alpha^{(a)} \otimes Y_\beta^{(s/b)} \quad (4.2.2)$$

where $X_\alpha^{(a)}$ and $Y_\beta^{(s/b)}$ are the atomic multipole basis and the site/bond-cluster multipole basis, respectively. Since the Hamiltonian H is fully symmetric for all the symmetry operations, only the SAMB characterized by the fully symmetric irreducible representation contributes to H . As a result, the TB Hamiltonian can be expressed as the linear combination of the fully symmetric Z_j as

$$H = \sum_j z_j Z_j \quad (4.2.3)$$

where z_j is the weight of each SAMB and is the model parameter. Since each Z_j is fully symmetric, the symmetry of a given system is precisely taken into account during the optimization process, and the resultant optimized TB model is also fully symmetric. Furthermore, the number of model parameters is equal to that of the SAMBs, in contrast to the Slater-Koster approach, in which some independent parameters depend on each other due to additional axial symmetry along the bond direction.

In the momentum space representation, the TB Hamiltonian is expressed by

$$\mathcal{H} = \sum_{\mathbf{R}} \sum_{ss'} \sum_{aa'} [H(\mathbf{k})]_{ss'}^{aa'} c_{as\mathbf{k}}^\dagger c_{a's'\mathbf{k}} \quad (4.2.4)$$

$$[H(\mathbf{k})]_{ss'}^{aa'} = \sum_{\mathbf{R}} [H(\mathbf{R})]_{ss'}^{aa'} e^{-i\mathbf{k}\cdot((\mathbf{R}+\mathbf{s})-\mathbf{s}')} \quad (4.2.5)$$

Using the final matrix form of the complete orthonormal SAMB given by Eq. (3.5.25),

$$Z_j(\mathbf{k}) = \sum_{\alpha\beta} C_{\alpha\beta}^j X_\alpha^{(a)} \otimes M_\beta^{(t)}(\mathbf{k}) \quad (4.2.6)$$

$H(\mathbf{k})$ can be expressed as

$$H(\mathbf{k}) = \sum_j z_j Z_j(\mathbf{k}) \quad (4.2.7)$$

In the next section, we show how to optimize z_j so as to reproduce the DFT band dispersion.

4.3 DFT-Based Symmetry-Adapted TB Model

This section presents a systematic generation scheme of the DFT-based symmetry-adapted TB model using the DNN-SAMB. In Sec. 4.3.1, we give an outline of the generation scheme. After that, we will show the detailed description of workflow of the DNN-SAMB in Sec. 4.3.2.

4.3.1 Outline

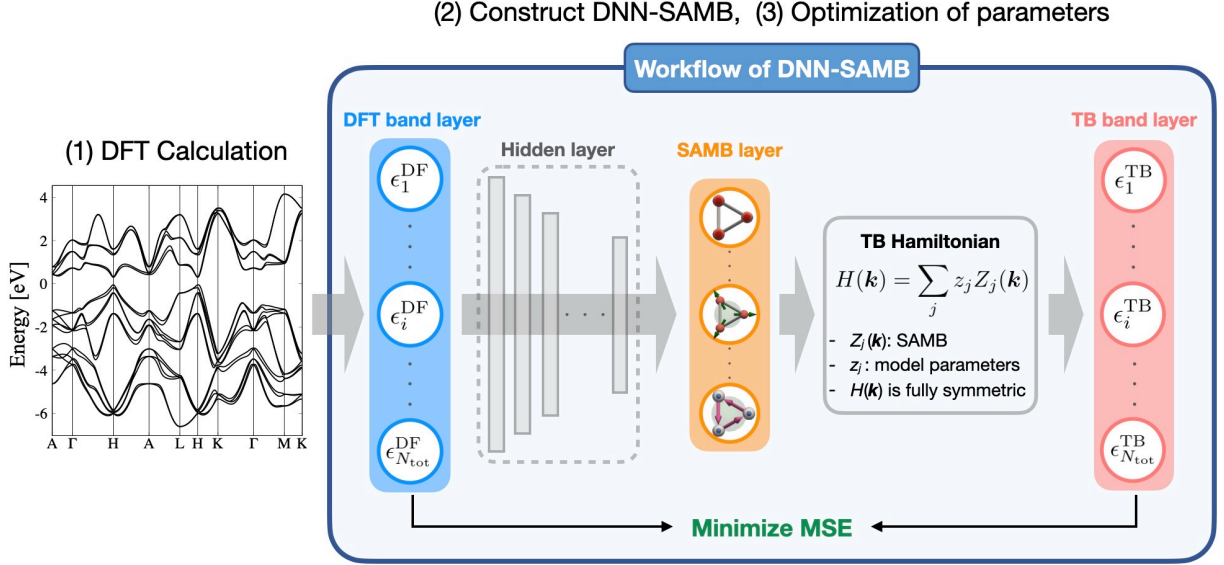


Figure 4.1: Generation scheme of the DFT-based symmetry-adapted TB model based on the DNN-SAMB.

In this section, we briefly show an outline of the generation scheme summarized in Fig. 4.1. The method consists of the following three steps:

(1) DFT Calculation

Prepare the DFT band dispersion data $\epsilon^{\text{DF}} = (\epsilon_1^{\text{DF}}, \epsilon_2^{\text{DF}}, \dots, \epsilon_{N_{\text{tot}}}^{\text{DF}})$, where $N_{\text{tot}} = N_k \times N_n$ is the total number of the eigenvalues, and N_k (N_n) is the number of \mathbf{k} points (bands). When the bands are entangled, one need to extract the bands of interest by implementing the disentanglement calculation by using the Wannier90 software package [72–74] (See Chap. 2), for instance.

(2) Construct DNN-SAMB

Generate SAMB $\mathbf{Z}(\mathbf{k}) = [Z_1(\mathbf{k}), Z_2(\mathbf{k}), \dots, Z_{N_z}(\mathbf{k})]$ from a minimum model information, such as the space group, site/bond-clusters, electron spin and orbital degrees of freedom to be considered. The TB Hamiltonian is constructed by the linear combination of $Z_j(\mathbf{k})$, $H(\mathbf{k}) = \sum_{j=1}^{N_z} z_j Z_j(\mathbf{k})$, where $\mathbf{z} = (z_1, z_2, \dots, z_{N_z})$ is the set of model parameters. Then, construct the fully-connected DNN-SAMB composed of the DFT band layer, hidden layer, SAMB layer, and TB band layers sequentially. The DFT band layer consists of the energy eigenvalues obtained from the DFT calculations, ϵ^{DF} , and this layer is connected to the hidden layer composed of the hidden neurons. Then, the last hidden layer is connected to the SAMB layer that consists of the weight of each SAMB, \mathbf{z} . In the TB band layer, we calculate the TB band dispersion $\epsilon^{\text{TB}}(\mathbf{z}) = (\epsilon_1^{\text{TB}}, \epsilon_2^{\text{TB}}, \dots, \epsilon_{N_{\text{tot}}}^{\text{TB}})$.

(3) Parameter Optimization

Based on the back-propagation algorithm [153, 178], \mathbf{z} and the additional parameters in the hidden layers are iteratively updated until the desired accuracy of the optimization is achieved.

4.3.2 Workflow of the DNN-SAMB

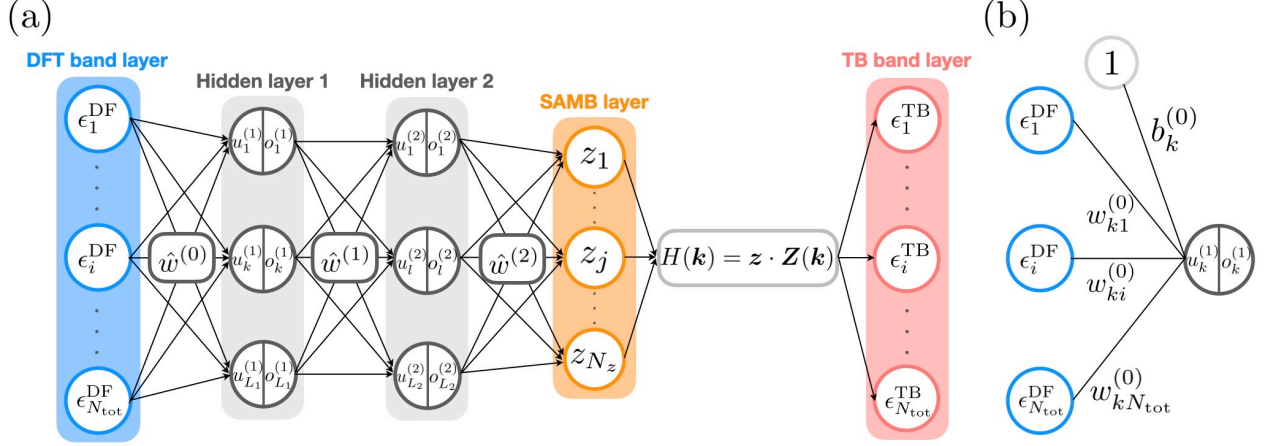


Figure 4.2: (a) Workflow of the DNN-SAMB that includes two hidden layers between the DFT band and SAMB layers. The circles represent the neurons, and the solid black arrows denote the weights that correspond to the strength of connections between neurons. $u_k^{(1)}(o_k^{(1)})$ and $u_l^{(2)}(o_l^{(2)})$ denote the input (output) of the 1st and 2nd hidden layers, respectively. L_1 and L_2 are the number of neurons in the 1st and 2nd hidden layers, respectively. (b) Schematic figure of a neural network between the DFT band and a single neuron in the 1st hidden layers. An input of the 1st hidden layer, $u_k^{(1)}$, is given by the sum of the product of weights $w_{ki}^{(0)}$ and eigenvalues ϵ_i^{DF} plus the bias $b_k^{(0)}$. Then, the corresponding output, $o_k^{(1)}$, is given by applying the activation function to $u_k^{(1)}$, $o_k^{(1)} = f(u_k^{(1)})$.

In this section, we show a workflow of the DNN-SAMB summarized in steps (2) and (3) in Fig. 4.1. It should be emphasized that the optimized \mathbf{z} implicitly depend on the input ϵ^{DF} . We express these nontrivial and nonlinear dependences by introducing the DNN-SAMB, a fully-connected DNN that connects every ϵ_i^{DF} to the model parameter z_j via the additional hidden layers. When the number of the hidden layers is N_h , the number of neurons in the 1st, 2nd, \dots , N_h th hidden layers are fixed as $L_1 = 2^{N_h} N_z$, $L_2 = 2^{N_h-1} N_z$, \dots , $L_{N_h} = 2^1 N_z$, respectively. Figure 4.2(a) represents an example of the workflow of DNN-SAMB with two hidden layers, $N_h = 2$. Every neuron depicted by the circles is connected by the solid black arrows that denote the weights \hat{w} corresponding to the strength of connections between neurons. As shown in Fig. 4.2(b), an output of the 1st hidden layer $o_k^{(1)}$ is given by

$$o_k^{(1)} = f(u_k^{(1)}), \quad u_k^{(1)} = \sum_i w_{ki}^{(0)} \epsilon_i^{\text{DF}} + b_k^{(0)} \quad (4.3.1)$$

where $w_{ki}^{(0)}$ represents the real weight between the i th eigenvalue ϵ_i^{DF} and the k th input $u_k^{(1)}$, in the first hidden layer, while $b_k^{(0)}$ denotes the real bias. Note that f represents the activation function, and we adopt the hyperbolic tangent $f(x) = \tanh(x)$. Similarly, the output of the 2nd hidden layer is given by

$$o_l^{(2)} = f(u_l^{(2)}), \quad u_l^{(2)} = \sum_k w_{lk}^{(1)} o_k^{(1)} + b_l^{(1)} \quad (4.3.2)$$

The j th weight of the SAMB z_j is obtained by

$$z_j = \sum_l w_{jl}^{(2)} o_l^{(2)} + b_j^{(2)} \quad (4.3.3)$$

When there are N_h hidden layers, the input and output of each hidden layer and \mathbf{z} are represented by the matrix form as

$$\begin{aligned}
\mathbf{o}^{(1)} &= f\left(\mathbf{u}^{(1)}\right), & \mathbf{u}^{(1)} &= \hat{w}^{(0)}\boldsymbol{\epsilon}^{\text{DF}} + \mathbf{b}^{(0)} \\
\mathbf{o}^{(2)} &= f\left(\mathbf{u}^{(2)}\right), & \mathbf{u}^{(2)} &= \hat{w}^{(1)}\mathbf{o}^{(1)} + \mathbf{b}^{(1)} \\
&\dots & & \\
\mathbf{o}^{(N_h)} &= f\left(\mathbf{u}^{(N_h)}\right), & \mathbf{u}^{(N_h)} &= \hat{w}^{(N_h-1)}\mathbf{o}^{(N_h-1)} + \mathbf{b}^{(N_h-1)} \\
\mathbf{z} &= \hat{w}^{(N_h)}\mathbf{o}^{(N_h)} + \mathbf{b}^{(N_h)}
\end{aligned} \tag{4.3.4}$$

As a result, we can express \mathbf{z} as the nonlinear function of $\boldsymbol{\epsilon}^{\text{DF}}$. Using \mathbf{z} , we can construct the TB Hamiltonian as

$$H(\mathbf{k}) = \mathbf{z} \cdot \mathbf{Z}(\mathbf{k}) \tag{4.3.5}$$

where $\mathbf{z} = (z_1, z_2, \dots, z_{N_z})$ and $\mathbf{Z}(\mathbf{k}) = (Z_1(\mathbf{k}), Z_2(\mathbf{k}), \dots, Z_{N_z}(\mathbf{k}))$. The TB band dispersion $\boldsymbol{\epsilon}^{\text{TB}}$ can be obtained by diagonalizing $H(\mathbf{k})$.

As shown above, expressing the model parameters \mathbf{z} as the nonlinear function of $\boldsymbol{\epsilon}^{\text{DF}}$, the optimization parameters are regarded as the weights and biases between neurons in addition to \mathbf{z} :

$$\begin{aligned}
&\hat{w}^{(0)}(L_1 \times N_{\text{tot}}), & \mathbf{b}^{(0)}(L_1) \\
&\hat{w}^{(1)}(L_2 \times L_1), & \mathbf{b}^{(1)}(L_2) \\
&\dots & \\
&\hat{w}^{(N_h-1)}(L_{N_h} \times L_{N_h-1}), & \mathbf{b}^{(N_h-1)}(L_{N_h}) \\
&\hat{w}^{(N_h)}(N_z \times L_{N_h}), & \mathbf{b}^{(N_h)}(N_z) \\
&\mathbf{z}(N_z)
\end{aligned} \tag{4.3.6}$$

In order to quantify the accuracy of the optimization, we introduce a loss function $L(\mathbf{z})$, which is defined by the dimensionless mean squared error (MSE) between the normalized energy eigenvalues of the DFT calculation and our TB model:

$$L(\mathbf{z}) = \frac{1}{2N_k N_n} \sum_{n\mathbf{k}} \left(\frac{\epsilon_{n\mathbf{k}}^{\text{TB}}(\mathbf{z}) - \epsilon_{n\mathbf{k}}^{\text{DF}}}{W} \right)^2 = \frac{1}{2N_{\text{tot}}} \left(\frac{\boldsymbol{\epsilon}^{\text{TB}}(\mathbf{z}) - \boldsymbol{\epsilon}^{\text{DF}}}{W} \right)^2 \tag{4.3.7}$$

By minimizing $L(\mathbf{z})$, we can optimize the model parameters \mathbf{z} .

The procedure to obtain the output, $L(\mathbf{z})$, from the input $\boldsymbol{\epsilon}^{\text{DF}}$ is the forward process. On the other hand, to update the optimization parameters so as to minimize the loss function $L(\mathbf{z})$, we need to calculate the gradient of $L(\mathbf{z})$ for all the optimization parameters using the back-propagation algorithm [153, 178]. Following the back-propagation algorithm, we compute the gradient of $L(\mathbf{z})$ for each optimization parameter through a chain rule. Contrary to the above forward process, the back-propagation computes the gradients from the output layer to the input layer sequentially. First, the gradient of the loss function with respect to the model parameters \mathbf{z} is given by

$$\nabla_{\mathbf{z}} L(\mathbf{z}) = \frac{1}{N_k N_n} \sum_{n\mathbf{k}} \left(\frac{\epsilon_{n\mathbf{k}}^{\text{TB}}(\mathbf{z}) - \epsilon_{n\mathbf{k}}^{\text{DF}}}{W} \right) \nabla_{\mathbf{z}} \epsilon_{n\mathbf{k}}^{\text{TB}}(\mathbf{z}) \simeq \frac{1}{N_k N_n} \sum_{n\mathbf{k}} \left(\frac{\epsilon_{n\mathbf{k}}^{\text{TB}}(\mathbf{z}) - \epsilon_{n\mathbf{k}}^{\text{DF}}}{W} \right) \langle \psi_{n\mathbf{k}} | \mathbf{Z}(\mathbf{k}) | \psi_{n\mathbf{k}} \rangle \tag{4.3.8}$$

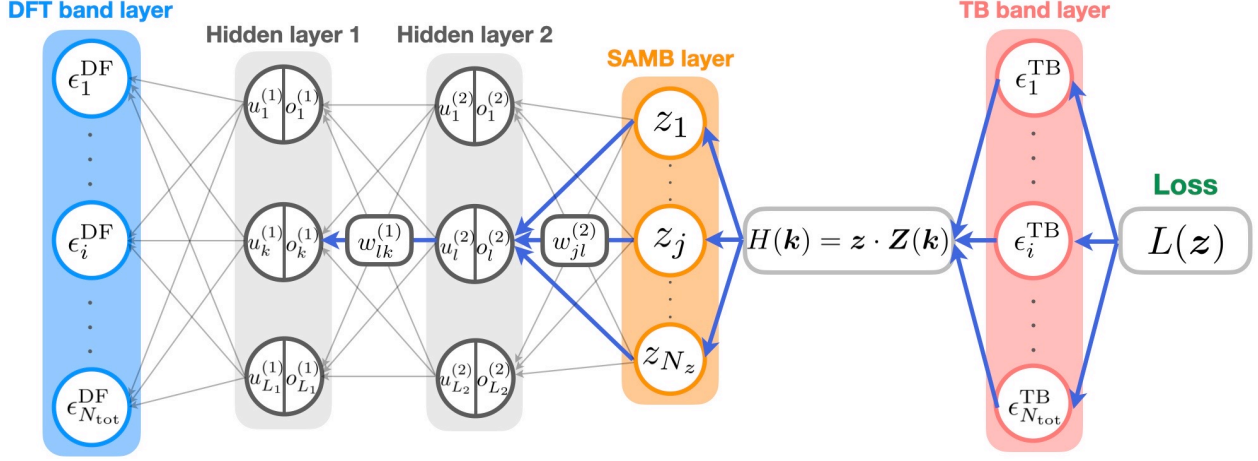


Figure 4.3: Back-propagation process of the derivative of $L(\mathbf{z})$ with respect to $w_{lk}^{(1)}$.

where the second equation is derived from the first-order perturbation theory [168, 175, 179]:

$$\epsilon_{n\mathbf{k}}^{\text{TB}}(\mathbf{z} + \delta\mathbf{z}) = \epsilon_{n\mathbf{k}}^{\text{TB}}(\mathbf{z}) + \nabla_{\mathbf{z}} \epsilon_{n\mathbf{k}}^{\text{TB}}(\mathbf{z}) \cdot \delta\mathbf{z} + O(\delta\mathbf{z}^2) \simeq \epsilon_{n\mathbf{k}}^{\text{TB}}(\mathbf{z}) + \langle \psi_{n\mathbf{k}} | \mathbf{Z}(\mathbf{k}) | \psi_{n\mathbf{k}} \rangle \cdot \delta\mathbf{z} + O(\delta\mathbf{z}^2) \quad (4.3.9)$$

Then, to update all weights and biases, we back-propagate $\nabla_{\mathbf{z}} L(\mathbf{z})$ from the SAMB layer toward the 1st hidden layer sequentially. For example, let us consider that there are only two hidden layers as shown in Fig. 4.2. For simplicity, we here neglect the bias without loss of generality. Following the chain rule, the derivative of $L(\mathbf{z})$ with respect to $w_{jl}^{(2)}$ is given by

$$\frac{\partial L}{\partial w_{jl}^{(2)}} = \frac{\partial L}{\partial z_j} \frac{\partial z_j}{\partial w_{jl}^{(2)}} = \left(\frac{\partial L}{\partial z_j} \right) o_l^{(2)} = \delta_j^{(2)} o_l^{(2)} \quad (4.3.10)$$

$$\delta_j^{(2)} = \frac{\partial L}{\partial z_j} \quad (4.3.11)$$

Then, the derivative of $L(\mathbf{z})$ with respect to $w_{lk}^{(1)}$ is given by

$$\frac{\partial L}{\partial w_{lk}^{(1)}} = \sum_j \frac{\partial L}{\partial z_j} \frac{\partial z_j}{\partial o_l^{(2)}} \frac{\partial o_l^{(2)}}{\partial u_l^{(2)}} \frac{\partial u_l^{(2)}}{\partial w_{lk}^{(1)}} = \left(\sum_j \frac{\partial L}{\partial z_j} w_{jl}^{(2)} f'(u_l^{(2)}) \right) o_k^{(1)} = \delta_l^{(1)} o_k^{(1)} \quad (4.3.12)$$

$$\delta_l^{(1)} = \sum_j \frac{\partial L}{\partial z_j} w_{jl}^{(2)} f'(u_l^{(2)}) = \sum_j \delta_j^{(2)} w_{jl}^{(2)} f'(u_l^{(2)}) \quad (4.3.13)$$

where $f'(x) = \tanh'(x) = \cosh^{-2}(x)$. Lastly, the derivative of $L(\mathbf{z})$ with respect to $w_{ki}^{(0)}$ is given by

$$\frac{\partial L}{\partial w_{ki}^{(0)}} = \sum_{jl} \frac{\partial L}{\partial z_j} \frac{\partial z_j}{\partial o_l^{(2)}} \frac{\partial o_l^{(2)}}{\partial u_l^{(2)}} \frac{\partial u_l^{(2)}}{\partial o_k^{(1)}} \frac{\partial o_k^{(1)}}{\partial u_k^{(1)}} \frac{\partial u_k^{(1)}}{\partial w_{ki}^{(0)}} = \left(\sum_{jl} \frac{\partial L}{\partial z_j} w_{jl}^{(2)} f'(u_l^{(2)}) w_{lk}^{(1)} f'(u_k^{(1)}) \right) \epsilon_i^{\text{DF}} = \delta_k^{(0)} \epsilon_i^{\text{DF}} \quad (4.3.14)$$

$$\delta_k^{(0)} = \sum_l \left(\sum_j \frac{\partial L}{\partial z_j} w_{jl}^{(2)} f'(u_l^{(2)}) \right) w_{lk}^{(1)} f'(u_k^{(1)}) = \sum_l \delta_l^{(1)} w_{lk}^{(1)} f'(u_k^{(1)}) \quad (4.3.15)$$

As a result, the derivative of $L(\mathbf{z})$ can be calculated by using the values of inputs u , outputs o , weights

w , and $\partial L/\partial z_j$, which can be obtained analytically without using numerical derivatives. Furthermore, these expressions indicate that $\delta_j^{(m)}$ can be calculated iteratively by using $\delta_j^{(m+1)}$, which has already been obtained. These are the most substantial advantages of using the back-propagation algorithm.

Using the derivatives of $L(\mathbf{z})$, each weight is updated based on the gradient descent algorithm as follows:

$$\hat{w}^{(n+1)} = \hat{w}^{(n)} - \alpha \frac{\partial L}{\partial \hat{w}^{(n)}} \quad (4.3.16)$$

where α is a learning rate, and $\hat{w}^{(n)}$ denotes the weights at the n th iteration of training. Note that in the practical calculation, we have used the Adam optimizer [180] to update all the optimization parameters.

As shown above, the back-propagation process is continuously optimizing all the optimization parameters until the numerical threshold for the loss function or the maximum number of training steps is reached. The hyperparameters, such as the numerical threshold, the maximum number of training steps, the number of hidden layers, and the learning rate, should be given in advance. The optimized model parameters \mathbf{z} are obtained by substituting the optimized weights and biases to Eq. (4.3.4). Using the optimized \mathbf{z} , we can construct the optimized symmetry-adapted TB Hamiltonian and obtain TB band dispersion that reproduces the DFT band dispersion. Note that if the above minimization is failed, one needs to modify the hyperparameters mentioned above or the choices of the orbitals and site/bond-clusters to be reconsidered. In addition, since the weights located upstream of the DNN-SAMB are not significantly changed, a moderate number of hidden layers should be adjusted. This is caused by the chain rule shown in Eq. (4.3.14), where the derivative of the activation function is always less than 1, $f'(x) = \cosh^{-2}(x) \leq 1$.

4.4 Usage Examples

In this section, we show some examples of using the above generation scheme based on DNN-SAMB for some typical materials: graphene in Sec. 4.4.1, SrVO₃ in Sec. 4.4.2, and MoS₂ in Sec. 4.4.3. We construct the DFT-based symmetry-adapted TB Hamiltonians of these materials based on the generation scheme. We will show the validity and advantages of our method in the following sections.

For the DFT calculations, we have used QUANTUM ESPRESSO open-source software package [66]. We have optimized the model parameters by using the TensorFlow framework [181], Keras library [182], and Adam optimizer [180].

4.4.1 Graphene

First, we demonstrate our method by taking a simple example, two-dimensional graphene. Following the three steps summarized in Sec. 4.3.1, we construct the DFT-based symmetry-adapted TB model for graphene.

DFT Calculation for Graphene

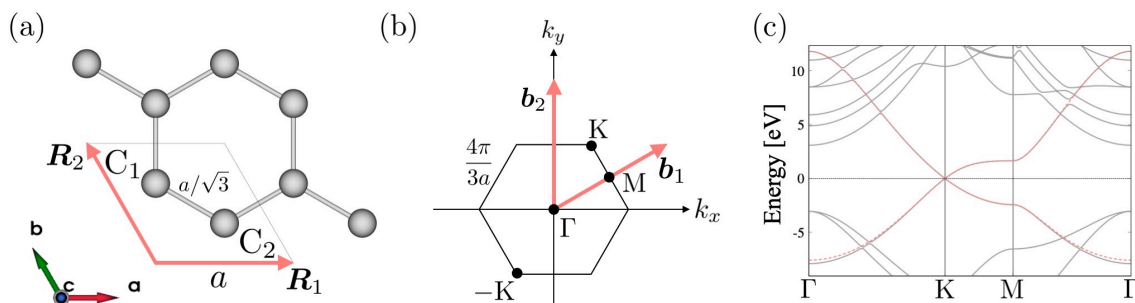


Figure 4.4: (a) Crystal structure and (b) Brillouin zone of the two-dimensional graphene. (c) Band dispersion obtained from the DFT calculation (solid grey lines) and the Wannier TB model (dashed red lines). The Fermi energy is taken as the origin.

Graphene has a honeycomb structure involving $C_1 = (1/3, 2/3, 0)$ and $C_2 = (2/3, 1/3, 0)$ sublattices in a unit cell, as shown in Fig. 4.4(a). The space group of graphene is $P6/mmm$ (#191, D_{6h}^1). We set the lattice constant to be $a = 2.435 \text{ \AA}$ and the length of the vacuum layer along the c axis to be $4 \times a$. We have used the Perdew-Zunger (PZ-LDA) correlation functional [183] (See Appendix A.5 in detail) and the ultrasoft pseudopotential. For the self-consistent field (SCF) calculation to solve the KS equation, we have used $(N_1, N_2, N_3) = (12, 12, 1)$ \mathbf{k} grid, while the kinetic energy cutoff of the Kohn-Sham wave functions is set to be 30 Ry, and the convergence threshold is set to be 1×10^{-10} Ry.

As shown in Fig. 4.4(c), the bands near the Fermi level are entangled. Therefore, we have used the Wannier90 open-source software package [72–74] to extract the two bands near the Fermi level. We choose the p_z orbital for each C atom as the initial guess function. The outer energy window is set to be $[-30 \text{ eV}, 12 \text{ eV}]$, while the inner energy window is set to be $[-3.0 \text{ eV}, 2.6 \text{ eV}]$. Then, we obtain the p_z -like two WFs as shown in Fig. 2.3(a), and the corresponding band dispersion is depicted by the solid red lines in Fig. 4.4(c). We optimize the symmetry-adapted TB model to reproduce these two DFT-based Wannier band dispersions.

Symmetry-Adapted TB Hamiltonian for Graphene

To construct the symmetry-adapted TB Hamiltonian for graphene, we first generate the SAMB. We consider $p_z \propto z$ orbital for each C atom. The Hilbert space consists of the two basis functions, $[|p_z; C_1\rangle, |p_z; C_2\rangle]$. Then, we construct the spinless TB Hamiltonian in a 2×2 matrix by using the SAMB Z_j as shown in Sec. 4.2. First, we prepare the atomic and site/bond-cluster multipole basis independently. Afterward, we construct the SAMB by combining them.

Atomic multipole basis

Within the spinless p_z orbital, there is only one active atomic E monopole,

$$Q_0^{(a)} = (1) \quad (4.4.1)$$

The irreducible representation of $Q_0^{(a)}$ is A_{1g} .

Site/bond-cluster multipole basis

To describe the crystal field Hamiltonian and the hopping Hamiltonian, we introduce the site-cluster E multipole basis and bond-cluster E/MT multipole basis defined in the (C_1, C_2) sublattice space. We restrict our demonstration up to the nearest-neighbor bond-cluster. There are two independent site-cluster multipole basis:

$$Q_0^{(s)} = \frac{1}{\sqrt{2}}(1, 1), \quad Q_{3a}^{(s)} = \frac{1}{\sqrt{2}}(1, -1) \quad (4.4.2)$$

While there are six independent bond-cluster multipole basis:

$$\begin{aligned} Q_0^{(b)} &= \frac{1}{\sqrt{6}}(1, 1, 1; 1, 1, 1) \\ Q_v^{(b)} &= \frac{1}{2\sqrt{3}}(1, 1, -2; 1, 1, -2) \\ Q_{xy}^{(b)} &= \frac{1}{2}(-1, 1, 0; -1, 1, 0) \\ T_x^{(b)} &= \frac{1}{2}(i, i, 0; -i, -i, 0) \\ T_y^{(b)} &= \frac{1}{2\sqrt{3}}(i, -i, 2i; -i, i, -2i) \\ T_{3a}^{(b)} &= \frac{1}{\sqrt{6}}(i, -i, -i; -i, i, i) \end{aligned} \quad (4.4.3)$$

The elements correspond to the following three bond vectors of the form $\mathbf{b}@\mathbf{c}$:

$$\begin{aligned} \mathbf{b}_1@\mathbf{c}_1 &= [2/3, 1/3, 0]@[0, 1/2, 0] \\ \mathbf{b}_2@\mathbf{c}_2 &= [1/3, -1/3, 0]@[1/2, 1/2, 0] \\ \mathbf{b}_3@\mathbf{c}_3 &= [1/3, 2/3, 0]@[1/2, 0, 0] \end{aligned} \quad (4.4.4)$$

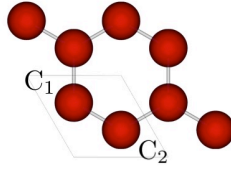
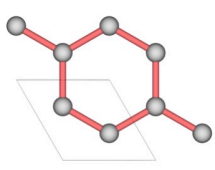
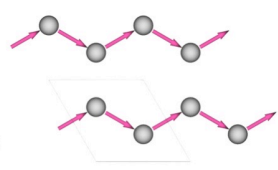
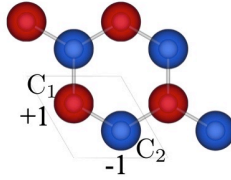
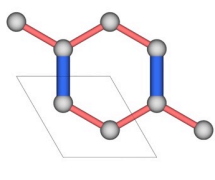
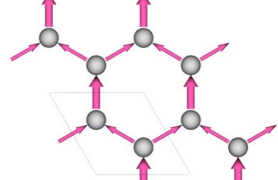
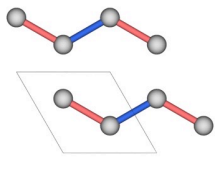
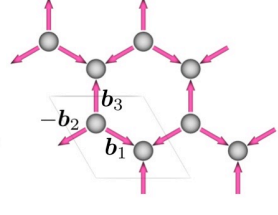
site-cluster	bond-cluster (Re)	bond-cluster (Im)
$Q_0^{(s)}$ A_{1g} 	$Q_0^{(b)}$ A_{1g} 	$T_x^{(b)}$ E_{1u} 
$Q_{3a}^{(s)}$ B_{1u} 	$Q_v^{(b)}$ E_{2g} 	$T_y^{(b)}$ E_{1u} 
	$Q_{xy}^{(b)}$ E_{2g} 	$T_{3a}^{(b)}$ B_{1u} 

Figure 4.5: Site/bond-cluster multipoles for graphene and their irreducible representations. The red and blue circles in the “site-cluster” column represent the weight and sign of the elements. The red and blue lines in the “bond-cluster (Re)” column represent the weight and sign of the real part of the elements. Similarly, the arrows in the “bond-cluster (Im)” column represent the weight and sign of the imaginary part of the elements.

The schematic figures of the site/bond-cluster multipole basis are shown in Fig. 4.5.

The final matrix forms of the site/bond-cluster multipoles are given by

$$Q_0^{(t,1)} = \frac{1}{\sqrt{2}} \begin{pmatrix} 1 & 0 \\ 0 & 1 \end{pmatrix}, \quad Q_{3a}^{(t)} = \frac{1}{\sqrt{2}} \begin{pmatrix} 1 & 0 \\ 0 & -1 \end{pmatrix}, \quad Q_0^{(t,2)} = \frac{1}{\sqrt{2}} \begin{pmatrix} 0 & 1 \\ 1 & 0 \end{pmatrix}, \quad T_{3a}^{(t)} = \frac{1}{\sqrt{2}} \begin{pmatrix} 0 & -i \\ i & 0 \end{pmatrix} \quad (4.4.5)$$

where $Q_0^{(t,1)}$ and $Q_0^{(t,2)}$ are the diagonal and off-diagonal basis, respectively.

Momentum multipole basis

To describe the real and imaginary parts of the hopping Hamiltonian, we introduce the momentum E and MT multipole basis by using Eqs. (3.5.18) and (3.5.19) as

$$Q_0(\mathbf{k}) = \frac{\sqrt{6}}{3} \left[2 \cos\left(\frac{k_x a}{2}\right) \cos\left(\frac{\sqrt{3}k_y a}{6}\right) + \cos\left(\frac{\sqrt{3}k_y a}{3}\right) \right] \quad (4.4.6)$$

$$Q_v(\mathbf{k}) = \frac{2\sqrt{3}}{3} \left[\cos\left(\frac{k_x a}{2}\right) \cos\left(\frac{\sqrt{3}k_y a}{6}\right) - \cos\left(\frac{\sqrt{3}k_y a}{3}\right) \right] \quad (4.4.7)$$

$$Q_{xy}(\mathbf{k}) = 2 \sin\left(\frac{k_x a}{2}\right) \sin\left(\frac{\sqrt{3}k_y a}{6}\right) \quad (4.4.8)$$

$$T_x(\mathbf{k}) = 2 \sin\left(\frac{k_x a}{2}\right) \cos\left(\frac{\sqrt{3}k_y a}{6}\right) \quad (4.4.9)$$

$$T_y(\mathbf{k}) = \frac{2\sqrt{3}}{3} \left[\sin\left(\frac{\sqrt{3}k_y a}{6}\right) \cos\left(\frac{k_x a}{2}\right) + \sin\left(\frac{\sqrt{3}k_y a}{3}\right) \right] \quad (4.4.10)$$

$$T_{3a}(\mathbf{k}) = \frac{\sqrt{6}}{3} \left[2 \sin\left(\frac{\sqrt{3}k_y a}{6}\right) \cos\left(\frac{k_x a}{2}\right) - \sin\left(\frac{\sqrt{3}k_y a}{3}\right) \right] \quad (4.4.11)$$

SAMB and symmetry-adapted TB Hamiltonian for graphene

Using Eqs. (4.4.1), (4.4.2), and (4.4.3), the SAMB is expressed by the direct product of the atomic multipole basis and the site/bond-cluster multipole basis. The only SAMB belonging to A_{1g} identity irreducible representation of D_{6h} contribute to the Hamiltonian. Therefore, considering the irreducible decompositions,

$$\begin{aligned} A_{1g/u} \otimes A_{1g/u} &= B_{1g/u} \otimes B_{1g/u} = A_{2g/u} \otimes A_{2g/u} = B_{2g/u} \otimes B_{2g/u} = A_{1g} \\ E_{1g/u} \otimes E_{1g/u} &= E_{2g/u} \otimes E_{2g/u} = A_{1g} \oplus A_{2g} \oplus E_{2g} \end{aligned} \quad (4.4.12)$$

we obtain the fully symmetric SAMB as follows:

$$Q_0^{(as)} = Q_0^{(a)} \otimes Q_0^{(s)} \quad (4.4.13)$$

$$Q_0^{(ab)} = Q_0^{(a)} \otimes Q_0^{(b)} \quad (4.4.14)$$

The final matrix form of them are explicitly given by

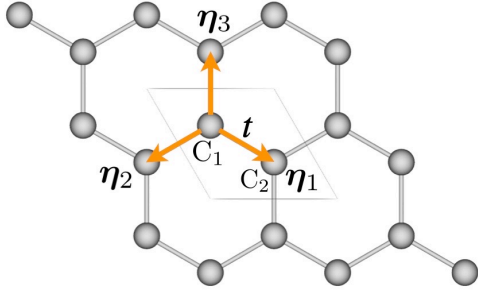
$$Q_0^{(as)} = Q_0^{(a)} \otimes Q_0^{(t,1)} = \frac{1}{\sqrt{2}} \begin{pmatrix} 1 & 0 \\ 0 & 1 \end{pmatrix} \quad (4.4.15)$$

$$Q_0^{(ab)}(\mathbf{k}) = \frac{1}{\sqrt{2}} Q_0^{(a)} \otimes \left(Q_0^{(t,2)} Q_0(\mathbf{k}) + T_{3a}^{(t)} T_{3a}(\mathbf{k}) \right) = \frac{1}{2} \left[\begin{pmatrix} 0 & 1 \\ 1 & 0 \end{pmatrix} Q_0(\mathbf{k}) + \begin{pmatrix} 0 & -i \\ i & 0 \end{pmatrix} T_{3a}(\mathbf{k}) \right] \quad (4.4.16)$$

Using these SAMB, the symmetry-adapted TB hamiltonian can be expressed as

$$H(\mathbf{k}) = z_1 Q_0^{(as)} + z_2 Q_0^{(ab)}(\mathbf{k}) \quad (4.4.17)$$

where z_1 and z_2 are the weights for each SAMB. Note that $Q_0^{(as)}$ corresponds to the onsite potential

$$H(\mathbf{k}) = t \begin{pmatrix} 0 & \sum_{i=1}^3 e^{i\mathbf{k}\cdot\boldsymbol{\eta}_i} \\ \sum_{i=1}^3 e^{-i\mathbf{k}\cdot\boldsymbol{\eta}_i} & 0 \end{pmatrix}$$


... Graphene contains **E monopole** & **MT octupole**

$$H(\mathbf{k}) = t \left(\begin{array}{c} \text{bond} \\ \times \\ \text{momentum} \end{array} \begin{array}{c} \text{E monopole} \\ \begin{array}{c} \text{Diagram: Three bonds with weights 1} \\ \text{Diagram: Brillouin zone with red regions at K and -K} \end{array} \\ \times \\ \begin{array}{c} A_{1g} \\ A_{1g} \end{array} \end{array} \right) Q_0^{(t,2)} \propto \begin{pmatrix} 0 & 1 \\ 1 & 0 \end{pmatrix} Q_0(\mathbf{k})$$

$$+ t \left(\begin{array}{c} \text{bond} \\ \times \\ \text{momentum} \end{array} \begin{array}{c} \text{MT octupole} \\ \begin{array}{c} \text{Diagram: Three bonds with weights 1, i, -i} \\ \text{Diagram: Brillouin zone with red and blue regions} \end{array} \\ \times \\ \begin{array}{c} B_{1u} \\ B_{1u} \end{array} \end{array} \right) T_{3a}^{(t)} \propto \begin{pmatrix} 0 & -i \\ i & 0 \end{pmatrix} T_{3a}(\mathbf{k})$$

$$Q_0(\mathbf{k}) = \frac{\sqrt{6}}{3} \left[2 \cos\left(\frac{k_x}{2}\right) \cos\left(\frac{\sqrt{3}k_y}{6}\right) + \cos\left(\frac{\sqrt{3}k_y}{3}\right) \right]$$

$$T_{3a}(\mathbf{k}) = \frac{\sqrt{6}}{3} \left[2 \sin\left(\frac{\sqrt{3}k_y}{6}\right) \cos\left(\frac{k_x}{2}\right) - \sin\left(\frac{\sqrt{3}k_y}{3}\right) \right]$$

Figure 4.6: Schematic figure of the multipole decomposition of the nearest neighbor hopping Hamiltonian of graphene. The Hamiltonian has hidden E monopole and MT octupole degrees of freedom.

causing the energy shift, while $Q_0^{(\text{ab})}(\mathbf{k})$ corresponds to the nearest-neighbor hopping. By decomposing the TB Hamiltonian by means of the multipole basis, we found the E monopole and MT octupole degrees of freedom, as shown in Fig. 4.6.

Let us focus on the electronic states near the Fermi level around the $\pm\mathbf{K}$ point,

$$\pm\mathbf{k}_K = \pm(1/3, 1/3, 0) \quad (4.4.18)$$

The expansions of $Q_0(\mathbf{k})$ and $T_{3a}(\mathbf{k})$ around the $\pm\mathbf{K}$ point are given by

$$Q_0(\pm\mathbf{k}_K + \mathbf{k}) \propto \mp \frac{\sqrt{2}}{4} (k_x + \sqrt{3}k_y) a + \mathcal{O}(k^2) \quad (4.4.19)$$

$$T_{3a}(\pm\mathbf{k}_K + \mathbf{k}) \propto -\frac{\sqrt{2}}{4} (\sqrt{3}k_x + k_y) a + \mathcal{O}(k^2) \quad (4.4.20)$$

Neglecting the energy shift term, $z_1 \rightarrow 0$, the hopping Hamiltonian around the $\pm\mathbf{K}$ point is given by

$$H(\pm\mathbf{k}_K + \mathbf{k}) \simeq z_2 a \frac{\sqrt{2}}{4} \begin{pmatrix} 0 & c(k_x \pm ik_y) \\ c^*(k_x \mp ik_y) & 0 \end{pmatrix}, \quad c = \frac{1}{2}(\mp 1 + i\sqrt{3}) \quad (4.4.21)$$

where c is the phase factor which can be excluded. Then, the band dispersion around the $\pm\mathbf{K}$ point is given by

$$\epsilon_{\pm, \mathbf{k}_K + \mathbf{k}} = \pm \frac{\sqrt{2}}{4} a |z_2| |\mathbf{k}| \quad (4.4.22)$$

Thus, the gradient of the linear band dispersion at the $\pm K$ point is characterized by the weight z_2 of $Q_0^{(\text{ab})}(\mathbf{k})$. Notably, its explicit value can be evaluated by using our method as shown in the following section.

In the next section, we consider up to 6th neighbor hoppings. The total Hamiltonian in the momentum space representation is given by

$$H(\mathbf{k}) = z_1 Q_0^{(\text{as})} + \sum_{n=1}^6 z_{i+1} Q_0^{(\text{ab},n)}(\mathbf{k}) \quad (4.4.23)$$

where $Q_0^{(\text{ab},n)}(\mathbf{k})$ corresponds to the n th neighbor hopping and their explicit expressions are given in Appendix D.1. There are 7 independent weights in total.

Parameter Optimization

Table 4.1: Parameters and hyperparameters used for the optimization process.

high symmetry lines	$\Gamma-K-M-\Gamma$
number of \mathbf{k} points	$N_k = 151$
number of bands	$N_n = 2$
total number of the eigenvalues	$N_{\text{tot}} = N_k \times N_n = 302$
maximum number of neighbor bonds	$N_{\text{max}}^{(b)} = 1-6$
number of hidden layers	$N_h = 0-6$
maximum number of iterations	$N_{\text{iter}} = 250$
learning rate	$\alpha = 0.1$

Table 4.2: $N_{\text{max}}^{(b)}$ dependence of the number of neurons and the optimization parameters in the DNN-SAMB with $N_h = 3$.

Layer	$N_{\text{max}}^{(b)} = 1$		2		3		4		5		6	
	neurons #	params #										
DFT band	302		302		302		302		302		302	
1st hidden	16	4848	24	7272	32	9696	40	12120	48	14736	56	16968
2nd hidden	8	136	12	300	16	528	20	820	24	1176	28	1596
3rd hidden	4	36	6	78	8	136	10	210	12	300	14	406
SAMB	2	10	3	21	4	36	5	55	6	78	7	105
TB band	302		302		302		302		302		302	
total #	634	5030	649	7671	664	10396	679	13205	694	16290	709	19075

In this section, we show the results of model parameter optimization of the TB model for graphene to demonstrate the validity of our generation scheme using the DNN-SAMB,

The parameters and hyperparameters used for the optimization process are summarized in Table 4.1. We choose the high symmetry lines $\Gamma-K-M-\Gamma$. We use bands at 50 \mathbf{k} points in each line, then the number of \mathbf{k} points is $N_k = 151$ and the number of the bands is $N_n = 2$. Thus, the total number of the eigenvalues is $N_{\text{tot}} = N_k \times N_n = 302$. For comparison, we change the maximum number of neighbor bonds from nearest to 6th neighbor bonds, $N_{\text{max}}^{(b)} = 1-6$, and we also change the number of hidden layers from 0 to 6, $N_h = 0-6$. When $N_h = 0$, the DFT band layer is directly connected to the SAMB layer. The maximum number of iterations is fixed as $N_{\text{iter}} = 250$ that is sufficient to reach convergence. The learning rate is fixed as $\alpha = 0.1$.

Table 4.2 shows the $N_{\text{max}}^{(b)}$ dependence of the number of neurons and the optimization parameters in the DNN-SAMB with $N_h = 3$. We also perform the parameter optimization using the conventional linear regression (LR) method without using the DNN-SAMB. Note that the total number of the optimization parameters for the LR method corresponds to the number of the SAMB. Although the total number of optimization parameters increases drastically by using the DNN-SAMB, the DNN-SAMB method is superior to the conventional LR method in terms of efficiency and less dependence on initial guess as shown below.

To investigate the dependence of the initial estimates of the parameters in the results of optimization, we have performed 50 optimization calculations with different random initial parameters for each pair of $(N_{\text{max}}^{(b)}, N_h)$.

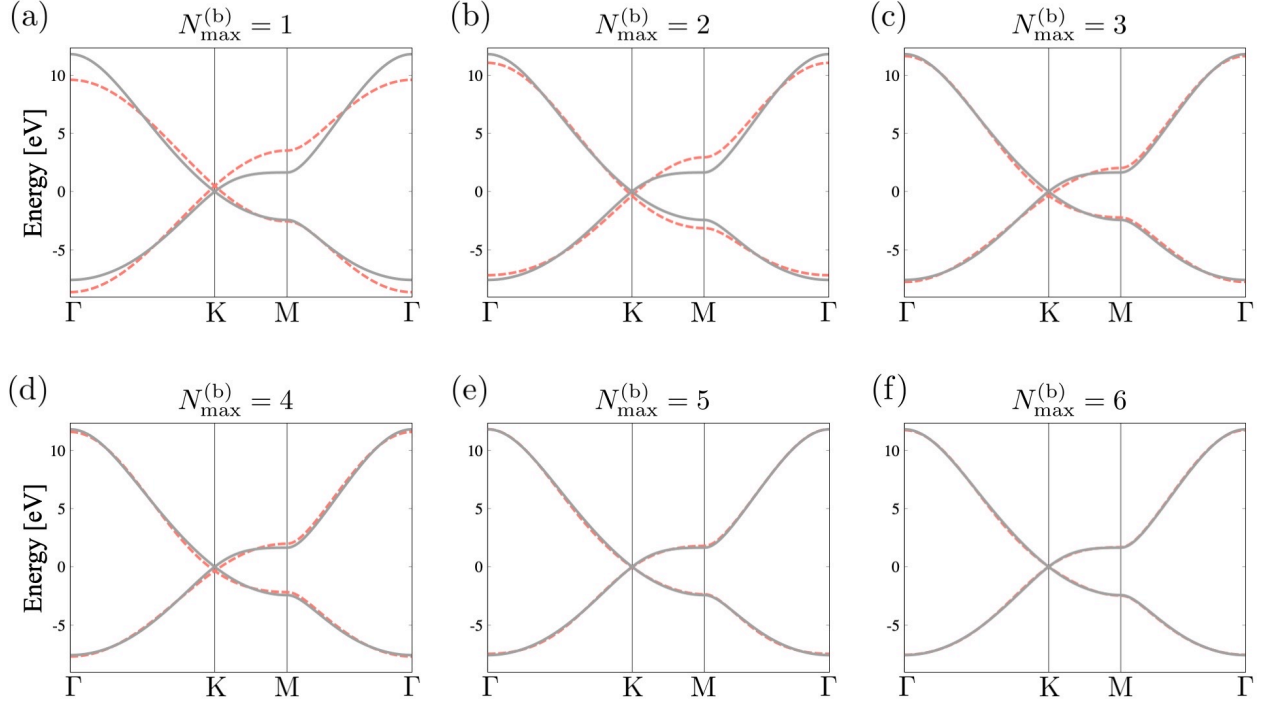


Figure 4.7: The comparisons of the band dispersion between the Wannier TB model (solid grey lines) and our TB models (dashed red lines) obtained using the DNN-SAMB with $N_h = 3$. (a)-(f) $N_{\max}^{(b)} = 1-6$. The Fermi energy is taken as the origin.

Table 4.3: The minimum, maximum, and average loss function, L_{\min} , L_{\max} , and L_{avg} in 50 optimization calculations with different initial guess using the LR method and DNN-SAMB with $N_h = 3$.

$N_{\max}^{(b)}$	L_{\min}		L_{\max}		L_{avg}	
	LR	DNN-SAMB	LR	DNN-SAMB	LR	DNN-SAMB
1	2.1×10^{-2}	2.1×10^{-2}	2.3×10^{-2}	2.1×10^{-2}	2.1×10^{-2}	2.1×10^{-2}
2	6.4×10^{-4}	6.4×10^{-4}	1.1×10^{-3}	6.4×10^{-4}	6.6×10^{-4}	6.4×10^{-4}
3	9.5×10^{-5}	9.5×10^{-5}	1.2×10^{-2}	2.1×10^{-3}	1.5×10^{-3}	3.5×10^{-4}
4	9.2×10^{-5}	9.2×10^{-5}	3.5×10^{-2}	1.1×10^{-2}	6.7×10^{-3}	4.7×10^{-4}
5	1.7×10^{-5}	1.7×10^{-5}	3.8×10^{-2}	3.3×10^{-4}	9.7×10^{-3}	1.3×10^{-4}
6	7.7×10^{-6}	7.7×10^{-6}	9.3×10^{-2}	3.2×10^{-4}	1.5×10^{-2}	1.4×10^{-4}

Figure 4.7 shows the results of optimization using the DNN-SAMB with $N_h = 3$. The quality of the optimization gradually improves as $N_{\max}^{(b)}$ increases. In particular, when $N_{\max}^{(b)} \geq 5$, the optimized TB model reproduces the DFT band dispersions with high accuracy. The results of optimization based on the LR method is shown in Appendix D.2.

Table 4.3 summarizes the $N_{\max}^{(b)}$ dependence of the minimum, maximum, and average loss function, L_{\min} , L_{\max} , and L_{avg} , in 50 optimization calculations with different initial guess using the LR method and DNN-SAMB with $N_h = 3$. Remarkably, by taking up to 6th neighbor hoppings, we have achieved an accuracy less than 10^{-5} of the MSE between the normalized energy eigenvalues of our TB model and the Wannier TB model. Moreover, as shown in Table 4.3, the LR method and our method using DNN-SAMB are almost identical for L_{\min} , whereas L_{\max} and L_{avg} of our method are always smaller than that of the LR method. These results indicate that our method based on the DNN-SAMB is more efficient than the LR method and shows less dependence on the initial guess of the optimization parameters.

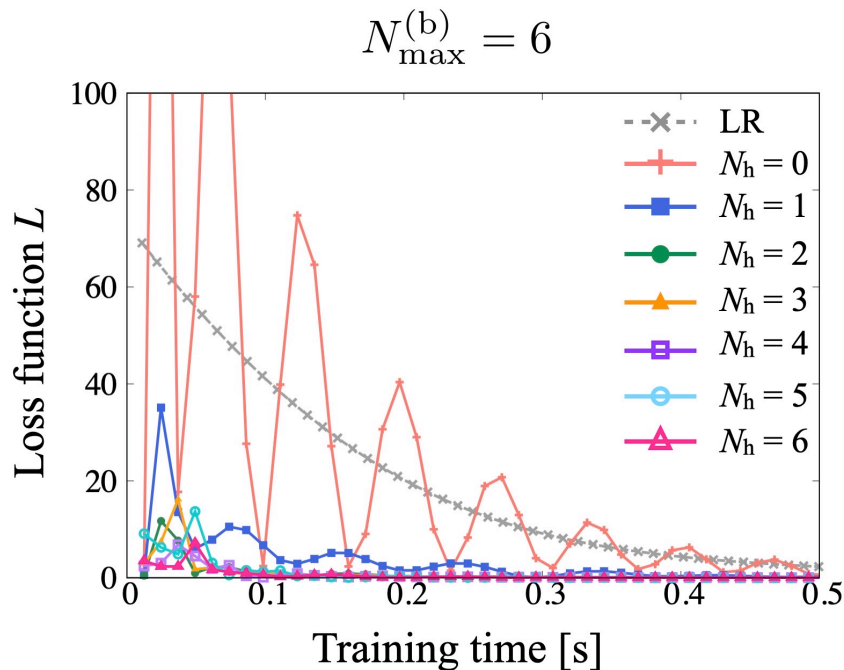


Figure 4.8: Convergence behavior of the loss function for the LR method (grey) and the DNN-SAMB with $N_h = 0$ (red), 1 (blue), 2 (green), 3 (orange), 4 (purple), 5 (turquoise), and 6 (pink), and $N_{\max}^{(b)} = 6$.

Table 4.4: The optimized model parameters z_j in eV units obtained by using DNN-SAMB with $N_h = 3$.

$N_{\max}^{(b)}$	1	2	3	4	5	6
z_1	0.029	-0.076	-0.076	-0.076	-0.190	-0.160
z_2	7.448	7.448	7.244	-7.273	7.273	-7.273
z_3		0.882	0.882	0.882	0.851	0.874
z_4			0.680	-0.698	0.698	-0.698
z_5				0.065	-0.065	0.065
z_6					0.212	0.202
z_7						-0.073

Next, we show the convergence behavior of the loss function for the LR method and our method using the DNN-SAMB with $N_{\max}^{(b)} = 6$ in Fig. 4.8. The results show that using DNN-SAMB leads to the rapid convergence of the loss function. The loss function converges more rapidly as N_h increases. On the other hand, the LR method shows relatively slow convergence behavior. Thus, our method with DNN-SAMB can reach convergence faster than the usual LR method.

We summarize the explicit values of the optimized model parameters in Table 4.4. As shown in Eqs. (4.4.17) and (4.4.23), z_1 and z_j ($2 \leq j \leq 7$) correspond to the energy shift term and the j th neighbor hopping, respectively. Remarkably, the value of the hopping terms does not change significantly as $N_{\max}^{(b)}$ increases, indicating our method works correctly. Furthermore, we find that the absolute value of z_2 , which characterizes the linear band dispersion around the $\pm K$ point as shown in Eq. (4.4.22), converges to $|z_2| = 7.273$. Note that the signs of z_2 , z_4 , and z_5 are not determined uniquely because they correspond to the hoppings between C_1 and C_2 atoms. The two different optimized models with opposite signs of these weights are interconverted by redefining the phase of $|C_2\rangle$ as $|C_2\rangle \rightarrow e^{i\pi} |C_2\rangle$.

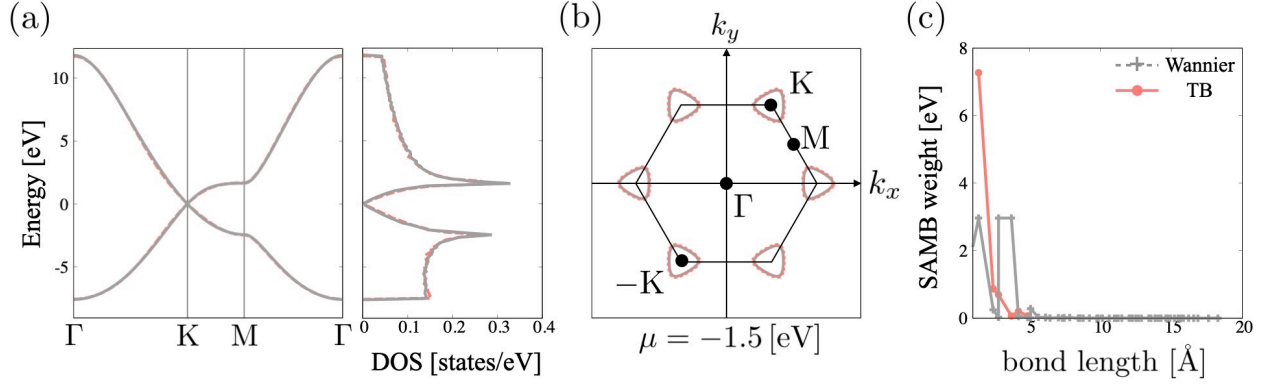


Figure 4.9: Optimized TB model obtained using the DNN-SAMB with $N_h = 3$ and $N_{\max}^{(b)} = 6$. The comparisons of the (a) band dispersion and density of states (DOS), (b) isoenergy surface ($\mu = -1.5$ [eV]), and the bond length dependence of the absolute maximum value of the hopping parameters ($2 \leq j \leq 7$) in eV units between the Wannier TB model (solid grey lines) and our TB model (dashed red lines). The Fermi energy is taken as the origin.

Figure 4.9 summarizes the optimized TB model obtained using the DNN-SAMB with $N_h = 3$ and $N_{\max}^{(b)} = 6$. As shown in Fig. 4.9(a) and (b), our TB model reproduces the band dispersion, the density of states (DOS), and the isoenergy surface obtained by the Wannier TB model. Moreover, as shown in Fig. 4.9(c), the magnitude of the hopping parameters of our TB model rapidly decreases for further neighbor hoppings, and the size of the model becomes compact. On the other hand, the Wannier TB model includes many long-range hopping parameters with negligible values.

As discussed above, by using the DNN-SAMB, we can efficiently construct the symmetry-adapted TB model for graphene that reproduces the calculation results obtained by the DFT-based Wannier model, such as the band dispersion, DOS, and Fermi surface, with high accuracy. As compared with the conventional LR method, our method based on the DNN-SAMB is superior concerning both the efficiency and less dependence on the initial guess of the optimization parameters. Moreover, our TB model contains the minimum number of model parameters, making it more compact than the Wannier TB model.

4.4.2 SrVO₃

Next, we show the results of using our method for bulk crystalline SrVO₃ that is a typical material and is often chosen as the benchmark for developing the methodology associated with DFT calculation.

DFT Calculation for SrVO₃

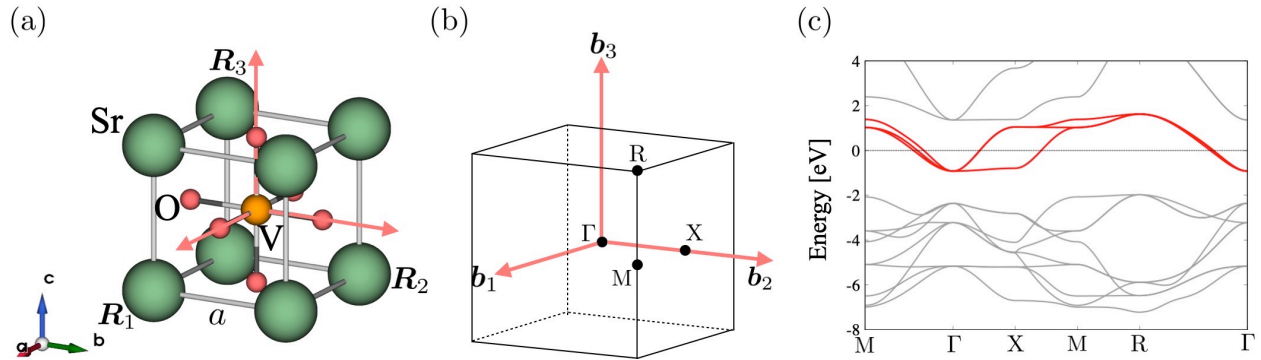


Figure 4.10: (a) Crystal structure and (b) Brillouin zone of bulk crystalline SrVO₃. (c) Band dispersion obtained from the DFT calculation, where the red solid lines represent the t_{2g} orbitals of V atom. The Fermi energy is taken as the origin.

The bulk crystalline SrVO₃ has the cubic structure including Sr, V, and O sublattices in a unit cell as shown in Fig. 4.10(a). The space group of SrVO₃ is $Pm\bar{3}m$ (#221, O_h^1). We set the lattice constant to be $a = 3.8409$ Å. For the DFT calculation, we use the PBEsol exchange-correlation functional [184] (See Appendix A.5 in detail) and the PAW pseudopotential. For the SCF calculation, we use $(N_1, N_2, N_3) = (6, 6, 6)$ \mathbf{k} grid, and the kinetic energy cutoff of the Kohn-Sham wave functions is set to be 100 Ry, and the convergence threshold for the SCF calculation is set to be 1×10^{-10} Ry.

As shown in Fig. 4.10(c), the bands near the Fermi level are isolated. As a result, we can directly fit our TB model to these bands obtained from the DFT calculation without using the Wannier90 [72–74]. The isolated three electronic states near the Fermi level are mainly composed of the t_{2g} orbitals of V atom as depicted by the solid red lines in Fig. 4.10(c). Therefore, we choose the (d_{yz}, d_{zx}, d_{xy}) orbitals of the V atom as basis functions for the TB model. Note that we only consider the V atom and neglect the contributions of the Sr and O atoms.

Symmetry-Adapted TB Hamiltonian for SrVO₃

To construct the symmetry-adapted TB model for SrVO₃, we first construct the SAMB. We use (d_{yz}, d_{zx}, d_{xy}) orbitals for each V atom. The Hilbert space consists of the three basis functions, $[|d_{yz}; V\rangle, |d_{zx}; V\rangle, |d_{xy}; V\rangle]$. Similar to the TB model for graphene, we first prepare the atomic and site/bond-cluster multipole basis independently, and then we construct the SAMB by combining them.

Atomic multipole basis

Within the spinless (d_{yz}, d_{zx}, d_{xy}) orbitals, there are 9 independent atomic multipole basis whose explicit operator expressions and matrix forms are summarized in Table 4.5.

Table 4.5: Operator expressions and matrix forms of the atomic multipole basis defined in the spinless d_{yz}, d_{zx}, d_{xy} orbitals in the point group O_h . E, M, ET, and MT stand for electric, magnetic, electric toroidal, and magnetic toroidal, respectively. The superscript (a) denotes the atomic multipole. \mathbf{l} and $\boldsymbol{\sigma}/2$ represent the dimensionless orbital and spin angular-momentum operators, and σ_i ($i = x, y, z$) and σ_0 are the Pauli matrices and 2×2 identity matrix.

rank	type	irrep.	symbol	expression	matrix element
0	E	A_{1g}^+	$Q_0^{(a)}$	1	$\frac{1}{\sqrt{3}} \begin{pmatrix} 1 & 0 & 0 \\ 0 & 1 & 0 \\ 0 & 0 & 1 \end{pmatrix}$
1	M	T_{1g}^-	$M_x^{(a)}, M_y^{(a)}, M_z^{(a)}$	l_x, l_y, l_z	$\frac{1}{\sqrt{2}} \begin{pmatrix} 0 & 0 & 0 \\ 0 & 0 & i \\ 0 & -i & 0 \end{pmatrix}, \frac{1}{\sqrt{2}} \begin{pmatrix} 0 & 0 & -i \\ 0 & 0 & 0 \\ i & 0 & 0 \end{pmatrix}, \frac{1}{\sqrt{2}} \begin{pmatrix} 0 & i & 0 \\ -i & 0 & 0 \\ 0 & 0 & 0 \end{pmatrix}$
2	E	E_g^+	$Q_u^{(a)}, Q_v^{(a)}$	$3z^2 - r^2, x^2 - y^2$	$\frac{1}{\sqrt{6}} \begin{pmatrix} -1 & 0 & 0 \\ 0 & -1 & 0 \\ 0 & 0 & 2 \end{pmatrix}, \frac{1}{\sqrt{2}} \begin{pmatrix} 1 & 0 & 0 \\ 0 & -1 & 0 \\ 0 & 0 & 0 \end{pmatrix}$
		T_{2g}^+	$Q_{yz}^{(a)}, Q_{zx}^{(a)}, Q_{xy}^{(a)}$	yz, zx, xy	$\frac{1}{\sqrt{2}} \begin{pmatrix} 0 & 0 & 0 \\ 0 & 0 & 1 \\ 0 & 1 & 0 \end{pmatrix}, \frac{1}{\sqrt{2}} \begin{pmatrix} 0 & 0 & 1 \\ 0 & 0 & 0 \\ 1 & 0 & 0 \end{pmatrix}, \frac{1}{\sqrt{2}} \begin{pmatrix} 0 & 1 & 0 \\ 1 & 0 & 0 \\ 0 & 0 & 0 \end{pmatrix}$

Site/bond-cluster multipole basis

To describe the crystal field Hamiltonian and the hopping Hamiltonian, we introduce the site-cluster E multipole basis and bond-cluster E/MT multipole basis. We restrict our demonstration up to the nearest-neighbor bond-cluster. Since the size of the cluster is 1, there is only one site-cluster E monopole basis:

$$Q_0^{(s)} = (1) \quad (4.4.24)$$

The final matrix form of $Q_0^{(s)}$ is also given by

$$Q_0^{(t)} = (1) \quad (4.4.25)$$

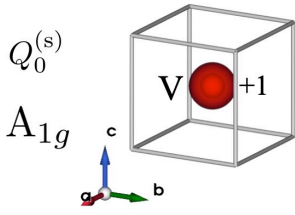
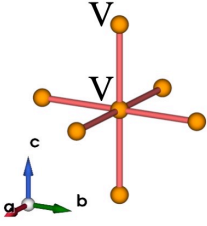
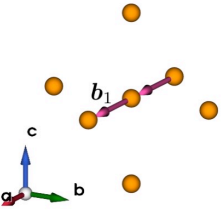
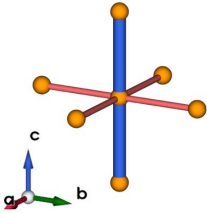
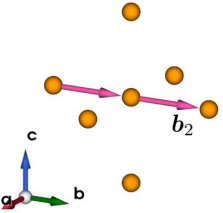
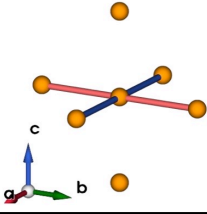
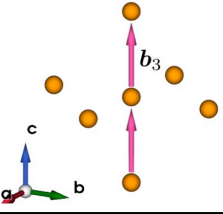
site-cluster	bond-cluster (Re)	bond-cluster (Im)
$Q_0^{(s)}$ A_{1g} 	$Q_0^{(b)}$ A_{1g} 	$T_x^{(b)}$ T_{1u} 
	$Q_u^{(b)}$ E_g 	$T_y^{(b)}$ T_{1u} 
	$Q_v^{(b)}$ E_g 	$T_z^{(b)}$ T_{1u} 

Figure 4.11: Schematic figures of the site/bond-cluster multipoles for SrVO_3 and their irreducible representations. The red and blue circles in the “site-cluster” column represent the weight and sign of the elements. The red and blue lines in the “bond-cluster (Re)” column represent the weight and sign of the real part of the elements. Similarly, the arrows in the “bond-cluster (Im)” column represent the weight and sign of the imaginary part of the elements.

There are six independent bond-cluster multipole basis:

$$\begin{aligned}
 Q_0^{(b)} &= \frac{1}{\sqrt{6}}(1, 1, 1; 1, 1, 1) \\
 Q_u^{(b)} &= \frac{1}{2\sqrt{3}}(-2, 1, 1; 1, 1, 1) \\
 Q_v^{(b)} &= \frac{1}{2}(0, -1, 1; 0, -1, 1) \\
 T_x^{(b)} &= \frac{1}{\sqrt{2}}(0, i, 0; 0, -i, 0) \\
 T_y^{(b)} &= \frac{1}{\sqrt{2}}(0, 0, i; 0, 0, -i) \\
 T_z^{(b)} &= \frac{1}{\sqrt{2}}(i, 0, 0; -i, 0, 0)
 \end{aligned} \tag{4.4.26}$$

The elements correspond to the bond vectors described by $\mathbf{b}@c$:

$$\begin{aligned}
 \mathbf{b}_1@c_1 &= [0, 0, 1]@[0, 0, 1/2] \\
 \mathbf{b}_2@c_2 &= [1, 0, 0]@[1/2, 0, 0] \\
 \mathbf{b}_3@c_3 &= [0, 1, 0]@[0, 1/2, 0]
 \end{aligned} \tag{4.4.27}$$

We schematically depict the site/bond-cluster multipole basis as shown in Fig. 4.11.

Momentum multipole basis

To describe the real and imaginary parts of the hopping Hamiltonian, we introduce the momentum E/MT multipole basis by using Eqs. (3.5.18) and (3.5.19) as

$$Q_0(\mathbf{k}) = \frac{\sqrt{6}}{3} [\cos k_x a + \cos k_y a + \cos k_z a] \quad (4.4.28)$$

$$Q_u(\mathbf{k}) = \frac{\sqrt{3}}{3} [\cos k_x a + \cos k_y a - 2 \cos k_z a] \quad (4.4.29)$$

$$Q_v(\mathbf{k}) = -\cos k_x a + \cos k_y a \quad (4.4.30)$$

$$T_x(\mathbf{k}) = \sqrt{2} \sin(k_x a) \quad (4.4.31)$$

$$T_y(\mathbf{k}) = \sqrt{2} \sin(k_y a) \quad (4.4.32)$$

$$T_z(\mathbf{k}) = \sqrt{2} \sin(k_z a) \quad (4.4.33)$$

SAMB and symmetry-adapted TB Hamiltonian for SrVO₃

Using the atomic multipole basis given by Table 4.5 and the site/bond-cluster multipole basis given by Eqs. (4.4.24) and (4.4.26), the SAMB is defined by the direct product of them. Note that the only SAMB belonging to A_{1g} identity irreducible representation of O_h contribute to the Hamiltonian. Considering the irreducible decompositions,

$$\begin{aligned} A_{1g/u} \otimes A_{1g/u} &= A_{2g/u} \otimes A_{2g/u} = A_{1g} \\ E_{g/u} \otimes E_{g/u} &= A_{1g} \oplus A_{2g} \oplus E_g \\ T_{1g/u} \otimes T_{1g/u} &= T_{2g/u} \otimes T_{2g/u} = A_{1g} \oplus E_g \oplus T_{1g} \oplus T_{2g} \end{aligned} \quad (4.4.34)$$

we obtain the fully symmetric SAMB as follows:

$$Q_0^{(\text{as})} = Q_0^{(\text{a})} \otimes Q_0^{(\text{s})} \quad (4.4.35)$$

$$Q_{0,1}^{(\text{ab})} = Q_0^{(\text{a})} \otimes Q_0^{(\text{b})} \quad (4.4.36)$$

$$Q_{0,2}^{(\text{ab})} = \frac{1}{\sqrt{2}} \left(Q_u^{(\text{a})} \otimes Q_u^{(\text{b})} + Q_v^{(\text{a})} \otimes Q_v^{(\text{b})} \right) \quad (4.4.37)$$

where the subscripts “1” and “2” denote the multiplicity. The final matrix forms of them are explicitly given by

$$Q_0^{(\text{as})} = Q_0^{(\text{a})} \otimes Q_0^{(\text{t})} = \frac{1}{\sqrt{3}} \begin{pmatrix} 1 & 0 & 0 \\ 0 & 1 & 0 \\ 0 & 0 & 1 \end{pmatrix} \quad (4.4.38)$$

$$Q_{0,1}^{(\text{ab})}(\mathbf{k}) = Q_0^{(\text{a})} \otimes Q_0(\mathbf{k}) = \frac{1}{\sqrt{3}} \begin{pmatrix} 1 & 0 & 0 \\ 0 & 1 & 0 \\ 0 & 0 & 1 \end{pmatrix} Q_0(\mathbf{k}) \quad (4.4.39)$$

$$\begin{aligned} Q_{0,2}^{(\text{ab})}(\mathbf{k}) &= \frac{1}{\sqrt{2}} \left(Q_u^{(\text{a})} \otimes Q_u(\mathbf{k}) + Q_v^{(\text{a})} \otimes Q_v(\mathbf{k}) \right) \\ &= \frac{1}{\sqrt{2}} \left[\frac{1}{\sqrt{6}} \begin{pmatrix} -1 & 0 & 0 \\ 0 & -1 & 0 \\ 0 & 0 & 2 \end{pmatrix} Q_u(\mathbf{k}) + \frac{1}{\sqrt{2}} \begin{pmatrix} 1 & 0 & 0 \\ 0 & -1 & 0 \\ 0 & 0 & 0 \end{pmatrix} Q_v(\mathbf{k}) \right] \end{aligned} \quad (4.4.40)$$

Using these SAMB, the symmetry-adapted TB hamiltonian is given by

$$H(\mathbf{k}) = z_1 Q_0^{(\text{as})} + z_2 Q_{0,1}^{(\text{ab})}(\mathbf{k}) + z_3 Q_{0,2}^{(\text{ab})}(\mathbf{k}) \quad (4.4.41)$$

where z_1 , z_2 , and z_3 are the weights for each SAMB and act as the model parameters. Note that $Q_0^{(\text{as})}$ corresponds to the onsite potential causing the energy shift, while $Q_{0,1}^{(\text{ab})}(\mathbf{k})$ and $Q_{0,2}^{(\text{ab})}(\mathbf{k})$ correspond to the nearest neighbor hoppings. Expressing the TB Hamiltonian by means of the multipole basis, we find the E quadrupoles degrees of freedom as shown in Eq. (4.4.40).

In the next section, we consider up to 6th neighbor hoppings. The total Hamiltonian in the momentum space representation is given by

$$\begin{aligned} H(\mathbf{k}) = & z_1 Q_0^{(\text{as})} + z_2 Q_{0,1}^{(\text{ab},1)}(\mathbf{k}) + z_3 Q_{0,2}^{(\text{ab},1)}(\mathbf{k}) \\ & + z_4 Q_{0,1}^{(\text{ab},2)}(\mathbf{k}) + z_5 Q_{0,2}^{(\text{ab},2)}(\mathbf{k}) + z_6 Q_{0,3}^{(\text{ab},2)}(\mathbf{k}) \\ & + z_7 Q_{0,1}^{(\text{ab},3)}(\mathbf{k}) + z_8 Q_{0,2}^{(\text{ab},3)}(\mathbf{k}) \\ & + z_9 Q_{0,1}^{(\text{ab},4)}(\mathbf{k}) + z_{10} Q_{0,2}^{(\text{ab},4)}(\mathbf{k}) \\ & + z_{11} Q_{0,1}^{(\text{ab},5)}(\mathbf{k}) + z_{12} Q_{0,2}^{(\text{ab},5)}(\mathbf{k}) + z_{13} Q_{0,3}^{(\text{ab},5)}(\mathbf{k}) + z_{14} Q_{0,4}^{(\text{ab},5)}(\mathbf{k}) \\ & + z_{15} Q_{0,1}^{(\text{ab},6)}(\mathbf{k}) + z_{16} Q_{0,2}^{(\text{ab},6)}(\mathbf{k}) + z_{17} Q_{0,3}^{(\text{ab},6)}(\mathbf{k}) + z_{18} Q_{0,4}^{(\text{ab},6)}(\mathbf{k}) \end{aligned} \quad (4.4.42)$$

where $Q_{0,m}^{(\text{ab},n)}(\mathbf{k})$ denotes the n th neighbor hopping with the multiplicity m , and their explicit expressions are given in Appendix E.1. There are 18 independent weights in total.

Parameter Optimization

Table 4.6: Parameters and hyperparameters used for the optimization process.

high symmetry lines	M- Γ -X-M-R- Γ
number of \mathbf{k} points	$N_k = 251$
number of bands	$N_n = 3$
total number of the eigenvalues	$N_{\text{tot}} = N_k \times N_n = 753$
maximum number of neighbor bonds	$N_{\text{max}}^{(b)} = 1-6$
number of hidden layers	$N_h = 0-6$
maximum number of iterations	$N_{\text{iter}} = 250$
learning rate	$\alpha = 0.01$

Table 4.7: $N_{\text{max}}^{(b)}$ dependence of the number of neurons and the optimization parameters in the DNN-SAMB with $N_h = 4$.

Layer	$N_{\text{max}}^{(b)} = 1$		2		3		4		5		6	
	neurons #	params #										
DFT band	753		753		753		753		753		753	
1st hidden	48	36192	96	72384	128	96512	160	120640	224	168896	288	217152
2nd hidden	24	1176	48	4656	64	8256	80	12880	112	25200	144	41616
3rd hidden	12	300	24	1176	32	2080	40	3240	56	6328	72	10440
4th hidden	6	78	12	300	16	528	20	820	28	1596	36	2628
SAMB	3	21	6	78	8	136	10	210	14	406	18	666
TB band	753		753		753		753		753		753	
total #	1599	37767	1692	78594	1754	107512	1816	137790	1940	202426	2064	272502

In this section, we show the results of the parameter optimization. The parameters and hyperparameters used for the optimization process are summarized in Table 4.1. We choose the high symmetry lines M- Γ -X-M-R- Γ . We use bands at 50 \mathbf{k} points in each line, then the number of \mathbf{k} points is $N_k = 251$ and the number of bands is $N_n = 3$. The total number of the eigenvalues is $N_{\text{tot}} = N_k \times N_n = 753$. For comparison, we change the maximum number of neighbor bonds from nearest to 6th neighbor bonds, $N_{\text{max}}^{(b)} = 1-6$, and we also change the number of hidden layers from 1 to 6, $N_h = 0-6$. The maximum number of iterations is fixed as $N_{\text{iter}} = 250$ that is sufficient to reach convergence. The learning rate is fixed as $\alpha = 0.01$. Table 4.7 shows the $N_{\text{max}}^{(b)}$ dependence of the number of neurons and the optimization parameters in the DNN-SAMB with $N_h = 4$. When $N_{\text{max}}^{(b)} = 6$, the total number of the optimization parameters is about 270000.

Similar to the previous section 4.4.1, we implement 50 optimization calculations with different random initial parameters for each pair of $(N_{\text{max}}^{(b)}, N_h)$ in order to investigate the dependence of the initial guess of the parameters in the results of optimization. In addition, we also perform the parameter optimization using the conventional LR method with $N_{\text{iter}} = 3000$ and $\alpha = 0.01$.

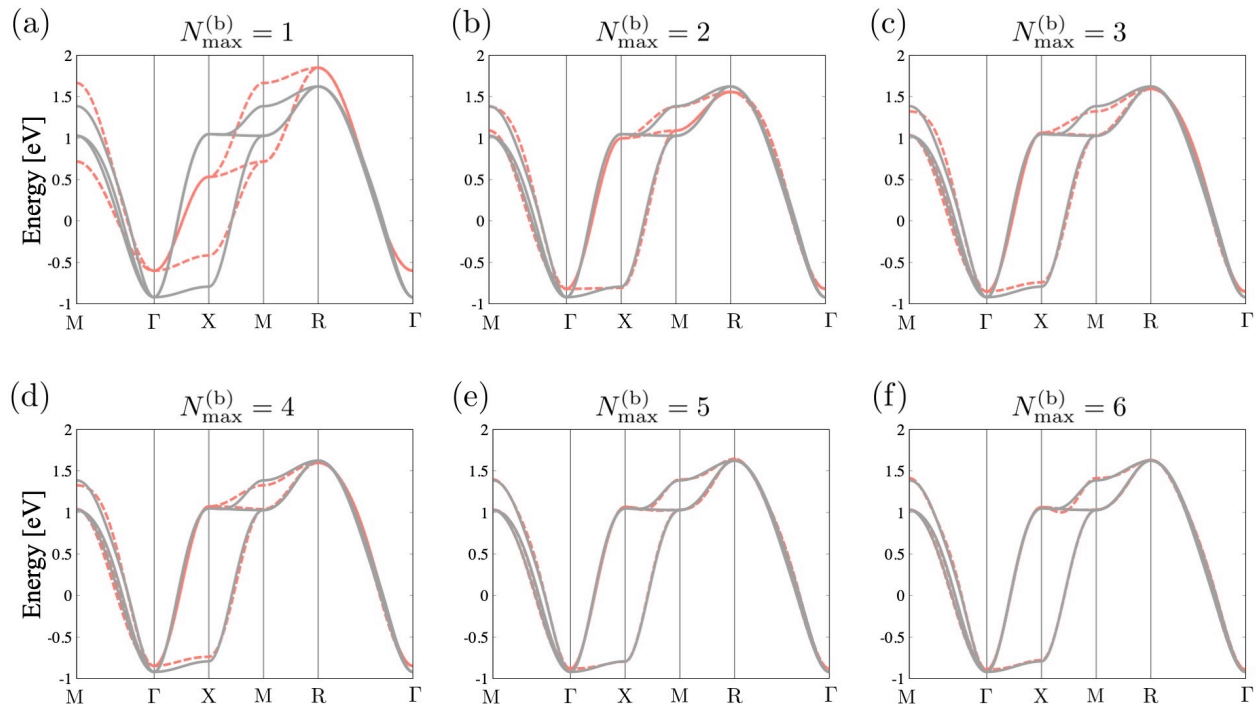


Figure 4.12: The comparisons of the band dispersion between the DFT calculation (solid grey lines) and our TB models (dashed red lines) obtained by using DNN-SAMB with $N_h = 4$. (a)-(f) $N_{\max}^{(b)} = 1-6$. The Fermi energy is taken as the origin.

Table 4.8: The minimum, maximum, and average loss function, L_{\min} , L_{\max} , and L_{avg} , in 50 optimization calculations with different initial guess using the LR method and the DNN-SAMB method with $N_h = 4$.

$N_{\max}^{(b)}$	L_{\min}		L_{\max}		L_{avg}	
	LR	DNN-SAMB	LR	DNN-SAMB	LR	DNN-SAMB
1	8.6×10^{-3}	8.6×10^{-3}	1.5×10^{-2}	1.5×10^{-2}	1.1×10^{-3}	1.0×10^{-3}
2	5.1×10^{-4}	5.1×10^{-4}	1.1×10^{-2}	1.1×10^{-2}	6.0×10^{-3}	2.4×10^{-3}
3	3.5×10^{-4}	3.5×10^{-4}	1.3×10^{-2}	1.1×10^{-2}	5.6×10^{-3}	2.6×10^{-3}
4	3.5×10^{-4}	3.5×10^{-4}	9.8×10^{-2}	9.7×10^{-3}	1.3×10^{-2}	1.9×10^{-3}
5	5.2×10^{-4}	7.2×10^{-5}	2.1×10^{-1}	8.5×10^{-3}	3.6×10^{-2}	4.6×10^{-4}
6	5.0×10^{-4}	5.3×10^{-5}	7.9×10^{-1}	9.1×10^{-3}	6.2×10^{-2}	8.9×10^{-4}

Figure 4.12 shows the results of parameter optimization using the DNN-SAMB with $N_h = 4$. As $N_{\max}^{(b)}$ increases, the quality of the optimization are increased gradually. In particular, when $N_{\max}^{(b)} \geq 5$, the obtained TB model reproduces the DFT band dispersions with high accuracy. The results of optimization based on the LR method is shown in Appendix E.2.

Table 4.8 summarizes the $N_{\max}^{(b)}$ dependence of the minimum, maximum, and average loss function, L_{\min} , L_{\max} , and L_{avg} , in 50 optimization calculations with different initial guess using the LR method and DNN-SAMB with $N_h = 4$. By taking more than 5th neighbors, we achieve an accuracy less than 10^{-4} of the MSE between the normalized energy eigenvalues of our TB model and the DFT calculation. Moreover, L_{\min} , L_{\max} and L_{avg} of the DNN-SAMB method are always smaller than that of the LR method, indicating that the DNN-SAMB method is more efficient than the LR method and shows less dependence on the initial guess of the optimization parameters.

Next, we show the convergence behavior of the loss function for the DNN-SAMB method with

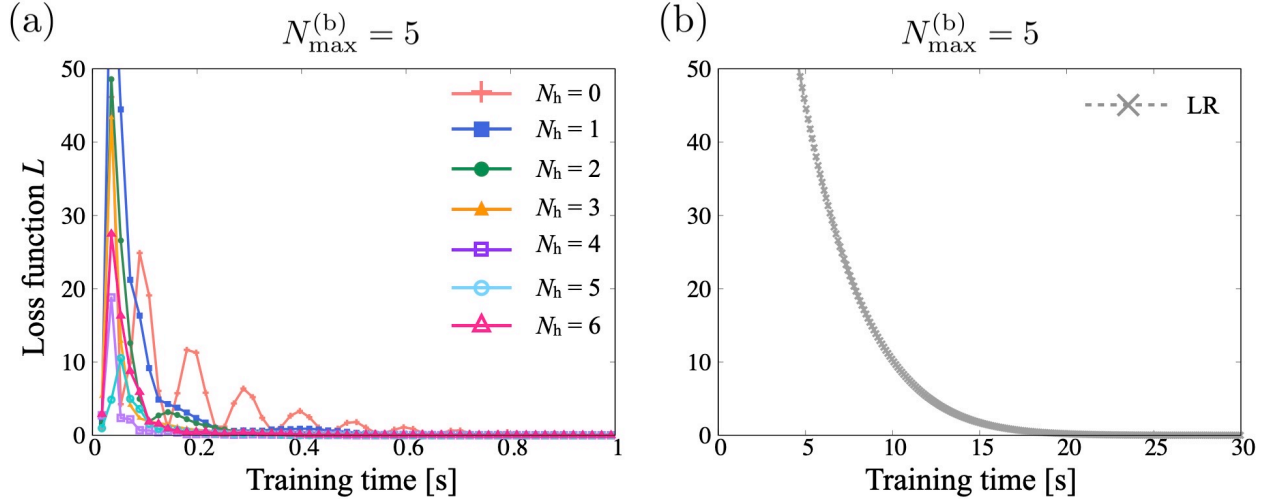


Figure 4.13: Convergence behavior of the loss function for (a) the DNN-SAMB with $N_h = 0$ (red), 1 (blue), 2 (green), 3 (orange), 4 (purple), 5 (turquoise), and 6 (pink) and (b) the LR method (grey) with $N_{\max}^{(b)} = 5$.

Table 4.9: The optimized model parameters z_j in eV units obtained using DNN-SAMB with $N_h = 4$.

$N_{\max}^{(b)}$	1	2	3	4	5	6
z_1	22.546	22.652	22.660	22.654	22.637	22.632
z_2	-0.867	-0.841	-0.826	-0.826	-0.791	-0.791
z_3	0.475	0.524	0.524	0.525	0.461	0.461
z_4		-0.158	-0.160	-0.160	-0.157	-0.147
z_5		0.268	0.268	0.269	0.265	0.274
z_6		-0.053	-0.042	-0.042	-0.043	0.141
z_7			-0.034	-0.034	-0.031	-0.030
z_8			-0.032	-0.031	-0.031	-0.287
z_9				0.006	0.0127	0.0156
z_{10}				-0.009	0.010	0.003
z_{11}					-0.033	-0.033
z_{12}					0.068	0.067
z_{13}					0.008	0.009
z_{14}					-0.001	0.130
z_{15}						-0.012
z_{16}						-0.011
z_{17}						-0.131
z_{18}						-0.089

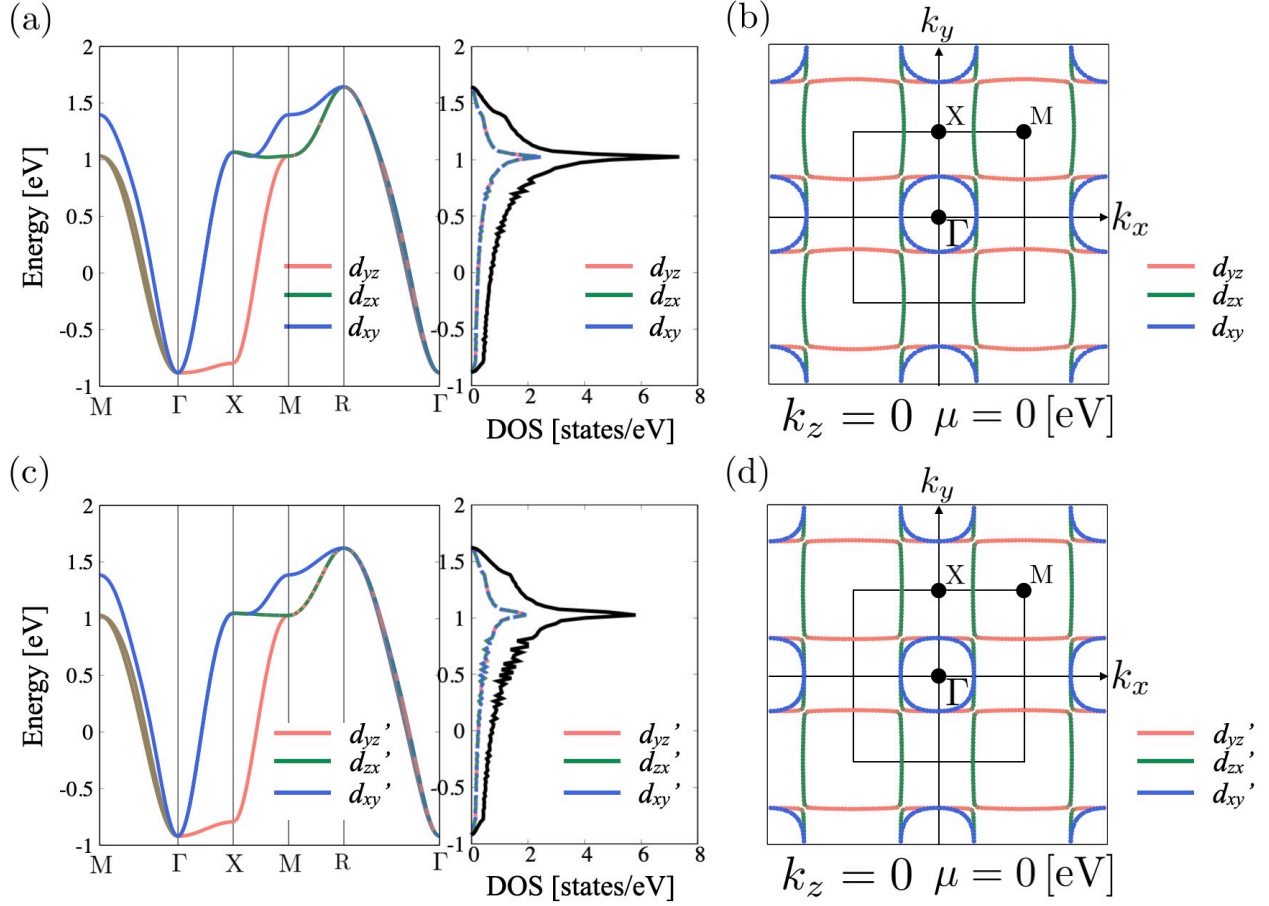


Figure 4.14: The atomic orbital dependence of (a) the band dispersion and DOS, and (b) the Fermi surfaces at $\mu = 0$ [eV] on the $k_z = 0$ plane of the optimized TB model with $N_h = 4$ and $N_{\max}^{(b)} = 5$. The red, green, and blue lines represent the atomic orbitals d_{yz} , d_{zx} , and d_{xy} , respectively. The MLWF dependence of (c) the band dispersion and DOS, and (d) the Fermi surfaces at $\mu = 0$ [eV] on the $k_z = 0$ plane of the Wannier TB model. The red, green, and blue lines represent the MLWFs that have similar symmetry properties of the atomic d orbitals, d'_{yz} , d'_{zx} , and d'_{xy} , respectively. The d'_{xy} orbital is shown in Fig. 2.2(b).

$N_{\max}^{(b)} = 6$ and the LR method in Fig. 4.13(a) and (b), respectively. As shown in Fig. 4.13(a), the loss function for the DNN-SAMB method converges rapidly owing to the use of the DNN-SAMB. On the other hand, as shown in Fig. 4.13(b), the LR method shows relatively slow convergence behavior. Thus, the DNN-SAMB method can reach convergence faster than the usual LR method.

We summarize the explicit values of the optimized weights for each SAMB in Table 4.9 obtained by using DNN-SAMB with $N_h = 4$. The optimized value of each hopping term does not change significantly as $N_{\max}^{(b)}$ increases, confirming that our method is working well.

Figures 4.14 (a) and (b) represent the orbital dependence of the band dispersion, DOS, and Fermi surfaces, which are calculated by our optimized TB model with $N_h = 4$ and $N_{\max}^{(b)} = 5$. While Figs. 4.14 (c) and (d) show that obtained from the DFT-based Wannier TB model. Note that d_{yz} , d_{zx} , and d_{xy} in Figs. 4.14 (a) and (b) denote the atomic orbitals, whereas d'_{yz} , d'_{zx} , and d'_{xy} in Figs. 4.14 (c) and (d) represent the MLWFs having similar symmetry properties of the above three atomic d orbitals. The results indicate that our TB model reproduces the band dispersion, DOS, Fermi surfaces, and their orbital dependences obtained by the Wannier TB model with high accuracy. It should be emphasized that the orbital basis functions used in our TB model is the pure atomic orbitals. Therefore, we can construct the matrix form of various electronic multipole operators, which

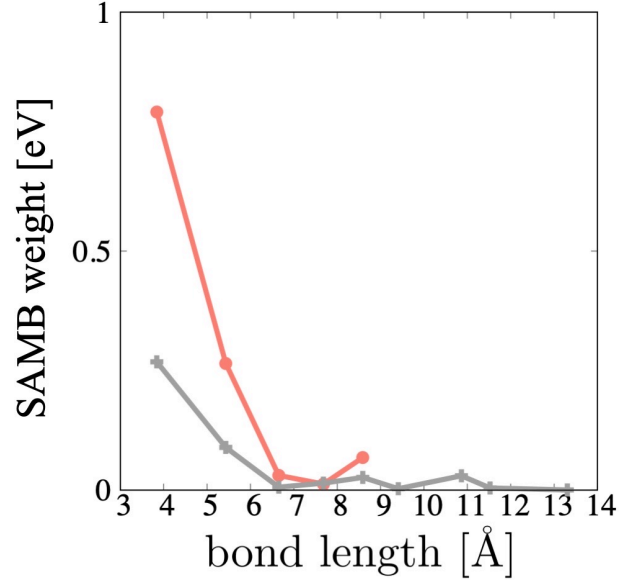


Figure 4.15: The comparison of the bond length dependence of the absolute maximum value of the hopping parameters ($2 \leq j \leq 18$) in eV units between the Wannier TB model (solid grey lines) and our TB model (dashed red lines) with $N_h = 4$ and $N_{\max}^{(b)} = 5$.

is in marked contrast to the Wannier TB model as mentioned in Sec. 2.1.

Moreover, as shown in Fig. 4.15, the magnitude of the hopping parameters of our TB model decreases for further neighbor hoppings, and the number of the parameters is less than the Wannier TB model. As a result, our TB model is more compact than the Wannier TB model.

As discussed above, by using the DNN-SAMB, we can efficiently construct the symmetry-adapted TB model for SrVO_3 . Remarkably, although our TB model contains fewer model parameters than the Wannier TB model, it retains high accuracy in reproducing the electronic structures, including orbital dependences. Note that the proposed method refers only to the energy eigenvalues. Therefore, there is no guarantee to reproduce the orbital dependence of the electronic states in the reference bands. Nevertheless, our optimized TB Hamiltonian well reproduce the orbital dependence of the electronic states as well. This success is ascribed to the use of the SAMB, which imposes strong constraint by symmetry.

4.4.3 MoS₂

As a more general example, we present the results of applying the present method to monolayer MoS₂ in this section.

DFT Calculation for Monolayer MoS₂

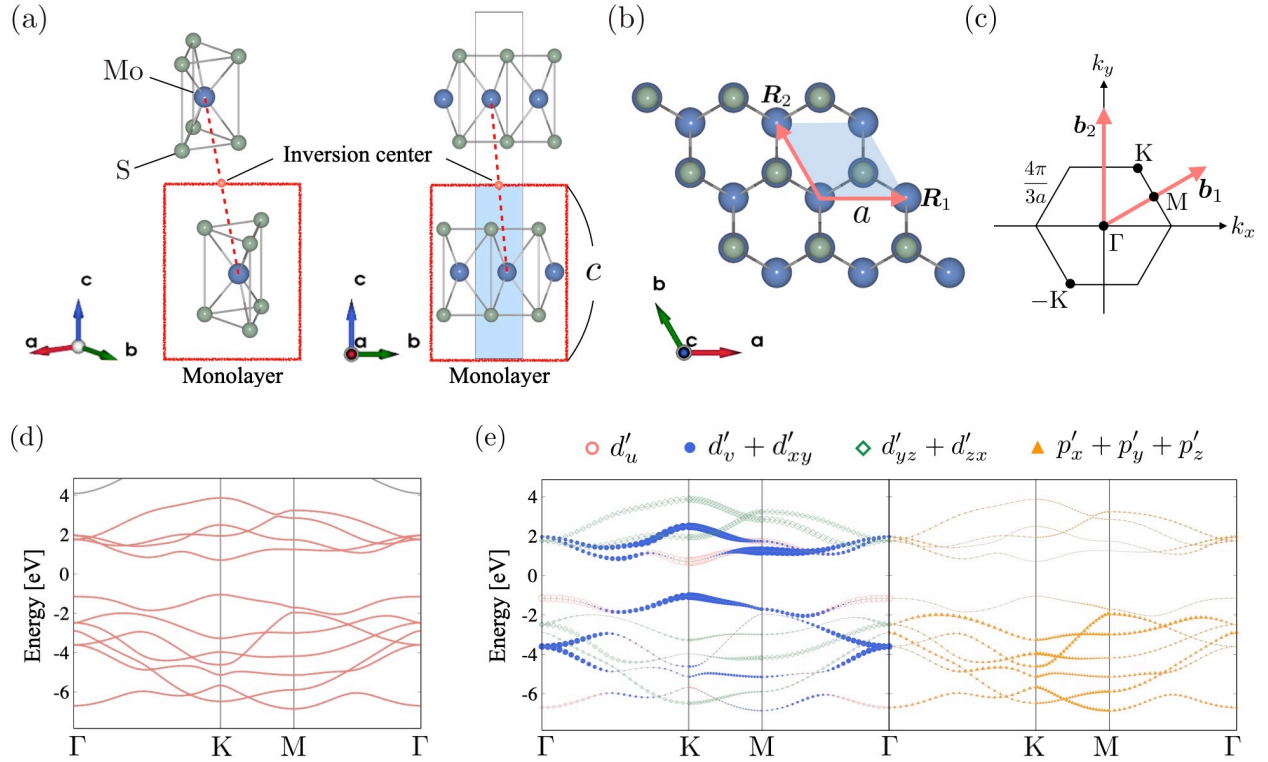


Figure 4.16: Crystal structure of (a) bulk and (b) monolayer MoS₂ where blue shaded area represents the unit cell. (c) The Brillouin zone of the monolayer MoS₂. (d) Band dispersion obtained from the DFT calculation (solid grey lines) and the Wannier TB model (dashed red lines). The Fermi energy is taken as the origin. (e), The Wannier orbitals dependence of the band dispersion. The red, green, and blue points represent the contributions of the d'_u , $d'_v + d'_{xy}$, and $d'_{yz} + d'_{zx}$ orbitals of Mo atom, while the orange points denote the contributions of the 3 p orbitals, $p'_x + p'_y + p'_z$, of S atoms. The size of the points represents the magnitude of contribution of each orbital.

The bulk MoS₂ consists of two units, and each unit is composed of one Mo atom located at the center of six S atoms at the corners of the triangular prism. The triangular prism constitutes a building block of a MoS₂ monolayer [185]. The bulk MoS₂ has the inversion center between two monolayers as shown in Fig. 4.16(a), whereas the monolayer MoS₂ lacks the inversion symmetry as shown in Fig. 4.16(b). The space group of monolayer MoS₂ is $P\bar{6}m2$ (#187, D_{3h}^1).

We set the lattice constant to be $a = 3.1661 \text{ \AA}$, and the length of the vacuum layer along the c axis to be $4 \times a$. The Mo atom is located at the origin $\text{Mo} = (0, 0, 0)$, and the two S atoms are located at $S_1 = (2/3, 1/3, z)$ and $S_2 = (2/3, 1/3, -z)$ with $z = 0.12425$. For the DFT calculation, we use the PBE exchange-correlation functional [186] (See Appendix A.5 in detail) and the PAW pseudopotential. The kinetic energy cutoff of the Kohn-Sham wave functions is 50 Ry, and the convergence threshold for the SCF calculation is set to be 1×10^{-10} Ry. We use $(N_1, N_2, N_3) = (12, 12, 1)$ grid.

As shown in Fig. 4.16(d), since the bands near the Fermi level are entangled, we optimize our TB model to reproduce the band dispersion obtained from the Wannier TB model represented by the

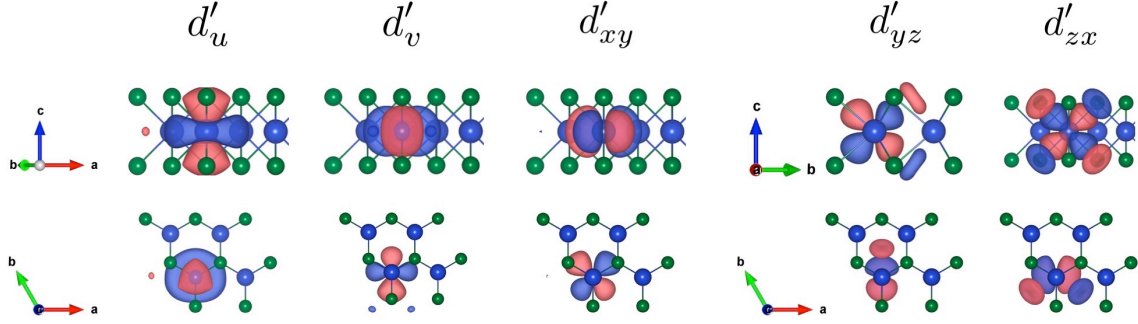


Figure 4.17: The five Wannier orbitals of MoS_2 , d'_u , d'_v , d'_{xy} , d'_{yz} , and d'_{zx} , which have similar symmetry properties of the atomic d orbitals.

solid red lines. Figure 4.16 (e) represents the Wannier orbitals dependence of the band dispersion. The five Wannier orbitals are depicted in Fig. 4.17.

The Mo five atomic d orbitals split into A'_1 (d_u), E' (d_v, d_{xy}), and E'' (d_{yz}, d_{zx}) orbitals owing to the trigonal prismatic structure of S atoms. The xy mirror symmetry hybridizes the A'_1 and E' orbitals, giving rise to the direct band gap at the K point. The top valance band and two bottom conduction bands are mainly composed of the A'_1 and E' orbitals, whereas E'' orbitals have less contribution near the Fermi level. On the other hand, the S three p orbitals contribute to the six bottom valance bands. We choose five atomic d orbitals ($d_u, d_v, d_{yz}, d_{zx}, d_{xy}$) for Mo atom and three atomic p orbitals (p_x, p_y, p_z) for two S atoms as the basis function of the TB model. Note that the SOC is neglected in the following calculations.

Symmetry-Adapted TB Hamiltonian for MoS₂

We first construct the SAMB for MoS₂. We consider five d orbitals ($d_u, d_v, d_{yz}, d_{zx}, d_{xy}$) for Mo atom and three p orbitals (p_x, p_y, p_z) for two S atoms, and the Hilbert space consisting of the eleven basis functions:

$$(|d_u; \text{Mo}\rangle, |d_v; \text{Mo}\rangle, |d_{yz}; \text{Mo}\rangle, |d_{zx}; \text{Mo}\rangle, |d_{xy}; \text{Mo}\rangle, |p_x; \text{S}_1\rangle, |p_y; \text{S}_1\rangle, |p_z; \text{S}_1\rangle, |p_x; \text{S}_2\rangle, |p_y; \text{S}_2\rangle, |p_z; \text{S}_2\rangle) \quad (4.4.43)$$

Then, we construct the spinless TB Hamiltonian in an 11×11 matrix by using the SAMB Z_j as shown in Sec. 4.2. First, we prepare the atomic and site/bond-cluster multipole basis for each site/bond-cluster independently, and then we construct the SAMB by combining them.

Atomic multipole basis

Within the spinless ($p_x, p_y, p_z, d_u, d_v, d_{yz}, d_{zx}, d_{xy}$) orbitals, there are 64 independent atomic multipole basis. The explicit operator expressions of these multipoles are summarized in Tables 4.10 and 4.12.

Table 4.10: Operator expressions of the even parity atomic multipoles defined in the spinless p and d non-hybrid orbitals in the point group D_{3h} . E, M, ET, and MT stand for electric, magnetic, electric toroidal, and magnetic toroidal, respectively. The superscript (a) denotes the atomic multipole. \mathbf{l} and $\boldsymbol{\sigma}/2$ represent the dimensionless orbital and spin angular-momentum operators, and σ_i ($i = x, y, z$) and σ_0 are the Pauli matrices and 2×2 identity matrix.

rank	type	irrep.	symbol	expression
0	E	A_1^+	$Q_0^{(a)}$	1
1	M	A_2^-	$M_z^{(a)}$	l_z
		E''^-	$M_x^{(a)}, M_y^{(a)}$	l_x, l_y
2	E	A_1^+	$Q_u^{(a)}$	$3z^2 - r^2$
		E'^+	$Q_v^{(a)}, Q_{xy}^{(a)}$	$x^2 - y^2, xy$
		E''^+	$Q_{yz}^{(a)}, Q_{zx}^{(a)}$	yz, zx
3	M	A_2^-	$M_{z\alpha}^{(a)}$	$\frac{1}{4}(3z^2 - r^2)l_z - \frac{1}{2}z(xl_x + yl_y)$
		$A_1''^-$	$M_{3a}^{(a)}$	$\frac{1}{2}(x^2 - y^2)l_x - xyl_y$
		$A_2''^-$	$M_{3b}^{(a)}$	$xyl_x + \frac{1}{2}(x^2 - y^2)l_y$
		E'^-	$M_{z\beta}^{(a)}, M_{xyz}^{(a)}$	$\frac{1}{4}(x^2 - y^2)l_z + \frac{1}{2}z(xl_x - yl_y), yzl_x + zxl_y + xyl_z$
		E''^+	$M_{3u}^{(a)}, M_{3v}^{(a)}$	$\frac{1}{2}(5z^2 - r^2)l_x + x(5zl_z - \mathbf{r} \cdot \mathbf{l}), \frac{1}{2}(5z^2 - r^2)l_y + y(5zl_z - \mathbf{r} \cdot \mathbf{l})$
4	E	A_1^+	$Q_{40}^{(a)}$	$\frac{1}{8}(35z^4 - 30z^2r^2 + 3r^4)$
		$A_1''^+$	$Q_{4a}^{(a)}$	$\frac{\sqrt{70}}{4}zx(x^2 - 3y^2)$
		$A_2''^+$	$Q_{4b}^{(a)}$	$\frac{\sqrt{70}}{4}yz(3x^2 - y^2)$
		E''^+	$Q_{4u\alpha}^{(a)}, Q_{4v\alpha}^{(a)}$	$\frac{\sqrt{10}}{4}zx(7z^2 - 3r^2), \frac{\sqrt{10}}{4}yz(7z^2 - 3r^2)$
		E'^+	$Q_{4u\beta 1}^{(a)}, Q_{4v\beta 1}^{(a)}$	$\frac{\sqrt{35}}{8}(x^4 - 6x^2y^2 + y^4), \frac{\sqrt{35}}{2}xy(x^2 - y^2)$
		E'^+	$Q_{4u\beta 2}^{(a)}, Q_{4v\beta 2}^{(a)}$	$\frac{\sqrt{5}}{4}(x^2 - y^2)(7z^2 - r^2), -\frac{\sqrt{5}}{2}xy(7z^2 - r^2)$

Table 4.12: Operator expressions of the odd parity atomic multipoles defined in the (p, d) hybrid orbitals in the point group D_{3h} . E, M, ET, and MT stand for electric, magnetic, electric toroidal, and magnetic toroidal, respectively. The superscript (a) denotes the atomic multipole. \mathbf{l} and $\boldsymbol{\sigma}/2$ represent the dimensionless orbital and spin angular-momentum operators, and σ_i ($i = x, y, z$) and σ_0 are the Pauli matrices and 2×2 identity matrix. $t_l^\alpha = 2(\mathbf{r} \times \mathbf{l})_\alpha / ((l+1)(l+2))$ and $g_l^{\alpha\beta} = 2/(l+1)l^\alpha t_l^\beta$ are the rank- l MT and ET multipole operator.

rank	type	irrep.	symbol	expression
1	E	$A_2^{''+}$	$Q_z^{(a)}$	z
		E'^+	$Q_x^{(a)}, Q_y^{(a)}$	x, y
1	MT	$A_2^{''-}$	$T_z^{(a)}$	$(\mathbf{r} \times \mathbf{l})_z$
		E'^-	$T_x^{(a)}, T_y^{(a)}$	$(\mathbf{r} \times \mathbf{l})_x, (\mathbf{r} \times \mathbf{l})_y$
2	M	$A_1^{''-}$	$M_u^{(a)}$	$3zl_z - \mathbf{r} \cdot \mathbf{l}$
		$E''-$	$M_v^{(a)}, M_{xy}^{(a)}$	$xl_x - yl_y, xl_y + yl_x$
		E'^-	$M_{yz}^{(a)}, M_{zx}^{(a)}$	$yl_z + zl_y, zl_x + xl_z$
	ET	$A_1^{''+}$	$G_u^{(a)}$	$3g_2^{zz} - \sum_\alpha g_2^{\alpha\alpha}$
		$E''+$	$G_v^{(a)}, G_{xy}^{(a)}$	$g_2^{xx} - g_2^{yy}, g_2^{xy}$
		E'^+	$G_{yz}^{(a)}, G_{zx}^{(a)}$	g_2^{yz}, g_2^{zx}
3	E	$A_2^{''+}$	$Q_{z\alpha}^{(a)}$	$\frac{1}{2}z(5z^2 - 3r^2)$
		$A_1^{'+}$	$Q_{3a}^{(a)}$	$\frac{\sqrt{10}}{4}y(3x^2 - y^2)$
		$A_2^{'+}$	$Q_{3b}^{(a)}$	$\frac{\sqrt{10}}{4}x(x^2 - 3y^2)$
		$E''+$	$Q_{z\beta}^{(a)}, Q_{xyz}^{(a)}$	$\frac{\sqrt{15}}{2}z(x^2 - y^2), \sqrt{15}xyz$
		E'^+	$Q_{3u}^{(a)}, Q_{3v}^{(a)}$	$\frac{\sqrt{6}}{4}x(5z^2 - r^2), \frac{\sqrt{6}}{4}y(5z^2 - r^2)$
	MT	$A_2^{''-}$	$T_{z\alpha}^{(a)}$	$\frac{1}{2}(3z^2 - r^2)t_3^z - z(xt_3^x + yt_3^y)$
		$A_1^{'-}$	$T_{3a}^{(a)}$	$(x^2 - y^2)t_3^x - 2xyt_3^y$
		$A_2^{'-}$	$T_{3b}^{(a)}$	$2xyt_3^x + (x^2 - y^2)t_3^y$
		$E''-$	$T_{z\beta}^{(a)}, T_{xyz}^{(a)}$	$\frac{1}{2}(x^2 - y^2)t_3^z + z(xt_3^x - yt_3^y), yzt_3^x + zxt_3^y + xyt_3^z$
		E'^-	$T_{3u}^{(a)}, T_{3v}^{(a)}$	$(5z^2 - r^2)t_3^x + 2x(5zt_3^z - \mathbf{r} \cdot \mathbf{t}_3), (5z^2 - r^2)t_3^y + 2y(5zt_3^z - \mathbf{r} \cdot \mathbf{t}_3)$

Rank block (2,2)

Matrix expressions of the 25 atomic multipoles defined in the non-hybrid $(d_u, d_v, d_{yz}, d_{zx}, d_{xy})$ orbitals are given by

$$Q_0^{(a)} = \frac{\sqrt{5}}{5} \begin{pmatrix} 1 & 0 & 0 & 0 & 0 \\ 0 & 1 & 0 & 0 & 0 \\ 0 & 0 & 1 & 0 & 0 \\ 0 & 0 & 0 & 1 & 0 \\ 0 & 0 & 0 & 0 & 1 \end{pmatrix} \quad (4.4.44)$$

$$M_z^{(a)} = \frac{\sqrt{10}}{10} \begin{pmatrix} 0 & 0 & 0 & 0 & 0 \\ 0 & 0 & 0 & 0 & 2i \\ 0 & 0 & 0 & i & 0 \\ 0 & 0 & -i & 0 & 0 \\ 0 & -2i & 0 & 0 & 0 \end{pmatrix} \quad (4.4.45)$$

$$M_x^{(a)} = \frac{\sqrt{10}}{10} \begin{pmatrix} 0 & 0 & \sqrt{3}i & 0 & 0 \\ 0 & 0 & i & 0 & 0 \\ -\sqrt{3}i & -i & 0 & 0 & 0 \\ 0 & 0 & 0 & 0 & -i \\ 0 & 0 & 0 & i & 0 \end{pmatrix}, M_y^{(a)} = \frac{\sqrt{10}}{10} \begin{pmatrix} 0 & 0 & 0 & \sqrt{3}i & 0 \\ 0 & 0 & 0 & -i & 0 \\ 0 & 0 & 0 & 0 & -i \\ -\sqrt{3}i & i & 0 & 0 & 0 \\ 0 & 0 & i & 0 & 0 \end{pmatrix} \quad (4.4.46)$$

$$Q_u^{(a)} = \frac{\sqrt{14}}{14} \begin{pmatrix} 2 & 0 & 0 & 0 & 0 \\ 0 & -2 & 0 & 0 & 0 \\ 0 & 0 & 1 & 0 & 0 \\ 0 & 0 & 0 & 1 & 0 \\ 0 & 0 & 0 & 0 & -2 \end{pmatrix} \quad (4.4.47)$$

$$Q_v^{(a)} = \frac{\sqrt{14}}{14} \begin{pmatrix} 0 & 2 & 0 & 0 & 0 \\ 2 & 0 & 0 & 0 & 0 \\ 0 & 0 & \sqrt{3} & 0 & 0 \\ 0 & 0 & 0 & -\sqrt{3} & 0 \\ 0 & 0 & 0 & 0 & 0 \end{pmatrix}, Q_{xy}^{(a)} = \frac{\sqrt{14}}{14} \begin{pmatrix} 0 & 0 & 0 & 0 & -2 \\ 0 & 0 & 0 & 0 & 0 \\ 0 & 0 & 0 & -\sqrt{3} & 0 \\ 0 & 0 & -\sqrt{3} & 0 & 0 \\ -2 & 0 & 0 & 0 & 0 \end{pmatrix} \quad (4.4.48)$$

$$Q_{yz}^{(a)} = \frac{\sqrt{14}}{14} \begin{pmatrix} 0 & 0 & 1 & 0 & 0 \\ 0 & 0 & -\sqrt{3} & 0 & 0 \\ 1 & -\sqrt{3} & 0 & 0 & 0 \\ 0 & 0 & 0 & 0 & -\sqrt{3} \\ 0 & 0 & 0 & -\sqrt{3} & 0 \end{pmatrix}, Q_{zx}^{(a)} = \frac{\sqrt{14}}{14} \begin{pmatrix} 0 & 0 & 0 & 1 & 0 \\ 0 & 0 & 0 & \sqrt{3} & 0 \\ 0 & 0 & 0 & 0 & -\sqrt{3} \\ 1 & \sqrt{3} & 0 & 0 & 0 \\ 0 & 0 & -\sqrt{3} & 0 & 0 \end{pmatrix} \quad (4.4.49)$$

$$M_{z\alpha}^{(a)} = \frac{\sqrt{10}}{10} \begin{pmatrix} 0 & 0 & 0 & 0 & 0 \\ 0 & 0 & 0 & 0 & -i \\ 0 & 0 & 0 & 2i & 0 \\ 0 & 0 & -2i & 0 & 0 \\ 0 & i & 0 & 0 & 0 \end{pmatrix} \quad (4.4.50)$$

$$M_{3a}^{(a)} = \frac{1}{2} \begin{pmatrix} 0 & 0 & 0 & 0 & 0 \\ 0 & 0 & 0 & i & 0 \\ 0 & 0 & 0 & 0 & -i \\ 0 & -i & 0 & 0 & 0 \\ 0 & 0 & i & 0 & 0 \end{pmatrix} \quad (4.4.51)$$

$$M_{3b}^{(a)} = \frac{1}{2} \begin{pmatrix} 0 & 0 & 0 & 0 & 0 \\ 0 & 0 & -i & 0 & 0 \\ 0 & i & 0 & 0 & 0 \\ 0 & 0 & 0 & 0 & -i \\ 0 & 0 & 0 & i & 0 \end{pmatrix} \quad (4.4.52)$$

$$M_{z\beta}^{(a)} = \frac{\sqrt{2}}{2} \begin{pmatrix} 0 & 0 & 0 & 0 & -i \\ 0 & 0 & 0 & 0 & 0 \\ 0 & 0 & 0 & 0 & 0 \\ 0 & 0 & 0 & 0 & 0 \\ i & 0 & 0 & 0 & 0 \end{pmatrix}, M_{xyz}^{(a)} = \frac{\sqrt{2}}{2} \begin{pmatrix} 0 & i & 0 & 0 & 0 \\ -i & 0 & 0 & 0 & 0 \\ 0 & 0 & 0 & 0 & 0 \\ 0 & 0 & 0 & 0 & 0 \\ 0 & 0 & 0 & 0 & 0 \end{pmatrix} \quad (4.4.53)$$

$$M_{3u}^{(a)} = \frac{\sqrt{14}}{14} \begin{pmatrix} 0 & 0 & 1 & 0 & 0 \\ 0 & 0 & -\sqrt{3} & 0 & 0 \\ 1 & -\sqrt{3} & 0 & 0 & 0 \\ 0 & 0 & 0 & 0 & -\sqrt{3} \\ 0 & 0 & 0 & -\sqrt{3} & 0 \end{pmatrix}, M_{3v}^{(a)} = \frac{\sqrt{14}}{14} \begin{pmatrix} 0 & 0 & 0 & 1 & 0 \\ 0 & 0 & 0 & \sqrt{3} & 0 \\ 0 & 0 & 0 & 0 & -\sqrt{3} \\ 1 & \sqrt{3} & 0 & 0 & 0 \\ 0 & 0 & -\sqrt{3} & 0 & 0 \end{pmatrix} \quad (4.4.54)$$

$$Q_{40} = \frac{\sqrt{70}}{70} \begin{pmatrix} 6 & 0 & 0 & 0 & 0 \\ 0 & 1 & 0 & 0 & 0 \\ 0 & 0 & -4 & 0 & 0 \\ 0 & 0 & 0 & -4 & 0 \\ 0 & 0 & 0 & 0 & 1 \end{pmatrix} \quad (4.4.55)$$

$$Q_{4a} = \frac{1}{2} \begin{pmatrix} 0 & 0 & 0 & 0 & 0 \\ 0 & 0 & 0 & 1 & 0 \\ 0 & 0 & 0 & 0 & 1 \\ 0 & 1 & 0 & 0 & 0 \\ 0 & 0 & 1 & 0 & 0 \end{pmatrix} \quad (4.4.56)$$

$$Q_{4b} = \frac{1}{2} \begin{pmatrix} 0 & 0 & 0 & 0 & 0 \\ 0 & 0 & 1 & 0 & 0 \\ 0 & 1 & 0 & 0 & 0 \\ 0 & 0 & 0 & 0 & -1 \\ 0 & 0 & 0 & -1 & 0 \end{pmatrix} \quad (4.4.57)$$

$$Q_{4u}^\alpha = \frac{\sqrt{7}}{14} \begin{pmatrix} 0 & 0 & 0 & 2\sqrt{3} & 0 \\ 0 & 0 & 0 & -1 & 0 \\ 0 & 0 & 0 & 0 & 1 \\ 2\sqrt{3} & -1 & 0 & 0 & 0 \\ 0 & 0 & 1 & 0 & 0 \end{pmatrix}, Q_{4v}^\alpha = \frac{\sqrt{7}}{14} \begin{pmatrix} 0 & 0 & 2\sqrt{3} & 0 & 0 \\ 0 & 0 & 1 & 0 & 0 \\ 2\sqrt{3} & 1 & 0 & 0 & 0 \\ 0 & 0 & 0 & 0 & 1 \\ 0 & 0 & 0 & 1 & 0 \end{pmatrix} \quad (4.4.58)$$

$$Q_{4u}^{\beta 1} = \frac{\sqrt{2}}{2} \begin{pmatrix} 0 & 0 & 0 & 0 & 0 \\ 0 & 0 & 0 & 0 & -1 \\ 0 & 0 & 0 & 0 & 0 \\ 0 & 0 & 0 & 0 & 0 \\ 0 & -1 & 0 & 0 & 0 \end{pmatrix}, Q_{4v}^{\beta 1} = \frac{\sqrt{2}}{2} \begin{pmatrix} 0 & 0 & 0 & 0 & 0 \\ 0 & -1 & 0 & 0 & 0 \\ 0 & 0 & 0 & 0 & 0 \\ 0 & 0 & 0 & 0 & 0 \\ 0 & 0 & 0 & 0 & 1 \end{pmatrix} \quad (4.4.59)$$

$$Q_{4u}^{\beta 2} = \frac{\sqrt{14}}{14} \begin{pmatrix} 0 & 0 & 0 & 0 & \sqrt{3} \\ 0 & 0 & 0 & 0 & 0 \\ 0 & 0 & 0 & -2 & 0 \\ 0 & 0 & -2 & 0 & 0 \\ \sqrt{3} & 0 & 0 & 0 & 0 \end{pmatrix}, Q_{4v}^{\beta 2} = \frac{\sqrt{14}}{14} \begin{pmatrix} 0 & -\sqrt{3} & 0 & 0 & 0 \\ -\sqrt{3} & 0 & 0 & 0 & 0 \\ 0 & 0 & 2 & 0 & 0 \\ 0 & 0 & 0 & -2 & 0 \\ 0 & 0 & 0 & 0 & 0 \end{pmatrix} \quad (4.4.60)$$

Rank block (1,1)

Matrix expressions of the 9 atomic multipoles defined in the non-hybrid (p_x, p_y, p_z) orbitals are given by

$$Q_0^{(a)} = \frac{\sqrt{3}}{3} \begin{pmatrix} 1 & 0 & 0 \\ 0 & 1 & 0 \\ 0 & 0 & 1 \end{pmatrix} \quad (4.4.61)$$

$$M_x^{(a)} = \frac{\sqrt{2}}{2} \begin{pmatrix} 0 & 0 & 0 \\ 0 & 0 & -i \\ 0 & i & 0 \end{pmatrix}, M_y^{(a)} = \frac{\sqrt{2}}{2} \begin{pmatrix} 0 & 0 & -i \\ 0 & 0 & 0 \\ i & 0 & 0 \end{pmatrix}, M_z^{(a)} = \frac{\sqrt{2}}{2} \begin{pmatrix} 0 & -i & 0 \\ i & 0 & 0 \\ 0 & 0 & 0 \end{pmatrix} \quad (4.4.62)$$

$$Q_u^{(a)} = \frac{\sqrt{6}}{6} \begin{pmatrix} -1 & 0 & 0 \\ 0 & -1 & 0 \\ 0 & 0 & 2 \end{pmatrix} \quad (4.4.63)$$

$$Q_{yz}^{(a)} = \frac{\sqrt{2}}{2} \begin{pmatrix} 0 & 0 & 0 \\ 0 & 0 & 1 \\ 0 & 1 & 0 \end{pmatrix}, Q_{zx}^{(a)} = \frac{\sqrt{2}}{2} \begin{pmatrix} 0 & 0 & 1 \\ 0 & 0 & 0 \\ 1 & 0 & 0 \end{pmatrix} \quad (4.4.64)$$

$$Q_v^{(a)} = \frac{\sqrt{2}}{2} \begin{pmatrix} -1 & 0 & 0 \\ 0 & 1 & 0 \\ 0 & 0 & 0 \end{pmatrix}, Q_{xy}^{(a)} = \frac{\sqrt{2}}{2} \begin{pmatrix} 0 & -1 & 0 \\ -1 & 0 & 0 \\ 0 & 0 & 0 \end{pmatrix} \quad (4.4.65)$$

Rank block (1,2)

Matrix expressions of the 30 atomic multipoles defined in the hybrid orbitals,

$$[(\langle p_x |, \langle p_y |, \langle p_z |), (|d_u\rangle, |d_v\rangle, |d_{yz}\rangle, |d_{zx}\rangle, |d_{xy}\rangle)] \quad (4.4.66)$$

are given by

$$Q_z^{(a)} = \frac{\sqrt{10}}{10} \begin{pmatrix} 0 & 0 & 0 & \sqrt{3} & 0 \\ 0 & 0 & \sqrt{3} & 0 & 0 \\ 2 & 0 & 0 & 0 & 0 \end{pmatrix} \quad (4.4.67)$$

$$Q_x^{(a)} = \frac{\sqrt{10}}{10} \begin{pmatrix} -1 & \sqrt{3} & 0 & 0 & 0 \\ 0 & 0 & 0 & 0 & -\sqrt{3} \\ 0 & 0 & 0 & \sqrt{3} & 0 \end{pmatrix}, Q_y^{(a)} = \frac{\sqrt{10}}{10} \begin{pmatrix} 0 & 0 & 0 & 0 & -\sqrt{3} \\ -1 & -\sqrt{3} & 0 & 0 & 0 \\ 0 & 0 & \sqrt{3} & 0 & 0 \end{pmatrix} \quad (4.4.68)$$

$$T_\alpha^{(a)} = iQ_\alpha \quad (4.4.69)$$

$$M_u^{(a)} = \frac{\sqrt{2}}{2} \begin{pmatrix} 0 & 0 & -i & 0 & 0 \\ 0 & 0 & 0 & i & 0 \\ 0 & 0 & 0 & 0 & 0 \end{pmatrix} \quad (4.4.70)$$

$$M_v^{(a)} = \frac{\sqrt{6}}{6} \begin{pmatrix} 0 & 0 & -i & 0 & 0 \\ 0 & 0 & 0 & -\frac{\sqrt{6}i}{6} & 0 \\ 0 & 0 & 0 & 0 & -2i \end{pmatrix}, M_{xy}^{(a)} = \frac{\sqrt{6}}{6} \begin{pmatrix} 0 & 0 & 0 & -i & 0 \\ 0 & 0 & i & 0 & 0 \\ 0 & 2i & 0 & 0 & 0 \end{pmatrix} \quad (4.4.71)$$

$$M_{yz}^{(a)} = \frac{\sqrt{6}}{6} \begin{pmatrix} -\sqrt{3}i & -i & 0 & 0 & 0 \\ 0 & 0 & 0 & 0 & i \\ 0 & 0 & 0 & i & 0 \end{pmatrix}, M_{zx}^{(a)} = \frac{\sqrt{6}}{6} \begin{pmatrix} 0 & 0 & 0 & 0 & i \\ -\sqrt{3}i & i & 0 & 0 & 0 \\ 0 & 0 & i & 0 & 0 \end{pmatrix} \quad (4.4.72)$$

$$G_\alpha^{(a)} = iM_\alpha^{(a)} \quad (4.4.73)$$

$$Q_{z\alpha}^{(a)} = \frac{\sqrt{5}}{5} \begin{pmatrix} 0 & 0 & 0 & -1 & 0 \\ 0 & 0 & -1 & 0 & 0 \\ \sqrt{3} & 0 & 0 & 0 & 0 \end{pmatrix} \quad (4.4.74)$$

$$Q_{3a}^{(a)} = \frac{\sqrt{2}}{2} \begin{pmatrix} 0 & 0 & 0 & 0 & -1 \\ 0 & 1 & 0 & 0 & 0 \\ 0 & 0 & 0 & 0 & 0 \end{pmatrix} \quad (4.4.75)$$

$$Q_{3b}^{(a)} = \frac{\sqrt{2}}{2} \begin{pmatrix} 0 & 1 & 0 & 0 & 0 \\ 0 & 0 & 0 & 0 & 1 \\ 0 & 0 & 0 & 0 & 0 \end{pmatrix} \quad (4.4.76)$$

$$Q_{3u}^{(a)} = \frac{\sqrt{3}}{3} \begin{pmatrix} 0 & 0 & -1 & 0 & 0 \\ 0 & 0 & 0 & -1 & 0 \\ 0 & 0 & 0 & 0 & 1 \end{pmatrix}, Q_{3v}^{(a)} = \frac{\sqrt{3}}{3} \begin{pmatrix} 0 & 0 & 0 & -1 & 0 \\ 0 & 0 & 1 & 0 & 0 \\ 0 & -1 & 0 & 0 & 0 \end{pmatrix} \quad (4.4.77)$$

$$Q_{z\beta}^{(a)} = \frac{\sqrt{30}}{30} \begin{pmatrix} 2\sqrt{3} & -1 & 0 & 0 & 0 \\ 0 & 0 & 0 & 0 & 1 \\ 0 & 0 & 0 & 4 & 0 \end{pmatrix}, Q_{xyz}^{(a)} = \frac{\sqrt{30}}{30} \begin{pmatrix} 0 & 0 & 0 & 0 & 1 \\ 2\sqrt{3} & 1 & 0 & 0 & 0 \\ 0 & 0 & 4 & 0 & 0 \end{pmatrix} \quad (4.4.78)$$

$$T_{\alpha}^{(a)} = iQ_{\alpha}^{(a)} \quad (4.4.79)$$

Site-cluster multipole basis

Next, we introduce the E site-cluster multipole basis for Mo and S site-clusters independently.

Since the size of the Mo site-cluster is 1, there is only one site-cluster E monopole basis:

$$Q_0^{(s,Mo)} = (1) \quad (4.4.80)$$

On the other hand, the size of the S site-cluster (S_1, S_2) is 2, there are two site-cluster E multipole basis:

$$Q_0^{(s,S)} = \frac{1}{\sqrt{2}}(1, 1), \quad Q_z^{(s,S)} = \frac{1}{\sqrt{2}}(1, -1) \quad (4.4.81)$$

The final matrix form of the on/off-site cluster multipole basis are given in the site space (Mo, S_1, S_2) as

$$Q_0^{(t,Mo)} = \begin{pmatrix} 1 & 0 & 0 \\ 0 & 0 & 0 \\ 0 & 0 & 0 \end{pmatrix} \quad (4.4.82)$$

$$Q_0^{(t,S)} = \frac{\sqrt{2}}{2} \begin{pmatrix} 0 & 0 & 0 \\ 0 & 1 & 0 \\ 0 & 0 & 1 \end{pmatrix}, \quad Q_z^{(t,S)} = \frac{\sqrt{2}}{2} \begin{pmatrix} 0 & 0 & 0 \\ 0 & 1 & 0 \\ 0 & 0 & -1 \end{pmatrix} \quad (4.4.83)$$

$$Q_0^{(t,S-S)} = \frac{\sqrt{2}}{2} \begin{pmatrix} 0 & 0 & 0 \\ 0 & 0 & 1 \\ 0 & 1 & 0 \end{pmatrix}, \quad T_z^{(t,S-S)} = \frac{\sqrt{2}}{2} \begin{pmatrix} 0 & 0 & 0 \\ 0 & 0 & i \\ 0 & -i & 0 \end{pmatrix} \quad (4.4.84)$$

$$Q_0^{(t,Mo-S)} = \frac{1}{2} \begin{pmatrix} 0 & 1 & 1 \\ 1 & 0 & 0 \\ 1 & 0 & 0 \end{pmatrix}, \quad Q_z^{(t,Mo-S)} = \frac{1}{2} \begin{pmatrix} 0 & 1 & -1 \\ 1 & 0 & 0 \\ -1 & 0 & 0 \end{pmatrix} \quad (4.4.85)$$

$$T_0^{(t,Mo-S)} = \frac{1}{2} \begin{pmatrix} 0 & i & i \\ i & 0 & 0 \\ i & 0 & 0 \end{pmatrix}, \quad T_z^{(t,Mo-S)} = \frac{1}{2} \begin{pmatrix} 0 & i & -i \\ i & 0 & 0 \\ -i & 0 & 0 \end{pmatrix} \quad (4.4.86)$$

Bond-cluster multipole basis

To describe the hopping Hamiltonian, we introduce the E/MT bond-cluster multipole basis. We restrict our demonstration up to the nearest-neighbor Mo–Mo, S–S, and Mo–S bond-clusters as shown in Fig. 4.18(a), (b), and (c), respectively.

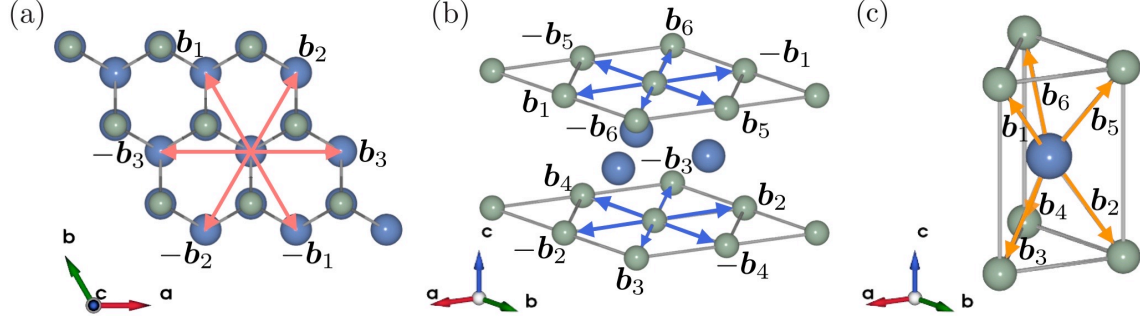


Figure 4.18: (a) Nearest-neighbor Mo–Mo, (b) S–S, and (c) Mo–S bond-clusters of monolayer MoS₂.

Nearest-neighbor Mo–Mo bond-cluster

There are six independent bond-cluster multipole basis:

$$\begin{aligned}
 Q_0^{(b, \text{Mo-Mo})} &= \frac{1}{\sqrt{6}}(1, 1, 1; 1, 1, 1) \\
 Q_v^{(b, \text{Mo-Mo})} &= \frac{1}{2\sqrt{3}}(1, 1, -2; 1, 1, -2) \\
 Q_{xy}^{(b, \text{Mo-Mo})} &= \frac{1}{2}(1, -1, 0; 1, -1, 0) \\
 T_x^{(b, \text{Mo-Mo})} &= \frac{1}{2}(-i, -i, 0; i, i, 0) \\
 T_y^{(b, \text{Mo-Mo})} &= \frac{1}{2\sqrt{3}}(i, -i, 2i; -i, i, -2i) \\
 T_{3b}^{(b, \text{Mo-Mo})} &= \frac{1}{\sqrt{6}}(i, -i, -i; -i, i, i)
 \end{aligned} \tag{4.4.87}$$

The elements correspond to the bond vectors described by $\mathbf{b}@\mathbf{c}$:

$$\begin{aligned}
 \mathbf{b}_1@\mathbf{c}_1 &= [0, 1, 0]@[0, 1/2, 0] \\
 \mathbf{b}_2@\mathbf{c}_2 &= [1, 1, 0]@[1/2, 1/2, 0] \\
 \mathbf{b}_3@\mathbf{c}_3 &= [-1, 0, 0]@[1/2, 0, 0]
 \end{aligned} \tag{4.4.88}$$

Nearest-neighbor S–S bond-cluster

There are twelve independent bond-cluster multipole basis:

$$\begin{aligned}
Q_0^{(b,S-S)} &= \frac{1}{2\sqrt{3}}(1, 1, 1, 1, 1, 1; 1, 1, 1, 1, 1, 1) \\
Q_z^{(b,S-S)} &= \frac{1}{2\sqrt{3}}(1, -1, -1, -1, 1, 1; 1, -1, -1, -1, 1, 1) \\
Q_v^{(b,S-S)} &= \frac{1}{2\sqrt{6}}(-2, -2, 1, 1, 1, 1; -2, -2, 1, 1, 1, 1) \\
Q_{xy}^{(b,S-S)} &= \frac{1}{2\sqrt{2}}(0, 0, -1, 1, 1, -1; 0, 0, -1, 1, 1, -1) \\
Q_{3u}^{(b,S-S)} &= \frac{1}{2\sqrt{6}}(-2, 2, -1, -1, 1, 1; -2, 2, -1, -1, 1, 1) \\
Q_{3v}^{(b,S-S)} &= \frac{1}{2\sqrt{2}}(0, 0, 1, -1, 1, -1; 0, 0, 1, -1, 1, -1) \\
T_x^{(b,S-S)} &= \frac{1}{2\sqrt{6}}(2i, -2i, i, i, -i, -i; -2i, 2i, -i, -i, i, i) \\
T_y^{(b,S-S)} &= \frac{1}{2\sqrt{2}}(0, 0, i, -i, i, -i; 0, 0, -i, i, -i, i) \\
T_{yz}^{(b,S-S)} &= \frac{1}{2\sqrt{6}}(2i, 2i, -i, -i, -i, -i; -2i, -2i, i, i, i, i) \\
T_{zx}^{(b,S-S)} &= \frac{1}{2\sqrt{2}}(0, 0, -i, i, i, -i; 0, 0, i, -i, -i, i) \\
T_{3b}^{(b,S-S)} &= \frac{1}{2\sqrt{3}}(i, -i, -i, -i, i, i; -i, i, i, i, -i, -i) \\
T_{4a}^{(b,S-S)} &= \frac{1}{2\sqrt{3}}(i, i, i, i, i, i; -i, -i, -i, -i, -i, -i)
\end{aligned} \tag{4.4.89}$$

The elements correspond to the bond vectors described by $\mathbf{b}@c$:

$$\begin{aligned}
\mathbf{b}_1@c_1 &= [1, 0, 0]@[1/6, 1/3, z] \\
\mathbf{b}_2@c_2 &= [-1, 0, 0]@[1/6, 1/3, -z] \\
\mathbf{b}_3@c_3 &= [1, 1, 0]@[1/6, 5/6, -z] \\
\mathbf{b}_4@c_4 &= [0, -1, 0]@[2/3, 5/6, -z] \\
\mathbf{b}_5@c_5 &= [0, 1, 0]@[2/3, 5/6, z] \\
\mathbf{b}_6@c_6 &= [-1, -1, 0]@[1/6, 5/6, z]
\end{aligned} \tag{4.4.90}$$

where $z = 0.12425$.

Nearest-neighbor Mo–S bond-cluster

There are twelve independent bond-cluster multipole basis:

$$\begin{aligned}
Q_0^{(b, \text{Mo-S})} &= \frac{1}{2\sqrt{3}}(1, 1, 1, 1, 1, 1; 1, 1, 1, 1, 1, 1) \\
Q_z^{(b, \text{Mo-S})} &= \frac{1}{2\sqrt{3}}(1, -1, -1, -1, 1, 1; 1, -1, -1, -1, 1, 1) \\
Q_v^{(b, \text{Mo-S})} &= \frac{1}{2\sqrt{6}}(1, 1, 1, -2, 1, -2; 1, 1, 1, -2, 1, -2) \\
Q_{xy}^{(b, \text{Mo-S})} &= \frac{1}{2\sqrt{2}}(1, -1, 1, 0, -1, 0; 1, -1, 1, 0, -1, 0) \\
Q_{yz}^{(b, \text{Mo-S})} &= \frac{1}{2\sqrt{6}}(1, -1, -1, 2, 1, -2; 1, -1, -1, 2, 1, -2) \\
Q_{zx}^{(b, \text{Mo-S})} &= \frac{1}{2\sqrt{2}}(1, 1, -1, 0, -1, 0; 1, 1, -1, 0, -1, 0) \\
T_0^{(b, \text{Mo-S})} &= \frac{1}{2\sqrt{3}}(i, i, i, i, i, i; -i, -i, -i, -i, -i, -i) \\
T_z^{(b, \text{Mo-S})} &= \frac{1}{2\sqrt{3}}(i, -i, -i, -i, i, i; -i, i, i, i, -i, -i) \\
T_x^{(b, \text{Mo-S})} &= \frac{1}{2\sqrt{2}}(i, -i, i, 0, -i, 0; -i, i, -i, 0, i, 0) \\
T_y^{(b, \text{Mo-S})} &= \frac{1}{2\sqrt{6}}(i, i, i, -2i, i, -2i; -i, -i, -i, 2i, -i, 2i) \\
T_{z\beta}^{(b, \text{Mo-S})} &= \frac{1}{2\sqrt{6}}(i, -i, -i, 2i, i, -2i; -i, i, i, -2i, -i, 2i) \\
T_{xyz}^{(b, \text{Mo-S})} &= \frac{1}{2\sqrt{2}}(i, i, -i, 0, -i, 0; -i, -i, i, 0, i, 0)
\end{aligned} \tag{4.4.91}$$

The elements correspond to the bond vectors described by $\mathbf{b}@\mathbf{c}$:

$$\begin{aligned}
\mathbf{b}_1@\mathbf{c}_1 &= [2/3, 1/3, z]@[1/3, 1/6, z/2] \\
\mathbf{b}_2@\mathbf{c}_2 &= [-1/3, 1/3, -z]@[5/6, 1/6, -z/2] \\
\mathbf{b}_3@\mathbf{c}_3 &= [2/3, 1/3, -z]@[1/3, 1/6, -z/2] \\
\mathbf{b}_4@\mathbf{c}_4 &= [-1/3, -2/3, -z]@[5/6, 2/3, -z/2] \\
\mathbf{b}_5@\mathbf{c}_5 &= [-1/3, 1/3, z]@[5/6, 1/6, z/2] \\
\mathbf{b}_6@\mathbf{c}_6 &= [-1/3, -2/3, z]@[5/6, 2/3, z/2]
\end{aligned} \tag{4.4.92}$$

where $z = 0.12425$.

SAMB and symmetry-adapted TB Hamiltonian for MoS₂

Considering the irreducible decompositions,

$$A'_{1/2} \otimes A'_{1/2} = A''_{1/2} \otimes A''_{1/2} = A'_1, \quad E' \otimes E' = E'' \otimes E'' = A'_1 \oplus A'_2 \oplus E' \tag{4.4.93}$$

we obtain the fully symmetric 28 SAMB as follows:

$$Q_0[\text{Mo}] = Q_0^{(a)} \otimes Q_0^{(s, \text{Mo})}, \quad Q_u[\text{Mo}] = Q_u^{(a)} \otimes Q_0^{(s, \text{Mo})}, \quad Q_{40}[\text{Mo}] = Q_{40}^{(a)} \otimes Q_0^{(s, \text{Mo})} \tag{4.4.94}$$

$$Q_0[\text{S}] = Q_0^{(a)} \otimes Q_0^{(s, \text{S})}, \quad Q_u[\text{S}] = Q_u^{(a)} \otimes Q_0^{(s, \text{S})} \tag{4.4.95}$$

$$\begin{aligned}
Q_0[\text{Mo} - \text{Mo}, 1] &= Q_0^{(a)} \otimes Q_0^{(b, [\text{Mo} - \text{Mo}])}, & Q_u[\text{Mo} - \text{Mo}] &= Q_u^{(a)} \otimes Q_0^{(b, [\text{Mo} - \text{Mo}])} \\
Q_{40}[\text{Mo} - \text{Mo}] &= Q_{40}^{(a)} \otimes Q_0^{(b, [\text{Mo} - \text{Mo}])} \\
Q_{3a}[\text{Mo} - \text{Mo}, 1] &= M_z^{(a)} \otimes T_{3b}^{(b, [\text{Mo} - \text{Mo}])}, & Q_{3a}[\text{Mo} - \text{Mo}, 2] &= M_{z\alpha}^{(a)} \otimes T_{3b}^{(b, [\text{Mo} - \text{Mo}])} \\
Q_0[\text{Mo} - \text{Mo}, 2] &= \frac{1}{\sqrt{2}} \left(Q_v^{(a)} \otimes Q_v^{(b, \text{Mo} - \text{Mo})} + Q_{xy}^{(a)} \otimes Q_{xy}^{(b, \text{Mo} - \text{Mo})} \right) \\
Q_u[\text{Mo} - \text{Mo}, 2] &= \frac{1}{\sqrt{2}} \left(Q_{4u\beta 1}^{(a)} \otimes Q_v^{(b, \text{Mo} - \text{Mo})} + Q_{4v\beta 1}^{(a)} \otimes Q_{xy}^{(b, \text{Mo} - \text{Mo})} \right) \\
Q_u[\text{Mo} - \text{Mo}, 3] &= \frac{1}{\sqrt{2}} \left(Q_{4u\beta 2}^{(a)} \otimes Q_v^{(b, \text{Mo} - \text{Mo})} + Q_{4v\beta 2}^{(a)} \otimes Q_{xy}^{(b, \text{Mo} - \text{Mo})} \right) \\
Q_{3a}[\text{Mo} - \text{Mo}, 3] &= \frac{1}{\sqrt{2}} \left(M_{z\beta}^{(a)} \otimes T_x^{(b, \text{Mo} - \text{Mo})} + M_{xyz}^{(a)} \otimes T_y^{(b, \text{Mo} - \text{Mo})} \right)
\end{aligned} \tag{4.4.96}$$

$$\begin{aligned}
Q_0[\text{S} - \text{S}, 1] &= Q_0^{(a)} \otimes Q_0^{(b, \text{S} - \text{S})}, & Q_u[\text{S} - \text{S}, 1] &= Q_u^{(a)} \otimes Q_0^{(b, \text{S} - \text{S})}, & Q_{3a}[\text{S} - \text{S}, 1] &= M_z^{(a)} \otimes T_{3b}^{(b, \text{S} - \text{S})} \\
Q_u[\text{S} - \text{S}, 2] &= \frac{1}{\sqrt{2}} \left(M_x^{(a)} \otimes T_{yz}^{(b, \text{S} - \text{S})} + M_y^{(a)} \otimes T_{zx}^{(b, \text{S} - \text{S})} \right) \\
Q_3[\text{S} - \text{S}, 2] &= \frac{1}{\sqrt{2}} \left(Q_{yz}^{(a)} \otimes Q_{3u}^{(b, \text{S} - \text{S})} + Q_{zx}^{(a)} \otimes Q_{3v}^{(b, \text{S} - \text{S})} \right) \\
Q_0[\text{S} - \text{S}, 2] &= \frac{1}{\sqrt{2}} \left(Q_v^{(a)} \otimes Q_v^{(b, \text{S} - \text{S})} + Q_{xy}^{(a)} \otimes Q_{xy}^{(b, \text{S} - \text{S})} \right)
\end{aligned} \tag{4.4.97}$$

$$\begin{aligned}
Q_0[\text{Mo} - \text{S}, 1] &= Q_z^{(a)} \otimes Q_z^{(b, \text{Mo} - \text{S})}, & Q_u[\text{Mo} - \text{S}, 1] &= Q_{z\alpha}^{(a)} \otimes Q_z^{(b, \text{Mo} - \text{S})} \\
Q_{3a}[\text{Mo} - \text{S}, 1] &= \frac{1}{\sqrt{2}} \left(Q_x^{(a)} \otimes Q_v^{(b, \text{Mo} - \text{S})} + Q_y^{(a)} \otimes Q_{xy}^{(b, \text{Mo} - \text{S})} \right) \\
Q_{3a}[\text{Mo} - \text{S}, 2] &= \frac{1}{\sqrt{2}} \left(G_{yz}^{(a)} \otimes Q_v^{(b, \text{Mo} - \text{S})} + G_{zx}^{(a)} \otimes Q_{xy}^{(b, \text{Mo} - \text{S})} \right) \\
Q_u[\text{Mo} - \text{S}, 2] &= \frac{1}{\sqrt{2}} \left(Q_{3u}^{(a)} \otimes Q_v^{(b, \text{Mo} - \text{S})} + Q_{3v}^{(a)} \otimes Q_{xy}^{(b, \text{Mo} - \text{S})} \right) \\
Q_{3a}[\text{Mo} - \text{S}, 3] &= \frac{1}{\sqrt{2}} \left(G_v^{(a)} \otimes Q_{yz}^{(b, \text{Mo} - \text{S})} + G_{xy}^{(a)} \otimes Q_{zx}^{(b, \text{Mo} - \text{S})} \right) \\
Q_{3a}[\text{Mo} - \text{S}, 4] &= \frac{1}{\sqrt{2}} \left(Q_{z\beta}^{(a)} \otimes Q_{yz}^{(b, \text{Mo} - \text{S})} + Q_{xyz}^{(a)} \otimes Q_{zx}^{(b, \text{Mo} - \text{S})} \right) \\
Q_{3a}[\text{Mo} - \text{S}, 5] &= Q_{3a}^{(a)} \otimes Q_0^{(b, \text{Mo} - \text{S})}
\end{aligned} \tag{4.4.98}$$

where the numbers in the parentheses denote the multiplicity. As shown in Eq. (4.4.98), the nearest neighbor Mo–S hoppings, $Q_{3a}[\text{Mo} - \text{S}, 2]$ and $Q_{3a}[\text{Mo} - \text{S}, 3]$ contain the ET quadrupoles, $G_{yz}^{(a)}$, $G_{zx}^{(a)}$, $G_v^{(a)}$, and $G_{xy}^{(a)}$. Using these SAMB, the TB hamiltonian can be expressed as

$$H = \sum_{j=1}^{28} z_j Z_j \tag{4.4.99}$$

The momentum representation of the SAMB is given in Appendix F.2.

Parameter Optimization

Table 4.14: Parameters and hyperparameters used for the optimization process.

high symmetry lines	$\Gamma-K-M-\Gamma$
number of \mathbf{k} points	$N_k = 151$
number of bands	$N_n = 11$
total number of the eigenvalues	$N_{\text{tot}} = N_k \times N_n = 1661$
maximum number of neighbor bonds	$N_{\text{max}}^{(b)} = 1-3$
number of hidden layers	$N_h = 0-3$
maximum number of iterations	$N_{\text{iter}} = 500$
learning rate	$\alpha = 0.01$

Table 4.15: $N_{\text{max}}^{(b)}$ dependence of the number of neurons and the optimization parameters in the DNN-SAMB with $N_h = 3$.

Layer	$N_{\text{max}}^{(b)} = 1$		2		3	
	neurons #	params #				
DFT band	1661		1661		1661	
1st hidden	224	372288	360	598320	592	983904
2nd hidden	112	25200	180	64980	296	175528
3rd hidden	56	6328	90	16290	148	43956
SAMB	28	1596	45	4095	74	11026
TB band	1661		1661		1661	
total #	4162	405412	3997	683685	4432	1214414

In this section, we show the results of the parameter optimization. The parameters and hyperparameters used for the optimization process are summarized in Table 4.14. We chose the high symmetry lines $\Gamma-K-M-\Gamma$. We use bands at 50 \mathbf{k} points in each line, then the number of \mathbf{k} points is $N_k = 151$ and the number of bands is $N_n = 11$. The total number of the eigenvalues is $N_{\text{tot}} = N_k \times N_n = 1661$. For comparison, we change the maximum number of neighbor bonds from nearest to 3rd neighbor Mo-Mo, S-S, and Mo-S bond-clusters, $N_{\text{max}}^{(b)} = 1-3$, and we also change the number of hidden layers from 1 to 3, $N_h = 1-3$. The maximum number of iterations is fixed as $N_{\text{iter}} = 500$ that is sufficient to reach convergence, and the learning rate is fixed as $\alpha = 0.01$. Table 4.15 shows the $N_{\text{max}}^{(b)}$ dependence of the number of neurons and the optimization parameters in the DNN-SAMB with $N_h = 3$. When $N_{\text{max}}^{(b)} = 3$, the total number of the optimization parameters is about 1200000.

Similar to the previous sections 4.4.1 and 4.4.2, we implement 50 optimization calculations with different random initial parameters for each pair of $(N_{\text{max}}^{(b)}, N_h)$. In addition, we also perform the parameter optimization using the conventional LR method with $N_{\text{iter}} = 3000$ and $\alpha = 0.01$.

The results of parameter optimization using the DNN-SAMB with $N_h = 3$ are shown in Figs. 4.19 (a)-(c). As shown in Figs. 4.19 (a)-(c), the quality of the optimization are improved gradually by increasing $N_{\text{max}}^{(b)}$. In particular, when $N_{\text{max}}^{(b)} = 3$, the obtained TB model reproduces the DFT-based Wannier band dispersions with high accuracy. As shown in Table 4.16, by taking up to 3rd neighbor Mo-Mo, S-S, and Mo-S bond-clusters, we achieved an accuracy less than 10^{-4} of the MSE between the normalized energy eigenvalues of our TB model and the Wannier TB model.

Meanwhile, as shown in Figs. 4.19 (d)-(f), the optimized results obtained using LR method show less quality especially when $N_{\text{max}}^{(b)} = 2$ and 3. This is because the numbers of optimization parameters are 45 and 74 when $N_{\text{max}}^{(b)} = 2$ and 3, the optimization quality highly depends on the initial guess

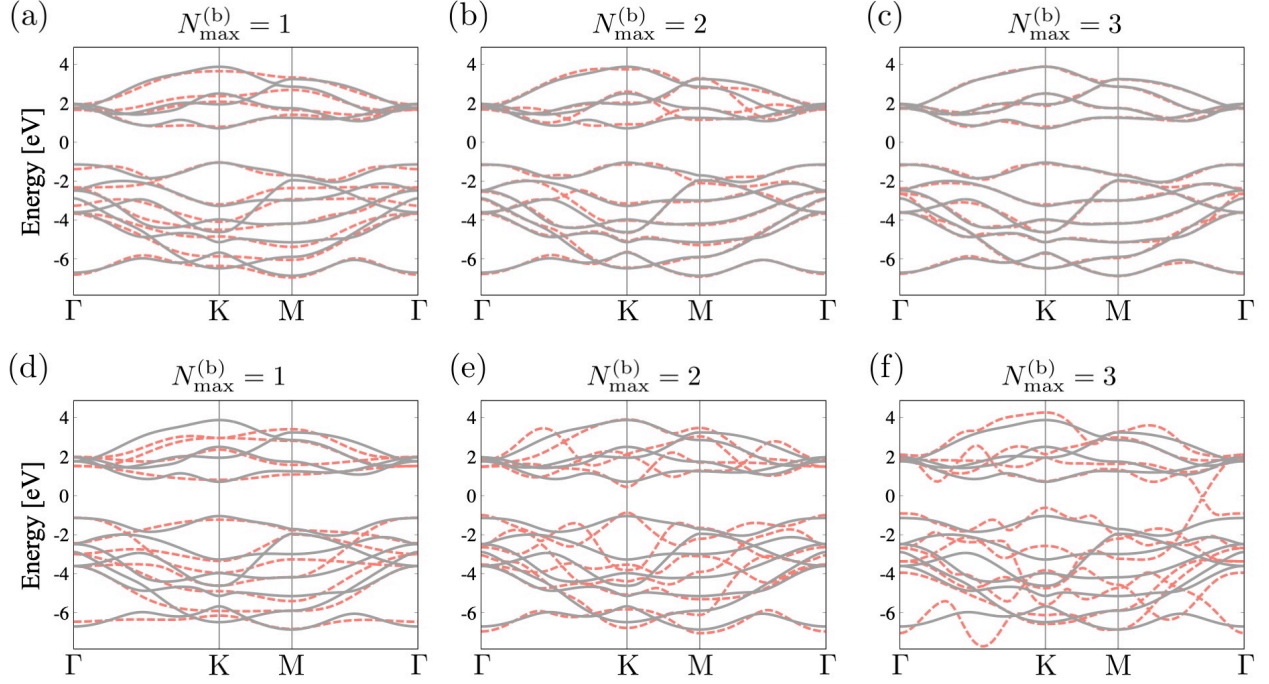


Figure 4.19: The comparisons of the band dispersion between the Wannier TB model (solid grey lines) and our TB models (dashed red lines) obtained by using DNN-SAMB and LR method. (a)-(c) The optimized results obtained by using DNN-SAMB with $N_{\max}^{(b)} = 1-3$ and $N_h = 3$. (d)-(e) The optimized results obtained by using LR method with $N_{\max}^{(b)} = 1-3$. The Fermi energy is taken as the origin.

Table 4.16: The minimum, maximum, and average loss function, L_{\min} , L_{\max} , and L_{avg} , in 50 optimization calculations with different initial guess using the LR method and the DNN-SAMB method with $N_h = 3$.

$N_{\max}^{(b)}$	L_{\min}		L_{\max}		L_{avg}	
	LR	DNN-SAMB	LR	DNN-SAMB	LR	DNN-SAMB
1	5.3×10^{-4}	1.6×10^{-4}	2.3×10^{-3}	1.5×10^{-3}	1.3×10^{-3}	4.7×10^{-4}
2	4.7×10^{-4}	9.3×10^{-5}	2.5×10^{-3}	8.7×10^{-4}	1.3×10^{-3}	3.8×10^{-4}
3	6.9×10^{-4}	2.5×10^{-5}	2.4×10^{-3}	6.4×10^{-4}	1.5×10^{-3}	2.5×10^{-4}

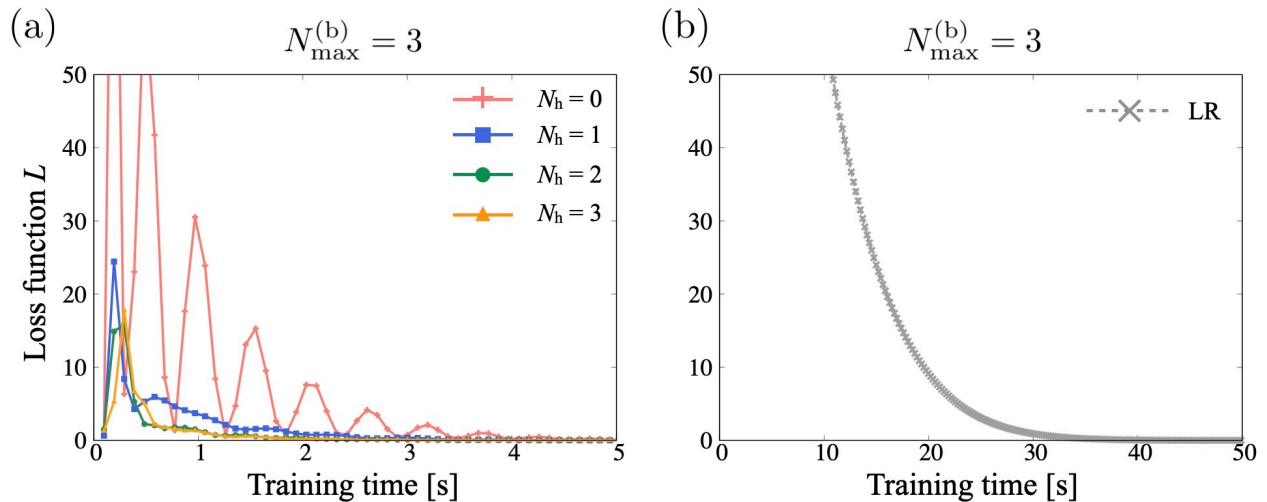


Figure 4.20: Convergence behavior of the loss function for (a) the DNN-SAMB with $N_h = 0$ (red), 1 (blue), 2 (green), and 3 (orange) and (b) the LR method (grey) with $N_{\max}^{(b)} = 3$.

Table 4.17: The optimized model parameters z_j of up to nearest-neighbor hopping in eV units obtained using DNN-SAMB with $N_h = 3$ and $N_{\max}^{(b)} = 3$.

z_1	z_2	z_3	z_4	z_5	z_6	z_7	z_8	z_9	z_{10}
6.573	-0.679	-0.510	-0.299	0.986	-0.225	-2.166	-1.717	-1.932	-0.500
z_{11}	z_{12}	z_{13}	z_{14}	z_{15}	z_{16}	z_{17}	z_{18}	z_{19}	z_{20}
0.460	-1.666	-0.075	0.715	0.683	-0.595	-1.262	0.915	-1.507	1.014
z_{21}	z_{22}	z_{23}	z_{24}	z_{25}	z_{26}	z_{27}	z_{28}		
0.217	-1.937	-0.577	-1.83	0.427	0.450	-2.520	0.839		

of them. Indeed, As shown in Table 4.16, L_{\min} , L_{\max} and L_{avg} of the LR method increase as $N_{\max}^{(b)}$ becomes larger.

Similar to the graphene and SrVO₃ models, L_{\min} , L_{\max} and L_{avg} of the DNN-SAMB method are always smaller than that of the LR method. Therefore, the DNN-SAMB method is more efficient than the LR method and shows less dependence on the initial guess of the optimization parameters.

Next, we show the convergence behavior of the loss function for the LR method and the DNN-SAMB method with $N_{\max}^{(b)} = 3$ in Fig. 4.20. As shown in Fig. 4.20(a), the loss function for the DNN-SAMB method converges rapidly owing to the use of the DNN-SAMB. As N_h increases, the loss function exhibits more rapid convergence behavior. On the other hand, as shown in Fig. 4.20(b), the LR method shows relatively slow convergence behavior. Thus, the DNN-SAMB method can reach convergence faster than the usual LR method.

We summarize the explicit values of the optimized weights for each SAMB up to nearest-neighbor hopping in Table 4.17 obtained by using DNN-SAMB with $N_h = 3$.

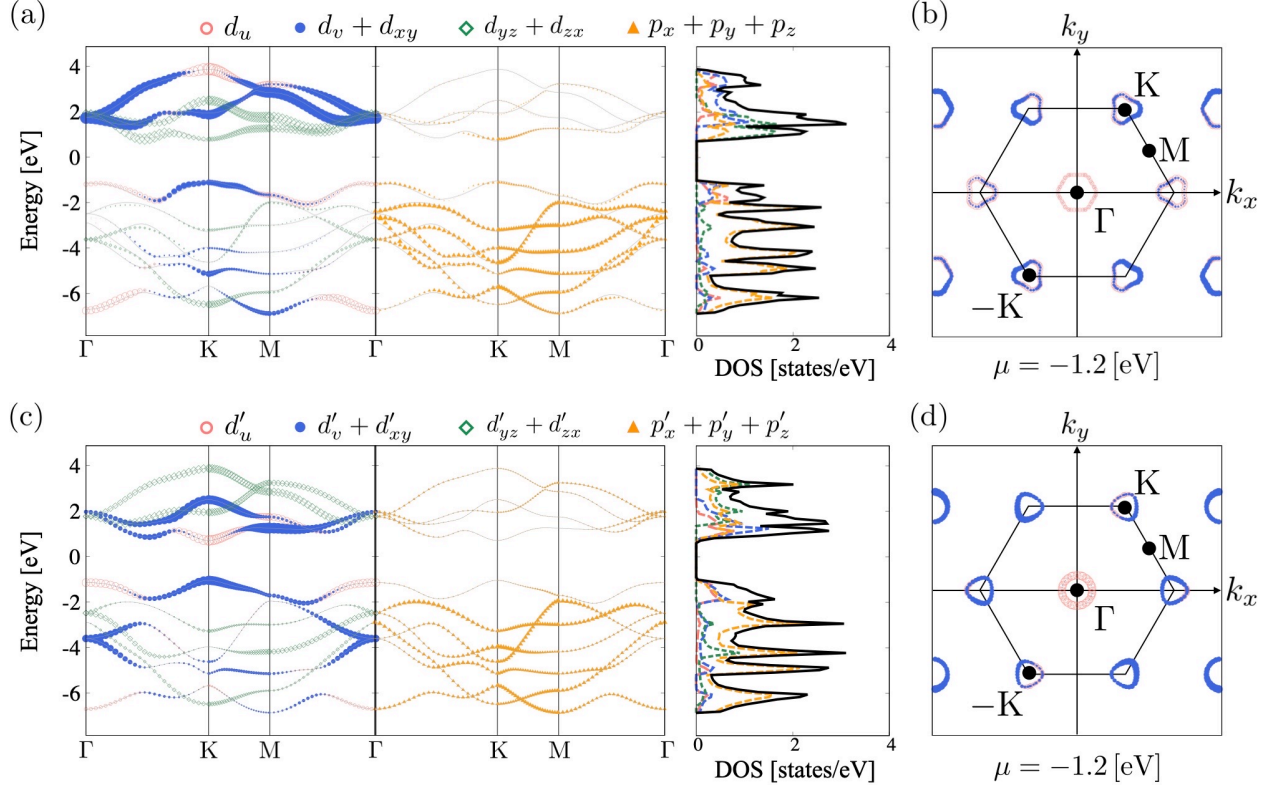


Figure 4.21: The atomic orbital dependence of (a) the band dispersion and DOS, and (b) the isoenergy surfaces at $\mu = -1.2$ [eV] of the optimized TB model with $N_h = 3$ and $N_{\max}^{(b)} = 3$. The MLWF dependence of (c) the band dispersion and DOS, and (d) the isoenergy surfaces at $\mu = -1.2$ [eV] of the Wannier TB model. The MLWFs are shown in Fig. 4.17.

Figure 4.21 (a) and (b) represent the atomic orbital dependence of the band dispersion, DOS, and the isoenergy surfaces, which are calculated by our optimized TB model obtained using the DNN-SAMB with $N_h = 3$ and $N_{\max}^{(b)} = 3$. While Figs. 4.21 (c) and (d) show that obtained from the DFT-based Wannier TB model. Our TB model reproduces the orbital dependence of the electronic states in the valance bands of the Wannier TB model. However, the orbital dependence of the conduction bands of our TB model is not consistent with that of the Wannier TB model. This is because our TB model is optimized to reproduce only the energy eigenvalues of the reference bands, and there is no guarantee to reproduce the orbital dependence of the reference bands. Since the TB model of MoS₂ includes both sublattice and orbital degrees of freedom and is more complicated than the relatively simple SrVO₃ model, it is difficult to reproduce the orbital dependence of the reference bands with high accuracy. This is a limitation of our method at moment, and we will improve a method to reproduce the orbital dependence of the reference bands in the future work.

As shown in Fig. 4.22, the magnitude of the hopping parameters of our TB model decreases for further neighbor hoppings. As a result, our TB model is more compact than the Wannier TB model.

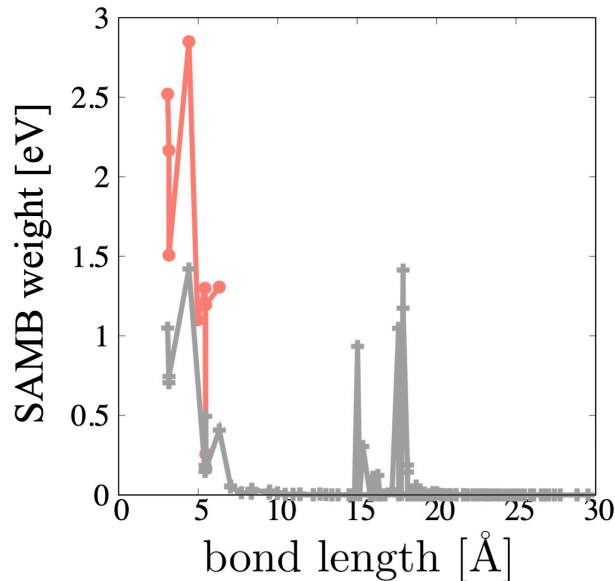


Figure 4.22: Bond length dependence of the absolute maximum value of the hopping parameters ($6 \leq j \leq 74$) in eV units between the Wannier TB model (solid grey lines) and our TB model (dashed red lines) with $N_h = 3$ and $N_{\max}^{(b)} = 3$.

4.5 Summary

In summary, we have developed a systematic generation scheme of the DFT-based symmetry-adapted tight-binding model which is described as the linear combination of the fully symmetric symmetry adapted multipole basis. We can optimize the weights of each multipole basis so as to reproduce the DFT band dispersion. Owing to the use of a deep neural network, the method shows high efficiency and less dependence on the initial guess of the optimization parameters. Since each multipole basis is fully symmetric, the obtained model precisely satisfies the symmetry of a given system with fewer parameters of the Wannier tight-binding model. In addition, our method is applicable to any crystallographic structure within 230 space group.

We have demonstrated our method by constructing the symmetry-adapted tight-binding model for graphene, SrVO_3 , and monolayer MoS_2 . The results indicate that our optimized tight-binding model can well reproduce the DFT or DFT-based Wannier band dispersions. We achieve an accuracy of less than 10^{-4} of the mean squared error between the normalized energy eigenvalues of our tight-binding model and that of the DFT or DFT-based Wannier calculation. Our tight-binding model can also roughly reproduce the orbital dependences of the band dispersion, density of states, and Fermi surfaces. Moreover, our tight-binding model is compact and contains fewer model parameters than the Wannier tight-binding model. In this way, our method is a powerful tool to systematically construct a symmetry-adapted tight-binding model with a small number of parameters, which reproduces the DFT band dispersion with high accuracy.

Lastly, the problems of the present method and their possible solutions are summarized below:

1. When the reference bands are entangled, we need to disentangle them by using the Wannier90
Referring to the disentanglement procedure implemented in Wannier90, we will develop a similar method without the use of Wannier90.
2. Optimization accuracy
In the present method, the input data of eigenvalues obtained from the DFT calculation are

first transformed into a one-dimensional vector and it is connected nonlinearly to every weight of the symmetry-adapted multipole basis. Consequently, the topology of the band structure at each \mathbf{k} point and the correlation between adjacent eigenvalues within and between bands are not considered. Since the band dispersions can be viewed as a 3D images, with the band indices corresponding to the color indices of a picture, using the convolutional neural network (CNN) [153] might be more appropriate choice than the DNN. Indeed, recent studies have discussed some methods using the CNN to systematically predict electronic band structures based on the DFT calculations [176, 177, 177]. Using the CNN instead of the DNN, the present method can be improved to consider the microscopic structures of the DFT band dispersion, and the optimization accuracy might be improved.

3. Orbital dependence is not considered in the optimization process

In the present method, the orbital dependence of the band dispersion is not considered. Therefore, we will develop an optimization method that considers the orbital dependence of the reference band in the future work.

4. Extension to phonon system

Since the present method is based on the symmetry, we can apply this method to phonon systems in a similar manner.

Chapter 5

Microscopic Description of Chirality

We investigate the microscopic origin of chirality, possible electric-field induced static rotational lattice deformation, and rotation-field induced electric polarization. We construct a DFT-based symmetry-adapted TB model for the elemental Te crystal as in the previous section. Based on this microscopic model, we clarify the quantum-mechanical operator expressions of the chirality and their weights numerically. We also elucidate essential couplings among polar and axial vectors with the same time-reversal properties that induce the electric-field induced rotation and its inverse response. Based on these couplings unique to chiral materials, we also propose a possible experimental approach to achieve absolute enantioselection by simultaneously applying electric and rotation fields, or magnetic field and electric current, and so on, as a conjugate field of the chirality. This chapter is based on the contents of Ref. [187] and is organized as follows. In Sec. 5.1, we briefly review recent studies on the origin of chirality and related phenomena. We show the symmetry-adapted TB model for the elemental Te in Sec. 5.2 and show the microscopic origin of the electric field induced static rotational lattice deformation in Sec. 5.4. Then, we discuss a possible experimental approach to achieve absolute enantioselection by simultaneously applying electric and rotation fields in Sec. 5.5. We summarize this chapter in Sec. 5.6.

5.1 Introduction

Chirality is three-dimensional geometric property exhibiting ubiquitously in nature. The definition of chirality was first given by Lord Kelvin in 1884 [188] as “any geometrical figure, or group of points, is chiral, if its image in a plane mirror, ideally realized, cannot be brought to coincide with itself.” In this regard, chiral systems must be three-dimensional because if the system is two-dimensional, rotational symmetry always connects the mirrored object to the original one. Later, Barron has extended the definition of chirality to dynamics of materials by using the term truly/falsey chirality which denote the chirality associated with \mathcal{T} -even/ \mathcal{T} -odd properties. In the present study, we focus on the \mathcal{T} -even (truly) chirality, $(\mathcal{P}, \mathcal{T}) = (-, +)$. Handedness or enantiomer in chiral materials, which is a static quantity, is characterized by a \mathcal{T} -even pseudoscalar quantity [189–192], whose sign corresponds to left or right handedness. This significant quantity in chiral materials has not fully been understood at microscopic level.

However, recent studies elucidated that the ET monopole G_0 corresponds to the order parameter for chirality [26, 64] based on the electronic multipole theory [25, 26, 28]. G_0 has the same symmetry properties as the \mathcal{T} -even pseudoscalar, $(\mathcal{P}, \mathcal{T}) = (-1, +1)$, which is consistent with the Barron’s definition of the \mathcal{T} -even chirality. G_0 belongs to the fully symmetric irreducible representation (IR) and becomes active only in the 11 chiral point groups, O, T, D_4 , C_4 , D_2 , C_2 , D_6 , C_6 , D_3 , C_3 , C_1 [26].

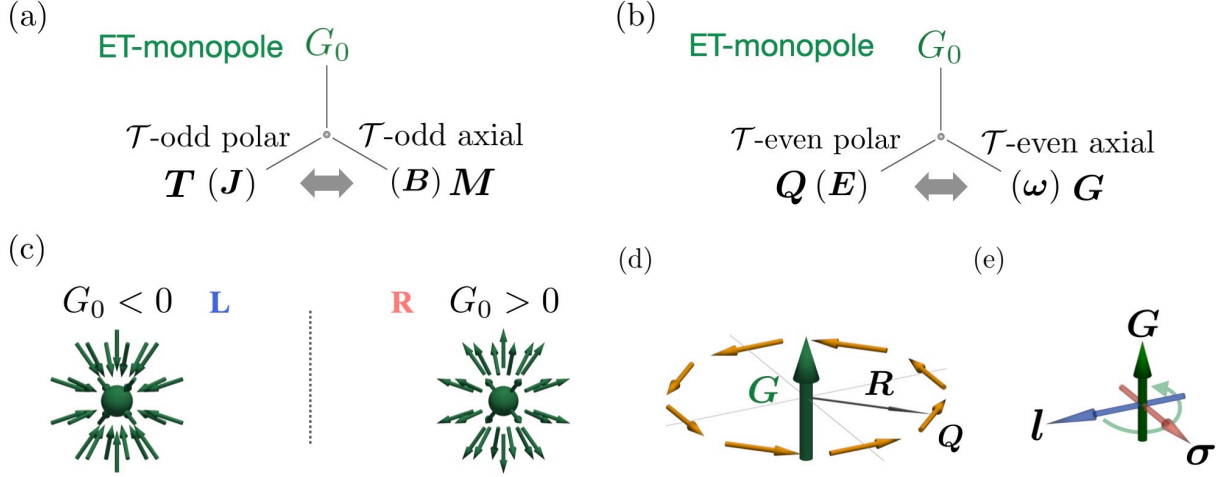


Figure 5.1: (a), (b) G_0 related essential couplings existing in chiral crystals. The conjugate fields of \mathbf{T} , \mathbf{M} , \mathbf{Q} , and \mathbf{G} , are given in the parenthesis. (c) ET monopole G_0 in terms of the flux structure of the ET dipoles \mathbf{G} , whose direction determines the handedness of the chirality. (d) Classical view of the ET dipole, which is a vortex-like alignment of the E dipoles, \mathbf{Q} . (e) The atomic ET dipole, which is an outer product of the orbital angular momentum \mathbf{l} and the spin angular momentum $\boldsymbol{\sigma}$.

Since the scalar products of polar and axial vectors with the same \mathcal{T} property belong to the same IR of G_0 , G_0 can couple with them in the sense of Landau free energy. For example, G_0 can couple with the scalar product of a MT dipole \mathbf{T} , $(\mathcal{P}, \mathcal{T}) = (-, -)$, and M dipole \mathbf{M} , $(\mathcal{P}, \mathcal{T}) = (+, -)$:

$$g G_0(\mathbf{T} \cdot \mathbf{M}) \quad (5.1.1)$$

where g is a coupling constant. Figure 5.1(a) schematically represents this coupling. As an electric current \mathbf{J} induces its conjugate quantity \mathbf{T} , it also induces \mathbf{M} through Eq. (5.1.1) in a chiral system with active G_0 . Indeed, the current-induced optical activity [193] and the kinetic magneto-electric (Edelstein) effect [54,55] were proposed and observed in elemental Te crystal [56–58]. On the contrary, the magnetic field \mathbf{B} induces not only \mathbf{M} but also \mathbf{T} through Eq. (5.1.1). Similarly, the Hamiltonian of chiral systems contains the \mathbf{k} -space representation of G_0 [26], *i.e.*, $\mathbf{k} \cdot \boldsymbol{\sigma}$, which is the origin of the hedgehog spin texture observed around the H point of the Brillouin zone in Te [194,195]. Meanwhile, from the microscopic point of view, the atomic ET monopole can be active in the spinful hybrid orbital space as the form $G_0^{(a)} = \mathbf{t} \cdot \boldsymbol{\sigma}$ ($\mathbf{t} = \mathbf{r} \times \mathbf{l}$ is the atomic MT dipole) (See Table 3.3).

As shown in Fig. 5.1(b), an ET monopole G_0 can couple with in another way:

$$g' G_0(\mathbf{Q} \cdot \mathbf{G}) \quad (5.1.2)$$

where \mathbf{Q} is an E dipole, $(\mathcal{P}, \mathcal{T}) = (-, +)$, and \mathbf{G} is an ET dipole $\mathbf{G} (\mathcal{P}, \mathcal{T}) = (+, +)$. Since a position vector \mathbf{R} has the same symmetry property of \mathbf{Q} , \mathbf{G} -flux structure, $\mathbf{R} \cdot \mathbf{G}$, exists in chiral crystals as shown in Fig. 5.1(c), where the direction of the fluxes characterizes the handedness. As shown in Fig. 5.1(d), a classical representation of \mathbf{G} is given by a vortex-like alignment of E dipoles \mathbf{Q} , $\mathbf{G}^{(c)} = \sum_j \mathbf{R}_j \times \mathbf{Q}_j$, where \mathbf{Q}_j denotes the E dipole at the position \mathbf{R}_j . $\mathbf{G}^{(c)}$ solely plays a role of the order parameter of the ferro-axial (rotational) orderings which have been observed in several materials, such as $\text{RbFe}(\text{MoO}_4)_2$ [34–39], NiTiO_3 [40–42], $\text{Ca}_5\text{Ir}_3\text{O}_{12}$ [39], superlattices of $\text{PbTiO}_3/\text{SrTiO}_3$ [43], and so on. Note that the rotational orderings are closely related to chirality through Eq. (5.1.2). Indeed, the spontaneous ferro-chiral structural transition observed in $\text{Ba}(\text{TiO})\text{Cu}_4(\text{PO}_4)_4$ [45], is realized by the emergence of the antiferroaxial ordering of the anti-polar units, which can be characterized by

finite G_0 .

Since $\mathbf{G}^{(c)}$ is given by a vortex-like alignment of E dipoles \mathbf{Q} as shown in Fig. 5.1(d), its conjugate field is a rotation of electric field, $\boldsymbol{\omega}_E = \nabla \times \mathbf{E}$, which is equivalent to time-dependent magnetic field through Maxwell's equation. Moreover, from the symmetry property of \mathbf{G} , a static lattice rotation $\boldsymbol{\omega} = \nabla \times \mathbf{u}$ (\mathbf{u} is a displacement vector of atoms) could be an alternative conjugate field to \mathbf{G} , provided a proper electron-lattice coupling. In this way, \mathbf{G} plays a significant role in the transverse rotational phonon modes discussed in both achiral [196–198] and chiral crystals [63, 199, 200]. In addition, the atomic ET dipole is defined as $\mathbf{G}^{(a)} = \mathbf{l} \times \boldsymbol{\sigma}$ as shown in Fig. 5.1(e), and then the Hamiltonian of chiral systems contain a lattice-spin-orbit coupling, $\mathbf{R} \cdot (\mathbf{l} \times \boldsymbol{\sigma})$, which induce the $\mathbf{G}^{(a)}$ -flux structure. Namely the atomic ET monopole is transformed as $G_0^{(a)} = \mathbf{t} \cdot \boldsymbol{\sigma} = (\mathbf{r} \times \mathbf{l}) \cdot \boldsymbol{\sigma} = \mathbf{r} \cdot (\mathbf{l} \times \boldsymbol{\sigma}) = \mathbf{r} \cdot \mathbf{G}^{(a)}$ that corresponds to the atomic scale $\mathbf{G}^{(a)}$ -flux structure.

As discussed above, there are G_0 -related third-order couplings in the free energy of chiral systems as shown in Figs. 5.1(a) and (b):

$$F_c^{(3)} = g_{\perp}^{(E)} G_0^{(1)} (Q_x G_x + Q_y G_y) + g_z^{(E)} G_0^{(2)} Q_z G_z + g_{\perp}^{(M)} G_0^{(3)} (T_x M_x + T_y M_y) + g_z^{(M)} G_0^{(4)} T_z M_z \quad (5.1.3)$$

The coupling constants satisfy $g_z^{(E/M)} = g_{\perp}^{(E/M)}$ in cubic chiral crystals belonging to O/T point group symmetries, otherwise $g_z \neq g_{\perp}$ (z is along the screw axis). Note that $G_0^{(1)}$, $G_0^{(2)}$, $G_0^{(3)}$, and $G_0^{(4)}$ can be independent ET monopoles in general. In this study, we focus on the couplings among G_0 , \mathbf{Q} , and \mathbf{G} . This coupling gives rise to a interconversion between a polar vector field such as the electric field or temperature gradient and an axial vector field such as a static rotation of the lattice. In other words, an electric-field induced rotation (EIR) and its inverse response, i.e., a rotation-field induced electric polarization (RIP), could appear in chiral materials. Note that one can apply a rotational lattice deformation using transverse ultrasonic wave as it generates both the strain and rotation fields. Although the RIP (called rotoelectricity there) was already predicted by Gopalan and Litvin based on the symmetry argument [201], its origin and the connection to the chirality remain unclear at the microscopic level. It should be also emphasized that the present EIR (static rotational deformation) is qualitatively different from a heat-current/electric-field induced phonon angular momentum, i.e., *dynamical* (\mathcal{T} -odd) lattice rotation, predicted by Hamada *et al.* [59, 60].

As shown above, the order parameter of chirality is the ET monopole G_0 in general. However, the explicit quantum treatment of G_0 , depending on the Hilbert space of the given chiral materials, has yet to be developed. With this circumstance, we develop a systematic prescription for clarifying the quantum-mechanical operator of G_0 and to evaluate it quantitatively. In the following sections, we take Te as a specific example and clarify the quantum-mechanical operators of G_0 in Te and their weights in the Hamiltonian. First, we construct a DFT-based symmetry-adapted TB model of Te using the band dispersion data obtained from the DFT calculation. Since the TB model is expressed as the linear combination of the SAMB, we can easily identify the quantum-mechanical operator of G_0 , and evaluate the relevant couplings to it quantitatively. Then, we elucidate the microscopic origin of the G_0 related responses, EIR and RIP. We also propose a possible experimental approach to achieve absolute enantioselection by utilizing the G_0 related couplings given in Eq. (5.1.3).

5.2 Tight-Binding Model for Te

Let us first construct the symmetry-adapted TB model for Te based on the generation scheme given in Chap. 4.

5.2.1 DFT Calculation for Te

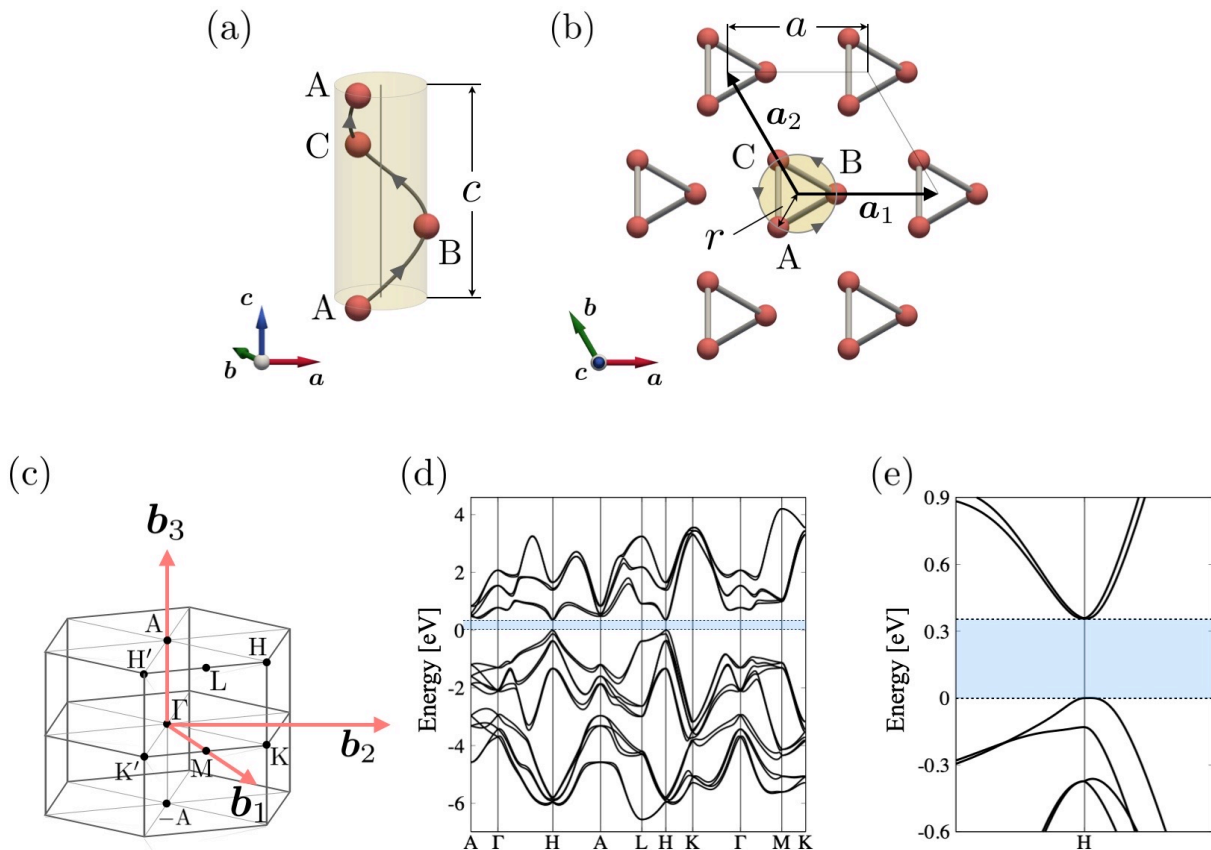


Figure 5.2: (a) Crystal structure of the right-handed Te. (b) A unit cell contains A, B, and C sublattices along a helical chain. (c) First Brillouin zone of Te. (d) The band dispersion of the Wannier TB model where the Fermi energy is taken as the origin and the blue shaded area represents the insulating gap. (e) The enlarged view of the band dispersion close to the Fermi level.

As shown in Fig. 5.2(a), the bulk Te crystal consists of the threefold-symmetric helical chains, which contain A, B, and C sublattices in a unit cell as shown in Fig. 5.2(b). The space group of the right- and left-handed Te are $P3_121$ (#152, D_3^4) and $P3_221$ (#154, D_3^6), respectively. Hereafter, we focus on the right-handed Te. The lattice constants are $a = 4.458 \text{ \AA}$, $c = 5.925 \text{ \AA}$, and relaxed value is $u = r/a = 0.274$ for the dimensionless helix parameter [202], where r denotes the radius of the helix. Since the bands near the Fermi level are entangled to the upper bands, we optimize our TB model so as to reproduce the Wannier TB model of Te. Figure 5.2(d) shows the band dispersion of the Wannier TB model of Te obtained by the fully relativistic DFT calculation using the HSE06 hybrid functional [203]. Although the energy gap at the H point is 0.356 eV in Fig. 5.2(e), several values of the energy gap were reported as the experimental value of 0.323 eV [204], the GW method of 0.314 eV [205], and the other fully relativistic calculations of 0.312 eV [206] and 0.322 eV [207]. Since the electronic states near the band edges (Fermi level) in Te mainly consist of three p orbitals, (p_x, p_y, p_z) [207], we consider the spinful TB Hamiltonian in 18×18 matrix.

5.2.2 Symmetry-Adapted TB Hamiltonian for Te

Let us consider the TB Hamiltonian given by

$$\mathcal{H}_0 = \mathcal{H}_{\text{CEF}} + \mathcal{H}_{\text{SOC}} + \sum_{n=1}^8 \mathcal{H}_t^{(n)} \quad (5.2.1)$$

where \mathcal{H}_{CEF} and \mathcal{H}_{SOC} represent the crystalline electric field (CEF) and spin-orbit coupling (SOC) within the unit cell, and $\mathcal{H}_t^{(n)}$ is the n -th neighbor hopping term. In this section, we express \mathcal{H}_{CEF} , \mathcal{H}_{SOC} , and the nearest-neighbor (NN) hopping $\mathcal{H}_t^{(1)}$ in terms of the SAMB according to the procedure given in Chap. 4. First, we introduce the atomic and site/bond-cluster multipole basis. Afterward, we generate the SAMB as a direct product of them.

Atomic Multipole Basis

Let us first introduce the atomic multipole basis within the Hilbert space of spinful p orbitals. There are 9 (27) independent spinless (spinful) E, M, ET, and MT atomic multipole basis. The explicit operator expressions and matrix elements of these basis are summarized in Table 5.1.

Table 5.1: Operator expressions and matrix elements of the atomic multipole basis defined in the spinful p_x, p_y, p_z orbitals in the point group D_3 . E, M, ET, and MT stand for electric, magnetic, electric toroidal, and magnetic toroidal, respectively. The superscript (a) denotes the atomic multipole. l and $\sigma/2$ represent the dimensionless orbital and spin angular-momentum operators, and σ_i ($i = x, y, z$) and σ_0 are the Pauli matrices and 2×2 identity matrix. The upper and lower parts separated by double line represent the spinless and spinful multipoles, respectively. The prime in the upper script represents the spinful multipole.

rank	type	irrep.	symbol	expression	matrix element
0	E	A_1^+	$Q_0^{(a)}$	1	$\frac{1}{\sqrt{6}} \begin{pmatrix} 1 & 0 & 0 \\ 0 & 1 & 0 \\ 0 & 0 & 1 \end{pmatrix} \sigma_0$
1	M	A_2^-	$M_z^{(a)}$	l_z	$\frac{1}{2} \begin{pmatrix} 0 & -i & 0 \\ i & 0 & 0 \\ 0 & 0 & 0 \end{pmatrix} \sigma_0$
		E^-	$M_x^{(a)}, M_y^{(a)}$	l_x, l_y	$\frac{1}{2} \begin{pmatrix} 0 & 0 & 0 \\ 0 & 0 & -i \\ 0 & i & 0 \end{pmatrix} \sigma_0, \quad \frac{1}{2} \begin{pmatrix} 0 & 0 & i \\ 0 & 0 & 0 \\ -i & 0 & 0 \end{pmatrix} \sigma_0$
2	E	A_1^+	$Q_u^{(a)}$	$3z^2 - r^2$	$\frac{1}{2\sqrt{3}} \begin{pmatrix} -1 & 0 & 0 \\ 0 & -1 & 0 \\ 0 & 0 & 2 \end{pmatrix} \sigma_0$
		E^+	$Q_{zx}^{(a)}, Q_{yz}^{(a)}$	zx, yz	$\frac{1}{2} \begin{pmatrix} 0 & 0 & 1 \\ 0 & 0 & 0 \\ 1 & 0 & 0 \end{pmatrix} \sigma_0, \quad \frac{1}{2} \begin{pmatrix} 0 & 0 & 0 \\ 0 & 0 & 1 \\ 0 & 1 & 0 \end{pmatrix} \sigma_0$
		E^+	$Q_v^{(a)}, Q_{xy}^{(a)}$	$x^2 - y^2, xy$	$\frac{1}{2} \begin{pmatrix} 1 & 0 & 0 \\ 0 & -1 & 0 \\ 0 & 0 & 0 \end{pmatrix} \sigma_0, \quad \frac{1}{2} \begin{pmatrix} 0 & 1 & 0 \\ 1 & 0 & 0 \\ 0 & 0 & 0 \end{pmatrix} \sigma_0$
0	E	A_1^+	$Q_0^{(a)'}$	—	$\frac{1}{\sqrt{3}} \mathbf{M}^{(a)} \cdot \boldsymbol{\sigma}$
1	M	A_2^-	$M_z^{(a)'} [1]$	—	$Q_0^{(a)} \sigma_z$
		E^-	$M_x^{(a)'} [1], M_y^{(a)'} [1]$	—	$Q_0^{(a)} \sigma_x, \quad Q_0^{(a)} \sigma_y$
		A_2^-	$M_z^{(a)'} [2]$	—	$\frac{1}{\sqrt{10}} [2Q_u^{(a)} \sigma_z + \sqrt{3} (Q_{yz}^{(a)} \sigma_y + Q_{zx}^{(a)} \sigma_x)]$
		E^-	$M_x^{(a)'} [2]$	—	$\frac{1}{\sqrt{10}} [(\sqrt{3}Q_v^{(a)} - Q_u^{(a)}) \sigma_x + \sqrt{3} (Q_{xy}^{(a)} \sigma_y + Q_{zx}^{(a)} \sigma_z)]$
			$M_y^{(a)'} [2]$	—	$-\frac{1}{\sqrt{10}} [(\sqrt{3}Q_v^{(a)} + Q_u^{(a)}) \sigma_y + \sqrt{3} (Q_{yz}^{(a)} \sigma_z + Q_{xy}^{(a)} \sigma_x)]$
	ET	A_2^+	$G_z^{(a)'}$	—	$\frac{1}{\sqrt{2}} (\mathbf{M}^{(a)} \times \boldsymbol{\sigma})_z$
		E^+	$G_x^{(a)'}, G_y^{(a)'}$	—	$\frac{1}{\sqrt{2}} (\mathbf{M}^{(a)} \times \boldsymbol{\sigma})_x, \quad \frac{1}{\sqrt{2}} (\mathbf{M}^{(a)} \times \boldsymbol{\sigma})_y$
2	E	A_1^+	$Q_u^{(a)'}$	—	$\frac{1}{\sqrt{6}} (3M_z^{(a)} \sigma_z - \mathbf{M}^{(a)} \cdot \boldsymbol{\sigma})$
		E^+	$Q_{zx}^{(a)'}, Q_{yz}^{(a)'}$	—	$\frac{1}{\sqrt{2}} (M_x^{(a)} \sigma_z + M_z^{(a)} \sigma_x), \quad \frac{1}{\sqrt{2}} (M_z^{(a)} \sigma_y + M_y^{(a)} \sigma_z)$
		E^+	$Q_v^{(a)'}, Q_{xy}^{(a)'}$	—	$\frac{1}{\sqrt{2}} (M_x^{(a)} \sigma_x - M_y^{(a)} \sigma_y), \quad \frac{1}{\sqrt{2}} (M_x^{(a)} \sigma_y + M_y^{(a)} \sigma_x)$
	MT	A_1^-	$T_u^{(a)'}$	—	$\frac{1}{\sqrt{2}} (Q_{yz}^{(a)} \sigma_x - Q_{zx}^{(a)} \sigma_y)$
		E^-	$T_{zx}^{(a)'}$	—	$\frac{1}{\sqrt{6}} [(\sqrt{3}Q_u^{(a)} - Q_v^{(a)}) \sigma_y - Q_{yz}^{(a)} \sigma_z + Q_{xy}^{(a)} \sigma_x]$
			$T_{yz}^{(a)'}$	—	$-\frac{1}{\sqrt{6}} [(\sqrt{3}Q_u^{(a)} + Q_v^{(a)}) \sigma_x + Q_{xy}^{(a)} \sigma_y - Q_{zx}^{(a)} \sigma_z]$
		E^-	$T_v^{(a)'}$	—	$\frac{1}{\sqrt{6}} (Q_{yz}^{(a)} \sigma_x + Q_{zx}^{(a)} \sigma_y - 2Q_{xy}^{(a)} \sigma_z)$
			$T_{xy}^{(a)'}$	—	$\frac{1}{\sqrt{6}} (-Q_{zx}^{(a)} \sigma_x + Q_{yz}^{(a)} \sigma_y + 2Q_v^{(a)} \sigma_z)$
3	M	A_1^-	$M_{3\gamma}^{(a)'}$	—	$\frac{1}{\sqrt{2}} (Q_v^{(a)} \sigma_x - Q_{xy}^{(a)} \sigma_y)$
		A_2^-	$M_{3\alpha}^{(a)'}$	—	$\frac{1}{\sqrt{5}} (\sqrt{3}Q_u^{(a)} \sigma_z - Q_{zx}^{(a)} \sigma_x - Q_{yz}^{(a)} \sigma_y)$
		A_2^-	$M_{3\beta}^{(a)'}$	—	$\frac{1}{\sqrt{2}} (Q_{xy}^{(a)} \sigma_x + Q_v^{(a)} \sigma_y)$
		E^-	$M_{3\alpha\alpha}^{(a)'}$	—	$\frac{1}{\sqrt{30}} [(2\sqrt{3}Q_u^{(a)} - Q_v^{(a)}) \sigma_x - Q_{xy}^{(a)} \sigma_y + 4Q_{zx}^{(a)} \sigma_z]$
			$M_{3\gamma\alpha}^{(a)'}$	—	$-\frac{1}{\sqrt{30}} [(2\sqrt{3}Q_u^{(a)} + Q_v^{(a)}) \sigma_y - Q_{xy}^{(a)} \sigma_x + 4Q_{yz}^{(a)} \sigma_z]$
		E^-	$M_{3\alpha\beta}^{(a)'}$	—	$\frac{1}{\sqrt{3}} (Q_v^{(a)} \sigma_z + Q_{zx}^{(a)} \sigma_x - Q_{yz}^{(a)} \sigma_y)$
			$M_{3\gamma\beta}^{(a)'}$	—	$-\frac{1}{\sqrt{3}} (Q_{xy}^{(a)} \sigma_z + Q_{yz}^{(a)} \sigma_x + Q_{zx}^{(a)} \sigma_y)$

Site/Bond-Cluster Multipole Basis

To describe \mathcal{H}_{CEF} and \mathcal{H}_{SOC} , and $\mathcal{H}_t^{(1)}$, we introduce the site/bond-cluster multipole basis defined in the ABC sublattice space. Here, we restrict our demonstration up to the NN hoppings.

There are three independent site-cluster multipole basis:

$$Q_0^{(s)} = \frac{1}{\sqrt{3}}(1, 1, 1), \quad Q_x^{(s)} = \frac{1}{\sqrt{6}}(-1, 2, -1), \quad Q_y^{(s)} = \frac{1}{\sqrt{2}}(-1, 0, 1) \quad (5.2.2)$$

While there six bond-cluster multipole basis:

$$Q_0^{(b)} = \frac{1}{\sqrt{6}}(1, 1, 1; 1, 1, 1) \\ Q_x^{(b)} = \frac{1}{2\sqrt{3}}(1, 1, -2; 1, 1, -2) \quad (5.2.3)$$

$$Q_y^{(b)} = \frac{1}{2}(-1, 1, 0; -1, 1, 0) \\ T_z^{(b)} = \frac{1}{\sqrt{6}}(i, -i, -i; -i, i, i) \\ T_x^{(b)} = \frac{1}{2}(i, i, 0; -i, -i, 0) \quad (5.2.4) \\ T_y^{(b)} = \frac{1}{2\sqrt{3}}(i, -i, 2i; -i, i, -2i)$$

The elements correspond to the bond vectors described by $\mathbf{b}@\mathbf{c}$:

$$\mathbf{b}_1@\mathbf{c}_1 = [2u, u, 1/3]@[0, 1 - u/2, 1/6] \\ \mathbf{b}_2@\mathbf{c}_2 = [u, -u, -1/3]@[u/2, u/2, 1/2] \quad (5.2.5) \\ \mathbf{b}_3@\mathbf{c}_3 = [u, 2u, -1/3]@[1 - u/2, 0, 5/6]$$

The schematic figures of the site/bond-cluster multipole basis are shown in Fig. 5.3.

The matrix form of the site/bond-cluster multipoles are summarized in Table 5.2.

SAMB and Symmetry-Adapted TB Hamiltonian for Te

Using the atomic and site/bond-cluster multipole basis, the SAMB is defined by the direct product of them. We show the SAMB belonging to A_1 identity irreducible representation of D_3^4 because the Hamiltonian must be fully-symmetric. Considering the irreducible decompositions,

$$A_1 \otimes A_1 = A_2 \otimes A_2 = A_1 \quad (5.2.6)$$

$$A_1 \otimes A_2 = A_2 \quad (5.2.7)$$

$$E \otimes E = A_1 \oplus A_2 \oplus E \quad (5.2.8)$$

$$A_1 \otimes E = A_2 \otimes E = E \quad (5.2.9)$$

we obtain the SAMB as summarized in Table 5.3. In addition, some SAMB belonging to A_2 and E irreducible representations are given, i.e., the E and ET dipoles, $Q_z^{(\text{as})'}$ and $G_z^{(\text{as})'}$ shown in Table 5.3.

Using the SAMB Z_j given in Sec. 5.2.2, the symmetry-adapted TB Hamiltonian of Te is constructed as

$$\mathcal{H}_0 = \sum_j z_j Z_j. \quad (5.2.10)$$

\mathcal{H}_{CEF} in Eq. (5.2.1) is expressed by using the four spinless (as) SAMB given in Sec. 5.2.2:

$$\mathcal{H}_{\text{CEF}} = \Delta_0^Q Q_0^{(\text{as})} + \Delta_1^Q Q_u^{(\text{as})} + \Delta_2^Q Q_{3\gamma}^{(\text{as})} + \Delta_1^G G_u^{(\text{as})}. \quad (5.2.11)$$

The atomic SOC \mathcal{H}_{SOC} is represented by using the five spinful (as) SAMB given in Sec. 5.2.2:

$$\mathcal{H}_{\text{SOC}} = \lambda_1^Q Q_0^{(\text{as})'} + \lambda_2^Q Q_u^{(\text{as})'} + \lambda_3^Q Q_{3\gamma}^{(\text{as})'} + \lambda_1^G G_{0\perp}^{(\text{as})'} + \lambda_2^G G_u^{(\text{as})'}. \quad (5.2.12)$$

Similarly, the NN hopping $\mathcal{H}_t^{(1)}$ is expressed as the linear combination of the six spinless and fifteen

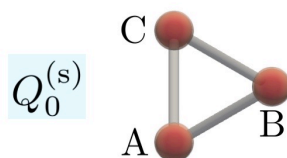
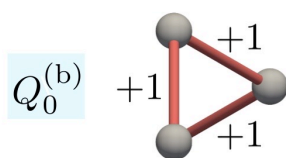
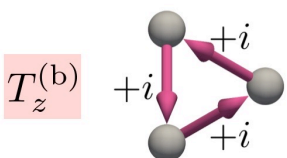
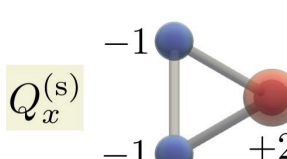
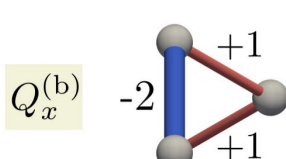
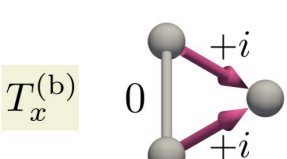
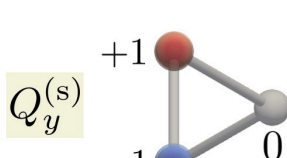
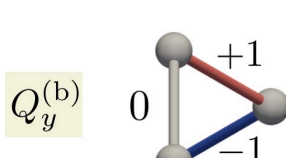
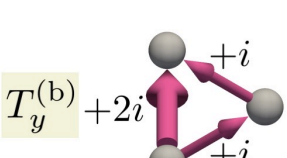
site-cluster	bond-cluster (Re)	bond-cluster (Im)
 $Q_0^{(\text{s})}$	 $Q_0^{(\text{b})}$	 $T_z^{(\text{b})}$
 $Q_x^{(\text{s})}$	 $Q_x^{(\text{b})}$	 $T_x^{(\text{b})}$
 $Q_y^{(\text{s})}$	 $Q_y^{(\text{b})}$	 $T_y^{(\text{b})}$

Figure 5.3: Schematic figures of cluster and bond multipoles. The blue, red, and green square cells denote that its irreducible representation is A_1 , A_2 , and E , respectively. The red and blue circles in the “site-cluster” column represent the weight and sign of the diagonal elements. The red and blue lines in the “bond-cluster (Re)” column represent the weight and sign of the real part of the off-diagonal elements. Similarly, the arrows in the “bond-cluster (Im)” column represent the weight and sign of the imaginary part of the off-diagonal elements. The gray lines represent zero values.

Table 5.2: Matrix elements of the site/bond-cluster multipole basis defined in the ABC sublattice space in the point group D_3 . E (MT) stands for electric (magnetic toroidal). The upper and lower parts separated by double line represent the cluster and bond multipoles.

rank	type	irrep.	symbol	matrix element
0	E	A_1^+	$Q_0^{(t,1)}$	$\frac{1}{\sqrt{3}} \begin{pmatrix} 1 & 0 & 0 \\ 0 & 1 & 0 \\ 0 & 0 & 1 \end{pmatrix}$
1	E	E^+	$Q_x^{(t,1)}, Q_y^{(t,1)}$	$\frac{1}{\sqrt{6}} \begin{pmatrix} -1 & 0 & 0 \\ 0 & 2 & 0 \\ 0 & 0 & -1 \end{pmatrix}, \frac{1}{\sqrt{2}} \begin{pmatrix} -1 & 0 & 0 \\ 0 & 0 & 0 \\ 0 & 0 & 1 \end{pmatrix}$
0	E	A_1^+	$Q_0^{(t,2)}$	$\frac{1}{\sqrt{6}} \begin{pmatrix} 0 & 1 & 1 \\ 1 & 0 & 1 \\ 1 & 1 & 0 \end{pmatrix}$
1	E	E^+	$Q_x^{(t,2)}, Q_y^{(t,2)}$	$\frac{1}{2\sqrt{3}} \begin{pmatrix} 0 & 1 & -2 \\ 1 & 0 & 1 \\ -2 & 1 & 0 \end{pmatrix}, \frac{1}{2} \begin{pmatrix} 0 & -1 & 0 \\ -1 & 0 & 1 \\ 0 & 1 & 0 \end{pmatrix}$
	MT	A_2^-	$T_z^{(t)}$	$\frac{1}{\sqrt{6}} \begin{pmatrix} 0 & -i & i \\ i & 0 & -i \\ -i & i & 0 \end{pmatrix}$
	E ⁻	E^-	$T_x^{(t)}, T_y^{(t)}$	$\frac{1}{2} \begin{pmatrix} 0 & -i & 0 \\ i & 0 & i \\ 0 & -i & 0 \end{pmatrix}, \frac{1}{2\sqrt{3}} \begin{pmatrix} 0 & -i & -2i \\ i & 0 & -i \\ 2i & i & 0 \end{pmatrix}$

spinful (ab) SAMB given in Sec. 5.2.2:

$$\begin{aligned}
\mathcal{H}_t^{(1)} = & t_1^Q Q_0^{(ab)} + t_2^Q Q_u^{(ab)} + t_3^Q Q_{3\gamma}^{(ab)} + t_1^G G_{0z}^{(ab)} + t_2^G G_{0\perp}^{(ab)} + t_3^G G_u^{(ab)} \\
& + \alpha_1^Q Q_0^{(ab)'} + \alpha_2^Q Q_u^{(ab)'} + \alpha_3^Q Q_{3\gamma}^{(ab)'} [1] + \alpha_4^Q Q_{3\gamma}^{(ab)'} [2] + \alpha_5^Q Q_{3\gamma}^{(ab)'} [3] + \alpha_6^Q Q_{3\gamma}^{(ab)'} [4] + \alpha_7^Q Q_{3\gamma}^{(ab)'} [5] \\
& + \alpha_1^G G_{0\perp}^{(ab)'} [1] + \alpha_2^G G_{0z}^{(ab)'} [1] + \alpha_3^G G_{0\perp}^{(ab)'} [2] + \alpha_4^G G_{0z}^{(ab)'} [2] + \alpha_5^G G_{0\perp}^{(ab)'} [3] + \alpha_6^G G_u^{(ab)'} [1] + \alpha_7^G G_u^{(ab)'} [2] \\
& + \alpha_8^G G_u^{(ab)'} [3].
\end{aligned} \tag{5.2.13}$$

Note that the higher-order terms $\mathcal{H}_t^{(i)}$ ($1 < i \leq 8$) are derived by the similar procedure. There are 255 independent parameters z_j in total, and 30 parameters are within the NN hopping; four CEF parameters, five SOC parameters, and twenty one NN intra-chain hopping parameters. Then, the weights z_j ($\Delta_i^Q, \lambda_i^Q, t_i^Q, \alpha_i^Q, \dots$ etc.) are determined so as to reproduce the DFT-based Wannier band dispersion based on the method shown in Chap. 4. In this model construction, terms containing G_0 are significant, since they characterize the chirality of Te.

The G_0 terms in Eq. (5.2.13) represent the chirality in the quantum-mechanical level, and their weights correspond to the ‘‘chiralization’’. Therefore, in the next section, we evaluate the weights of them by optimizing the TB model so as to reproduce the DFT-based Wannier band dispersion of Te.

Table 5.3: The explicit expressions of the SAMB. E and ET stand for electric and electric toroidal, respectively. The superscript (as) ((ab)) denotes the direct product of the cluster and atomic (bond and atomic) multipoles. The first, second, third, and fourth parts separated by double line represent the spinless (as), spinful (as), spinless (ab), and spinful (ab) multipoles. The number in the square bracket is the multiplicity to distinguish the independent multipoles.

rank	type	irrep.	symbol	expression
0	E	A_1^+	$Q_0^{(as)}$	$Q_0^{(a)} \otimes Q_0^{(s)}$
2	E	A_1^+	$Q_u^{(as)}$	$Q_u^{(a)} \otimes Q_0^{(s)}$
	ET	A_1^+	$G_u^{(as)}$	$\frac{1}{\sqrt{2}} \left(Q_{yz}^{(a)} \otimes Q_x^{(s)} - Q_{zx}^{(a)} \otimes Q_y^{(s)} \right)$
3	E	A_1^+	$Q_{3\gamma}^{(as)}$	$\frac{1}{\sqrt{2}} \left(Q_v^{(a)} \otimes Q_x^{(s)} - Q_{xy}^{(a)} \otimes Q_y^{(s)} \right)$
0	E	A_1^+	$Q_0^{(as)'} $	$Q_0^{(a)'} \otimes Q_0^{(s)}$
	ET	A_1^+	$G_{0\perp}^{(as)'}$	$\frac{1}{\sqrt{2}} \left(G_x^{(a)'} \otimes Q_x^{(s)} + G_y^{(a)'} \otimes Q_y^{(s)} \right)$
1	E	A_2^+	$Q_z^{(as)'}$	$\frac{1}{\sqrt{2}} \left(G_y^{(a)'} \otimes Q_x^{(s)} - G_x^{(a)'} \otimes Q_y^{(s)} \right)$
	ET	A_2^+	$G_z^{(as)'}$	$G_z^{(a)'} \otimes Q_0^{(s)}$
2	E	A_1^+	$Q_u^{(as)'}$	$Q_u^{(a)'} \otimes Q_0^{(s)}$
	ET	A_1^+	$G_u^{(as)'}$	$\frac{1}{\sqrt{2}} \left(Q_{yz}^{(a)'} \otimes Q_x^{(s)} - Q_{zx}^{(a)'} \otimes Q_y^{(s)} \right)$
3	E	A_1^+	$Q_{3\gamma}^{(as)'}$	$\frac{1}{\sqrt{2}} \left(Q_v^{(a)'} \otimes Q_x^{(s)} - Q_{xy}^{(a)'} \otimes Q_y^{(s)} \right)$
0	E	A_1^+	$Q_0^{(ab)}$	$Q_0^{(a)} \otimes Q_0^{(b)}$
	ET	A_1^+	$G_{0z}^{(ab)}$	$M_z^{(a)} \otimes T_z^{(b)}$
		A_1^+	$G_{0\perp}^{(ab)}$	$\frac{1}{\sqrt{2}} \left(M_x^{(a)} \otimes T_x^{(b)} + M_y^{(a)} \otimes T_y^{(b)} \right)$
2	E	A_1^+	$Q_u^{(ab)}$	$Q_u^{(a)} \otimes Q_0^{(b)}$
	ET	A_1^+	$G_u^{(ab)}$	$\frac{1}{\sqrt{2}} \left(Q_{yz}^{(a)} \otimes Q_x^{(b)} - Q_{zx}^{(a)} \otimes Q_y^{(b)} \right)$
3	E	A_1^+	$Q_{3\gamma}^{(ab)}$	$\frac{1}{\sqrt{2}} \left(Q_v^{(a)} \otimes Q_x^{(b)} - Q_{xy}^{(a)} \otimes Q_y^{(b)} \right)$
0	E	A_1^+	$Q_0^{(ab)'}$	$Q_0^{(a)'} \otimes Q_0^{(b)}$
	ET	A_1^+	$G_{0\perp}^{(ab)'} [1]$	$\frac{1}{\sqrt{2}} \left(G_x^{(a)'} \otimes Q_x^{(b)} + G_y^{(a)'} \otimes Q_y^{(b)} \right)$
		A_1^+	$G_{0z}^{(ab)'} [1]$	$M_z^{(a)'} [1] \otimes T_z^{(b)}$
		A_1^+	$G_{0\perp}^{(ab)'} [2]$	$\frac{1}{\sqrt{2}} \left(M_x^{(a)'} [1] \otimes T_x^{(b)} + M_y^{(a)'} [1] \otimes T_y^{(b)} \right)$
		A_1^+	$G_{0z}^{(ab)'} [2]$	$M_z^{(a)'} [2] \otimes T_z^{(b)}$
		A_1^+	$G_{0\perp}^{(ab)'} [3]$	$\frac{1}{\sqrt{2}} \left(M_x^{(a)'} [2] \otimes T_x^{(b)} + M_y^{(a)'} [2] \otimes T_y^{(b)} \right)$
2	E	A_1^+	$Q_u^{(ab)'}$	$Q_u^{(a)'} \otimes Q_0^{(b)}$
	ET	A_1^+	$G_u^{(ab)'} [1]$	$\frac{1}{\sqrt{2}} \left(Q_{yz}^{(a)'} \otimes Q_x^{(b)} - Q_{zx}^{(a)'} \otimes Q_y^{(b)} \right)$
		A_1^+	$G_u^{(ab)'} [2]$	$\frac{1}{\sqrt{2}} \left(T_{yz}^{(a)'} \otimes T_x^{(b)} - T_{zx}^{(a)'} \otimes T_y^{(b)} \right)$
		A_1^+	$G_u^{(ab)'} [3]$	$\frac{1}{\sqrt{2}} \left(M_{3x\alpha}^{(a)'} \otimes T_x^{(b)} - M_{3y\alpha}^{(a)'} \otimes T_y^{(b)} \right)$
3	E	A_1^+	$Q_{3\gamma}^{(ab)'} [1]$	$\frac{1}{\sqrt{2}} \left(Q_v^{(a)'} \otimes Q_x^{(b)} - Q_{xy}^{(a)'} \otimes Q_y^{(b)} \right)$
		A_1^+	$Q_{3\gamma}^{(ab)'} [2]$	$M_{3\alpha}^{(a)'} \otimes T_z^{(b)}$
		A_1^+	$Q_{3\gamma}^{(ab)'} [3]$	$M_{3\beta}^{(a)'} \otimes T_z^{(b)}$
		A_1^+	$Q_{3\gamma}^{(ab)'} [4]$	$\frac{1}{\sqrt{2}} \left(T_v^{(a)'} \otimes T_x^{(b)} - T_{xy}^{(a)'} \otimes T_y^{(b)} \right)$
		A_1^+	$Q_{3\gamma}^{(ab)'} [5]$	$\frac{1}{\sqrt{2}} \left(M_{3y\beta}^{(a)'} \otimes T_x^{(b)} + M_{3x\beta}^{(a)'} \otimes T_y^{(b)} \right)$

5.3 Parameter Optimization

Table 5.4: Parameters and hyperparameters used for the optimization process.

high symmetry lines	A- Γ -H-A-L-J-K- Γ -M-K.
number of \mathbf{k} points	$N_k = 451$
number of bands	$N_n = 18$
total number of the eigenvalues	$N_{\text{tot}} = N_k \times N_n = 8118$
maximum number of neighbor bonds	$N_{\text{max}}^{(b)} = 8$
number of hidden layers	$N_h = 4$
maximum number of iterations	$N_{\text{iter}} = 500$
learning rate	$\alpha = 0.01$

Table 5.5: The number of neurons and the optimization parameters in the DNN-SAMB with $N_h = 4$.

Layer	$N_{\text{max}}^{(b)} = 8$	
	neurons #	params #
DFT band	8118	
1st hidden	4080	33125520
2nd hidden	2040	8325240
3rd hidden	1020	2081820
4rd hidden	510	520710
SAMB	255	130305
TB band	8118	
total #	24141	44183595

In this section, we show the results of the parameter optimization and the weight of each SAMB z_j given by Eqs. (5.2.11), (5.2.12), and (5.2.13), to reproduce the Wannier band dispersions obtained by the DFT calculation using the HSE06 hybrid functional [203]. We choose the high symmetry lines A- Γ -H-A-L-J-K- Γ -M-K. We use bands at 50 \mathbf{k} points in each line, then the number of \mathbf{k} points is $N_k = 451$ and the number of bands is $N_n = 18$. The total number of the eigenvalues is $N_{\text{tot}} = N_k \times N_n = 8118$. We consider up to 8th neighbor bond-cluster, $N_{\text{max}}^{(b)} = 8$, and we fix the number of hidden layers as $N_h = 4$. The maximum number of iterations is fixed as $N_{\text{iter}} = 500$ that is sufficient to reach convergence, and the learning rate is fixed as $\alpha = 0.01$. Table 5.5 shows the number of neurons and the optimization parameters in the DNN-SAMB. The total number of the SAMB is 255 by considering up to 8th neighbor hopping.

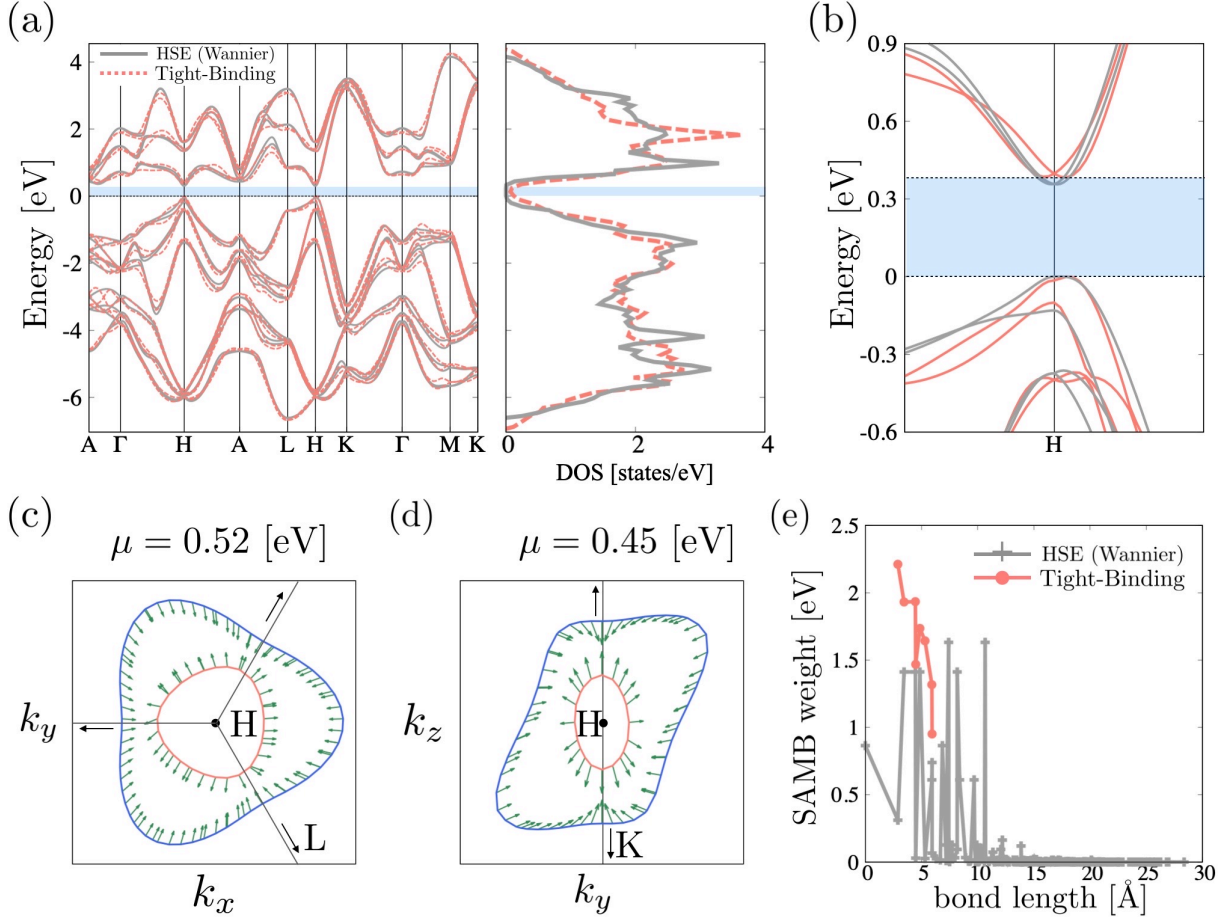


Figure 5.4: (a) The comparison of the band dispersion and DOS between our optimized TB model (dashed red lines) and the DFT-based Wannier TB model (solid grey lines). The Fermi energy is taken as the origin, and the blue shaded area represents the band gap. (b) The enlarged view of the band dispersion near the Fermi level. (c), (d) The Spin texture around the H point of the Brillouin zone in Te at the energy, (a) +0.52 eV and (b) +0.45 eV from the Fermi energy. The green arrows denote the spin direction projected onto each plane. (e) The comparison of the bond length dependence of the absolute maximum value of the hopping parameters in eV units between the Wannier TB model (solid grey lines) and our TB model (dashed red lines) considering up to 8th neighbor hoppings.

Following the workflow of the DNN-SAMB shown in Chap. 4, we optimize 255 weights of the SAMB by minimizing the MSE:

$$L(\mathbf{z}) = \frac{1}{2N_{\mathbf{k}}N_n} \sum_{n\mathbf{k}} \left(\frac{\epsilon_{n\mathbf{k}}^{\text{TB}}(\mathbf{z}) - \epsilon_{n\mathbf{k}}^{\text{DF}}}{W} \right)^2, \quad (5.3.1)$$

where $\epsilon_{n\mathbf{k}}^{\text{DF}}$ and $\epsilon_{n\mathbf{k}}^{\text{TB}}(\mathbf{z})$ are the n -th energy eigenvalue of DFT-based Wannier model and our TB model, and W is the bandwidth of the Wannier model.

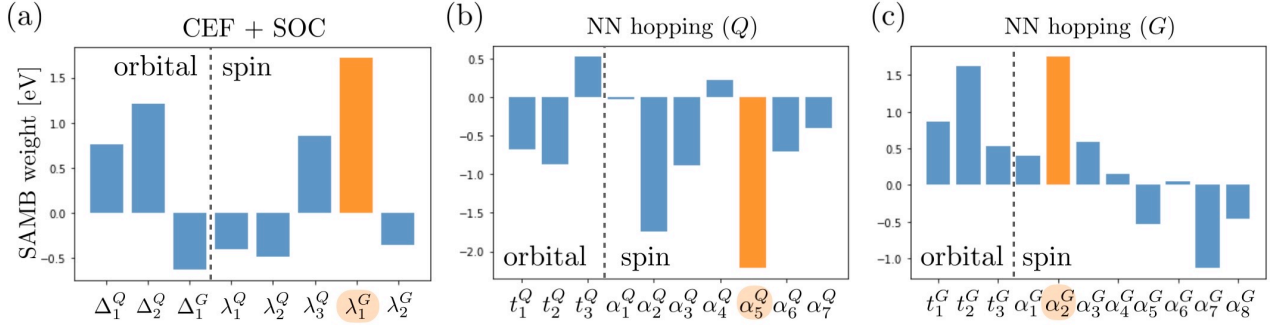
The comparison of the band dispersion and DOS between our TB model and the Wannier TB model are shown in Fig. 5.4(a). By taking up to the 8th neighbors, we achieve the accuracy,

$L(\mathbf{z}) = 4.4 \times 10^{-5}$. As shown in Fig. 5.4(b), the energy gap at the H point of our optimized TB model of 0.380 eV is slight larger than that of the reference band of 0.356 eV.

Figures 5.4(c) and (d) show the hedgehog spin texture of the electronic states near the bottom of the conduction band calculated using the obtained TB model. Although the present method does not ensure the reproduction of the spin textures of the reference bands, the optimized TB model roughly

Table 5.6: The optimized parameters of the TB model of Te. The parameters are in units of eV.

Δ_0^Q	Δ_1^Q	Δ_2^Q	Δ_1^G	λ_1^Q	λ_2^Q	λ_3^Q	λ_1^G	λ_2^G
17.98	0.7596	1.214	-0.6235	-0.3969	-0.4858	0.8596	1.718	-0.3465
t_1^Q	t_2^Q	t_3^Q	t_1^G	t_2^G	t_3^G			
-0.6801	-0.8710	0.5200	0.8700	1.624	0.5276			
α_1^Q	α_2^Q	α_3^Q	α_4^Q	α_5^Q	α_6^Q	α_7^Q		
-0.02656	-1.745	-0.8838	0.2195	-2.212	-0.7095	-0.4033		
α_1^G	α_2^G	α_3^G	α_4^G	α_5^G	α_6^G	α_7^G	α_8^G	
0.4031	1.749	0.5854	0.1484	-0.5261	0.04437	-1.126	-0.4538	

Figure 5.5: (a) The optimized parameters in \mathcal{H}_{CEF} and \mathcal{H}_{SOC} . (b), (c) The optimized parameters of the (b) E and (c) ET multipoles in $\mathcal{H}_t^{(1)}$. The orange bars represent the maximum value in each group.

reproduces that obtained by the DFT calculation [194, 195]. This success is ascribed to the use of the SAMB, which imposes strong constraint by symmetry.

Figure 5.4(e) describes the comparison of the bond length dependence of the absolute maximum value of the hopping parameters between the Wannier TB model and our TB model considering up to 8th neighbor hoppings. This result indicates that the magnitude of the parameters decreases for further neighbor hoppings. It should be emphasized that the total number of parameters is much less than that of the Wannier TB model.

The optimized weights of SAMB in \mathcal{H}_{CEF} , \mathcal{H}_{SOC} , and $\mathcal{H}_t^{(1)}$ are summarized in Table 5.6 and Fig. 5.5. Among these SAMB, the most dominant contributions containing the ET monopole G_0 are $G_{0\perp}^{(\text{as})}$ in \mathcal{H}_{SOC} and $G_{0z}^{(\text{ab})}$, $G_{0\perp}^{(\text{ab})}$ in $\mathcal{H}_t^{(1)}$, which are explicitly given by (See Table 5.3)

$$G_{0\perp}^{(\text{as})} = \frac{1}{\sqrt{2}} \left(Q_x^{(\text{s})} \otimes G_x^{(\text{a})} + Q_y^{(\text{s})} \otimes G_y^{(\text{a})} \right), \quad (5.3.2)$$

$$G_{0z}^{(\text{ab})} = T_z^{(\text{b})} \otimes \sigma_z^{(\text{a})}, \quad (5.3.3)$$

$$G_{0\perp}^{(\text{ab})} = \frac{1}{\sqrt{2}} \left(T_x^{(\text{b})} \otimes \sigma_x^{(\text{a})} + T_y^{(\text{b})} \otimes \sigma_y^{(\text{a})} \right), \quad (5.3.4)$$

The weight of $G_{0\perp}^{(\text{as})}$ is $\lambda_1^G = 1.718$ eV which is the most dominant contribution among $\mathcal{H}_{\text{CEF}} + \mathcal{H}_{\text{SOC}}$, and that of $G_{0z}^{(\text{ab})}$ is $\alpha_2^G = 1.749$ eV which is the most dominant contribution among the ET multipoles

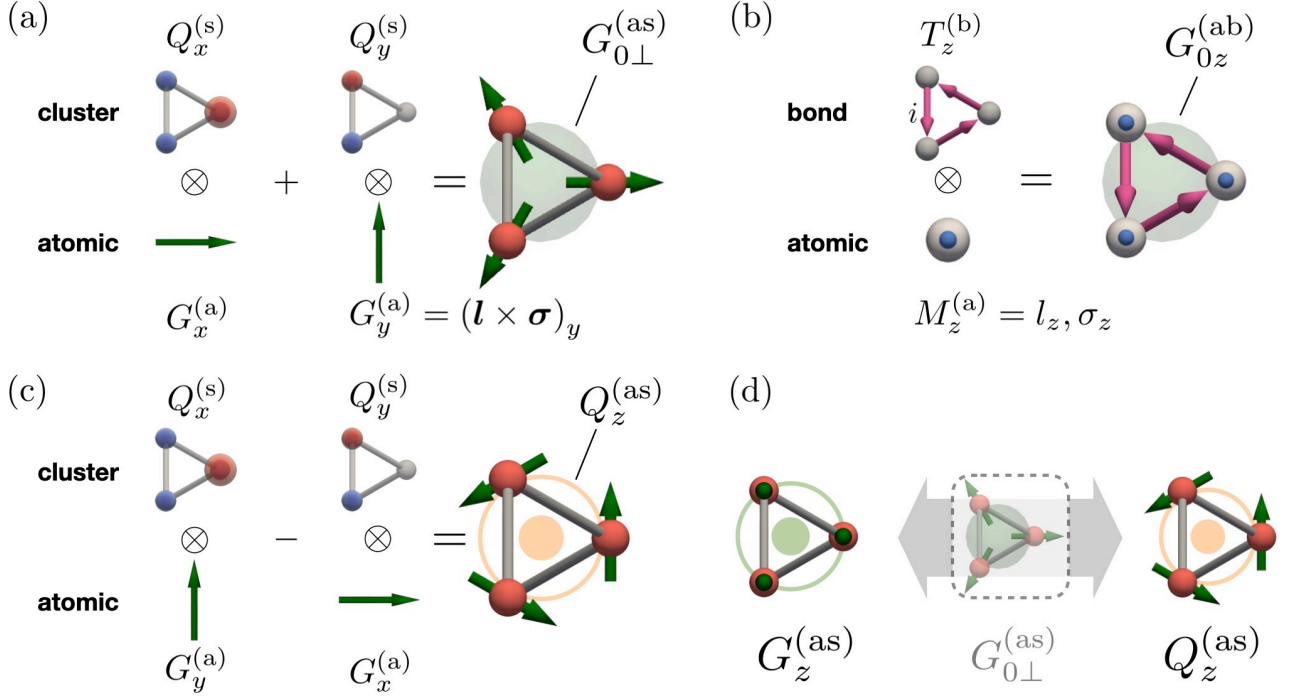


Figure 5.6: Schematic picture of multipole basis for Te. (a) Local ET monopole, $G_{0\perp}^{(as)}$, (b) itinerant ET monopole, $G_{0z}^{(ab)}$, and (c) local E dipole, $Q_z^{(as)}$. (d) The inter-parity coupling between the ET dipole $G_z^{(as)}$ and E dipole $Q_z^{(as)}$ via $G_{0\perp}^{(as)}$.

in $\mathcal{H}_t^{(t)}$, while that of $G_{0\perp}^{(ab)}$ is $\alpha_3^G = 0.5854$ eV. Note that $G_{0z}^{(as)}$ does not appear as shown in Table 5.3, because the z component of the E dipole $Q_z^{(s)}$ identically vanishes in the present Hilbert space. Here, $\mathbf{G}^{(a)} = \mathbf{l} \times \boldsymbol{\sigma}$ is the atomic ET dipole (\mathbf{l} and $\boldsymbol{\sigma}$ are the dimensionless orbital and half of spin angular momenta, respectively). $Q_\mu^{(s)}$ ($\mu = x, y$) and $T_\mu^{(b)}$ ($\mu = x, y, z$) are the μ component of the site-cluster E dipole and bond-cluster MT dipole, which are defined in Eqs. (5.2.3) and (5.2.4), respectively. Although there are also the spinless version of $G_{0z}^{(ab)}$ and $G_{0\perp}^{(ab)}$ which are given by replacing $\boldsymbol{\sigma}$ with \mathbf{l} in Eqs. (5.3.3) and (5.3.4), the weight of these multipole basis is much smaller than that for the spinful ones.

Figures 5.6(a) and (b) schematically show $G_{0\perp}^{(as)}$ and $G_{0z}^{(ab)}$, respectively. As shown in Fig. 5.6(a), $G_{0\perp}^{(as)}$ is the local ET monopole having the $\mathbf{G}^{(a)}$ -flux structure in the unit cell as Eq. (5.1.2). On the other hand, $G_{0z}^{(ab)}$ in Fig. 5.6(b) is the itinerant ET monopole which is a kind of off-site SOC corresponding to the spin-dependent imaginary hopping. The itinerant ET monopole $G_{0z}^{(ab)}$ is the main origin of the Edelstein effect observed in Te [57, 58].

Moreover, the Fourier transform of $G_{0z}^{(ab)}$ together with $G_{0\perp}^{(ab)}$ give rise to the hedgehog spin texture around the H point in the momentum space as shown in Figs. 5.4(c) and (d) [194, 195]. The expansions of the Fourier-transform of the itinerant ET monopoles matrix $G_{0z}^{(ab)'}[1]$ and $G_{0\perp}^{(ab)'}[2]$ around the H point, \mathbf{k}_H , are given as

$$G_{0z}^{(ab)'}[1](\mathbf{k}_H + \mathbf{k}) = \begin{pmatrix} 0 & 1 & 1 \\ 1 & 0 & 1 \\ 1 & 1 & 0 \end{pmatrix} \otimes (C_z k_z \sigma_z) + \dots, \quad (5.3.5)$$

$$G_{0\perp}^{(ab)'}[2](\mathbf{k}_H + \mathbf{k}) = \begin{pmatrix} 0 & 1 & 1 \\ 1 & 0 & 1 \\ 1 & 1 & 0 \end{pmatrix} \otimes (C_x k_x \sigma_x + C_y k_y \sigma_y) + \dots, \quad (5.3.6)$$

where the off-diagonal 3×3 matrix is defined in the ABC sublattice space, and the explicit values of the coefficients C_z , C_x , and C_y are given by

$$C_z = -\frac{c}{18} [4 \sin^2(\pi u) - 3] = 0.2221, \quad (5.3.7)$$

$$C_x = -\frac{\sqrt{3}au}{8} [2 \cos(2\pi u + \pi/3) + 1] = 0.2321, \quad (5.3.8)$$

$$C_y = -\frac{au}{24} [9 \sin(2\pi u) + 5\sqrt{3} \cos(2\pi u)\sqrt{3}] = 0.4718. \quad (5.3.9)$$

Since both α_2^G and α_3^G , corresponding to $G_{0z}^{(ab)'}[1]$ and $G_{0\perp}^{(ab)'}[2]$, and C_z , C_x , and C_y are positive, the momentum-space representation of the SOC Hamiltonian around the H point is summarized as

$$\mathcal{H}_{\text{SOC}}(\mathbf{k}_H + \mathbf{k}) = \begin{pmatrix} 0 & 1 & 1 \\ 1 & 0 & 1 \\ 1 & 1 & 0 \end{pmatrix} (c_x k_x \sigma_x + c_y k_y \sigma_y + c_z k_z \sigma_z), \quad (5.3.10)$$

where c_i ($i = x, y, z$) are positive constants. From the above results, the highest-weight term $G_{0z}^{(ab)'}[1]$ together with $G_{0\perp}^{(ab)'}[2]$ are the key elements to exhibit the hedgehog spin texture.

These ET monopoles, $G_{0z}^{(ab)}$ and $G_{0\perp}^{(as)}$, play roles of $G_0^{(1)}$ and $G_0^{(2)}$ in Eq. (5.1.3), respectively. As discussed below, both of them give dominant contributions to the EIR and RIP.

5.4 Electric-Field Induced Rotation

In this section, we demonstrate the inter-parity conversion between polar and axial vectors expected to occur in chiral materials via Eq. (5.1.3). Using the obtained TB model, we investigate the electric-field induced ET dipole response from a microscopic point of view.

Let us consider the linear electric-field induced ET dipole response described by $G_i = d_{i;j}E_j$. Following Ref. [26] and using E dipoles, Q_μ ($\mu = x, y, z$), and ET monopole, G_0 , and quadrupoles, G_ν ($\nu = u, v, yz, zx, xy$), the response tensor $d_{i;j}$ is expressed from symmetry point of view as

$$d = \begin{pmatrix} G_0 - G_u + G_v & G_{xy} + Q_z & G_{zx} - Q_y \\ G_{xy} - Q_z & G_0 - G_u - G_v & G_{yz} + Q_x \\ G_{zx} + Q_y & G_{yz} - Q_x & G_0 + 2G_u \end{pmatrix} \quad (5.4.1)$$

Then, nonzero d occurs in the 17 gyrotropic point groups in which one of Q_μ , G_0 , and G_ν belong to the fully symmetric irreducible representation (see Table XVI in Ref. [26]). In particular, the longitudinal response occurs in eleven chiral point groups, O, T, D_4 , C_4 , D_2 , C_2 , D_6 , C_6 , D_3 , C_3 , C_1 and two achiral gyrotropic point groups, D_{2d} and S_4 (G_v belongs to the fully symmetric irreducible representation). This constraint is similar to that for the so-called Villari effect in magnetism but the latter requires time-reversal symmetry breaking in contrast to EIR. In the point group D_3 , Eq. (5.4.1) is reduced as

$$d = \begin{pmatrix} G_0 - G_u & 0 & 0 \\ 0 & G_0 - G_u & 0 \\ 0 & 0 & G_0 + 2G_u \end{pmatrix} \quad (5.4.2)$$

Thus, only longitudinal responses can be realized in Te, and then we focus on the screw axis component, $G_z = d_{z;z}E_z$.

Before showing the results, we explicitly define the local E- and ET-dipole operators that describe the input and output of the response. The definition of the E dipole $Q_z^{(\text{as})}$ is given by (See Table 5.3)

$$Q_z^{(\text{as})} = \frac{1}{\sqrt{2}} \left(Q_x^{(\text{s})} \otimes G_y^{(\text{a})} - Q_y^{(\text{s})} \otimes G_x^{(\text{a})} \right), \quad (5.4.3)$$

Eq. (5.4.3) is similar to Eq. (5.3.2) with a minus sign for the second term, which is schematically shown in Fig. 5.6(c), i.e., the vortex-like alignment of $G_x^{(\text{a})}$ and $G_y^{(\text{a})}$ (cf. the roles of \mathbf{G} and \mathbf{Q} are reverted in Fig. 5.1(d)). The static rotational response is also described by the ET dipole (See Table 5.3),

$$G_z^{(\text{as})} = Q_0^{(\text{s})} \otimes G_z^{(\text{a})} \quad (5.4.4)$$

Using the Kubo formula, the response function in $G_z^{(\text{as})} = d_{z;z}E_z$ is expressed as

$$d_{z;z} = d_{z;z}^{\text{P}}[Q] + d_{z;z}^{\text{VV}}[Q] + d_{z;z}^{\text{VV}}[v], \quad (5.4.5)$$

$$d_{z;z}^{\text{P}}[Q] = \frac{ec}{N} \sum_{\mathbf{k}n\mathbf{m}}^{\epsilon_{n\mathbf{k}} = \epsilon_{m\mathbf{k}}} \frac{\partial f_{n\mathbf{k}}}{\partial \epsilon_{n\mathbf{k}}} G_{z\mathbf{k}}^{n\mathbf{m}} Q_{z\mathbf{k}}^{m\mathbf{n}}, \quad (5.4.6)$$

$$d_{z;z}^{\text{VV}}[Q] = \frac{ec}{N} \sum_{\mathbf{k}n\mathbf{m}}^{\epsilon_{n\mathbf{k}} \neq \epsilon_{m\mathbf{k}}} \frac{f_{n\mathbf{k}} - f_{m\mathbf{k}}}{\epsilon_{n\mathbf{k}} - \epsilon_{m\mathbf{k}}} G_{z\mathbf{k}}^{n\mathbf{m}} Q_{z\mathbf{k}}^{m\mathbf{n}}, \quad (5.4.7)$$

$$d_{z;z}^{\text{VV}}[v] = -\frac{e\hbar}{iN} \sum_{\mathbf{k}n\mathbf{m}}^{\epsilon_{n\mathbf{k}} \neq \epsilon_{m\mathbf{k}}} \frac{f_{n\mathbf{k}} - f_{m\mathbf{k}}}{(\epsilon_{n\mathbf{k}} - \epsilon_{m\mathbf{k}})^2} G_{z\mathbf{k}}^{n\mathbf{m}} v_{z\mathbf{k}}^{m\mathbf{n}}. \quad (5.4.8)$$

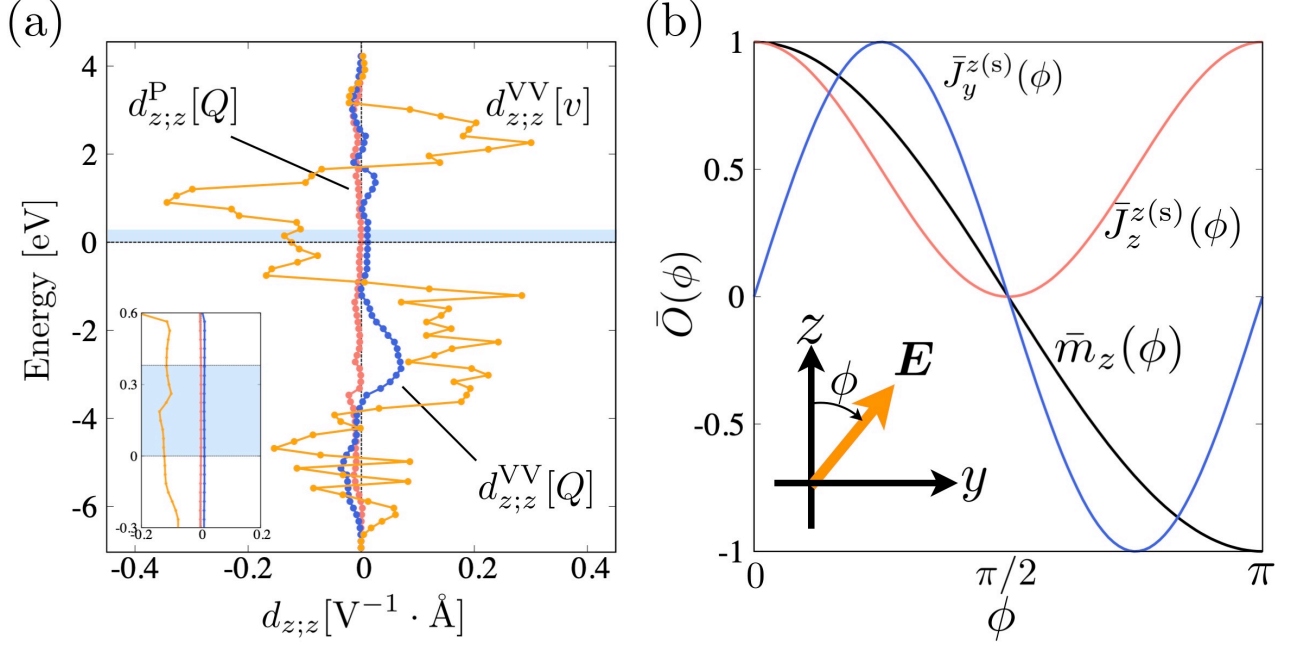


Figure 5.7: (a) Chemical potential μ dependence of $d_{z;z}^P$ and $d_{z;z}^{VV}$ with Eqs. (5.4.6), (5.4.7), and (5.4.8) at $T = 0.01$ eV, and $N = 64^3$. The inset shows the enlarged plot near the Fermi level. (b) The electric-field angle dependence of the spin current in yz plane $\bar{J}_y^{z(s)}(\phi) \propto \cos^2(\phi)$ and $\bar{J}_z^{z(s)}(\phi) \propto \sin(2\phi)$, and the magnetization due to the Edelstein effect, $\bar{m}_z(\phi) \propto \cos(\phi)$. $\bar{O}(\phi)$ denotes the normalized value of $O(\phi)$ by its absolute maximum value.

Here, the matrix element of an operator is $O_{ik}^{nm} = \langle \psi_{nk} | \hat{O}_i | \psi_{mk} \rangle$, $f_{nk} = f(\epsilon_{nk})$ denotes the Fermi distribution function, e (> 0) is the elementary charge, c is the lattice constant, and N is the number of lattice sites. The response functions $d_{z;z}^P$ and $d_{z;z}^{VV}$ represent the intra-band Pauli contribution proportional to the DOS, and inter-band van Vleck contributions, respectively. $[Q]$ and $[v]$ denote the contributions from the local E dipole and itinerant hopping process via the velocity operator, $\mathbf{v}_{\mathbf{k}} = \partial \mathcal{H}_0 / \partial \hbar \mathbf{k}$, respectively. Note that $d_{z;z}^P[v]$ vanishes identically by the symmetry. We have used $N = 64^3$ and the temperature $T = 0.01$ eV in the following results.

Figure 5.7(a) shows the chemical potential μ dependence of the response functions. The inter-band contribution from the itinerant hopping process, $d_{z;z}^{VV}[v]$, is always dominant irrespective of μ , and the EIR occurs even in the insulator. Note that the EIR and RIP could occur in any chiral insulators, which are qualitatively different from the kinetic magneto-electric (Edelstein) effect expected only in metals due to its intra-band origin. Note that the inverse RIP process is also expected to occur in both metals and insulators, as their response functions are common with Eqs. (5.4.6) and (5.4.7).

Based on the systematic analysis method [1], we elucidate the dominant contribution in the response function $d_{z;z}$. For simplicity, we here consider the TB Hamiltonian in the momentum space including up to the NN hoppings:

$$h(\mathbf{k}) = \mathcal{H}_{\text{CEF}} + \mathcal{H}_{\text{SOC}} + \mathcal{H}_t^{(1)}(\mathbf{k}). \quad (5.4.9)$$

The essential parameters in $d_{z;z}[Q]$ which is the contributions arising from the local E dipole ($Q_z^{(\text{as})'}$) are given by evaluating the following quantity [1],

$$\Gamma_{z;z}^{ij}[Q] = \sum_{\mathbf{k}} \text{Tr} \left[G_{z\mathbf{k}}^{(\text{as})'} h^i(\mathbf{k}) Q_{z\mathbf{k}}^{(\text{as})'} h^j(\mathbf{k}) \right], \quad (5.4.10)$$

where $G_{z\mathbf{k}}^{(\text{as})'}$ ($Q_{z\mathbf{k}}^{(\text{as})'}$) is the ET (E) dipole operator matrix at \mathbf{k} , and $h^i(\mathbf{k})$ represents the i -th power of the Hamiltonian matrix at \mathbf{k} , respectively.

In order to clarify the most dominant contributions to $d_{z;z}[Q]$, we show the lowest-order term of Eq. (5.4.10) at $(i, j) = (1, 0)$:

$$\Gamma_{z;z}^{10}[Q] = \frac{\sqrt{3}}{24}(\Delta_1^G - \sqrt{2}\lambda_2^G). \quad (5.4.11)$$

As a result, both Δ_1^G and λ_2^G corresponding to the local ET quadrupoles, $G_u^{(\text{as})}$ and $G_u^{(\text{as})'}$, contribute to $d_{z;z}[Q]$. Note that the higher-order terms of Eq. (5.4.10), which give less important contributions than the lowest-order one, consist of a linear combination of the terms proportional to the local and itinerant ET monopoles and quadrupoles. These results are consistent with the above symmetry argument and Eq. (5.4.2).

On the other hand, the essential parameters in $d_{z;z}^{\text{VV}}[v]$ which is the van Vleck contribution arising from the itinerant hopping process via the velocity operator, $v_{\mathbf{k}} = \partial h(\mathbf{k})/\partial \hbar \mathbf{k}$, is given by evaluating the following quantity [1],

$$\text{Im} [\Gamma_{z;z}^{ij}[v]] = \sum_{\mathbf{k}} \text{Tr} \left[G_{z\mathbf{k}}^{(\text{as})'} h^i(\mathbf{k}) v_{z\mathbf{k}} h^j(\mathbf{k}) \right]. \quad (5.4.12)$$

where $v_{z\mathbf{k}}$ is the z component of the velocity operator.

Similar to Eq. (5.4.11), the most dominant contributions to $d_{z;z}^{\text{VV}}[v]$ is arising from the lowest-order term at $(i, j) = (1, 0)$ in Eq. (5.4.12):

$$\text{Im} [\Gamma_{z;z}^{10}[v]] = \frac{79}{720} \left[(\sqrt{2}\alpha_1^Q - \alpha_2^Q)(2\sqrt{6}\alpha_2^G - 3t_1^G) - \frac{3\sqrt{3}}{2}(\alpha_1^G - \alpha_6^G)t_2^G - 3\sqrt{2}(\alpha_1^G + \alpha_6^G)\alpha_3^G \right] + F(\{\mathbf{z}\}) \quad (5.4.13)$$

$$\begin{aligned} F(\{\mathbf{z}\}) = & -\frac{79}{7200} \left[-15\sqrt{10}\alpha_1^G\alpha_5^G - 10\sqrt{15}\alpha_1^Q\alpha_4^G - 4\sqrt{30}\alpha_2^Q\alpha_4^G + 18\sqrt{5}\alpha_2^Q\alpha_4^Q - 30\sqrt{2}\alpha_3^Q\alpha_6^Q \right. \\ & - 30\alpha_3^Q\alpha_7^Q - 18\sqrt{15}\alpha_4^G t_2^Q + 18\sqrt{10}\alpha_4^Q t_2^Q - 6\sqrt{10}\alpha_5^G\alpha_6^G - 27\sqrt{5}\alpha_5^G t_3^G \\ & \left. + 15\sqrt{2}\alpha_6^G\alpha_7^G + 12\sqrt{10}\alpha_6^G\alpha_8^G + 30\alpha_6^Q t_3^Q - 15\alpha_7^G t_3^G - 30\sqrt{2}\alpha_7^Q t_3^Q + 24\sqrt{5}\alpha_8^G t_3^G \right]. \end{aligned} \quad (5.4.14)$$

Since both α_2^Q and α_2^G corresponding to the itinerant E quadrupole and ET monopole, $Q_u^{(\text{ab})'}$ and $G_{0z}^{(\text{ab})'}$ [1], are relatively large parameters as shown in Figs. 5.5(c) and (d), the term proportional to $\alpha_2^Q\alpha_2^G$ in the first term of Eq. (5.4.13) is the most dominant contribution to $d_{z;z}^{\text{VV}}[v]$. On the other hand, the second term of Eq. (5.4.13), $F(\{\mathbf{z}\})$, is less important as shown in Figs. 5.5(c) and (d). Using the optimized values, $\Delta_1^G = -0.6235$ eV, $\lambda_2^G = -0.3465$ eV, $\alpha_2^Q = -1.745$ eV, and $\alpha_2^G = 1.749$ eV, the ratio of the term proportional to $\alpha_2^Q\alpha_2^G$ in Eq. (5.4.13) to the Eq. (5.4.11) is given by

$$r = \frac{\frac{79\sqrt{6}}{360}\alpha_2^Q\alpha_2^G}{\frac{\sqrt{3}}{24}(\Delta_1^G - \sqrt{2}\lambda_2^G)} \sim 170. \quad (5.4.15)$$

This result indicates that $d_{z;z}^{\text{VV}}[v]$ is dominant, which is consistent with the numerical result as shown in Fig. 5.7(a) and the highest-weight of the ET monopole $G_{0z}^{(\text{ab})'}$ [1] gives the most dominant contribution to $d_{z;z}^{\text{VV}}[v]$. Thus, the itinerant ET monopole $G_{0z}^{(\text{ab})'}$ is the key component of the EIR response in Te.

Although we have concentrated on the electronic responses in the above, the actual static rotational lattice deformation should occur via electron-lattice couplings. When we restrict our discus-

sion to a static rotational lattice deformation with the angle ω_z with respect to z screw axis, the electron-lattice coupling can be evaluated by rotating inversely the electronic system by the angle $-\omega_z$ [208–210]:

$$\mathcal{H}_{\text{el-rot}}^{(z)} = e^{-ij_z^{(\text{as})}\omega_z}\mathcal{H}_0e^{ij_z^{(\text{as})}\omega_z} - \mathcal{H}_0 = i[\mathcal{H}_0, j_z^{(\text{as})}]\omega_z + \dots \quad (5.4.16)$$

where $j_z^{(\text{as})} = Q_0^{(\text{s})} \otimes (l_z + \sigma_z/2)$ represents the total angular momentum. We find the most important contribution from $\lambda_1^G G_{0\perp}^{(\text{as})}$ term in \mathcal{H}_0 as

$$\mathcal{H}_{\text{el-rot}}^{(z)} \sim \lambda_1^G Q_z^{(\text{as})}\omega_z, \quad (5.4.17)$$

with $\lambda_1^G = 1.718$ eV. Similarly, the perpendicular components are obtained, and they are a factor $1/\sqrt{2}$ smaller than $\mathcal{H}_{\text{el-rot}}^{(z)}$. This term causes the electric polarization directly by applying a lattice rotation field with transverse ultrasound waves, for instance.

The induced electronic ET dipole can also be indirectly observed by spin current measurements. When the induced ET dipole by the electric field E_z is present, two types of nonlinear spin currents are expected: $J_z^{z(\text{s})} = \sigma_{z;z}^{z(\text{s})}E_z^2$ and $J_y^{z(\text{s})} = \sigma_{y;y}^{z(\text{s})}E_yE_z$, where $J_\mu^{\nu(\text{s})} \equiv (J_\mu\sigma_\nu + \sigma_\nu J_\mu)/2$ is the spin current operator where J_μ is the electric current operator. As shown in Fig. 5.7(b), the electric-field angle ϕ dependences of $J_\mu^{\nu(\text{s})}$ in yz plane are given by $J_z^{z(\text{s})}(\phi) \propto \cos^2(\phi)$ and $J_y^{z(\text{s})}(\phi) \propto \sin(2\phi)$, respectively. Note that they are in marked contrast to that of the magnetization due to the Edelstein effect, $m_z(\phi) = \alpha_{z;z}^{(\text{J})}E_z \propto \cos(\phi)$. Thus, the electric-field induced ET dipole is verifiable by examining the ϕ dependence of $J_z^{z(\text{s})}(\phi)$ and $J_y^{z(\text{s})}(\phi)$.

5.5 Absolute Enantioselection by Rotation and Electric Fields

Finally, we propose a possible experimental approach to achieve absolute enantioselection in chiral materials without using seed crystals [211]. As shown phenomenologically and microscopically, there are couplings among G_0 , \mathbf{G} , and \mathbf{Q} in chiral materials. Since the conjugate field of \mathbf{Q} is an electric field \mathbf{E} and that of \mathbf{G} is a rotation field $\boldsymbol{\omega}$ such as a rotation of electric field or equivalently time-dependent magnetic field, the conjugate field of chirality, that is G_0 , is a product of polar and axial vector fields, E_μ and ω_μ . In the electromagnetism, it is known as the quantity called zilch, which describes optical chirality [212]. Therefore, as shown in Fig. 5.8 in the case of $\mu = z$, absolute enantioselection can be achieved by simultaneous application of electric (E_μ) and rotation (ω_μ) fields, for instance. The sign

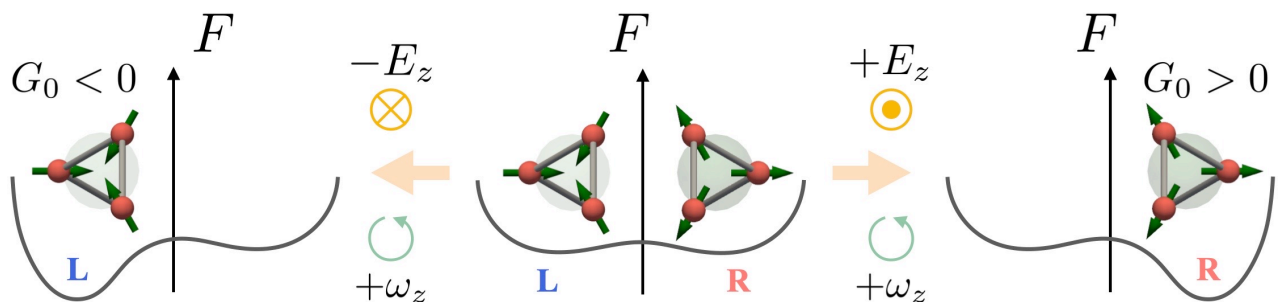


Figure 5.8: Free-energy differences for absolute enantioselection under simultaneous application of rotation (ω_z) and electric (E_z) fields. The sign of $\omega_z E_z$ controls the preferred handedness during crystallization process.

of $\omega_\mu E_\mu$ controls the preferred handedness during crystallization process, as shown in the left-most and right-most panels in Fig. 5.8. It should be emphasized that a time-dependent magnetic field $B_\mu(t)$ is favorable with the constant time derivative or net accumulation with definite sign. Additionally, both electric and magnetic fields must be parallel with each other. Moreover, G_0 could also couple with $M_\mu T_\mu$ as shown in Eq. (5.1.1). Thus, the combined static magnetic field and time-dependent electric field (i.e., $\nabla \times \mathbf{B}$, which is a conjugate field of T_μ), or the combined static magnetic field and electric current, can be used to achieve absolute enantioselection as well. This generic approach is applicable to any chiral material.

5.6 Summary

We have unveiled the microscopic description of chirality and possible electric-field induced static rotational lattice deformation and its inverse response, rotation-field induced electric polarization.

First, based on the symmetry and electronic multipole theory, we have phenomenologically shown that the chirality corresponds to the electric toroidal monopole G_0 , which couples with the G_0 -type quantities as in Eqs. (5.1.1)-(5.1.3). Note that their conjugate fields are the electric and magnetic parts of the optical zilch [212], for instance. Thus, the essential couplings as Eqs. (5.1.1)-(5.1.3), which arise from the higher-order coupling of our TB hamiltonian, are the key element for both the electric-field induced static rotational lattice deformation and its inverse response.

Second, we have constructed the DFT-based realistic tight-binding model of elemental Te crystal in terms of the symmetry-adapted multipole basis. As a result, we have derived the quantum-mechanical operator expressions of G_0 . Then, from the result of the parameter optimization, we have elucidated that the local and itinerant G_0 , shown in Fig. 5.6(b), are the most dominant contributions in the optimized Hamiltonian. We have also clarified that the itinerant G_0 is the key element to exhibit the hedgehog spin texture in the momentum space.

Third, using the realistic tight-binding model, we have elucidated that an inter-band process, driven by the itinerant G_0 is the crucial ingredient in electric-field induced static rotational lattice deformation and its inverse response. These responses occur even in the insulators, which is in marked contrast to the kinetic magneto-electric (Edelstein) effect observed in Te.

Lastly, based on the above responses, we have proposed a generic experimental approach to realize the absolute enantioselection in chiral materials by the conjugate field of the chirality, such as simultaneously applied electric and rotation fields, or magnetic field and electric current, and so on. Since the larger magnitude of a coupling between G_0 and its conjugate field is favorable for efficient achievement of an absolute enantioselection, the quantitative experimental observation of the responses related to the coupling is crucially important in future development.

Chapter 6

Summary

In this thesis, we have developed a generation scheme of a density-functional theory (DFT) based effective tight-binding (TB) model by means of the symmetry-adapted multipole theory. Using the generation scheme, we have constructed the DFT-based realistic tight-binding model for graphene, SrVO₃, MoS₂, and elemental Tellurium crystals. In particular, we have investigated the microscopic description of chirality and its related responses. Since we have already summarized the results in each chapter, we here summarize this thesis by highlighting the main results.

In Chap. 2, we have clarified the advantages and disadvantages of using a de facto standard DFT-based tight-binding model based on the Wannier functions and atomic orbitals. Although the Wannier TB model is superior in terms of its quantification and the localization of the Wannier functions, the symmetry of the given system is not taken into account in the model construction process. Due to the irrelevance of the symmetry in the model construction, the microscopic expression of the order parameter and the microscopic mechanism of their related physics often remain unclear. On the other hand, the widely used Slater-Koster approach takes partially into account the symmetry and provides an intuitive understanding of the electronic band structure and various physics of interest base on a few parameters. However, essential parameters would often be lost in the TB model owing to the lack of the effect from the surrounding environment around the bond of the electron hopping.

In Chap. 3, we have introduced the symmetry-adapted multipole basis. First, we have decomposed the electronic degrees of freedom into orbital/spin and the sublattice parts which are described by the atomic multipole basis and the site/bond-cluster multipole basis, respectively. We have clarified that the both atomic and site/bond-cluster multipole basis constitute the complete orthonormal basis set in the given Hilbert space. By combining the atomic and site/bond-cluster multipole basis, we have constructed the symmetry-adapted multipole basis which enable us to describe any electronic degrees of freedom in the isolated and periodic multi-site systems, such as molecules and crystals.

In Chap. 4, we have demonstrated a systematic generation scheme of the DFT-based symmetry-adapted tight-binding model given by the linear combination of the symmetry-adapted multipole basis. We optimize the model parameters, i.e., the weights of each multipole basis, so as to reproduce a given DFT band dispersion. To efficiently optimize the weights, we utilized machine learning techniques and introduced a deep neural network where the symmetry-adapted multipole basis plays a role of a neuron in the network. With the use of the deep neural network, we can perform highly efficient optimization with high accuracy and less initial guess dependence of the model parameters. We have demonstrated our method for graphene, SrVO₃, and monolayer MoS₂. We have achieved accuracy of less than 10^{-4} of the mean squared error between the normalized energy eigenvalues of the optimized tight-binding model and that of the DFT or DFT-based Wannier calculation. Most remarkably, we obtain highly accurate optimized TB model although our TB model contains fewer model parameters than the Wannier TB model. The proposed method refers only to the energy

eigenvalues. As a consequence, there is no guarantee to reproduce the orbital dependence of the electronic states in the reference bands. Nevertheless, the optimized TB Hamiltonian well reproduce the orbital dependence of the electronic states of SrVO₃. This success is ascribed to the use of the symmetry-adapted multipole basis, which imposes strong constraint by symmetry. However, when the model contains multiple sublattices or orbitals, such as monolayer MoS₂, our method can not precisely reproduce the orbital dependence of the electronic states of the reference bands. Thus, it is a future work to develop an optimization method that takes into account the orbital dependence of the reference bands. It should be emphasized that our method is applicable to any crystallographic structure within 230 space group. Furthermore, the deep neural network consisting of the symmetry-adapted multipole basis could be useful in various fields such as materials informatics.

In Chap. 5, we have elucidated the microscopic description of chirality, i.e., electric toroidal monopole, by taking elemental Te crystal as the simplest example of chiral crystals. Based on the systematic generation scheme introduced in Chap. 4, we have constructed the DFT-based realistic tight-binding Hamiltonian of Te. Then, we have elucidated that the local and itinerant electric toroidal monopoles are the most dominant contributions in the Hamiltonian. Furthermore, we have clarified that the itinerant electric toroidal monopole is the crucial element to realize the possible electric-field induced static rotational lattice deformation. In contrast to the kinetic magneto-electric (Edelstein) effect observed in chiral metals, the above response and its inverse response, a rotation-field induced electric polarization, could appear in both chiral metals and insulators. Lastly, we have also proposed a possible experimental approach to realize the absolute enantioselection in chiral materials by means of the conjugate field of chirality. The conjugate field of chirality is a product of polar and axial vectors with the same time-reversal symmetry, such as electric and rotation fields, or magnetic field and electric current, and so on. The sign of the combined field controls the preferred handedness during the crystallization process.

In future works, based on the proposed generation scheme of the DFT-based tight-binding model, we will study various unconventional multipole orders, including chirality, and their related linear and nonlinear responses. We will also resolve some of the difficulties in the present method. In particular, we will develop a method to reproduce the orbital dependence of the reference bands, which will broaden the range of applications of our method. For example, the improved method is expected to allow us to discuss the relationship between band topology and multipole basis. We will also extend the range of the method from the electronic system to the phononic system. We can use the method to discuss the chiral-phonon-related phenomena and the unconventional spin-triplet superconductivity mediated by a proper electron-phonon coupling hidden in the chiral materials.

Appendix A

Density Functional Theory

A.1 Born-Oppenheimer Approximation

Some approximations are indispensable to calculate the many-body problem of materials consisting of electrons and nuclei. The first step is the Born-Oppenheimer (BO) approximation [213]. BO approximation is based on the fact that the kinetic energy of nuclei is much smaller than that of electrons, which rationalizes neglecting the nuclear motion and simplifies the problem to the interacting electronic systems within the space-fixed nuclei.

Let us consider the non-relativistic Schrödinger equation of electrons and nuclei in materials:

$$H\Psi(\mathbf{r}, \mathbf{R}) = E\Psi(\mathbf{r}, \mathbf{R}) \quad (\text{A.1.1})$$

where $H(E)$ is the total Hamiltonian (energy spectra) of the system and $\Psi(\mathbf{r}, \mathbf{R})$ is the many body wave function containing N_e electrons $\mathbf{r} = (\mathbf{r}_1, \mathbf{r}_2, \dots, \mathbf{r}_{N_e})$ and N_n nuclei $\mathbf{R} = (\mathbf{R}_1, \mathbf{R}_2, \dots, \mathbf{R}_{N_n})$. The explicit expression of the Hamiltonian is given by

$$H = T^{(e)} + T^{(n)} + V^{(ee)} + V^{(nn)} + V^{(en)} \quad (\text{A.1.2})$$

$$T^{(e)} = -\sum_i^{N_e} \frac{\hbar^2}{2m_e} \nabla_i^2, \quad T^{(n)} = -\sum_I^{N_n} \frac{\hbar^2}{2M_I} \nabla_I^2 \quad (\text{A.1.3})$$

$$V^{(ee)} = \frac{e^2}{2} \sum_{i>j} \frac{1}{|\mathbf{r}_i - \mathbf{r}_j|}, \quad V^{(nn)} = \frac{e^2}{2} \sum_{I>J} \frac{z_I z_J}{|\mathbf{R}_I - \mathbf{R}_J|}, \quad V^{(en)} = -e^2 \sum_i^{N_e} \sum_I^{N_n} \frac{z_I}{|\mathbf{r}_i - \mathbf{R}_I|} \quad (\text{A.1.4})$$

where m_e , M_I , and e are mass of electrons, mass of nuclei, and elementary charge, respectively. $T^{(e)}$ ($T^{(n)}$) represents the kinetic energy operator of electrons (nuclei). $V^{(ee)}$, $V^{(nn)}$, and $V^{(en)}$ describe the Coulomb interactions between pairs of electrons, pairs of nuclei, and between electrons and nuclei, respectively. The Hamiltonian includes microscopic information about the system, i.e., crystallographic symmetry, species and positions of atoms, and interactions between pairs of electrons and nuclei.

The BO approximation is based on $T^{(e)} \gg T^{(n)}$ because $m_e/M \ll 1$ (M is an average value of M_I). As a consequence, $T^{(n)}$ can be approximately neglected in Eq. (A.1.2) and the nuclear positions \mathbf{R} are fixed in space. In the range of the BO approximation, the electronic Hamiltonian is given by

$$H^{(e)} = T^{(e)} + V^{(ee)} + V_{\text{ext}}(\mathbf{R}) + E^{(nn)}(\mathbf{R}) \quad (\text{A.1.5})$$

where $V_{\text{ext}}(\mathbf{R}) \equiv V^{(en)}(\text{fixed } \mathbf{R})$ represents the external potential from the nuclei fixed in space and

$E^{(\text{nn})}(\mathbf{R}) \equiv V^{(\text{nn})}(\text{fixed } \mathbf{R})$ is a constant value of the interaction between pairs of nuclei fixed in space. The corresponding Schrödinger equation is given by

$$H^{(\text{e})}\Psi^{(\text{e})}(\mathbf{r}; \mathbf{R}) = E^{(\text{e})}\Psi^{(\text{e})}(\mathbf{r}; \mathbf{R}) \quad (\text{A.1.6})$$

where $\Psi_n^{(\text{e})}(\mathbf{r}; \mathbf{R})$ is an electronic wave function as a function of \mathbf{R} . Note that $T^{(\text{e})}$ and $V^{(\text{ee})}$ are material-independent terms, while microscopic information unique to the system is involved in V_{ext} . The BO approximation separates the electronic and nuclear degrees of freedom, and then the many-body wave function is expressed as a multiplication of the electronic and nuclear parts:

$$\Psi(\mathbf{r}, \mathbf{R}) \simeq \Phi^{(\text{n})}(\mathbf{R})\Psi^{(\text{e})}(\mathbf{r}; \mathbf{R}) \quad (\text{A.1.7})$$

where $\Phi^{(\text{n})}(\mathbf{R})$ is a nuclear wave function obtained by solving the following nuclear Schrödinger equation:

$$H^{(\text{n})}\Phi^{(\text{n})}(\mathbf{R}) = E\Phi^{(\text{n})}(\mathbf{R}) \quad (\text{A.1.8})$$

$$H^{(\text{n})} \equiv T^{(\text{n})} + E^{(\text{e})} \quad (\text{A.1.9})$$

A.2 Density Functional Theory

This section summarizes the concept of DFT and several related approximations [214–219]. In this section, we neglect the spin degrees of freedom for simplicity without loss of generality.

A.2.1 Hohenberg-Kohn Theorems

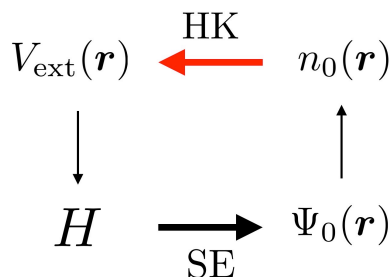


Figure A.1: Schematic picture of the Hohenberg-Kohn Theorem I. Based on the Schrödinger equation (SE), described by a black thick arrow, $V_{\text{ext}}(\mathbf{r})$ determines the Hamiltonian H , $\Psi_0(\mathbf{r})$, and $n_0(\mathbf{r})$ in a sequence. The Hohenberg-Kohn Theorem I is described by a red arrow, which complete the one-to-one correspondence between $V_{\text{ext}}(\mathbf{r})$ and $n_0(\mathbf{r})$.

According to the Born-Oppenheimer (BO) approximation [213] (See Appendix A.1 in detail), we focus on the electron degrees of freedom and consider the electronic Hamiltonian:

$$H = T + V_{\text{int}} + V_{\text{ext}} \quad (\text{A.2.1})$$

$$T = -\sum_i^N \frac{\hbar^2}{2m_e} \nabla_i^2, \quad V_{\text{int}} = \frac{e^2}{2} \sum_{i>j} \frac{1}{|\mathbf{r}_i - \mathbf{r}_j|}, \quad V_{\text{ext}} = -e^2 \sum_i^N \sum_I^M \frac{z_I}{|\mathbf{r}_i - \mathbf{R}_I|} \quad (\text{A.2.2})$$

The heart of DFT is based on the two Hohenberg-Kohn Theorems [220]:

- I. The external potential $V_{\text{ext}}(\mathbf{r})$, which reproduce the ground-state electron density $n_0(\mathbf{r})$, is uniquely determined by $n_0(\mathbf{r})$.

The proof of Theorem I is given in Appendix A.3. Since the Hamiltonian H is also obtained by Theorem I, many-body states including ground-state $\Psi_0(\mathbf{r})$ and any excited state $\Psi_n(\mathbf{r})$ are determined uniquely by $n_0(\mathbf{r})$. Furthermore, any physical quantity obtained by using $\Psi_n(\mathbf{r})$, such as total energy, kinetic energy, and the expectation value of Coulomb potential, is also determined by $n_0(\mathbf{r})$. Note that Theorem I provides no prescription for solving the many-body problem with given $V_{\text{ext}}(\mathbf{r})$. The schematic picture of Theorem I is shown in Fig. A.1.

- II. The total energy as the electron density functional is given by

$$E[n] = F[n] + \int d\mathbf{r} n(\mathbf{r})V_{\text{ext}}(\mathbf{r}) \quad (\text{A.2.3})$$

$$F[n] = T[n] + E_{\text{int}}[n] \quad (\text{A.2.4})$$

where $F[n]$ is defined universally independent of the systems. Based on the variational principle, the electron density that gives the minimum energy corresponds to the ground-state electron density.

The proof of Theorem II is given in Appendix A.4. Theorem II enables us to obtain the ground-state energy without solving the many-body problem. It should be emphasized that there are still two problems. First, Theorem II only provides the properties of the ground state, and no information on the excited states is given. Second, although Theorem II proves the existence of $F[n]$, the explicit expression of $F[n]$ has been still unknown until the present day.

A.2.2 Kohn-Sham Approach

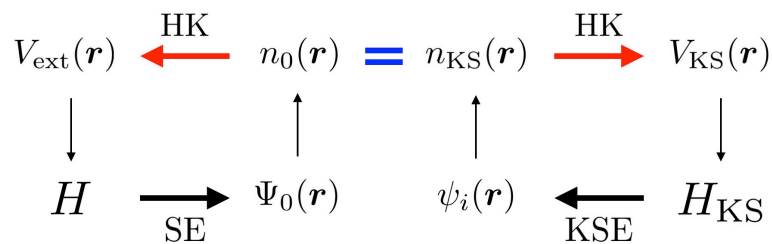


Figure A.2: Schematic picture of the KS approach. A blue symbol of “=” represents the equivalency between the exact many-body system and the auxiliary one-particle system. By solving the KS equation self-consistently, one can obtain the KS orbitals $\psi_i(\mathbf{r})$. In principle, $\psi_i(\mathbf{r})$ determines any property of the exact many-body system.

Following the Hohenberg-Kohn Theorems, we can obtain the exact ground-state energy and electron density by minimizing the functional $E[n]$. However, there is still no concrete prescription for solving the many-body problem because of the absence of the exact form of $F[n]$. Nevertheless, the DFT calculation has been widely used since the advent of an approach proposed by Kohn and Sham in 1965, so-called Kohn-Sham (KS) approach [221].

A crucial idea of the KS approach is to replace the difficult-to-analyze many-body system with an auxiliary one-particle system described by

$$H_{\text{KS}} = T + V_{\text{KS}}(\mathbf{r}) \quad (\text{A.2.5})$$

where $V_{\text{KS}}(\mathbf{r})$ represents an auxiliary external potential whose explicit expression is not given at this stage. The KS approach assumes that the ground-state electron density of the auxiliary system $n_{\text{KS}}(\mathbf{r})$ is equivalent to that of the exact ground-state of the real system, $n_0(\mathbf{r}) = n_{\text{KS}}(\mathbf{r})$ as shown in Fig. A.2. Since the Hohenberg-Kohn Theorems hold even in the absence of the Coulomb interaction among electrons, $V_{\text{KS}}(\mathbf{r})$ is uniquely determined by $n_0(\mathbf{r})$. The ground-state wave function of Eq. (A.2.5) is given by the Slater determinant of the KS orbitals $|\psi_1(\mathbf{r}) \cdots \psi_N(\mathbf{r})|$ (N is the number of electrons) with the energy eigenvalues $\{\epsilon_i(\mathbf{r})\}$. As a result, the electron density is given by

$$n(\mathbf{r}) = n_{\text{KS}}(\mathbf{r}) = \sum_{i=1}^N |\psi_i(\mathbf{r})|^2 \quad (\text{A.2.6})$$

and the kinetic energy is given by

$$T_{\text{KS}}[n] = \frac{\hbar^2}{2m_e} \sum_{i=1}^N \int d\mathbf{r} |\nabla \psi_i(\mathbf{r})|^2 \quad (\text{A.2.7})$$

Here, let us define the Hartree energy as

$$E_{\text{H}}[n] = \frac{e^2}{2} \int d\mathbf{r} d\mathbf{r}' \frac{n(\mathbf{r})n(\mathbf{r}')}{|\mathbf{r} - \mathbf{r}'|} \quad (\text{A.2.8})$$

Using $T_{\text{KS}}[n]$ and $E_{\text{H}}[n]$, the total energy functional given in Eq. (A.2.3) recast as follow:

$$E_{\text{KS}}[n] = T_{\text{KS}}[n] + E_{\text{H}}[n] + E_{\text{xc}}[n] + \int d\mathbf{r} n(\mathbf{r})V_{\text{ext}}(\mathbf{r}) \quad (\text{A.2.9})$$

$$E_{\text{xc}}[n] = F[n] - (T_{\text{KS}}[n] + E_{\text{H}}[n]) = (T[n] - T_{\text{KS}}[n]) + (E_{\text{int}}[n] - E_{\text{H}}[n]) \quad (\text{A.2.10})$$

$$F[n] = T[n] + E_{\text{int}}[n] \quad (\text{A.2.11})$$

where $E_{\text{xc}}[n]$ represents the exchange-correlation energy that is also the functional of $n(\mathbf{r})$. $E_{\text{xc}}[n]$ is the difference between the kinetic energy (interaction energy) of the exact many-body system and that of the auxiliary one-body system where the electron-electron interaction is replaced with the Hartree energy. In other words, all difficulties in the calculation are absorbed in $E_{\text{xc}}[n]$.

Using Lagrange's method of undetermined multipliers, the variational equation of Eq. (A.2.9) with respect to $\psi_i^*(\mathbf{r})$ is given by

$$H_{\text{KS}}\psi_i(\mathbf{r}) = \epsilon_i\psi_i(\mathbf{r}) \quad (\text{A.2.12})$$

Equation (A.2.12) is called KS equation, and $\psi_i(\mathbf{r})$ and ϵ_i are KS orbital and KS energy corresponding to $\psi_i(\mathbf{r})$, respectively. Note that ϵ_i is introduced as an undetermined multiplier under the normalization condition $\langle \psi_i | \psi_i \rangle = 1$. KS Hamiltonian H_{KS} is explicitly given by

$$H_{\text{KS}} = -\frac{\hbar^2}{2m_e} \nabla^2 + V_{\text{KS}}(\mathbf{r}) \quad (\text{A.2.13})$$

$$V_{\text{KS}}(\mathbf{r}) = V_{\text{ext}}(\mathbf{r}) + V_{\text{H}}(\mathbf{r}) + V_{\text{xc}}(\mathbf{r}) \quad (\text{A.2.14})$$

$$V_{\text{H}}(\mathbf{r}) = \frac{\delta E_{\text{H}}}{\delta n(\mathbf{r})} = \int d\mathbf{r}' \frac{n'(\mathbf{r}')}{|\mathbf{r} - \mathbf{r}'|} \quad (\text{A.2.15})$$

$$V_{\text{xc}}(\mathbf{r}) = \frac{\delta E_{\text{xc}}}{\delta n(\mathbf{r})} \quad (\text{A.2.16})$$

By solving Eq. (A.2.12) self-consistently, the ground-state wave function and energy are obtained,

and the total energy is given by Eq. (A.2.9).

Following Hellman-Feynman theorem, $E_{\text{xc}}[n]$ can be reexpressed as

$$E_{\text{xc}}[n] = \frac{e^2}{2} \int d\mathbf{r} d\mathbf{r}' \frac{n(\mathbf{r})n(\mathbf{r}')}{|\mathbf{r} - \mathbf{r}'|} [\bar{g}(\mathbf{r}, \mathbf{r}') - 1] \quad (\text{A.2.17})$$

$$\bar{g}(\mathbf{r}, \mathbf{r}') = \int_0^1 d\lambda \left[1 + \frac{\langle \Psi_\lambda | \delta \hat{n}(\mathbf{r}) \delta \hat{n}(\mathbf{r}') | \Psi_\lambda \rangle - \delta(\mathbf{r} - \mathbf{r}')n(\mathbf{r})}{n(\mathbf{r})n(\mathbf{r}')} \right] \quad (\text{A.2.18})$$

where $\delta \hat{n}(\mathbf{r}) = \hat{n}(\mathbf{r}) - n(\mathbf{r})$, Ψ_λ is the electron wave function when the electron charge is $\sqrt{\lambda}e^2$ ($0 \leq \lambda \leq 1$), and $\bar{g}(\mathbf{r}, \mathbf{r}')$ is the pair-correlation function averaged over λ . In Eq. (A.2.17),

$$n_{\text{xc}}(\mathbf{r}, \mathbf{r}') = n(\mathbf{r}') [\bar{g}(\mathbf{r}, \mathbf{r}') - 1] \quad (\text{A.2.19})$$

$$\int d\mathbf{r}' n_{\text{xc}}(\mathbf{r}, \mathbf{r}') = -1 \quad (\text{A.2.20})$$

is called the exchange-correlation hole. Thus, Eq. (A.2.17) can be interpreted as the Coulomb interaction between the electron and exchange-correlation hole:

$$E_{\text{xc}}[n] = \int d\mathbf{r} n(\mathbf{r}) \epsilon_{\text{xc}}([n], \mathbf{r}) \quad (\text{A.2.21})$$

$$\epsilon_{\text{xc}}([n], \mathbf{r}) = \frac{e^2}{2} \int d\mathbf{r}' \frac{n_{\text{xc}}(\mathbf{r}, \mathbf{r}')}{|\mathbf{r} - \mathbf{r}'|} \quad (\text{A.2.22})$$

where $\epsilon_{\text{xc}}([n], \mathbf{r})$ is a per volume exchange-correlation energy.

By using the spherical harmonics $Y_{lm}(\hat{\mathbf{r}})$, $\hat{\mathbf{r}} = \mathbf{r}/|\mathbf{r}|$, $n_{\text{xc}}(\mathbf{r}, \mathbf{r}')$ is expressed as

$$n_{\text{xc}}(\mathbf{r}, \mathbf{r}') = \sum_{l=0}^{\infty} \sum_{m=-l}^l n_{lm}(\mathbf{r}, |\mathbf{r} - \mathbf{r}'|) Y_{lm}(\widehat{\mathbf{r} - \mathbf{r}'}) \quad (\text{A.2.23})$$

$$n_{lm}(\mathbf{r}, |\mathbf{r} - \mathbf{r}'|) = \int d\hat{\mathbf{r}} n_{\text{xc}}(\mathbf{r}, \mathbf{r}') Y_{lm}^*(\hat{\mathbf{r}}) \quad (\text{A.2.24})$$

Substituting Eq. (A.2.23) into Eq. (A.2.22), $\epsilon_{\text{xc}}([n], \mathbf{r})$ is expanded as

$$\epsilon_{\text{xc}}([n], \mathbf{r}) = \frac{e^2}{2} \sqrt{\pi} \int_0^\infty d\eta \eta^2 \frac{n_{00}(\mathbf{r}, \eta)}{\eta}, \quad \eta = |\mathbf{r} - \mathbf{r}'| \quad (\text{A.2.25})$$

This result indicates that the exchange-correlation energy depends only on the angular mean of $n_{\text{xc}}(\mathbf{r}, \mathbf{r}')$ instead of its detailed shape. In other words, the exact hole density can be replaced with a more straightforward definition that reproduces the angular mean of the original one, rationalizing the local-density approximation discussed below.

Note that the KS approach is a rigorous formulation since no approximation except for the BO approximation is applied at the present stage. Therefore, if the exact form of $\epsilon_{\text{xc}}([n], \mathbf{r})$ is discovered, the ground-state electron density and energy of the many-body system are obtained by solving the KS equation. However, since $\epsilon_{\text{xc}}([n], \mathbf{r})$ is a complicated functional that depends on the KS orbitals $\psi_i(\mathbf{r})$, the remaining problem is how to define an approximate form of $\epsilon_{\text{xc}}([n], \mathbf{r})$. The reliability of the KS approach depends on the validity of the approximate form of $\epsilon_{\text{xc}}([n], \mathbf{r})$.

The local density approximation (LDA) [221] is a well-known approximation that the exchange-correlation energy is replaced with that of the homogeneous electron gas, $\epsilon_{\text{xc}}^{\text{LDA}}(n(\mathbf{r})) = \epsilon_{\text{xc}}^{\text{hom}}(n(\mathbf{r}))$. Although LDA provides surprisingly well results, especially for light metals, it is rationalized only when the electron density is homogeneous. See Appendix A.5 in detail.

As a next step, LDA was revised by considering the exchange-correlation energy as the functional of not only $n(\mathbf{r})$ but also the absolute value of its gradient $|\nabla n(\mathbf{r})|$, $\epsilon_{\text{xc}}^{\text{GGA}}(n(\mathbf{r}), |\nabla n(\mathbf{r})|)$, which is called the generalized gradient approximation (GGA) [222–225]. GGA is one of the most widely used approximations in various field of science, and there are several definitions of $\epsilon_{\text{xc}}^{\text{GGA}}$ proposed by Becke (B88) [226], J. P. Perdew and Y. Wang (PW91) [222, 225], J. P. Perdew, Burke and Ernzerhof (PBE) [186], and so on.

As discussed above, by using approximate expression of the exchange-correlation energy, the KS equation can be solved numerically. Since the potential (input) in the KS Hamiltonian depends on the electron density $n(\mathbf{r})$ (output), an iterative procedure is necessary to find the KS orbital and energy, which is often called a self-consistent field (SCF) calculation as shown in Fig. A.3.

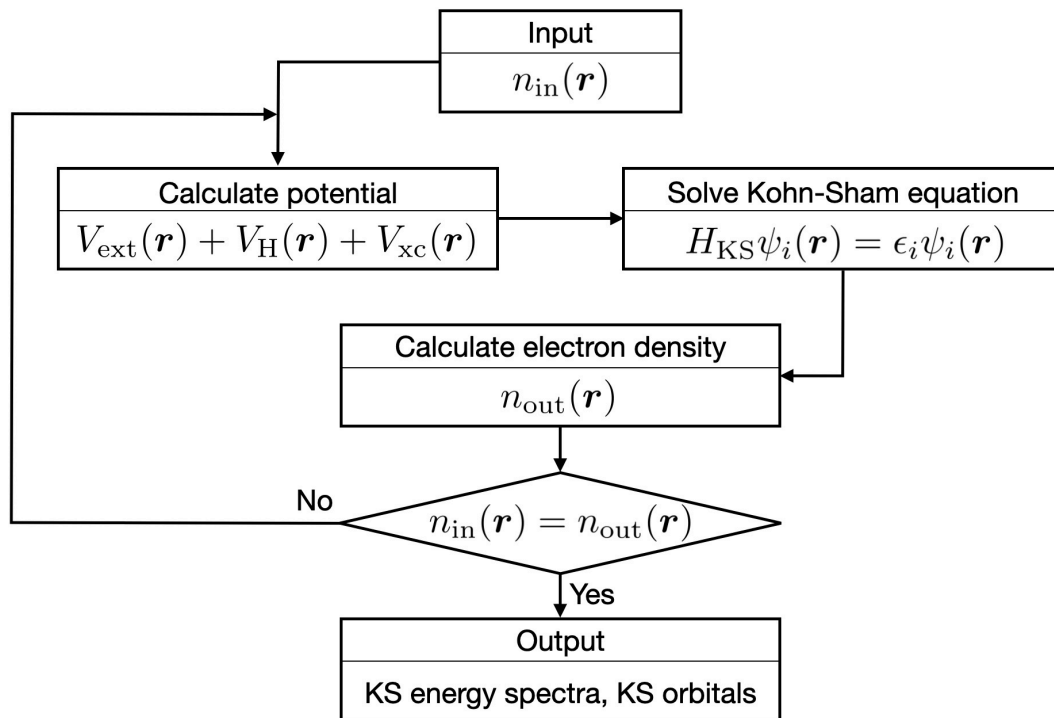


Figure A.3: Workflow of the SCF calculation of the KS equation.

A.3 Proof of Hohenberg-Kohn Theorem I

Let us assume that two different external potentials $V_{\text{ext}}^{(1)}(\mathbf{r})$ and $V_{\text{ext}}^{(2)}(\mathbf{r})$ give the same ground-state electron density $n_0(\mathbf{r})$ (the ground-state is not degenerate) [220]. $V_{\text{ext}}^{(1)}(\mathbf{r})$ and $V_{\text{ext}}^{(2)}(\mathbf{r})$ give two different Hamiltonians $H^{(1)}$ and $H^{(2)}$ and two different ground-state wave functions $\Psi^{(1)}$ and $\Psi^{(2)}$. Then, since $\Psi^{(2)}$ ($\Psi^{(1)}$) is not the ground-state of $H^{(1)}$ ($H^{(2)}$), the following inequalities are satisfied as

$$E^{(1)} = \langle \Psi^{(1)} | H^{(1)} | \Psi^{(1)} \rangle < \langle \Psi^{(2)} | H^{(1)} | \Psi^{(2)} \rangle = E^{(2)} + \int d\mathbf{r} [V_{\text{ext}}^{(1)}(\mathbf{r}) - V_{\text{ext}}^{(2)}(\mathbf{r})] n_0(\mathbf{r}) \quad (\text{A.3.1})$$

$$E^{(2)} = \langle \Psi^{(2)} | H^{(2)} | \Psi^{(2)} \rangle < \langle \Psi^{(1)} | H^{(2)} | \Psi^{(1)} \rangle = E^{(1)} + \int d\mathbf{r} [V_{\text{ext}}^{(2)}(\mathbf{r}) - V_{\text{ext}}^{(1)}(\mathbf{r})] n_0(\mathbf{r}) \quad (\text{A.3.2})$$

By adding the both sides of Eqs. (A.3.1) and (A.3.2), a contradictory inequality is obtained as $E^{(1)} + E^{(2)} < E^{(1)} + E^{(2)}$. As a consequence, the assumption that $V_{\text{ext}}^{(1)}(\mathbf{r})$ and $V_{\text{ext}}^{(2)}(\mathbf{r})$ give the same ground-state electron density $n_0(\mathbf{r})$ is incorrect. In other words, the external potential $V_{\text{ext}}(\mathbf{r})$, which reproduces the ground-state electron density $n_0(\mathbf{r})$, is uniquely determined by $n_0(\mathbf{r})$.

A.4 Proof of Hohenberg-Kohn Theorem II

Let us consider the set of wave functions $\{\Psi_\alpha(\mathbf{r})\}$ that each $\Psi_\alpha(\mathbf{r})$ gives the same electron density $n(\mathbf{r})$ (not ground-state electron density) [227, 228]. The total energy for $\Psi_\alpha(\mathbf{r})$ is given by

$$E_\alpha = \langle \Psi_\alpha | H | \Psi_\alpha \rangle = \langle \Psi_\alpha | T | \Psi_\alpha \rangle + \langle \Psi_\alpha | V_{\text{int}} | \Psi_\alpha \rangle + \int d\mathbf{r} V_{\text{ext}}(\mathbf{r}) n(\mathbf{r}) \quad (\text{A.4.1})$$

Then, by fixing the value of $n(\mathbf{r})$ and determining $\Psi_\alpha(\mathbf{r})$ that gives minimum of $\{E_\alpha\}$, the resultant total energy becomes the functional of $n(\mathbf{r})$:

$$E[n] = \min_\alpha [\langle \Psi_\alpha | T | \Psi_\alpha \rangle + \langle \Psi_\alpha | V_{\text{int}} | \Psi_\alpha \rangle] + \int d\mathbf{r} V_{\text{ext}}(\mathbf{r}) n(\mathbf{r}) \quad (\text{A.4.2})$$

$$= F[n] + \int d\mathbf{r} V_{\text{ext}}(\mathbf{r}) n(\mathbf{r}) \quad (\text{A.4.3})$$

$$F[n] \equiv \min_\alpha [\langle \Psi_\alpha | T | \Psi_\alpha \rangle + \langle \Psi_\alpha | V_{\text{int}} | \Psi_\alpha \rangle] = T[n] + E_{\text{int}}[n] \quad (\text{A.4.4})$$

$F[n]$ is determined by $n(\mathbf{r})$ uniquely. Based on the variational principle, the electron density $n(\mathbf{r})$ that gives the minimum energy is nothing but the ground-state electron density $n_0(\mathbf{r})$.

A.5 Various Approximations for Exchange-Correlation Energy

As discussed in Sec. A.2.2, the exchange-correlation energy functional $E_{\text{xc}}[n]$ must be approximately treated in the practical calculation. The representative approximations are the local density approximation (LDA) and generalized gradient approximation (GGA). Since there are numbers of formulation of LDA and GGA, some major definitions of functionals and their properties are shown in this section.

A.5.1 Local Density Approximation

In the KS approach, by explicitly separating the kinetic energy and long-range Hartree energy terms, it can be justified to approximately treat $E_{xc}[n]$ as a local functional of $n(\mathbf{r})$. As a first step, $E_{xc}[n]$ is approximately expressed as an exchange-correlation energy of the homogeneous electron gas with the local electron density $n(\mathbf{r})$:

$$E_{xc}^{\text{LDA}}[n] = \int d\mathbf{r} n(\mathbf{r}) \epsilon_{xc}^{\text{hom}}(n(\mathbf{r})) \quad (\text{A.5.1})$$

This is the local density approximation (LDA) [221]. $\epsilon_{xc}^{\text{hom}}$ is a per volume exchange-correlation energy of the homogeneous electron gas that is separated into the exchange and correlation contributions

$$\epsilon_{xc}^{\text{hom}}(n(\mathbf{r})) = \epsilon_x^{\text{hom}}(n(\mathbf{r})) + \epsilon_c^{\text{hom}}(n(\mathbf{r})) \quad (\text{A.5.2})$$

where the former is explicitly given by

$$\epsilon_x^{\text{hom}}(n(\mathbf{r})) = -\frac{3e^2}{4} \left(\frac{3}{\pi}\right)^{1/3} n(\mathbf{r})^{1/3} \quad (\text{A.5.3})$$

Although the exact form of $\epsilon_c^{\text{hom}}(n(\mathbf{r}))$ is unknown, there are some approximate analytical definitions.

1. Perdew-Zunger (PZ-LDA) correlation functional [183]

$$\epsilon_c^{\text{PZ-LDA}}(r_s) = \begin{cases} -0.0480 - 0.0116r_s + 0.0311 \ln(r_s) + 0.0020r_s \ln(r_s) & (r_s < 1) \\ -0.1423/(1 + 1.0529\sqrt{r_s} + 0.3334r_s) & (r_s > 1) \end{cases} \quad (\text{A.5.4})$$

where r_s is the Wigner-Seitz radius given by

$$\frac{4}{3}\pi r_s^3 = \frac{1}{n} \quad (\text{A.5.5})$$

2. Vosko-Wilk-Nusair (VWN-LDA) correlation functional [229]

$$\epsilon_c^{\text{VWN-LDA}}(r_s) = \frac{A}{2} \left\{ \ln \left[\frac{r_s}{r_s + b\sqrt{r_s} + c} \right] + \frac{2b}{\sqrt{4c - b^2}} \tan^{-1} \left(\frac{\sqrt{4c - b^2}}{2\sqrt{r_s + b}} \right) - \frac{bx_0}{x_0^2 + bx_0 + c} \left[\ln \left(\frac{(\sqrt{r_s - x_0})^2}{r_s + b\sqrt{r_s} + c} \right) + \frac{2(b + 2x_0)}{\sqrt{4c - b^2}} \tan^{-1} \left(\frac{\sqrt{4c - b^2}}{2\sqrt{r_s + b}} \right) \right] \right\} \quad (\text{A.5.6})$$

where $x_0 = -0.10498$, $b = 3.72744$, $c = 12.9352$, $A = 0.0621814$.

3. Perdew-Wang (PW-LDA) correlation functional [222, 225]

$$\epsilon_c^{\text{PW-LDA}}(r_s) = -2a \int dr n(1 - \alpha r_s) \ln \left[1 + \frac{1}{2a (\beta_1 r_s^{1/2} + \beta_2 r_s + \beta_3 r_s^{3/2} + \beta_4 r_s^2)} \right] \quad (\text{A.5.7})$$

where $a = 0.031097$, $\alpha = 0.21370$, $\beta_1 = 7.5957$, $\beta_2 = 3.5876$, $\beta_3 = 1.6382$, $\beta_4 = 0.49294$.

Note that these correlation functionals are obtained recursively by fitting some numerical quantum

Monte Carlo (QMC) calculation [230] that gives exact results for the homogeneous electron gas [231–233].

A.5.2 Generalized Gradient Approximation

The next approximation is to treat $E_{xc}[n]$ as the functional of not only $n(\mathbf{r})$ but also the absolute value of its gradient $|\nabla n(\mathbf{r})|$:

$$E_{xc}^{\text{GGA}}[n] = \int d\mathbf{r} n(\mathbf{r}) \epsilon_{xc}(n(\mathbf{r}), |\nabla n(\mathbf{r})|) \quad (\text{A.5.8})$$

This is so-called the generalized gradient approximation (GGA) [222–225] and $\epsilon_{xc}(n(\mathbf{r}), |\nabla n(\mathbf{r})|)$ represents the per volume exchange-correlation energy that is separated into the exchange and correlation contributions

$$\epsilon_{xc}(n(\mathbf{r}), |\nabla n(\mathbf{r})|) = \epsilon_x(n(\mathbf{r}), |\nabla n(\mathbf{r})|) + \epsilon_c(n(\mathbf{r}), |\nabla n(\mathbf{r})|) \quad (\text{A.5.9})$$

Although the exact forms of $\epsilon_x(n(\mathbf{r}), |\nabla n(\mathbf{r})|)$ and $\epsilon_c(n(\mathbf{r}), |\nabla n(\mathbf{r})|)$ are unknown, there are some approximate analytical definitions.

- Exchange functional

The exchange functional of GGA has a conventional general form:

$$E_x^{\text{GGA}} = -\frac{e^2}{2} \sum_{\sigma}^{\uparrow, \downarrow} \int d\mathbf{r} n_{\sigma}^{4/3}(\mathbf{r}) K(x_{\sigma}) \quad (\text{A.5.10})$$

where n_{σ} is the spin $\sigma = \uparrow, \downarrow$ electron density, and x_{σ} is the dimensionless parameter given by

$$x_{\sigma} = \frac{|\nabla n_{\sigma}|}{n_{\sigma}^{4/3}} \quad (\text{A.5.11})$$

In the case of LDA,

$$K^{\text{LDA}} = 3 \left(\frac{3}{4\pi} \right)^{1/3} \quad (\text{A.5.12})$$

1. Becke (B88) exchange functional [226]

$$K^{\text{B88-GGA}}(x_{\sigma}) = K^{\text{LDA}} + \frac{2ax_{\sigma}^2}{1 + 6ax_{\sigma} \sinh^{-1}(x_{\sigma})} \quad (\text{A.5.13})$$

where $a = 0.0042$.

2. Perdew-Wang (PW91) exchange functional [222, 225]

$$K^{\text{PW91-GGA}}(x_{\sigma}) = \frac{K^{\text{LDA}}}{1 + 6ax_{\sigma} \sinh^{-1}(x_{\sigma}) + 0.004x_{\sigma}^4/(48\pi^2)^{4/3}} \times \left\{ 1 + 6ax_{\sigma} \sinh^{-1}(x_{\sigma}) + \left[0.2743 - 0.1508 \exp\left(-100x_{\sigma}^2/(48\pi^2)^{2/3}\right) \right] x_{\sigma}^2/(48\pi^2)^{2/3} \right\} \quad (\text{A.5.14})$$

where a is same as that of B88 exchange functional.

3. Perdew-Burke-Ernzerhof (PBE) exchange functional [186]

$$K^{\text{PBE-GGA}}(x_\sigma) = K^{\text{LDA}} \left[1 + \kappa - \frac{\kappa}{1 + \mu x_\sigma^2 / (48\pi^2)^{2/3} \kappa} \right] \quad (\text{A.5.15})$$

where $\mu = 0.21951$ and $\kappa = 0.804$.

• Correlation functional

1. Perdew-Wang (PW91) correlation functional [222]

$$\epsilon_c^{\text{PW91}}[n, s, t] = \epsilon_c^{\text{PW-LDA}}(r_s) + H[n, s, t] \quad (\text{A.5.16})$$

$$H[n, s, t] = \frac{\beta^2}{2\alpha} \ln \left(1 + \frac{2\alpha}{\beta} \frac{t^2 + At^4}{1 + At^2 + A^2t^4} \right) + C_{c0} \left(C_1 + \frac{C_2 + C_3r_s + C_4r_s^2}{1 + C_5r_s + C_6r_s^2 + C_7r_s^3} - C_{c1} \right) t^2 \exp(-100s^2) \quad (\text{A.5.17})$$

$$A = \frac{2\alpha}{\beta} \left[\exp \left(\frac{-2\alpha\epsilon_c^{\text{PW-LDA}}(r_s)}{\beta^2 n} \right) - 1 \right]^{-1}, \quad s = \frac{|\nabla n|}{2k_F n}, \quad t = \frac{|\nabla n|}{2k_s n} \quad (\text{A.5.18})$$

where $k_F = (3\pi^2 n)^{1/3}$ and $k_s = (4k_F/\pi)^{1/2}$. The explicit values of $\alpha, \beta, C_{c0}, C_{c1}, C_i$ ($i = 1 \sim 7$) are given in Refs. [225, 234].

2. Perdew-Burke-Ernzerhof (PBE) correlation functional [186]

$$\epsilon_c^{\text{PBE-GGA}}[n, \zeta, t] = \epsilon_c^{\text{PW-LDA}}(r_s) + H[n, \zeta, t] \quad (\text{A.5.19})$$

$$H[n, \zeta, t] = \frac{e^2}{a_B} \gamma \phi^3 \ln \left(1 + \frac{\beta t^2}{\gamma} \frac{1 + At^2}{1 + At^2 + A^2t^4} \right) \quad (\text{A.5.20})$$

$$A = \frac{\beta}{\gamma} \left[\exp \left(-\frac{\epsilon_c^{\text{PW-LDA}}(r_s)}{\gamma \phi^3 e^2 / a_B} \right) - 1 \right]^{-1} \quad (\text{A.5.21})$$

$$\phi = \frac{(1 + \zeta)^{3/2} + (1 - \zeta)^{3/2}}{2}, \quad t = \frac{|\nabla n|}{2\phi k_s n}, \quad k_s = \sqrt{\frac{4k_F}{\pi a_B}}, \quad a_B = \frac{\hbar^2}{m_e e^2} \quad (\text{A.5.22})$$

where $\zeta = (n_\uparrow - n_\downarrow)/n$ is a spin polarization and $\gamma = 0.031091$ and $\beta = 0.066725$.

In addition to GGA, the meta GGA functionals, which include the second derivative of $n(\mathbf{r})$, has been proposed [235, 236]. In spite of these improvements, LDA/GGA is still insufficient to estimate the energy band gap correctly. In particular, LDA/GGA usually underestimates the band gap of the strongly correlated $3d$ insulators. To consider the strong Coulomb repulsion between pairs of electrons, a methodology that accounts for a phenomenological Hubbard U parameter in LDA/GGA has been proposed (LDA/GGA + U) [237]. There is another approximate approach using the so-called hybrid functional that is based on the ansatz that the exact exchange functional is defined between the Hartree-Fock and GGA exchange functionals, such as the B3LYP [238], PBE0 [239], and HSE [240], and so on.

Appendix B

Atomic Orbitals

We summarize the atomic orbitals used as the initial trial wave function for the Wannier function in the Wannier90 software package [72–74]. We write the atomic orbitals as

$$\varphi_{nlm}(\mathbf{r}) = R_{nl}(r)g_{lm}(\hat{\mathbf{r}}) \quad (\text{B.0.1})$$

where $R_{nl}(r)$ is a radial part and $g_{lm}(\hat{\mathbf{r}})$ is a real representation of angular part (m is a subscript of the real representation orbitals) wave functions, respectively.

B.1 Radial Part

As for the radial function $R_{nl}(r)$, the set of solutions to the radial part of the hydrogenic Schrödinger equation for $l = 0$ (1s, 2s, 3s orbitals) is available:

$$R_1(r) \equiv 2\alpha^{3/2} \exp(-\alpha r) \quad (\text{B.1.1})$$

$$R_2(r) \equiv \frac{1}{2\sqrt{2}}\alpha^{3/2}(2 - \alpha r) \exp(-\alpha r/2) \quad (\text{B.1.2})$$

$$R_3(r) \equiv \sqrt{\frac{4}{27}}\alpha^{3/2} (1 - 2\alpha r/3 + 2\alpha^2 r^2/27) \exp(-\alpha r/3) \quad (\text{B.1.3})$$

where the subscript $l = 0$ in R_{nl} is neglected and $\alpha = Z/a_B$ (a_B is the Bohr radius). The default value of α is $\alpha = 1.0$. $R_n(r)$ is orthonormal,

$$\int dr r^2 R_n(r) R_{n'}(r) = \delta_{nn'} \quad (\text{B.1.4})$$

B.2 Angular Part

As for the angular part of the atomic wave function, the real representation for s , p , d , and f orbitals are defined by [26]

$$\begin{aligned} &\underline{s(l=0)} \\ &g_s = \frac{1}{\sqrt{4\pi}} \end{aligned} \quad (\text{B.2.1})$$

$$\begin{aligned} &\underline{p(l=1)} \\ &g_x = \sqrt{\frac{3}{4\pi}} \frac{x}{r}, \quad g_y = \sqrt{\frac{3}{4\pi}} \frac{y}{r}, \quad g_z = \sqrt{\frac{3}{4\pi}} \frac{z}{r} \end{aligned} \quad (\text{B.2.2})$$

$d(l = 2)$

$$\begin{aligned}
g_u &= \sqrt{\frac{5}{4\pi}} \frac{1}{2} \frac{3z^2 - r^2}{r^2}, & g_v &= \sqrt{\frac{5}{4\pi}} \frac{\sqrt{3}}{2} \frac{x^2 - y^2}{r^2}, & g_{yz} &= \sqrt{\frac{5}{4\pi}} \sqrt{3} \frac{yz}{r^2} \\
g_{zx} &= \sqrt{\frac{5}{4\pi}} \sqrt{3} \frac{zx}{r^2}, & g_{xy} &= \sqrt{\frac{5}{4\pi}} \sqrt{3} \frac{xy}{r^2}
\end{aligned} \tag{B.2.3}$$

 $f(l = 3)$

$$\begin{aligned}
g_{xyz} &= \sqrt{\frac{7}{4\pi}} \sqrt{15} \frac{xyz}{r^3} \\
g_x^\alpha &= \sqrt{\frac{7}{4\pi}} \frac{1}{2} \frac{x(5x^2 - 3r^2)}{r^3}, & g_y^\alpha &= \sqrt{\frac{7}{4\pi}} \frac{1}{2} \frac{y(5y^2 - 3r^2)}{r^3}, & g_z^\alpha &= \sqrt{\frac{7}{4\pi}} \frac{1}{2} \frac{z(5z^2 - 3r^2)}{r^3} \\
g_x^\beta &= \sqrt{\frac{7}{4\pi}} \frac{\sqrt{15}}{2} \frac{x(y^2 - z^2)}{r^3}, & g_y^\beta &= \sqrt{\frac{7}{4\pi}} \frac{\sqrt{15}}{2} \frac{y(z^2 - x^2)}{r^3}, & g_z^\beta &= \sqrt{\frac{7}{4\pi}} \frac{\sqrt{15}}{2} \frac{z(x^2 - y^2)}{r^3}
\end{aligned} \tag{B.2.4}$$

Here, l in g_{lm} is neglected and g_m is orthonormal,

$$\int d\hat{\mathbf{r}} g_m(\hat{\mathbf{r}}) g_{m'}(\hat{\mathbf{r}}) = \delta_{mm'} \tag{B.2.5}$$

B.3 Slater-Koster Parameters

Table B.1: Slater-Koster parameters [99]. (l, m, n) is the direction cosine of the bond.

$V_{s,s}$	$V_{ss\sigma}$
$V_{s,x}$	$lV_{sp\sigma}$
$V_{x,x}$	$l^2V_{pp\sigma} + (1-l^2)V_{pp\pi}$
$V_{x,y}$	$lm(V_{pp\sigma} - V_{pp\pi})$
$V_{x,z}$	$ln(V_{pp\sigma} - V_{pp\pi})$
$V_{s,xy}$	$\sqrt{3}lmV_{sd\sigma}$
V_{s,x^2-y^2}	$\frac{1}{2}\sqrt{3}(l^2-m^2)V_{sd\sigma}$
$V_{s,3z^2-r^2}$	$[n^2 - \frac{1}{2}(l^2+m^2)]V_{sd\sigma}$
$V_{x,xy}$	$\sqrt{3}l^2mV_{pd\sigma} + m(1-2l^2)V_{pd\pi}$
$V_{x,yz}$	$\sqrt{3}lmnV_{pd\sigma} - 2lmnV_{pd\pi}$
$V_{x,zx}$	$\sqrt{3}l^2nV_{pd\sigma} + n(1-2l^2)V_{pd\pi}$
V_{x,x^2-y^2}	$\frac{1}{2}\sqrt{3}l(l^2-m^2)V_{pd\sigma} + l(1-l^2+m^2)V_{pd\pi}$
V_{y,x^2-y^2}	$\frac{1}{2}\sqrt{3}m(l^2-m^2)V_{pd\sigma} - m(1+l^2-m^2)V_{pd\pi}$
V_{z,x^2-y^2}	$\frac{1}{2}\sqrt{3}n(l^2-m^2)V_{pd\sigma} - n(l^2-m^2)V_{pd\pi}$
$V_{x,3z^2-r^2}$	$l[n^2 - \frac{1}{2}(l^2+m^2)]V_{pd\sigma} - \sqrt{3}ln^2V_{pd\pi}$
$V_{y,3z^2-r^2}$	$m[n^2 - \frac{1}{2}(l^2+m^2)]V_{pd\sigma} - \sqrt{3}mn^2V_{pd\pi}$
$V_{z,3z^2-r^2}$	$n[n^2 - \frac{1}{2}(l^2+m^2)]V_{pd\sigma} + \sqrt{3}n(l^2+m^2)V_{pd\pi}$
$V_{xy,xy}$	$3l^2m^2V_{dd\sigma} + (l^2+m^2-4l^2m^2)V_{dd\pi} + (n^2+l^2m^2)V_{dd\delta}$
$V_{xy,yz}$	$3lm^2nV_{dd\sigma} + ln(1-4m^2)V_{dd\pi} + ln(m^2-1)V_{dd\delta}$
$V_{xy,zx}$	$3l^2mnV_{dd\sigma} + mn(1-4l^2)V_{dd\pi} + mn(l^2-1)V_{dd\delta}$
V_{xy,x^2-y^2}	$\frac{3}{2}lm(l^2-m^2)V_{dd\sigma} + 2lm(m^2-l^2)V_{dd\pi} + \frac{1}{2}lm(l^2-m^2)V_{dd\delta}$
V_{yz,x^2-y^2}	$\frac{3}{2}mn(l^2-m^2)V_{dd\sigma} - mn[1+2(l^2-m^2)]V_{dd\pi} + mn[1+\frac{1}{2}(l^2-m^2)]V_{dd\delta}$
V_{zx,x^2-y^2}	$\frac{3}{2}nl(l^2-m^2)V_{dd\sigma} + nl[1-2(l^2-m^2)]V_{dd\pi} - nl[1-\frac{1}{2}(l^2-m^2)]V_{dd\delta}$
$V_{xy,3z^2-r^2}$	$\sqrt{3}lm[n^2 - \frac{1}{2}(l^2+m^2)]V_{dd\sigma} - 2\sqrt{3}lmn^2V_{dd\pi} + \frac{1}{2}\sqrt{3}lm(1+n^2)V_{dd\delta}$
$V_{yz,3z^2-r^2}$	$\sqrt{3}mn[n^2 - \frac{1}{2}(l^2+m^2)]V_{dd\sigma} + \sqrt{3}mn(l^2+m^2-n^2)V_{dd\pi} - \frac{1}{2}\sqrt{3}mn(l^2+m^2)V_{dd\delta}$
$V_{zx,3z^2-r^2}$	$\sqrt{3}ln[n^2 - \frac{1}{2}(l^2+m^2)]V_{dd\sigma} + \sqrt{3}ln(l^2+m^2-n^2)V_{dd\pi} - \frac{1}{2}\sqrt{3}ln(l^2+m^2)V_{dd\delta}$
$V_{x^2-y^2,x^2-y^2}$	$\frac{3}{4}(l^2-m^2)^2V_{dd\sigma} + [l^2+m^2-(l^2-m^2)^2]V_{dd\pi} + [n^2+\frac{1}{4}(l^2-m^2)^2]V_{dd\delta}$
$V_{x^2-y^2,3z^2-r^2}$	$\frac{1}{2}\sqrt{3}(l^2-m^2)[n^2 - \frac{1}{2}(l^2+m^2)]V_{dd\sigma} + \sqrt{3}n^2(m^2-l^2)V_{dd\pi} + \frac{1}{4}\sqrt{3}(1+n^2)(l^2-m^2)V_{dd\delta}$
$V_{3z^2-r^2,3z^2-r^2}$	$[n^2 - \frac{1}{2}(l^2+m^2)]^2V_{dd\sigma} + 3n^2(l^2+m^2)V_{dd\pi} + \frac{3}{4}(l^2+m^2)^2V_{dd\delta}$

Appendix C

Multipole

C.1 Vector Spherical Harmonics

Detailed information about the vector spherical harmonics is summarized in Appendix A in Ref. [110].

The vector spherical harmonics \mathbf{Y}_{lm}^{l+k} is defined by [108, 110]

$$\mathbf{Y}_{lm}^{l+k}(\hat{\mathbf{r}}) = \sum_{n=-1}^1 \langle l+k, m-n; 1, n | lm \rangle Y_{l+k, m-n}(\hat{\mathbf{r}}) \mathbf{e}_{1n}, \quad (k = \pm 1) \quad (\text{C.1.1})$$

$$\mathbf{e}_{10} = \mathbf{e}_z, \quad \mathbf{e}_{1\pm} = \mp \frac{1}{\sqrt{2}} (\mathbf{e}_x \pm i\mathbf{e}_y) \quad (\text{C.1.2})$$

Using the spherical harmonics Y_{lm} , the explicit expression of \mathbf{Y}_{lm}^{l+k} is given by

$$\mathbf{Y}_{lm}^l(\hat{\mathbf{r}}) = \frac{1}{\sqrt{l(l+1)}} l Y_{lm}(\hat{\mathbf{r}}), \quad (\text{C.1.3})$$

$$\mathbf{Y}_{lm}^{l-1}(\hat{\mathbf{r}}) = \frac{1}{\sqrt{l(2l+1)}} [l\hat{\mathbf{r}} - i(\hat{\mathbf{r}} \times \mathbf{l})] Y_{lm}(\hat{\mathbf{r}}), \quad (\text{C.1.4})$$

$$\mathbf{Y}_{lm}^{l+1}(\hat{\mathbf{r}}) = \frac{-1}{\sqrt{(l+1)(2l+1)}} [(l+1)\hat{\mathbf{r}} + i(\hat{\mathbf{r}} \times \mathbf{l})] Y_{lm}(\hat{\mathbf{r}}). \quad (\text{C.1.5})$$

$\mathbf{Y}_{lm}^{l+k}(\hat{\mathbf{r}})$ is an eigenfunction of the orbital angular momentum operator,

$$\mathbf{l}^2 \mathbf{Y}_{lm}^{l+k}(\hat{\mathbf{r}}) = l(l+1) \mathbf{Y}_{lm}^{l+k}(\hat{\mathbf{r}}) \quad (\text{C.1.6})$$

and satisfies the following relation,

$$\left[\mathbf{Y}_{lm}^{l+k}(\hat{\mathbf{r}}) \right]^* = (-1)^{m+k+1} \mathbf{Y}_{l-m}^{l+k}(\hat{\mathbf{r}}) \quad (\text{C.1.7})$$

The vector spherical harmonics satisfy the projective orthogonality relation and completeness relation:

$$\int d\hat{\mathbf{r}} \mathbf{Y}_{l_1 m_1}^{l_1+k_1*}(\hat{\mathbf{r}}) \cdot \mathbf{Y}_{l_2 m_2}^{l_2+k_2}(\hat{\mathbf{r}}) = \delta_{l_1 l_2} \delta_{m_1 m_2} \delta_{k_1 k_2} \quad (\text{C.1.8})$$

$$\sum_{l=0}^{\infty} \sum_{m=-l}^l \sum_{k=0, \pm 1} \mathbf{Y}_{lm}^{l+k\dagger}(\hat{\mathbf{r}}) \mathbf{Y}_{lm}^{l+k}(\hat{\mathbf{r}}') = \hat{I} \delta(\hat{\mathbf{r}} - \hat{\mathbf{r}}') = \hat{I} \frac{1}{\sin \theta} \delta(\theta - \theta') \delta(\phi - \phi') \quad (\text{C.1.9})$$

where \hat{I} is a 3×3 identity matrix.

C.2 Cubic and Hexagonal Harmonics

Table C.1: The upper and lower parts separated by double line represent the cubic and hexagonal harmonics (E multipoles in unit of $-e$) up to rank 4 in the cubic O_h and hexagonal D_{6h} point groups, respectively. In the irreducible representation (irrep.), the subscript and superscript represent the spatial parity (even: g , odd: u) and time reversal property (even: $+$, odd: $-$).

rank	irrep.	symbol	definition
0	A_{1g}^+	Q_0	1
1	T_{1u}^+	Q_x, Q_y, Q_z	x, y, z
2	E_g^+	Q_u, Q_v	$\frac{1}{2}(3z^2 - r^2), \frac{\sqrt{3}}{2}(x^2 - y^2)$
	T_{2g}^+	Q_{yz}, Q_{zx}, Q_{xy}	$\sqrt{3}yz, \sqrt{3}zx, \sqrt{3}xy$
3	A_{2u}^+	Q_{xyz}	$\sqrt{15}xyz$
	T_{1u}^+	$Q_x^\alpha, Q_y^\alpha, Q_z^\alpha$	$\frac{1}{2}x(5x^2 - 3r^2), \frac{1}{2}y(5y^2 - 3r^2), \frac{1}{2}z(5z^2 - 3r^2)$
	T_{2u}^+	$Q_x^\beta, Q_y^\beta, Q_z^\beta$	$\frac{\sqrt{15}}{2}x(y^2 - z^2), \frac{\sqrt{15}}{2}y(z^2 - x^2), \frac{\sqrt{15}}{2}z(x^2 - y^2)$
4	A_{1g}^+	Q_4	$\frac{5\sqrt{21}}{12}(x^4 + y^4 + z^4 - \frac{3}{5}r^4)$
	E_g^+	Q_{4u}, Q_{4v}	$\frac{7\sqrt{15}}{6}\left[z^4 - \frac{x^4 + y^4}{2} - \frac{3}{7}r^2(3z^2 - r^2)\right], \frac{7\sqrt{5}}{4}\left[x^4 - y^4 - \frac{6}{7}r^2(x^2 - y^2)\right]$
	T_{1g}^+	$Q_{4x}^\alpha, Q_{4y}^\alpha, Q_{4z}^\alpha$	$\frac{\sqrt{35}yz(y-z)(y+z)}{2}, -\frac{\sqrt{35}zx(x-z)(x+z)}{2}, \frac{\sqrt{35}xy(x-y)(x+y)}{2}$
	T_{2g}^+	$Q_{4x}^\beta, Q_{4y}^\beta, Q_{4z}^\beta$	$\frac{\sqrt{5}}{2}yz(7x^2 - r^2), \frac{\sqrt{5}}{2}zx(7y^2 - r^2), \frac{\sqrt{5}}{2}xy(7z^2 - r^2)$
0	A_{1g}^+	Q_0	1
1	A_{2u}	Q_z	z
	E_{1u}	Q_x, Q_y	x, y
2	A_{1g}^+	Q_u	$\frac{1}{2}(3z^2 - r^2)$
	E_{1g}^+	Q_{zx}, Q_{yz}	$\sqrt{3}zx, \sqrt{3}yz$
	E_{2g}^+	Q_v, Q_{xy}	$\frac{\sqrt{3}}{2}(x^2 - y^2), -\sqrt{3}xy$
3	A_{2u}^+	Q_z^α	$\frac{1}{2}z(5z^2 - 3r^2)$
	B_{1u}^+	Q_{3a}	$\frac{\sqrt{10}}{4}y(3x^2 - y^2)$
	B_{2u}^+	Q_{3b}	$\frac{\sqrt{10}}{4}x(x^2 - 3y^2)$
	E_{1u}^+	Q_{3u}, Q_{3v}	$\frac{\sqrt{6}}{4}x(5z^2 - r^2), \frac{\sqrt{6}}{4}y(5z^2 - r^2)$
	E_{2u}^+	Q_z^β, Q_{xyz}	$\frac{\sqrt{15}}{2}z(x^2 - y^2), \sqrt{15}xyz$
4	A_{1g}^+	Q_{40}	$\frac{1}{8}(35z^4 - 30z^2r^2 + 3r^4)$
	B_{1g}^+	Q_{4a}	$\frac{\sqrt{70}}{4}zx(x^2 - 3y^2)$
	B_{2g}^+	Q_{4b}	$\frac{\sqrt{70}}{4}yz(3x^2 - y^2)$
	E_{1g}^+	$Q_{4u}^\alpha, Q_{4v}^\alpha$	$\frac{\sqrt{10}}{4}zx(7z^2 - 3r^2), \frac{\sqrt{10}}{4}yz(7z^2 - 3r^2)$
	E_{2g}^+	$Q_{4u}^\beta, Q_{4v}^\beta$	$\frac{\sqrt{35}}{8}(x^4 - 6x^2y^2 + y^4), \frac{\sqrt{35}}{2}xy(x^2 - y^2)$
	E_{2g}^+	$Q_{4u}^{\beta 2}, Q_{4v}^{\beta 2}$	$\frac{\sqrt{5}}{4}(x^2 - y^2)(7z^2 - r^2), -\frac{\sqrt{5}}{2}xy(7z^2 - r^2)$

C.3 Projection-Based Clebsch-Gordan Coefficients

C.3.1 Projection Operators

Let us consider two independent complete orthonormal multipole basis sets $\{X_\alpha\}$ and $\{Y_\beta\}$, where α and β are the labels specifying the individual basis which are expressed as $\alpha = (X_\alpha, l_\alpha, \Gamma_\alpha, m_\alpha, \gamma_\alpha)$: X_α , l_α , Γ_α , m_α and γ_α are the type $Q/M/T/G$, rank, irreducible representation, multiplicity, and component of the multipole basis, respectively. Note that the time reversal and spatial inversion parities (t, p) ($p = 0(1)$ represents polar (axial)) are uniquely determined by specifying X_α . Specifically, (t, p) of Q , M , T , and G are $(1, 0)$, $(-1, 1)$, $(-1, 0)$, $(1, 1)$, respectively.

Hereafter, we use the bracket notation given by Eq. (3.1.1) in the main text. Since the direct products between X_α and Y_β constitute a complete orthonormal basis set, we can also construct a combined basis by their linear combination as

$$|Z_j\rangle = \sum_{\alpha\beta} C_{\alpha\beta}^j |X_\alpha \otimes Y_\beta\rangle \quad (\text{C.3.1})$$

where $j = (\Gamma, m, \gamma)$, and Γ , m , and γ are the irreducible representation of the point group, multiplicity, and component, respectively. $C_{\alpha\beta}^j$ is the point-group version of the Clebsch-Gordan (CG) coefficient obtained by using the projection operator as follows.

A basis function $|\phi_{\Gamma\gamma}\rangle$, which is characterized by the irreducible representation Γ and its component γ , is transformed by the symmetry operation \mathcal{G} as

$$\mathcal{G}|\phi_{\Gamma\gamma}\rangle = \sum_{\gamma'} D_{\gamma'\gamma}^\Gamma(\mathcal{G})|\phi_{\Gamma\gamma'}\rangle \quad (\text{C.3.2})$$

where $G(\Gamma)$ is the representation matrix satisfying the great orthogonality theorem:

$$\frac{d_\Gamma}{N_g} \sum_{\mathcal{G}} D_{ij}^\Gamma(\mathcal{G}) D_{kl}^{\Gamma'*}(\mathcal{G}) = \delta_{ik} \delta_{jl} \delta_{\Gamma\Gamma'} \quad (\text{C.3.3})$$

where d_Γ and N_g denote the dimension of Γ representation and the number of symmetry operations. Then, the projection operator is defined by

$$\mathcal{P}_{\Gamma\gamma}(\gamma') = \frac{d_\Gamma}{N_g} \sum_{\mathcal{G}} D_{\gamma'\gamma}^{\Gamma*}(\mathcal{G}) \mathcal{G} \quad (\text{C.3.4})$$

Using Eqs. (C.3.2) and (C.3.3), $\mathcal{P}_{\Gamma\gamma}(\gamma')$ acts on arbitrary basis given by the linear combination of $|\phi_{\Gamma\gamma}\rangle$, $|\psi\rangle = \sum_{\Gamma\gamma} c(\Gamma\gamma, \psi) |\phi_{\Gamma\gamma}\rangle$ as

$$\mathcal{P}_{\Gamma\gamma}(\gamma') |\psi\rangle = c(\Gamma\gamma', \psi) |\phi_{\Gamma\gamma}\rangle \quad (\text{C.3.5})$$

Thus, the projection operator $\mathcal{P}_{\Gamma\gamma}(\gamma')$ extracts the basis $|\phi_{\Gamma\gamma}\rangle$ and the coefficient $c(\Gamma\gamma', \psi)$ from $|\psi\rangle$.

C.3.2 Clebsch-Gordan Coefficients

Based on the above, let us introduce a projection operator $\mathcal{P}_j(\gamma'_j)$ that acts on $|X_\alpha \otimes Y_\beta\rangle$ and extract a j basis with its component γ'_j , $|W_j^{\alpha\beta}(\gamma'_j)\rangle$:

$$|W_j^{\alpha\beta}(\gamma'_j)\rangle = \mathcal{P}_j(\gamma'_j) |X_\alpha \otimes Y_\beta\rangle \quad (\text{C.3.6})$$

Since the time reversal and spatial inversion parities (t, p) of $|W_j^{\alpha\beta}(\gamma'_j)\rangle$ and $|X_\alpha \otimes Y_\beta\rangle$ must be same, the projection operator can be explicitly defined by

$$\mathcal{P}_j(\gamma'_j) = \delta(t_j t_\alpha t_\beta, +) \Delta_{l_j l_\alpha l_\beta}^{p_j p_\alpha p_\beta} \frac{d_{\Gamma_j}}{N_g} \sum_{\mathcal{G}} D_{\gamma'_j \gamma'_j}^{\Gamma_j^*}(\mathcal{G}) \mathcal{G}_X \mathcal{G}_Y \quad (\text{C.3.7})$$

where $\delta(t_j t_\alpha t_\beta, +)$ and $\Delta_{l_j l_\alpha l_\beta}^{p_j p_\alpha p_\beta}$ denote the selection rules due to the time reversal and spacial inversion parities, and they are defined by

$$\delta(t_j t_\alpha t_\beta, +) = \begin{cases} 1 & t_j t_\alpha t_\beta = 1 \\ 0 & t_j t_\alpha t_\beta = -1 \end{cases} \quad (\text{C.3.8})$$

$$\Delta_{l_j l_\alpha l_\beta}^{p_j p_\alpha p_\beta} = (l_j + p_j + l_\alpha + p_\alpha + l_\beta + p_\beta) \bmod 2 \quad (\text{C.3.9})$$

Using Eq. (C.3.7) and $\alpha' = (X_\alpha, l_\alpha, \Gamma_\alpha, m_\alpha, \gamma'_\alpha)$, $\beta' = (X_\beta, l_\beta, \Gamma_\beta, m_\beta, \gamma'_\beta)$, Eq. (C.3.6) is reexpressed as

$$\begin{aligned} |W_j^{\alpha\beta}(\gamma'_j)\rangle &= \sum_{\gamma'_\alpha \gamma'_\beta} p_{\alpha' \beta'}^{j(\gamma'_j)}(\alpha, \beta) |X_{\alpha'} \otimes Y_{\beta'}\rangle \\ p_{\alpha' \beta'}^{j(\gamma'_j)}(\alpha, \beta) &\equiv \delta(t_j t_\alpha t_\beta, +) \Delta_{l_j l_\alpha l_\beta}^{p_j p_\alpha p_\beta} \frac{d_{\Gamma_j}}{N_g} \sum_{\mathcal{G}} D_{\gamma'_j \gamma'_j}^{\Gamma_j^*}(\mathcal{G}) D_{\gamma'_\alpha \gamma_\alpha}^{\Gamma_\alpha}(\mathcal{G}) D_{\gamma'_\beta \gamma_\beta}^{\Gamma_\beta}(\mathcal{G}) \end{aligned} \quad (\text{C.3.10})$$

where $p_{\alpha' \beta'}^{j(\gamma'_j)}(\alpha, \beta)$ is obtained based on the information of the representation matrices $\hat{D}^\Gamma(\mathcal{G})$ for all irreducible representations and the set of labels (j, α, β) .

From the selection rules given by Eqs. (C.3.8) and (C.3.9), the time reversal parities $t_\alpha t_\beta$ and t_j must be same, and when $l_\alpha + l_\beta$ and l_j differ by an even (odd) number, the spatial parities of $p_\alpha + p_\beta$ and p_j must be equal (different). Due to these facts, given $|X_\alpha \otimes Y_\beta\rangle$, $Q_{2m} (T_{2m})$ and $G_{2n+1} (M_{2n+1})$ or $Q_{2m+1} (T_{2m+1})$ and $G_{2n} (M_{2n})$ become indistinguishable when both of them belonging to the same irreducible representation, In addition, the rank l_j obtained by combining X_α and Y_β satisfies $|l_\alpha - l_\beta| \leq l_j \leq l_\alpha + l_\beta$, and only its parity (even or odd) is precisely preserved. Then, l_j is defined uniquely by choosing the smallest even or odd number within the scope of it, which is expressed by following equation,

$$l_j = |l_\alpha - l_\beta| + (p_\alpha + p_\beta + p_j) \bmod 2 \quad (\text{C.3.11})$$

Since $\hat{W}_j^{\alpha\beta}(\gamma'_j)$ is not orthogonal, it should be orthogonalized by the Gram-Schmidt orthonormalization. Basis having different ranks may be mixed in this procedure, since the Gram-Schmidt orthogonalization procedure subtracts overlapping of lower rank basis. Nevertheless, the rank before orthogonalization can be used as it is. In addition, Q and T ($p = 0$) are generated preferentially against G and M in the orthogonalization procedure.

Appendix D

Graphene

D.1 Multipole Basis for Graphene

The explicit expressions of $Q_0^{(\text{ab},n)}(\mathbf{k})$ ($n = 3, 4$) given Eq. (4.4.23) in the main text are given by

$$Q_0^{(\text{ab},n)}(\mathbf{k}) = \frac{1}{\sqrt{2}} Q_0^{(\text{a})} \otimes \left(Q_0^{(\text{t},2)} Q_0^{(n)}(\mathbf{k}) + T_{3a}^{(\text{t})} T_{3a}^{(n)}(\mathbf{k}) \right) \quad (\text{D.1.1})$$

and $Q_0^{(\text{ab},n)}(\mathbf{k})$ ($n = 2, 5, 6$) are given by

$$Q_0^{(\text{ab},n)}(\mathbf{k}) = Q_0^{(\text{a})} \otimes Q_0^{(n)}(\mathbf{k}) \quad (\text{D.1.2})$$

where $Q_0^{(n)}(\mathbf{k})$ and $T_{3a}^{(n)}(\mathbf{k})$ ($n = 2, \dots, 6$) are given by

$$Q_0^{(2)}(\mathbf{k}) = \frac{\sqrt{6}}{3} \left[2 \cos\left(\frac{k_x}{2}\right) \cos\left(\frac{\sqrt{3}k_y}{2}\right) + \cos(k_x) \right] \quad (\text{D.1.3})$$

$$Q_0^{(3)}(\mathbf{k}) = \frac{\sqrt{6}}{3} \left[-2 \sin^2\left(\frac{\sqrt{3}k_y}{3}\right) + 2 \cos(k_x) \cos\left(\frac{\sqrt{3}k_y}{3}\right) + 1 \right] \quad (\text{D.1.4})$$

$$Q_0^{(4)}(\mathbf{k}) = \frac{\sqrt{3}}{3} \left[\cos\left(\frac{k_x}{2} - \frac{5\sqrt{3}k_y}{6}\right) + \cos\left(\frac{k_x}{2} + \frac{5\sqrt{3}k_y}{6}\right) + \cos\left(k_x - \frac{2\sqrt{3}k_y}{3}\right) \right. \\ \left. + \cos\left(k_x + \frac{2\sqrt{3}k_y}{3}\right) + \cos\left(\frac{9k_x - \sqrt{3}k_y}{6}\right) + \cos\left(\frac{9k_x + \sqrt{3}k_y}{6}\right) \right] \quad (\text{D.1.5})$$

$$Q_0^{(5)}(\mathbf{k}) = \frac{\sqrt{6}}{3} \left[2 \cos\left(\frac{3k_x}{2}\right) \cos\left(\frac{\sqrt{3}k_y}{2}\right) + \cos(\sqrt{3}k_y) \right] \quad (\text{D.1.6})$$

$$Q_0^{(6)}(\mathbf{k}) = \frac{\sqrt{6}}{3} \left[-2 \sin^2(k_x) + 2 \cos(k_x) \cos(\sqrt{3}k_y) + 1 \right] \quad (\text{D.1.7})$$

$$T_{3a}^{(3)}(\mathbf{k}) = \frac{2\sqrt{6}}{3} \left[-\cos(k_x) + \cos\left(\frac{\sqrt{3}k_y}{3}\right) \right] \sin\left(\frac{\sqrt{3}k_y}{3}\right) \quad (\text{D.1.8})$$

$$T_{3a}^{(4)}(\mathbf{k}) = \frac{\sqrt{3}}{3} \left[-\sin\left(\frac{k_x}{2} - \frac{5\sqrt{3}k_y}{6}\right) + \sin\left(\frac{k_x}{2} + \frac{5\sqrt{3}k_y}{6}\right) + \sin\left(k_x - \frac{2\sqrt{3}k_y}{3}\right) \right]$$

$$- \sin \left(k_x + \frac{2\sqrt{3}k_y}{3} \right) + \sin \left(\frac{9k_x - \sqrt{3}k_y}{6} \right) - \sin \left(\frac{9k_x + \sqrt{3}k_y}{6} \right) \Big] \quad (\text{D.1.9})$$

$$T_{3a}^{(5)}(\mathbf{k}) = \frac{\sqrt{6}}{3} \left[-2 \sin \left(\frac{\sqrt{3}k_y}{2} \right) \cos \left(\frac{3k_x}{2} \right) + \sin \left(\sqrt{3}k_y \right) \right] \quad (\text{D.1.10})$$

D.2 Comparison of Band Dispersion

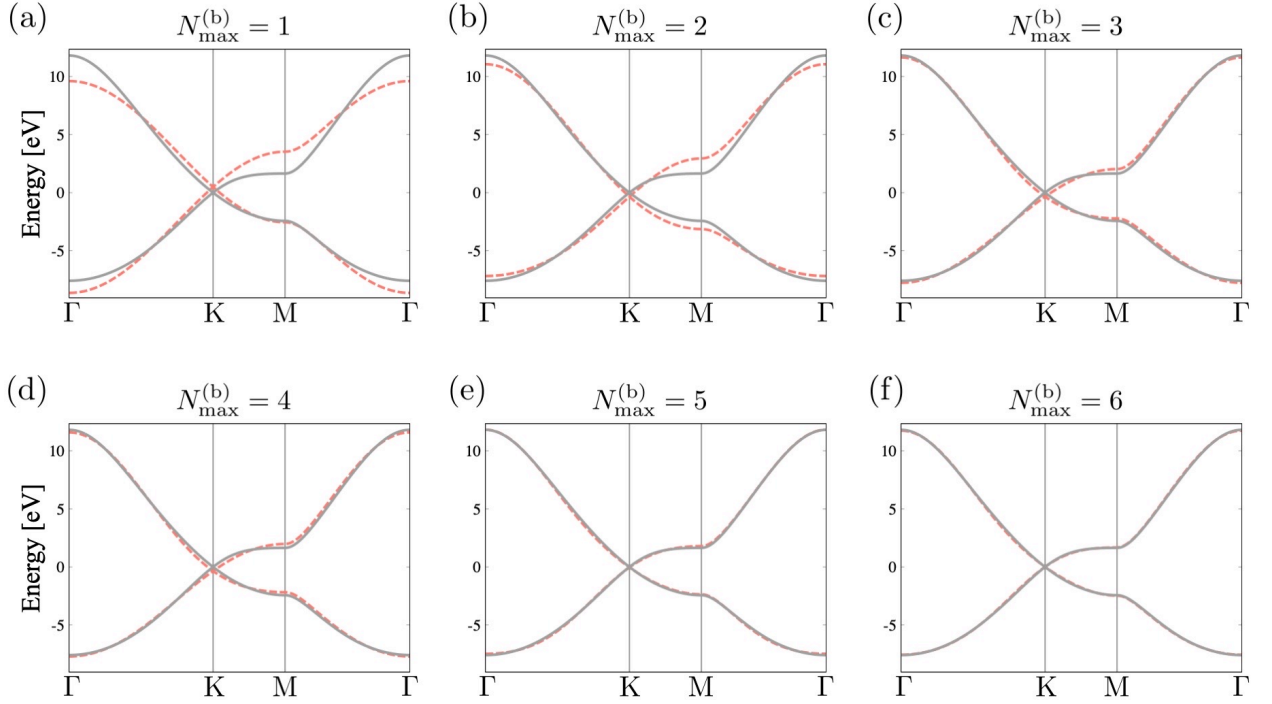


Figure D.1: The comparisons of the band dispersion between DFT calculation (solid grey lines) and our TB models (dashed red lines) obtained by the linear regression. (a)-(f) $N_{\max}^{(b)} = 1-6$. The Fermi energy is taken as the origin.

Appendix E

SrVO₃

E.1 Multipole Basis for SrVO₃

The explicit expressions of $Q_{0,m}^{(\text{ab},n)}(\mathbf{k})$ ($n = 1 \sim 6, m = 1, 2$) given Eq. (4.4.42) in the main text are given by

$$Q_{0,1}^{(\text{ab},n)}(\mathbf{k}) = Q_0^{(\text{a})} \otimes Q_0^{(n)}(\mathbf{k}) \quad (\text{E.1.1})$$

$$Q_{0,2}^{(\text{ab})}(\mathbf{k}) = \frac{1}{\sqrt{2}} \left(Q_u^{(\text{a})} \otimes Q_u^{(n)}(\mathbf{k}) + Q_v^{(\text{a})} \otimes Q_v^{(n)}(\mathbf{k}) \right) \quad (\text{E.1.2})$$

On the other hand, the explicit expressions of $Q_{0,m}^{(\text{ab},n)}(\mathbf{k})$ ($m = 3, 4$) are given by

$$Q_{0,3}^{(\text{ab},n)}(\mathbf{k}) (n = 2, 3, 6) = Q_{0,4}^{(\text{ab},5)}(\mathbf{k}) = \frac{1}{\sqrt{3}} \left(Q_{yz}^{(\text{a})} \otimes Q_{yz}^{(n)}(\mathbf{k}) + Q_{zx}^{(\text{a})} \otimes Q_{zx}^{(n)}(\mathbf{k}) + Q_{xy}^{(\text{a})} \otimes Q_{xy}^{(n)}(\mathbf{k}) \right) \quad (\text{E.1.3})$$

$$Q_{0,3}^{(\text{ab},5)}(\mathbf{k}) = \frac{1}{\sqrt{2}} \left(Q_u^{(\text{a})} \otimes Q_{4u}^{(n)}(\mathbf{k}) + Q_v^{(\text{a})} \otimes Q_{4v}^{(n)}(\mathbf{k}) \right) \quad (\text{E.1.4})$$

$$Q_{0,4}^{(\text{ab},6)}(\mathbf{k}) = \frac{1}{\sqrt{3}} \left(Q_{yz}^{(\text{a})} \otimes Q_{4x}^{(n)}(\mathbf{k}) + Q_{zx}^{(\text{a})} \otimes Q_{4y}^{(n)}(\mathbf{k}) + Q_{xy}^{(\text{a})} \otimes Q_{4z}^{(n)}(\mathbf{k}) \right) \quad (\text{E.1.5})$$

$Q_0^{(n)}(\mathbf{k}), (Q_u^{(n)}(\mathbf{k}), Q_v^{(n)}(\mathbf{k})), (Q_{4u}^{(n)}(\mathbf{k}), Q_{4v}^{(n)}(\mathbf{k})), (Q_{yz}^{(n)}(\mathbf{k}), Q_{zx}^{(n)}(\mathbf{k}), Q_{xy}^{(n)}(\mathbf{k})),$
and $(Q_{4x}^{(n)}(\mathbf{k}), Q_{4y}^{(n)}(\mathbf{k}), Q_{4z}^{(n)}(\mathbf{k}))$ are given by

$$Q_0^{(2)}(\mathbf{k}) = \frac{2\sqrt{3}}{3} [\cos(k_x) \cos(k_y) + \cos(k_x) \cos(k_z) + \cos(k_y) \cos(k_z)] \quad (\text{E.1.6})$$

$$Q_0^{(3)}(\mathbf{k}) = 2\sqrt{2} \cos(k_x) \cos(k_y) \cos(k_z) \quad (\text{E.1.7})$$

$$Q_0^{(4)}(\mathbf{k}) = \frac{\sqrt{6}}{3} [\cos(2k_x) + \cos(2k_y) + \cos(2k_z)] \quad (\text{E.1.8})$$

$$Q_0^{(5)}(\mathbf{k}) = \frac{\sqrt{6}}{3} [\cos(k_x) \cos(2k_y) + \cos(k_x) \cos(2k_z) + \cos(2k_x) \cos(k_y) + \cos(2k_x) \cos(k_z) + \cos(k_y) \cos(2k_z) + \cos(2k_y) \cos(k_z)] \quad (\text{E.1.9})$$

$$Q_0^{(6)}(\mathbf{k}) = \frac{2\sqrt{6}}{3} [\cos(k_x) \cos(k_y) \cos(2k_z) + \cos(k_x) \cos(2k_y) \cos(k_z) + \cos(2k_x) \cos(k_y) \cos(k_z)] \quad (\text{E.1.10})$$

$$Q_u^{(2)}(\mathbf{k}) = \frac{\sqrt{6}}{3} [2 \cos(k_x) \cos(k_y) - \cos(k_x) \cos(k_z) - \cos(k_y) \cos(k_z)] \quad (\text{E.1.11})$$

$$Q_u^{(4)}(\mathbf{k}) = \frac{\sqrt{3}}{3} [\cos(2k_x) + \cos(2k_y) - 2 \cos(2k_z)] \quad (\text{E.1.12})$$

$$Q_u^{(5)}(\mathbf{k}) = \frac{\sqrt{3}}{21} [13 \cos(k_x) \cos(2k_y) - 2 \cos(k_x) \cos(2k_z) + 13 \cos(2k_x) \cos(k_y) - 11 \cos(2k_x) \cos(k_z) - 2 \cos(k_y) \cos(2k_z) - 11 \cos(2k_y) \cos(k_z)] \quad (\text{E.1.13})$$

$$Q_u^{(6)}(\mathbf{k}) = \frac{2\sqrt{3}}{3} [2 \cos(k_x) \cos(k_y) \cos(2k_z) - \cos(k_x) \cos(2k_y) \cos(k_z) - \cos(2k_x) \cos(k_y) \cos(k_z)] \quad (\text{E.1.14})$$

$$Q_v^{(2)}(\mathbf{k}) = \sqrt{2} [-\cos(k_x) + \cos(k_y)] \cos(k_z) \quad (\text{E.1.15})$$

$$Q_v^{(4)}(\mathbf{k}) = -\cos(2k_x) + \cos(2k_y) \quad (\text{E.1.16})$$

$$Q_v^{(5)}(\mathbf{k}) = -\frac{3 \cos(k_x) \cos(2k_y)}{7} - \frac{8 \cos(k_x) \cos(2k_z)}{7} + \frac{3 \cos(2k_x) \cos(k_y)}{7} - \frac{5 \cos(2k_x) \cos(k_z)}{7} + \frac{8 \cos(k_y) \cos(2k_z)}{7} + \frac{5 \cos(2k_y) \cos(k_z)}{7} \quad (\text{E.1.17})$$

$$Q_v^{(6)}(\mathbf{k}) = 2 [-\cos(k_x) \cos(2k_y) + \cos(2k_x) \cos(k_y)] \cos(k_z) \quad (\text{E.1.18})$$

$$Q_{4u}^{(5)}(\mathbf{k}) = \frac{3 \cos(k_x) \cos(2k_y)}{7} - \frac{8 \cos(k_x) \cos(2k_z)}{7} + \frac{3 \cos(2k_x) \cos(k_y)}{7} + \frac{5 \cos(2k_x) \cos(k_z)}{7} - \frac{8 \cos(k_y) \cos(2k_z)}{7} + \frac{5 \cos(2k_y) \cos(k_z)}{7} \quad (\text{E.1.19})$$

$$Q_{yz}^{(2)}(\mathbf{k}) = 2 \sin(k_y) \sin(k_z) \quad (\text{E.1.20})$$

$$Q_{zx}^{(2)}(\mathbf{k}) = 2 \sin(k_z) \sin(k_x) \quad (\text{E.1.21})$$

$$Q_{xy}^{(2)}(\mathbf{k}) = 2 \sin(k_x) \sin(k_y) \quad (\text{E.1.22})$$

$$Q_{yz}^{(3)}(\mathbf{k}) = 2\sqrt{2} \sin(k_y) \sin(k_z) \cos(k_x) \quad (\text{E.1.23})$$

$$Q_{zx}^{(3)}(\mathbf{k}) = 2\sqrt{2} \sin(k_z) \sin(k_x) \cos(k_y) \quad (\text{E.1.24})$$

$$Q_{xy}^{(3)}(\mathbf{k}) = 2\sqrt{2} \sin(k_x) \sin(k_y) \cos(k_z) \quad (\text{E.1.25})$$

$$Q_{yz}^{(5)}(\mathbf{k}) = 2\sqrt{2} [\cos(k_y) + \cos(k_z)] \sin(k_y) \sin(k_z) \quad (\text{E.1.26})$$

$$Q_{zx}^{(5)}(\mathbf{k}) = 2\sqrt{2} [\cos(k_z) + \cos(k_x)] \sin(k_z) \sin(k_x) \quad (\text{E.1.27})$$

$$Q_{xy}^{(5)}(\mathbf{k}) = 2\sqrt{2} [\cos(k_x) + \cos(k_y)] \sin(k_x) \sin(k_y) \quad (\text{E.1.28})$$

$$Q_{yz}^{(6)}(\mathbf{k}) = \frac{4\sqrt{89}}{89} [4 \sin^2(k_x) + 9 \cos(k_x) \cos(k_y) + 9 \cos(k_z) \cos(k_x) - 2] \sin(k_y) \sin(k_z) \quad (\text{E.1.29})$$

$$Q_{zx}^{(6)}(\mathbf{k}) = \frac{4\sqrt{89}}{89} [4 \sin^2(k_y) + 9 \cos(k_x) \cos(k_y) + 9 \cos(k_y) \cos(k_z) - 2] \sin(k_z) \sin(k_x) \quad (\text{E.1.30})$$

$$Q_{xy}^{(6)}(\mathbf{k}) = \frac{4\sqrt{89}}{89} [4 \sin^2(k_z) + 9 \cos(k_z) \cos(k_x) + 9 \cos(k_y) \cos(k_z) - 2] \sin(k_x) \sin(k_y) \quad (\text{E.1.31})$$

$$Q_{4x}^{(6)}(\mathbf{k}) = \frac{2\sqrt{178}}{89} [18 \sin^2(k_x) - 4 \cos(k_x) \cos(k_y) - 4 \cos(k_z) \cos(k_x) - 9] \sin(k_y) \sin(k_z) \quad (\text{E.1.32})$$

$$Q_{4y}^{(6)}(\mathbf{k}) = \frac{2\sqrt{178}}{89} [18 \sin^2(k_y) - 4 \cos(k_x) \cos(k_y) - 4 \cos(k_y) \cos(k_z) - 9] \sin(k_z) \sin(k_x) \quad (\text{E.1.33})$$

$$Q_{4z}^{(6)}(\mathbf{k}) = \frac{2\sqrt{178}}{89} [18 \sin^2(k_z) - 4 \cos(k_z) \cos(k_x) - 4 \cos(k_y) \cos(k_z) - 9] \sin(k_x) \sin(k_y) \quad (\text{E.1.34})$$

E.2 Comparison of Band Dispersion

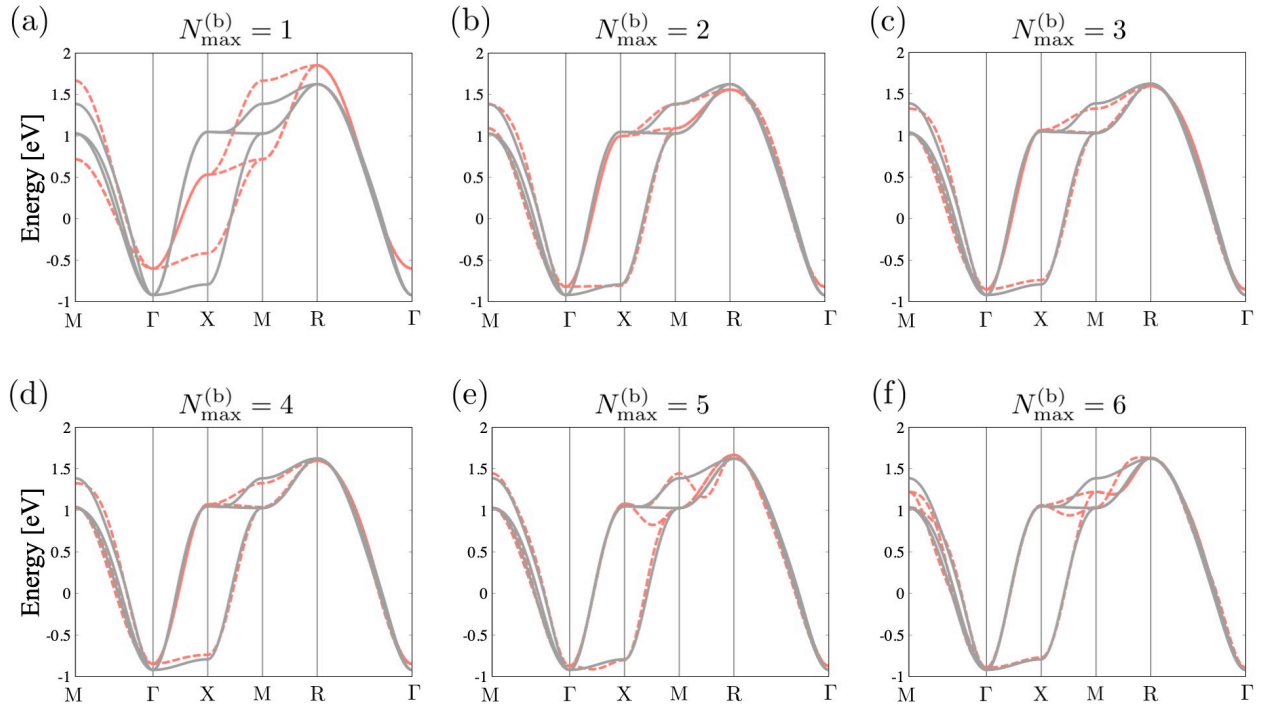


Figure E.1: The comparisons of the band dispersion between DFT calculation (solid grey lines) and our TB models (dashed red lines) obtained by the linear regression. (a)-(f) $N_{\max}^{(b)}=1-6$. The Fermi energy is taken as the origin.

Appendix F

MoS₂

F.1 Momentum Multipole Basis

F.1.1 Nearest-Neighbor Mo–Mo Bond-Cluster

$$\begin{aligned}
Q_0^{(\text{Mo-Mo})}(\mathbf{k}) &= \frac{\sqrt{6}}{3} \left[2 \cos\left(\frac{k_x a}{2}\right) \cos\left(\frac{\sqrt{3}k_y a}{2}\right) + \cos(k_x a) \right] \\
Q_v^{(\text{Mo-Mo})}(\mathbf{k}) &= \frac{2\sqrt{3}}{3} \left[\cos\left(\frac{k_x a}{2}\right) \cos\left(\frac{\sqrt{3}k_y a}{2}\right) - \cos(k_x a) \right] \\
Q_{xy}^{(\text{Mo-Mo})}(\mathbf{k}) &= 2 \sin\left(\frac{k_x a}{2}\right) \sin\left(\frac{\sqrt{3}k_y a}{2}\right) \\
T_x^{(\text{Mo-Mo})}(\mathbf{k}) &= -\frac{2\sqrt{3}}{3} \left[\sin\left(\frac{k_x a}{2}\right) \cos\left(\frac{\sqrt{3}k_y a}{2}\right) + \sin(k_x a) \right] \\
T_y^{(\text{Mo-Mo})}(\mathbf{k}) &= -2 \sin\left(\frac{\sqrt{3}k_y a}{2}\right) \cos\left(\frac{k_x a}{2}\right) \\
T_{3b}^{(\text{Mo-Mo})}(\mathbf{k}) &= \frac{\sqrt{6}}{3} \left[-2 \sin\left(\frac{k_x a}{2}\right) \cos\left(\frac{\sqrt{3}k_y a}{2}\right) + \sin(k_x a) \right]
\end{aligned} \tag{F.1.1}$$

F.1.2 Nearest-Neighbor S–S Bond-Cluster

$$\begin{aligned}
Q_0^{(\text{S-S})}(\mathbf{k}) &= \frac{\sqrt{6}}{3} \left[2 \cos\left(\frac{k_x a}{2}\right) \cos\left(\frac{\sqrt{3}k_y a}{2}\right) + \cos(k_x a) \right] \\
Q_v^{(\text{S-S})}(\mathbf{k}) &= \frac{2\sqrt{3}}{3} \left[\cos\left(\frac{k_x a}{2}\right) \cos\left(\frac{\sqrt{3}k_y a}{2}\right) - \cos(k_x a) \right], & Q_{xy}^{(\text{S-S})}(\mathbf{k}) &= 2 \sin\left(\frac{k_x a}{2}\right) \sin\left(\frac{\sqrt{3}k_y a}{2}\right) \\
T_x^{(\text{S-S})}(\mathbf{k}) &= \frac{2\sqrt{3}}{3} \left[\sin\left(\frac{k_x a}{2}\right) \cos\left(\frac{\sqrt{3}k_y a}{2}\right) + \sin(k_x a) \right], & T_y^{(\text{S-S})}(\mathbf{k}) &= 2 \sin\left(\frac{\sqrt{3}k_y a}{2}\right) \cos\left(\frac{k_x a}{2}\right) \\
T_{3b}^{(\text{S-S})}(\mathbf{k}) &= \frac{\sqrt{6}}{3} \left[-2 \sin\left(\frac{k_x a}{2}\right) \cos\left(\frac{\sqrt{3}k_y a}{2}\right) + \sin(k_x a) \right]
\end{aligned} \tag{F.1.2}$$

F.1.3 Nearest-Neighbor Mo–S Bond-Cluster

$$\begin{aligned}
Q_0^{(\text{Mo-S})}(\mathbf{k}) &= \frac{2\sqrt{3}}{3} \left[2 \cos\left(\frac{k_x a}{2}\right) \cos\left(\frac{\sqrt{3}k_y a}{6}\right) + \cos\left(\frac{\sqrt{3}k_y a}{3}\right) \right] \cos\left(\frac{497k_z c}{4000}\right) \\
Q_z^{(\text{Mo-S})}(\mathbf{k}) &= \frac{2\sqrt{3}}{3} \left[-2 \sin\left(\frac{\sqrt{3}k_y a}{6}\right) \cos\left(\frac{k_x a}{2}\right) + \sin\left(\frac{\sqrt{3}k_y a}{3}\right) \right] \sin\left(\frac{497k_z c}{4000}\right) \\
Q_v^{(\text{Mo-S})}(\mathbf{k}) &= \frac{2\sqrt{6}}{3} \left[\cos\left(\frac{k_x a}{2}\right) \cos\left(\frac{\sqrt{3}k_y a}{6}\right) - \cos\left(\frac{\sqrt{3}k_y a}{3}\right) \right] \cos\left(\frac{497k_z c}{4000}\right) \\
Q_{xy}^{(\text{Mo-S})}(\mathbf{k}) &= -2\sqrt{2} \sin\left(\frac{k_x a}{2}\right) \sin\left(\frac{\sqrt{3}k_y a}{6}\right) \cos\left(\frac{497k_z c}{4000}\right) \\
Q_{yz}^{(\text{Mo-S})}(\mathbf{k}) &= -\frac{2\sqrt{6}}{3} \left[\sin\left(\frac{\sqrt{3}k_y a}{6}\right) \cos\left(\frac{k_x a}{2}\right) + \sin\left(\frac{\sqrt{3}k_y a}{3}\right) \right] \sin\left(\frac{497k_z c}{4000}\right) \\
Q_{zx}^{(\text{Mo-S})}(\mathbf{k}) &= -2\sqrt{2} \sin\left(\frac{497k_z c}{4000}\right) \sin\left(\frac{k_x a}{2}\right) \cos\left(\frac{\sqrt{3}k_y a}{6}\right) \\
T_0^{(\text{Mo-S})}(\mathbf{k}) &= \frac{2\sqrt{3}}{3} \left[2 \sin\left(\frac{\sqrt{3}k_y a}{6}\right) \cos\left(\frac{k_x a}{2}\right) - \sin\left(\frac{\sqrt{3}k_y a}{3}\right) \right] \cos\left(\frac{497k_z c}{4000}\right) \\
T_z^{(\text{Mo-S})}(\mathbf{k}) &= \frac{2\sqrt{3}}{3} \left[2 \cos\left(\frac{k_x a}{2}\right) \cos\left(\frac{\sqrt{3}k_y a}{6}\right) + \cos\left(\frac{\sqrt{3}k_y a}{3}\right) \right] \sin\left(\frac{497k_z c}{4000}\right) \\
T_x^{(\text{Mo-S})}(\mathbf{k}) &= 2\sqrt{2} \sin\left(\frac{k_x a}{2}\right) \cos\left(\frac{497k_z c}{4000}\right) \cos\left(\frac{\sqrt{3}k_y a}{6}\right) \\
T_y^{(\text{Mo-S})}(\mathbf{k}) &= \frac{2\sqrt{6}}{3} \left[\sin\left(\frac{\sqrt{3}k_y a}{6}\right) \cos\left(\frac{k_x a}{2}\right) + \sin\left(\frac{\sqrt{3}k_y a}{3}\right) \right] \cos\left(\frac{497k_z c}{4000}\right) \\
T_{xyz}^{(\text{Mo-S})}(\mathbf{k}) &= -2\sqrt{2} \sin\left(\frac{497k_z c}{4000}\right) \sin\left(\frac{k_x a}{2}\right) \sin\left(\frac{\sqrt{3}k_y a}{6}\right) \\
T_{z\beta}^{(\text{Mo-S})}(\mathbf{k}) &= \frac{2\sqrt{6}}{3} \left[\cos\left(\frac{k_x a}{2}\right) \cos\left(\frac{\sqrt{3}k_y a}{6}\right) - \cos\left(\frac{\sqrt{3}k_y a}{3}\right) \right] \sin\left(\frac{497k_z c}{4000}\right)
\end{aligned} \tag{F.1.3}$$

F.2 Momentum Space Representation of the SAMB

Using the momentum multipoles given in Eqs. (F.1.1)-(F.1.3), the \mathbf{k} representation of the SAMB are given by

$$Q_0[\text{Mo}] = Q_0^{(a)} \otimes Q_0^{(t,\text{Mo})}, \quad Q_u[\text{Mo}] = Q_u^{(a)} \otimes Q_0^{(t,\text{Mo})}, \quad Q_{40}[\text{Mo}] = Q_{40}^{(a)} \otimes Q_0^{(t,\text{Mo})} \quad (\text{F.2.1})$$

$$Q_0[\text{S}] = Q_0^{(a)} \otimes Q_0^{(t,\text{S})}, \quad Q_u[\text{S}] = Q_u^{(a)} \otimes Q_0^{(t,\text{S})} \quad (\text{F.2.2})$$

$$\begin{aligned} Q_0(\mathbf{k})[\text{Mo} - \text{Mo}, 1] &= Q_0^{(a)} \otimes Q_0^{(t,\text{Mo})} Q_0^{(\text{Mo}-\text{Mo})}(\mathbf{k}), \quad Q_u(\mathbf{k})[\text{Mo} - \text{Mo}] = Q_u^{(a)} \otimes Q_0^{(t,\text{Mo})} Q_0^{(\text{Mo}-\text{Mo})}(\mathbf{k}) \\ Q_{40}(\mathbf{k})[\text{Mo} - \text{Mo}] &= Q_{40}^{(a)} \otimes Q_0^{(t,\text{Mo})} Q_0^{(\text{Mo}-\text{Mo})}(\mathbf{k}), \quad Q_{3a}(\mathbf{k})[\text{Mo} - \text{Mo}, 1] = M_z^{(a)} \otimes Q_0^{(t,\text{Mo})} T_{3b}^{(\text{Mo}-\text{Mo})}(\mathbf{k}) \\ Q_{3a}(\mathbf{k})[\text{Mo} - \text{Mo}, 2] &= M_{z\alpha}^{(a)} \otimes Q_0^{(t,\text{Mo})} T_{3b}^{(\text{Mo}-\text{Mo})}(\mathbf{k}) \\ Q_0(\mathbf{k})[\text{Mo} - \text{Mo}, 2] &= \frac{1}{\sqrt{2}} \left(Q_v^{(\text{Mo}-\text{Mo})}(\mathbf{k}) Q_v^{(a)} + Q_{xy}^{(\text{Mo}-\text{Mo})}(\mathbf{k}) Q_{xy}^{(a)} \right) \otimes Q_0^{(t,\text{Mo})} \\ Q_u(\mathbf{k})[\text{Mo} - \text{Mo}, 2] &= \frac{1}{\sqrt{2}} \left(Q_v^{(\text{Mo}-\text{Mo})}(\mathbf{k}) Q_{4u\beta 1}^{(a)} + Q_{xy}^{(\text{Mo}-\text{Mo})}(\mathbf{k}) Q_{4v\beta 1}^{(a)} \right) \otimes Q_0^{(t,\text{Mo})} \\ Q_u(\mathbf{k})[\text{Mo} - \text{Mo}, 3] &= \frac{1}{\sqrt{2}} \left(Q_v^{(\text{Mo}-\text{Mo})}(\mathbf{k}) Q_{4u\beta 2}^{(a)} + Q_{xy}^{(\text{Mo}-\text{Mo})}(\mathbf{k}) Q_{4v\beta 2}^{(a)} \right) \otimes Q_0^{(t,\text{Mo})} \\ Q_{3a}(\mathbf{k})[\text{Mo} - \text{Mo}, 3] &= \frac{1}{\sqrt{2}} \left(T_x^{(\text{Mo}-\text{Mo})}(\mathbf{k}) M_{z\beta}^{(a)} + T_y^{(\text{Mo}-\text{Mo})}(\mathbf{k}) M_{xyz}^{(a)} \right) \otimes Q_0^{(t,\text{Mo})} \end{aligned} \quad (\text{F.2.3})$$

$$\begin{aligned} Q_0(\mathbf{k})[\text{S} - \text{S}, 1] &= Q_0^{(a)} \otimes Q_0^{(t,\text{S})} Q_0^{(\text{S}-\text{S})}(\mathbf{k}), \quad Q_u(\mathbf{k})[\text{S} - \text{S}, 1] = Q_u^{(a)} \otimes Q_0^{(t,\text{S})} Q_0^{(\text{S}-\text{S})}(\mathbf{k}) \\ Q_{3a}(\mathbf{k})[\text{S} - \text{S}, 1] &= M_z^{(a)} \otimes Q_0^{(t,\text{S})} T_{3b}^{(\text{S}-\text{S})}(\mathbf{k}) \\ Q_u(\mathbf{k})[\text{S} - \text{S}, 2] &= \frac{1}{\sqrt{2}} \left(T_x^{(\text{S}-\text{S})}(\mathbf{k}) M_x^{(a)} + T_y^{(\text{S}-\text{S})}(\mathbf{k}) M_y^{(a)} \right) \otimes Q_z^{(t,\text{S})} \\ Q_3(\mathbf{k})[\text{S} - \text{S}, 2] &= \frac{1}{\sqrt{2}} \left(Q_v^{(\text{S}-\text{S})}(\mathbf{k}) Q_{yz}^{(a)} + Q_{xy}^{(\text{S}-\text{S})}(\mathbf{k}) Q_{zx}^{(a)} \right) \otimes Q_z^{(t,\text{S})} \\ Q_0(\mathbf{k})[\text{S} - \text{S}, 2] &= \frac{1}{\sqrt{2}} \left(Q_v^{(\text{S}-\text{S})}(\mathbf{k}) Q_v^{(a)} + Q_{xy}^{(\text{S}-\text{S})}(\mathbf{k}) Q_{xy}^{(a)} \right) \otimes Q_0^{(t,\text{S})} \end{aligned} \quad (\text{F.2.4})$$

$$\begin{aligned} Q_0(\mathbf{k})[\text{Mo} - \text{S}, 1] &= \\ \frac{1}{2} Q_z^{(a)} \otimes &\left[Q_0^{(t,\text{Mo}-\text{S})} Q_z^{(\text{Mo}-\text{S})}(\mathbf{k}) + Q_z^{(t,\text{Mo}-\text{S})} Q_0^{(\text{Mo}-\text{S})}(\mathbf{k}) - T_0^{(t,\text{Mo}-\text{S})} T_z^{(\text{Mo}-\text{S})}(\mathbf{k}) - T_z^{(t,\text{Mo}-\text{S})} T_0^{(\text{Mo}-\text{S})}(\mathbf{k}) \right] \\ Q_u(\mathbf{k})[\text{Mo} - \text{S}, 1] &= \\ \frac{1}{2} Q_{z\alpha}^{(a)} \otimes &\left[Q_0^{(t,\text{Mo}-\text{S})} Q_z^{(\text{Mo}-\text{S})}(\mathbf{k}) + Q_z^{(t,\text{Mo}-\text{S})} Q_0^{(\text{Mo}-\text{S})}(\mathbf{k}) - T_0^{(t,\text{Mo}-\text{S})} T_z^{(\text{Mo}-\text{S})}(\mathbf{k}) - T_z^{(t,\text{Mo}-\text{S})} T_0^{(\text{Mo}-\text{S})}(\mathbf{k}) \right] \\ Q_{3a}(\mathbf{k})[\text{Mo} - \text{S}, 1] &= \\ \frac{\sqrt{2}}{4} Q_x^{(a)} \otimes &\left[Q_0^{(t,\text{Mo}-\text{S})} Q_{xy}^{(\text{Mo}-\text{S})}(\mathbf{k}) + Q_z^{(t,\text{Mo}-\text{S})} Q_{zx}^{(\text{Mo}-\text{S})}(\mathbf{k}) - T_0^{(t,\text{Mo}-\text{S})} T_x^{(\text{Mo}-\text{S})}(\mathbf{k}) - T_z^{(t,\text{Mo}-\text{S})} T_{xyz}^{(\text{Mo}-\text{S})}(\mathbf{k}) \right] \\ &+ \frac{\sqrt{2}}{4} Q_y^{(a)} \otimes \left[Q_0^{(t,\text{Mo}-\text{S})} Q_v^{(\text{Mo}-\text{S})}(\mathbf{k}) + Q_z^{(t,\text{Mo}-\text{S})} Q_{yz}^{(\text{Mo}-\text{S})}(\mathbf{k}) - T_0^{(t,\text{Mo}-\text{S})} T_y^{(\text{Mo}-\text{S})}(\mathbf{k}) - T_z^{(t,\text{Mo}-\text{S})} T_{z\beta}^{(\text{Mo}-\text{S})}(\mathbf{k}) \right] \end{aligned}$$

$$\begin{aligned} Q_{3a}(\mathbf{k})[\text{Mo} - \text{S}, 2] &= \\ \frac{\sqrt{2}}{4} G_{yz}^{(a)} \otimes &\left[Q_0^{(t,\text{Mo}-\text{S})} Q_{xy}^{(\text{Mo}-\text{S})}(\mathbf{k}) + Q_z^{(t,\text{Mo}-\text{S})} Q_{zx}^{(\text{Mo}-\text{S})}(\mathbf{k}) - T_0^{(t,\text{Mo}-\text{S})} T_x^{(\text{Mo}-\text{S})}(\mathbf{k}) - T_z^{(t,\text{Mo}-\text{S})} T_{xyz}^{(\text{Mo}-\text{S})}(\mathbf{k}) \right] \\ &+ \frac{\sqrt{2}}{4} G_{zx}^{(a)} \otimes \left[Q_0^{(t,\text{Mo}-\text{S})} Q_v^{(\text{Mo}-\text{S})}(\mathbf{k}) + Q_z^{(t,\text{Mo}-\text{S})} Q_{yz}^{(\text{Mo}-\text{S})}(\mathbf{k}) - T_0^{(t,\text{Mo}-\text{S})} T_y^{(\text{Mo}-\text{S})}(\mathbf{k}) - T_z^{(t,\text{Mo}-\text{S})} T_{z\beta}^{(\text{Mo}-\text{S})}(\mathbf{k}) \right] \end{aligned}$$

$$\begin{aligned}
& Q_u(\mathbf{k})[\text{Mo} - \text{S}, 2] = \\
& \frac{\sqrt{2}}{4} Q_{3u}^{(a)} \otimes \left[Q_0^{(t, \text{Mo-S})} Q_{xy}^{(\text{Mo-S})}(\mathbf{k}) + Q_z^{(t, \text{Mo-S})} Q_{zx}^{(\text{Mo-S})}(\mathbf{k}) - T_0^{(t, \text{Mo-S})} T_x^{(\text{Mo-S})}(\mathbf{k}) - T_z^{(t, \text{Mo-S})} T_{xyz}^{(\text{Mo-S})}(\mathbf{k}) \right] \\
& + \frac{\sqrt{2}}{4} Q_{3v}^{(a)} \otimes \left[Q_0^{(t, \text{Mo-S})} Q_v^{(\text{Mo-S})}(\mathbf{k}) + Q_z^{(t, \text{Mo-S})} Q_{yz}^{(\text{Mo-S})}(\mathbf{k}) - T_0^{(t, \text{Mo-S})} T_y^{(\text{Mo-S})}(\mathbf{k}) - T_z^{(t, \text{Mo-S})} T_{z\beta}^{(\text{Mo-S})}(\mathbf{k}) \right] \\
& Q_{3a}(\mathbf{k})[\text{Mo} - \text{S}, 3] = \\
& \frac{\sqrt{2}}{4} G_v^{(a)} \otimes \left[Q_0^{(t, \text{Mo-S})} Q_{zx}^{(\text{Mo-S})}(\mathbf{k}) + Q_z^{(t, \text{Mo-S})} Q_{xy}^{(\text{Mo-S})}(\mathbf{k}) - T_0^{(t, \text{Mo-S})} T_{xyz}^{(\text{Mo-S})}(\mathbf{k}) - T_z^{(t, \text{Mo-S})} T_x^{(\text{Mo-S})}(\mathbf{k}) \right] \\
& + \frac{\sqrt{2}}{4} G_{xy}^{(a)} \otimes \left[Q_0^{(t, \text{Mo-S})} Q_{yz}^{(\text{Mo-S})}(\mathbf{k}) + Q_z^{(t, \text{Mo-S})} Q_v^{(\text{Mo-S})}(\mathbf{k}) - T_0^{(t, \text{Mo-S})} T_{z\beta}^{(\text{Mo-S})}(\mathbf{k}) - T_z^{(t, \text{Mo-S})} T_y^{(\text{Mo-S})}(\mathbf{k}) \right] \\
& Q_{3a}(\mathbf{k})[\text{Mo} - \text{S}, 4] = \\
& \frac{\sqrt{2}}{4} Q_{z\beta}^{(a)} \otimes \left[Q_0^{(t, \text{Mo-S})} Q_{zx}^{(\text{Mo-S})}(\mathbf{k}) + Q_z^{(t, \text{Mo-S})} Q_{xy}^{(\text{Mo-S})}(\mathbf{k}) - T_0^{(t, \text{Mo-S})} T_{xyz}^{(\text{Mo-S})}(\mathbf{k}) - T_z^{(t, \text{Mo-S})} T_x^{(\text{Mo-S})}(\mathbf{k}) \right] \\
& + \frac{\sqrt{2}}{4} Q_{xyz}^{(a)} \otimes \left[Q_0^{(t, \text{Mo-S})} Q_{yz}^{(\text{Mo-S})}(\mathbf{k}) + Q_z^{(t, \text{Mo-S})} Q_v^{(\text{Mo-S})}(\mathbf{k}) - T_0^{(t, \text{Mo-S})} T_{z\beta}^{(\text{Mo-S})}(\mathbf{k}) - T_z^{(t, \text{Mo-S})} T_y^{(\text{Mo-S})}(\mathbf{k}) \right] \\
& Q_{3a}(\mathbf{k})[\text{Mo} - \text{S}, 5] = \\
& \frac{1}{2} Q_{3a}^{(a)} \otimes \left[Q_0^{(t, \text{Mo-S})} Q_0^{(\text{Mo-S})}(\mathbf{k}) + Q_z^{(t, \text{Mo-S})} Q_z^{(\text{Mo-S})}(\mathbf{k}) - T_0^{(t, \text{Mo-S})} T_0^{(\text{Mo-S})}(\mathbf{k}) - T_z^{(t, \text{Mo-S})} T_z^{(\text{Mo-S})}(\mathbf{k}) \right]
\end{aligned} \tag{F.2.5}$$

Bibliography

- [1] R. Oiwa and H. Kusunose, *J. Phys. Soc. Jpn.* **91**, 014701 (2022).
- [2] N. Nagaosa, J. Sinova, S. Onoda, A. H. MacDonald, and N. P. Ong, *Rev. Mod. Phys.* **82**, 1539 (2010).
- [3] D. Xiao, M.-C. Chang, and Q. Niu, *Rev. Mod. Phys.* **82**, 1959 (2010).
- [4] M. Gradhand, D. V. Fedorov, F. Pientka, P. Zahn, I. Mertig, and B. L. Györfy, *J. Phys. Condens. Matter* **24**, 213202 (2012).
- [5] P. N. Argyres, *Phys. Rev.* **97**, 334 (1955).
- [6] T. Nagamiya, S. Tomiyoshi, and Y. Yamaguchi, *Solid State Commun.* **42**, 385 (1982).
- [7] W. Feng, G.-Y. Guo, J. Zhou, Y. Yao, and Q. Niu, *Phys. Rev. B* **92**, 144426 (2015).
- [8] T. Higo, H. Man, D. B. Gopman, L. Wu, T. Koretsune, O. M. J. van 't Erve, Y. P. Kabanov, D. Rees, Y. Li, M.-T. Suzuki, S. Patankar, M. Ikhlas, C. L. Chien, R. Arita, R. D. Shull, J. Orenstein, and S. Nakatsuji, *Nat. Photon.* **12**, 73 (2018).
- [9] J. M. Luttinger, *Phys. Rev.* **135**, A1505 (1964).
- [10] D. Xiao, Y. Yao, Z. Fang, and Q. Niu, *Phys. Rev. Lett.* **97**, 026603 (2006).
- [11] M. Ikhlas, T. Tomita, T. Koretsune, M.-T. Suzuki, D. Nishio-Hamane, R. Arita, Y. Otani, and S. Nakatsuji, *Nat. Phys.* **13**, 1085 (2017).
- [12] D. Destraz, L. Das, S. S. Tsirkin, Y. Xu, T. Neupert, J. Chang, A. Schilling, A. G. Grushin, J. Kohlbrecher, L. Keller, P. Pupal, E. Pomjakushina, and J. S. White, *npj Quantum Mater.* **5**, 5 (2020).
- [13] L. Šmejkal, R. González-Hernández, T. Jungwirth, and J. Sinova, *Sci. Adv.* **6**, eaaz8809 (2020).
- [14] X. Li, A. H. MacDonald, and H. Chen, *arXiv:1902.10650*, (2019).
- [15] Z. Feng, X. Zhou, L. Šmejkal, L. Wu, Z. Zhu, H. Guo, R. González-Hernández, X. Wang, H. Yan, P. Qin, X. Zhang, H. Wu, H. Chen, Z. Meng, L. Liu, Z. Xia, J. Sinova, T. Jungwirth, and Z. Liu, *Nat. Electron.* **5**, 735 (2022).
- [16] M. Naka, S. Hayami, H. Kusunose, Y. Yanagi, Y. Motome, and H. Seo, *Phys. Rev. B* **102**, 075112 (2020).
- [17] S. Hayami and H. Kusunose, *Phys. Rev. B* **103**, L180407 (2021).
- [18] H. Chen, Q. Niu, and A. H. MacDonald, *Phys. Rev. Lett.* **112**, 017205 (2014).

- [19] J. Kübler and C. Felser, *EPL* **108**, 67001 (2014).
- [20] S. Nakatsuji, N. Kiyohara, and T. Higo, *Nature* **527**, 212 (2015).
- [21] N. Kiyohara, T. Tomita, and S. Nakatsuji, *Phys. Rev. Appl.* **5**, 064009 (2016).
- [22] A. K. Nayak, J. E. Fischer, Y. Sun, B. Yan, J. Karel, A. C. Komarek, C. Shekhar, N. Kumar, W. Schnelle, J. Kübler, C. Felser, and S. S. P. Parkin, *Sci. Adv.* **2**, e1501870 (2016).
- [23] H. Yang, Y. Sun, Y. Zhang, W.-J. Shi, S. S. P. Parkin, and B. Yan, *New J. Phys.* **19**, 015008 (2017).
- [24] K. Akiba, K. Iwamoto, T. Sato, S. Araki, and T. C. Kobayashi, *Phys. Rev. Research* **2**, 043090 (2020).
- [25] S. Hayami and H. Kusunose, *J. Phys. Soc. Jpn.* **87**, 033709 (2018).
- [26] S. Hayami, M. Yatsushiro, Y. Yanagi, and H. Kusunose, *Phys. Rev. B* **98**, 165110 (2018).
- [27] H. Watanabe and Y. Yanase, *Phys. Rev. B* **98**, 245129 (2018).
- [28] H. Kusunose, R. Oiwa, and S. Hayami, *J. Phys. Soc. Jpn.* **89**, 104704 (2020).
- [29] M.-T. Suzuki, T. Koretsune, M. Ochi, and R. Arita, *Phys. Rev. B* **95**, 094406 (2017).
- [30] P. W. Anderson and H. Hasegawa, *Phys. Rev.* **100**, 675 (1955).
- [31] K. Ohgushi, S. Murakami, and N. Nagaosa, *Phys. Rev. B* **62**, R6065 (2000).
- [32] Y. Taguchi, Y. Oohara, H. Yoshizawa, N. Nagaosa, and Y. Tokura, *Science* **291**, 2573 (2001).
- [33] S.-S. Zhang, H. Ishizuka, H. Zhang, G. B. Halász, and C. D. Batista, *Phys. Rev. B* **101**, 024420 (2020).
- [34] M. Kenzelmann, G. Lawes, A. B. Harris, G. Gasparovic, C. Broholm, A. P. Ramirez, G. A. Jorge, M. Jaime, S. Park, Q. Huang, A. Y. Shapiro, and L. A. Demianets, *Phys. Rev. Lett.* **98**, 267205 (2007).
- [35] T. Inami, *J. Solid State Chem.* **180**, 2075 (2007).
- [36] A. Waśkowska, L. Gerward, J. Staun Olsen, W. Morgenroth, M. Maćzka, and K. Hermanowicz, *J. Phys. Condens.* **22**, 055406 (2010).
- [37] S.-W. Cheong, D. Talbayev, V. Kiryukhin, and A. Saxena, *npj Quantum Mater.* **3**, 1 (2018).
- [38] W. Jin, E. Drueke, S. Li, A. Admasu, R. Owen, M. Day, K. Sun, S.-W. Cheong, and L. Zhao, *Nat. Phys.* **16**, 42 (2020).
- [39] H. Hanate, T. Hasegawa, S. Hayami, S. Tsutsui, S. Kawano, and K. Matsuhira, *J. Phys. Soc. Jpn.* **90**, 063702 (2021).
- [40] M. Lerch, H. Boysen, R. Neder, F. Frey, and W. Laqua, *J. Phys. Chem. Solids* **53**, 1153 (1992).
- [41] T. Hayashida, Y. Uemura, K. Kimura, S. Matsuoka, D. Morikawa, S. Hirose, K. Tsuda, T. Hasegawa, and T. Kimura, *Nat. Commun.* **11**, 4582 (2020).

- [42] T. Hayashida, Y. Uemura, K. Kimura, S. Matsuoka, M. Hagihala, S. Hirose, H. Morioka, T. Hasegawa, and T. Kimura, *Phys. Rev. Mater.* **5**, 124409 (2021).
- [43] A. K. Yadav, C. T. Nelson, S. L. Hsu, Z. Hong, J. D. Clarkson, C. M. Schlepütz, A. R. Damodaran, P. Shafer, E. Arenholz, L. R. Dedon, D. Chen, A. Vishwanath, A. M. Minor, L. Q. Chen, J. F. Scott, L. W. Martin, and R. Ramesh, *Nature* **530**, 198 (2016).
- [44] S. Hayami, R. Oiwa, and H. Kusunose, *J. Phys. Soc. Jpn.* **91**, 113702 (2022).
- [45] T. Hayashida, K. Kimura, D. Urushihara, T. Asaka, and T. Kimura, *J. Am. Chem. Soc.* **143**, 3638 (2021).
- [46] B. Göhler, V. Hamelbeck, T. Z. Markus, M. Kettner, G. F. Hanne, Z. Vager, R. Naaman, and H. Zacharias, *Science* **331**, 894 (2011).
- [47] K. Michaeli, D. N. Beratan, D. H. Waldeck, and R. Naaman, *Proc. Nat. Acad. Sci.* **116**, 5931 (2019).
- [48] O. Ben Dor, S. Yochelis, A. Radko, K. Vankayala, E. Capua, A. Capua, S.-H. Yang, L. T. Baczewski, S. S. P. Parkin, R. Naaman, and Y. Paltiel, *Nat. Commun.* **8**, 14567 (2017).
- [49] R. Naaman, Y. Paltiel, and D. H. Waldeck, *Acc. Chem. Res.* **53**, 2659 (2020).
- [50] M. Suda, Y. Thathong, V. Promarak, H. Kojima, M. Nakamura, T. Shiraogawa, M. Ehara, and H. M. Yamamoto, *Nat. Commun.* **10**, 2455 (2019).
- [51] A. Inui, R. Aoki, Y. Nishiue, K. Shiota, Y. Kousaka, H. Shishido, D. Hirobe, M. Suda, J. Ohe, J. Kishine, H. M. Yamamoto, and Y. Togawa, *Phys. Rev. Lett.* **124**, 166602 (2020).
- [52] Y. Nabei, D. Hirobe, Y. Shimamoto, K. Shiota, A. Inui, Y. Kousaka, Y. Togawa, and H. M. Yamamoto, *Appl. Phys. Lett.* **117**, 052408 (2020).
- [53] K. Shiota, A. Inui, Y. Hosaka, R. Amano, Y. Ōnuki, M. Hedō, T. Nakama, D. Hirobe, J. Ohe, J. Kishine, H. M. Yamamoto, H. Shishido, and Y. Togawa, *Phys. Rev. Lett.* **127**, 126602 (2021).
- [54] T. Yoda, T. Yokoyama, and S. Murakami, *Sci. Rep.* **5**, 12024 (2015).
- [55] T. Yoda, T. Yokoyama, and S. Murakami, *Nano Lett.* **18**, 916 (2018).
- [56] V. A. Shalygin, A. N. Sofronov, L. E. Vorob'ev, and I. I. Farbshtein, *Phys. Solid State* **54**, 2362 (2012).
- [57] T. Furukawa, Y. Shimokawa, K. Kobayashi, and T. Itou, *Nat. Commun.* **8**, 954 (2017).
- [58] T. Furukawa, Y. Watanabe, N. Ogasawara, K. Kobayashi, and T. Itou, *Phys. Rev. Research* **3**, 023111 (2021).
- [59] M. Hamada, E. Minamitani, M. Hirayama, and S. Murakami, *Phys. Rev. Lett.* **121**, 175301 (2018).
- [60] M. Hamada and S. Murakami, *Phys. Rev. B* **101**, 144306 (2020).
- [61] J. Kishine, A. S. Ovchinnikov, and A. A. Tereshchenko, *Phys. Rev. Lett.* **125**, 245302 (2020).
- [62] H. Chen, W. Wu, J. Zhu, Z. Yang, W. Gong, W. Gao, S. A. Yang, and L. Zhang, *Nano Lett.* **22**, 1688 (2022).

- [63] K. Ishito, H. Mao, Y. Kousaka, Y. Togawa, S. Iwasaki, T. Zhang, S. Murakami, J. Kishine, and T. Satoh, *Nat. Phys.* **19**, 35 (2023).
- [64] J. Kishine, H. Kusunose, and H. M. Yamamoto, *Isr. J. Chem.* **62**, e202200049 (2022).
- [65] G. Kresse and J. Hafner, *Phys. Rev. B* **47**, 558 (1993).
- [66] P. Giannozzi, S. Baroni, N. Bonini, M. Calandra, R. Car, C. Cavazzoni, D. Ceresoli, G. L. Chiarotti, M. Cococcioni, I. Dabo, A. D. Corso, S. de Gironcoli, S. Fabris, G. Fratesi, R. Gebauer, U. Gerstmann, C. Gougoussis, A. Kokalj, M. Lazzeri, L. Martin-Samos, N. Marzari, F. Mauri, R. Mazzarello, S. Paolini, A. Pasquarello, L. Paulatto, C. Sbraccia, S. Scandolo, G. Sclauzero, A. P. Seitsonen, A. Smogunov, P. Umari, and R. M. Wentzcovitch, *J. Phys. Condens.* **21**, 395502 (2009).
- [67] P. Blaha, K. Schwarz, F. Tran, R. Laskowski, G. K. H. Madsen, and L. D. Marks, *J. Chem. Phys.* **152**, 074101 (2020).
- [68] T. Ozaki, *Phys. Rev. B* **67**, 155108 (2003).
- [69] X. Gonze, J. M. Beuken, R. Caracas, F. Detraux, M. Fuchs, G. M. Rignanese, L. Sindic, M. Verstraete, G. Zerah, F. Jollet, M. Torrent, A. Roy, M. Mikami, P. Ghosez, J. Y. Raty, and D. C. Allan, *Comput. Mater. Sci.* **25**, 478 (2002).
- [70] M. J. Frisch, G. W. Trucks, H. B. Schlegel, G. E. Scuseria, M. A. Robb, J. R. Cheeseman, G. Scalmani, V. Barone, G. A. Petersson, H. Nakatsuji, X. Li, M. Caricato, A. V. Marenich, J. Bloino, B. G. Janesko, R. Gomperts, B. Mennucci, H. P. Hratchian, J. V. Ortiz, A. F. Izmaylov, J. L. Sonnenberg, D. Williams-Young, F. Ding, F. Lipparini, F. Egidi, J. Goings, B. Peng, A. Petrone, T. Henderson, D. Ranasinghe, V. G. Zakrzewski, J. Gao, N. Rega, G. Zheng, W. Liang, M. Hada, M. Ehara, K. Toyota, R. Fukuda, J. Hasegawa, M. Ishida, T. Nakajima, Y. Honda, O. Kitao, H. Nakai, T. Vreven, K. Throssell, J. A. Montgomery, Jr., J. E. Peralta, F. Ogliaro, M. J. Bearpark, J. J. Heyd, E. N. Brothers, K. N. Kudin, V. N. Staroverov, T. A. Keith, R. Kobayashi, J. Normand, K. Raghavachari, A. P. Rendell, J. C. Burant, S. S. Iyengar, J. Tomasi, M. Cossi, J. M. Millam, M. Klene, C. Adamo, R. Cammi, J. W. Ochterski, R. L. Martin, K. Morokuma, O. Farkas, J. B. Foresman, and D. J. Fox, *Gaussian 16 Revision C.01*, (2016).
- [71] N. Marzari, A. A. Mostofi, J. R. Yates, I. Souza, and D. Vanderbilt, *Rev. Mod. Phys.* **84**, 1419 (2012).
- [72] A. A. Mostofi, J. R. Yates, Y.-S. Lee, I. Souza, D. Vanderbilt, and N. Marzari, *Comput. Phys. Commun.* **178**, 685 (2008).
- [73] A. A. Mostofi, J. R. Yates, G. Pizzi, Y.-S. Lee, I. Souza, D. Vanderbilt, and N. Marzari, *Comput. Phys. Commun.* **185**, 2309 (2014).
- [74] G. Pizzi, V. Vitale, R. Arita, S. Blügel, F. Freimuth, G. Géranton, M. Gibertini, D. Gresch, C. Johnson, T. Koretsune, J. Ibañez-Azpiroz, H. Lee, J.-M. Lihm, D. Marchand, A. Marrazzo, Y. Mokrousov, J. I. Mustafa, Y. Nohara, Y. Nomura, L. Paulatto, S. Poncé, T. Ponweiser, J. Qiao, F. Thöle, S. S. Tsirkin, M. Wierzbowska, N. Marzari, D. Vanderbilt, I. Souza, A. A. Mostofi, and J. R. Yates, *J. Phys. Condens.* **32**, 165902 (2020).
- [75] G. H. Wannier, *Phys. Rev.* **52**, 191 (1937).

- [76] J. R. Yates, X. Wang, D. Vanderbilt, and I. Souza, Phys. Rev. B **75**, 195121 (2007).
- [77] N. Marzari and D. Vanderbilt, Phys. Rev. B **56**, 12847 (1997).
- [78] I. Souza, N. Marzari, and D. Vanderbilt, Phys. Rev. B **65**, 035109 (2001).
- [79] Y. Nomura and R. Arita, Phys. Rev. B **92**, 245108 (2015).
- [80] F. Aryasetiawan, M. Imada, A. Georges, G. Kotliar, S. Biermann, and A. I. Lichtenstein, Phys. Rev. B **70**, 195104 (2004).
- [81] K. Nakamura, R. Arita, Y. Yoshimoto, and S. Tsuneyuki, Phys. Rev. B **74**, 235113 (2006).
- [82] R. Resta, Ferroelectrics **136**, 51 (1992).
- [83] R. Resta, Rev. Mod. Phys. **66**, 899 (1994).
- [84] R. Resta, J. Phys. Condens. **22**, 123201 (2010).
- [85] R. D. King-Smith and D. Vanderbilt, Phys. Rev. B **47**, 1651 (1993).
- [86] D. Vanderbilt and R. D. King-Smith, Phys. Rev. B **48**, 4442 (1993).
- [87] D. Vanderbilt: *Berry Phases in Electronic Structure Theory: Electric Polarization, Orbital Magnetization and Topological Insulators*, (Cambridge University Press, 2018).
- [88] C. Ederer and N. A. Spaldin, Phys. Rev. B **76**, 214404 (2007).
- [89] N. A. Spaldin, M. Fechner, E. Bousquet, A. Balatsky, and L. Nordström, Phys. Rev. B **88**, 094429 (2013).
- [90] F. Thöle, M. Fechner, and N. A. Spaldin, Phys. Rev. B **93**, 195167 (2016).
- [91] S. Tomiyoshi, J. Phys. Soc. Jpn. **51**, 803 (1982).
- [92] P. J. Brown, V. Nunez, F. Tasset, J. B. Forsyth, and P. Radhakrishna, J. Phys. Condens. **2**, 9409 (1990).
- [93] S. Tomiyoshi and Y. Yamaguchi, J. Phys. Soc. Jpn. **51**, 2478 (1982).
- [94] P. J. Brown, V. Nunez, F. Tasset, J. B. Forsyth, and P. Radhakrishna, J. Phys. Condens. **2**, 9409 (1990).
- [95] S. S. Tsirkin, npj Comput. Mater. **7**, 1 (2021).
- [96] Y.-Y. Tai, W. Zhu, H. Choi, and J.-X. Zhu, TBM3: Tight-Binding Model for Materials at Mesoscale, <https://github.com/TDIV/TBM3>, (2016).
- [97] D. Gresch, Q. Wu, G. W. Winkler, R. Häuselmann, M. Troyer, and A. A. Soluyanov, Phys. Rev. Mater. **2**, 103805 (2018).
- [98] R. Sakuma, Phys. Rev. B **87**, 235109 (2013).
- [99] J. C. Slater and G. F. Koster, Phys. Rev. **94**, 1498 (1954).
- [100] M. Nakhaee, S. A. Ketabi, and F. M. Peeters, Comput. Phys. Commun. **254**, 107379 (2020).

- [101] M.-T. Suzuki, T. Nomoto, R. Arita, Y. Yanagi, S. Hayami, and H. Kusunose, *Phys. Rev. B* **99**, 174407 (2019).
- [102] S. Hayami, Y. Yanagi, and H. Kusunose, *Phys. Rev. B* **102**, 144441 (2020).
- [103] V. Dubovik and A. Cheshkov, *Sov. J. Part. Nuclei* **5**, 318 (1975).
- [104] L. D. Landau and E. M. Lifshitz: *The Classical Theory of Fields*, 4th ed. (Butterworth-Heinemann, Oxford, 1980).
- [105] J. D. Jackson: *Classical electrodynamics*, 3rd ed. (Wiley, New York, 1999).
- [106] R. J. Blin-Stoyle, *Rev. Mod. Phys.* **28**, 75 (1956).
- [107] I. B. Zel'Dovich, *Sov. Phys. J. Exp. Theor. Phys.* **6**, 1184 (1958).
- [108] J. M. Blatt and V. F. Weisskopf: *Theoretical nuclear physics*, (Dover Publications, New York, 1991).
- [109] R. Shiina, H. Shiba, and P. Thalmeier, *J. Phys. Soc. Jpn.* **66**, 1741 (1997).
- [110] H. Kusunose, *J. Phys. Soc. Jpn.* **77**, 064710 (2008).
- [111] Y. Kuramoto, *Prog. Theor. Phys. Suppl.* **176**, 77 (2008).
- [112] P. Santini, S. Carretta, G. Amoretti, R. Caciuffo, N. Magnani, and G. H. Lander, *Rev. Mod. Phys.* **81**, 807 (2009).
- [113] Y. Kuramoto, H. Kusunose, and A. Kiss, *J. Phys. Soc. Jpn.* **78**, 072001 (2009).
- [114] M.-T. Suzuki, H. Ikeda, and P. M. Oppeneer, *J. Phys. Soc. Jpn.* **87**, 041008 (2018).
- [115] T. Kaelberer, V. A. Fedotov, N. Papasimakis, D. P. Tsai, and N. I. Zheludev, *Science* **330**, 1510 (2010).
- [116] V. Savinov, V. A. Fedotov, and N. I. Zheludev, *Phys. Rev. B* **89**, 205112 (2014).
- [117] N. Papasimakis, V. A. Fedotov, V. Savinov, T. A. Raybould, and N. I. Zheludev, *Nat. Mater.* **15**, 263 (2016).
- [118] M. Takigawa, H. Yasuoka, T. Tanaka, and Y. Ishizawa, *J. Phys. Soc. Jpn.* **52**, 728 (1983).
- [119] B. Lüthi, S. Blumenröder, B. Hillebrands, E. Zirngiebl, G. Güntherodt, and K. Winzer, *Z. Phys.* **58**, 31 (1984).
- [120] J. M. Effantin, J. Rossat-Mignod, P. Burlet, H. Bartholin, S. Kunii, and T. Kasuya, *J. Magn. Mater.* **47-48**, 145 (1985).
- [121] W. A. C. Erkelens, L. P. Regnault, P. Burlet, J. Rossat-Mignod, S. Kunii, and T. Kasuya, *J. Magn. Mater.* **63-64**, 61 (1987).
- [122] S. Nakamura, T. Goto, S. Kunii, K. Iwashita, and A. Tamaki, *J. Phys. Soc. Jpn.* **63**, 623 (1994).
- [123] O. Sakai, R. Shiina, H. Shiba, and P. Thalmeier, *J. Phys. Soc. Jpn.* **66**, 3005 (1997).
- [124] R. Shiina, O. Sakai, H. Shiba, and P. Thalmeier, *J. Phys. Soc. Jpn.* **67**, 941 (1998).

- [125] A. Sakai and S. Nakatsuji, *J. Phys. Soc. Jpn.* **80**, 063701 (2011).
- [126] T. Onimaru, K. T. Matsumoto, Y. F. Inoue, K. Umeo, T. Sakakibara, Y. Karaki, M. Kubota, and T. Takabatake, *Phys. Rev. Lett.* **106**, 177001 (2011).
- [127] A. Sakai, K. Kuga, and S. Nakatsuji, *J. Phys. Soc. Jpn.* **81**, 083702 (2012).
- [128] T. Onimaru, N. Nagasawa, K. T. Matsumoto, K. Wakiya, K. Umeo, S. Kittaka, T. Sakakibara, Y. Matsushita, and T. Takabatake, *Phys. Rev. B* **86**, 184426 (2012).
- [129] M. Tsujimoto, Y. Matsumoto, T. Tomita, A. Sakai, and S. Nakatsuji, *Phys. Rev. Lett.* **113**, 267001 (2014).
- [130] K. T. Matsumoto, T. Onimaru, K. Wakiya, K. Umeo, and T. Takabatake, *J. Phys. Soc. Jpn.* **84**, 063703 (2015).
- [131] T. Kubo, H. Kotegawa, H. Tou, R. Higashinaka, A. Nakama, Y. Aoki, and H. Sato, *J. Phys. Soc. Jpn.* **84**, 074701 (2015).
- [132] T. Onimaru and H. Kusunose, *J. Phys. Soc. Jpn.* **85**, 082002 (2016).
- [133] T. Onimaru, K. Izawa, K. T. Matsumoto, T. Yoshida, Y. Machida, T. Ikeura, K. Wakiya, K. Umeo, S. Kittaka, K. Araki, T. Sakakibara, and T. Takabatake, *Phys. Rev. B* **94**, 075134 (2016).
- [134] Y. Kuramoto, J. Otsuki, A. Kiss, and H. Kusunose, *Prog. Theor. Phys. Suppl.* **160**, 134 (2005).
- [135] T. Maehira and T. Hotta, *J. Phys. Soc. Jpn.* **75**, 262 (2006).
- [136] K. Kubo and Y. Kuramoto, *J. Phys. Soc. Jpn.* **73**, 216 (2004).
- [137] D. Mannix, Y. Tanaka, D. Carbone, N. Bernhoeft, and S. Kunii, *Phys. Rev. Lett.* **95**, 117206 (2005).
- [138] K. Kuwahara, K. Iwasa, M. Kohgi, N. Aso, M. Sera, and F. Iga, *J. Phys. Soc. Jpn.* **76**, 093702 (2007).
- [139] T. Matsumura, T. Yonemura, K. Kunimori, M. Sera, and F. Iga, *Phys. Rev. Lett.* **103**, 017203 (2009).
- [140] P. Santini and G. Amoretti, *Phys. Rev. Lett.* **85**, 2188 (2000).
- [141] J. A. Paixão, C. Detlefs, M. J. Longfield, R. Caciuffo, P. Santini, N. Bernhoeft, J. Rebizant, and G. H. Lander, *Phys. Rev. Lett.* **89**, 187202 (2002).
- [142] O. Sakai, R. Shiina, and H. Shiba, *J. Phys. Soc. Jpn.* **74**, 457 (2005).
- [143] Y. Tokunaga, D. Aoki, Y. Homma, S. Kambe, H. Sakai, S. Ikeda, T. Fujimoto, R. E. Walstedt, H. Yasuoka, E. Yamamoto, A. Nakamura, and Y. Shiokawa, *Phys. Rev. Lett.* **97**, 257601 (2006).
- [144] N. Magnani, S. Carretta, R. Caciuffo, P. Santini, G. Amoretti, A. Hiess, J. Rebizant, and G. H. Lander, *Phys. Rev. B* **78**, 104425 (2008).
- [145] M.-T. Suzuki, N. Magnani, and P. M. Oppeneer, *Phys. Rev. B* **82**, 241103 (2010).
- [146] A. Ochiai, S. Matsuda, Y. Ikeda, Y. Shimizu, S. Toyoshima, H. Aoki, and K. Katoh, *J. Phys. Soc. Jpn.* **80**, 123705 (2011).

- [147] Y. Shimura, T. Sakakibara, K. Iwakawa, K. Sugiyama, and Y. Ōnuki, *J. Phys. Soc. Jpn.* **81**, 103601 (2012).
- [148] M. Yatsushiro and S. Hayami, *J. Phys. Soc. Jpn.* **88**, 054708 (2019).
- [149] S. Hayami, Y. Yanagi, H. Kusunose, and Y. Motome, *Phys. Rev. Lett.* **122**, 147602 (2019).
- [150] C. Schwartz, *Phys. Rev.* **97**, 380 (1955).
- [151] V. M. Dubovik, L. A. Tosunyan, and V. V. Tugushev, *Zh. Eksp. Teor. Fiz* **90**, 590 (1986).
- [152] V. M. Dubovik and V. V. Tugushev, *Phys. Rep.* **187**, 145 (1990).
- [153] Y. LeCun, Y. Bengio, and G. Hinton, *Nature* **521**, 436 (2015).
- [154] G. Carleo, I. Cirac, K. Cranmer, L. Daudet, M. Schuld, N. Tishby, L. Vogt-Maranto, and L. Zdeborová, *Rev. Mod. Phys.* **91**, 045002 (2019).
- [155] G. Montavon, M. Rupp, V. Gobre, A. Vazquez-Mayagoitia, K. Hansen, A. Tkatchenko, K.-R. Müller, and O. A. v. Lilienfeld, *New J. Phys.* **15**, 095003 (2013).
- [156] P. O. Dral, O. A. von Lilienfeld, and W. Thiel, *J. Chem. Theory Comput.* **11**, 2120 (2015).
- [157] H. Li, C. Collins, M. Tanha, G. J. Gordon, and D. J. Yaron, *J. Chem. Theory Comput.* **14**, 5764 (2018).
- [158] J. J. Kranz, M. Kubillus, R. Ramakrishnan, O. A. von Lilienfeld, and M. Elstner, *J. Chem. Theory Comput.* **14**, 2341 (2018).
- [159] M. Stöhr, L. Medrano Sandonas, and A. Tkatchenko, *J. Phys. Chem. Lett.* **11**, 6835 (2020).
- [160] J. Westermayr, M. Gastegger, K. T. Schütt, and R. J. Maurer, *J. Chem. Phys.* **154**, 230903 (2021).
- [161] L. M. Ghiringhelli, J. Vybiral, S. V. Levchenko, C. Draxl, and M. Scheffler, *Phys. Rev. Lett.* **114**, 105503 (2015).
- [162] Y. Liu, T. Zhao, W. Ju, and S. Shi, *J. Materiomics.* **3**, 159 (2017).
- [163] S. Lu, Q. Zhou, Y. Ouyang, Y. Guo, Q. Li, and J. Wang, *Nat. Commun.* **9**, 3405 (2018).
- [164] J. Schmidt, M. R. G. Marques, S. Botti, and M. A. L. Marques, *npj Comput. Mater.* **5**, 83 (2019).
- [165] L.-F. Arsenault, A. Lopez-Bezanilla, O. A. von Lilienfeld, and A. J. Millis, *Phys. Rev. B* **90**, 155136 (2014).
- [166] J. Carrasquilla and R. G. Melko, *Nat. Phys.* **13**, 431 (2017).
- [167] Z. Shi, E. Tsymbalov, M. Dao, S. Suresh, A. Shapeev, and J. Li, *Proc. Nat. Acad. Sci.* **116**, 4117 (2019).
- [168] V. Peano, F. Sapper, and F. Marquardt, *Phys. Rev. X* **11**, 021052 (2021).
- [169] J. Carrete, N. Mingo, S. Wang, and S. Curtarolo, *Adv. Funct. Mater.* **24**, 7427 (2014).
- [170] S. Ju, T. Shiga, L. Feng, Z. Hou, K. Tsuda, and J. Shiomi, *Phys. Rev. X* **7**, 021024 (2017).

- [171] G. Pilania, A. Mannodi-Kanakkithodi, B. P. Uberuaga, R. Ramprasad, J. E. Gubernatis, and T. Lookman, *Sci. Rep.* **6**, 19375 (2016).
- [172] J. Lee, A. Seko, K. Shitara, K. Nakayama, and I. Tanaka, *Phys. Rev. B* **93**, 115104 (2016).
- [173] Y. Zhuo, A. Mansouri Tehrani, and J. Brgoch, *J. Phys. Chem. Lett.* **9**, 1668 (2018).
- [174] M. Nakhaee, S. A. Ketabi, and F. M. Peeters, *J. Appl. Phys.* **128**, 215107 (2020).
- [175] Z. Wang, S. Ye, H. Wang, J. He, Q. Huang, and S. Chang, *npj Comput. Mater.* **7**, 11 (2021).
- [176] E. Tsybalov, Z. Shi, M. Dao, S. Suresh, J. Li, and A. Shapeev, *npj Comput. Mater.* **7**, 76 (2021).
- [177] Z. Wang, S. Ye, H. Wang, Q. Huang, J. He, and S. Chang, *Sci. China Mater.* **65**, 3157 (2022).
- [178] D. E. Rumelhart, G. E. Hinton, and R. J. Williams, *Nature* **323**, 533 (1986).
- [179] H. Fujita, Y. O. Nakagawa, S. Sugiura, and M. Oshikawa, *Phys. Rev. B* **97**, 075114 (2018).
- [180] D. P. Kingma and L. J. Ba, Adam: a method for stochastic optimization, *Proc. 3rd Int. Conf. Learn. Represent.*, (2015).
- [181] M. Abadi, P. Barham, J. Chen, Z. Chen, A. Davis, J. Dean, M. Devin, S. Ghemawat, G. Irving, M. Isard, M. Kudlur, J. Levenberg, R. Monga, S. Moore, D. G. Murray, B. Steiner, P. Tucker, V. Vasudevan, P. Warden, M. Wicke, Y. Yu, and X. Zheng, TensorFlow: a system for large-scale machine learning, *Proc. 12th USENIX Conference on Operating Systems Design and Implementation* **16**, 265 (2016).
- [182] A. Gulli and S. Pal: *Deep learning with Keras*, (Packt Publishing Ltd, 2017).
- [183] J. P. Perdew and A. Zunger, *Phys. Rev. B* **23**, 5048 (1981).
- [184] J. P. Perdew, A. Ruzsinszky, G. I. Csonka, O. A. Vydrov, G. E. Scuseria, L. A. Constantin, X. Zhou, and K. Burke, *Phys. Rev. Lett.* **100**, 136406 (2008).
- [185] E. Cappelluti, R. Roldán, J. A. Silva-Guillén, P. Ordejón, and F. Guinea, *Phys. Rev. B* **88**, 075409 (2013).
- [186] J. P. Perdew, K. Burke, and M. Ernzerhof, *Phys. Rev. Lett.* **77**, 3865 (1996).
- [187] R. Oiwa and H. Kusunose, *Phys. Rev. Lett.* **129**, 116401 (2022).
- [188] W. T. Kelvin: *The molecular tactics of a crystal*, (Oxford, Clarendon Press, 1894).
- [189] L. D. Barron, *Chem. Soc. Rev.* **15**, 189 (1986).
- [190] L. D. Barron, *J. Am. Chem. Soc.* **108**, 5539 (1986).
- [191] L. D. Barron: *Molecular Light Scattering and Optical Activity*, 2nd ed. (Cambridge University Press, 2004).
- [192] L. D. Barron, *Rend. Fis. Acc. Lincei* **24**, 179 (2013).
- [193] L. E. Vorob'ev, E. L. Ivchenko, G. E. Pikus, I. I. Farbshteĭn, V. A. Shalygin, and A. V. Shturbin, *JETP Lett.* **29**, 441 (1979).

- [194] M. Hirayama, R. Okugawa, S. Ishibashi, S. Murakami, and T. Miyake, *Phys. Rev. Lett.* **114**, 206401 (2015).
- [195] M. Sakano, M. Hirayama, T. Takahashi, S. Akebi, M. Nakayama, K. Kuroda, K. Taguchi, T. Yoshikawa, K. Miyamoto, T. Okuda, K. Ono, H. Kumigashira, T. Ideue, Y. Iwasa, N. Mitsuishi, K. Ishizaka, S. Shin, T. Miyake, S. Murakami, T. Sasagawa, and T. Kondo, *Phys. Rev. Lett.* **124**, 136404 (2020).
- [196] L. Zhang and Q. Niu, *Phys. Rev. Lett.* **115**, 115502 (2015).
- [197] H. Chen, W. Zhang, Q. Niu, and L. Zhang, *2D Mater.* **6**, 012002 (2018).
- [198] H. Zhu, J. Yi, M.-Y. Li, J. Xiao, L. Zhang, C.-W. Yang, R. A. Kaindl, L.-J. Li, Y. Wang, and X. Zhang, *Science* **359**, 579 (2018).
- [199] J. Kishine, A. S. Ovchinnikov, and A. A. Tereshchenko, *Phys. Rev. Lett.* **125**, 245302 (2020).
- [200] Y. Chen, M. Kadic, and M. Wegener, *Nat. Commun.* **12**, 3278 (2021).
- [201] V. Gopalan and D. B. Litvin, *Nat. Mater.* **10**, 376 (2011).
- [202] N. Bouad, L. Chapon, R.-M. Marin-Ayral, F. Bouree-Vigneron, and J.-C. Tedenac, *J. Solid State Chem.* **173**, 189 (2003).
- [203] J. Paier, M. Marsman, K. Hummer, G. Kresse, I. C. Gerber, and J. G. Ángyán, *J. Chem. Phys.* **124**, 154709 (2006).
- [204] V. B. Anzin, M. I. Eremets, Y. V. Kosichkin, A. I. Nadezhdinskii, and A. M. Shirokov, *Phys. Status Solidi A* **42**, 385 (1977).
- [205] M. Hirayama, R. Okugawa, S. Ishibashi, S. Murakami, and T. Miyake, *Phys. Rev. Lett.* **114**, 206401 (2015).
- [206] S. S. Tsirkin, P. A. Puente, and I. Souza, *Phys. Rev. B* **97**, 035158 (2018).
- [207] M. Cheng, S. Wu, Z.-Z. Zhu, and G.-Y. Guo, *Phys. Rev. B* **100**, 035202 (2019).
- [208] T. Goto, A. Tamaki, T. Fujimura, and H. Unoki, *J. Phys. Soc. Jpn.* **55**, 1613 (1986).
- [209] T. Kuromaru, H. Kusunose, and Y. Kuramoto, *J. Phys. Soc. Jpn.* **70**, 521 (2001).
- [210] R. Kurihara, K. Mitsumoto, M. Akatsu, Y. Nemoto, T. Goto, Y. Kobayashi, and M. Sato, *J. Phys. Soc. Jpn.* **86**, 064706 (2017).
- [211] Y. Kousaka, T. Koyama, K. Ohishi, K. Kakurai, V. Hutanu, H. Ohsumi, T. Arima, A. Tokuda, M. Suzuki, N. Kawamura, A. Nakao, T. Hanashima, J. Suzuki, J. Campo, Y. Miyamoto, A. Sera, K. Inoue, and J. Akimitsu, *Phys. Rev. Mater.* **1**, 071402(R) (2017).
- [212] I. Proskurin, A. S. Ovchinnikov, P. Nosov, and J. Kishine, *New J. Phys.* **19**, 063021 (2017).
- [213] M. Born and R. Oppenheimer, *Ann. Phys.* **389**, 457 (1927).
- [214] R. G. Parr and Y. Weitao: *Density-Functional Theory of Atoms and Molecules*, (Oxford University Press, USA, 1994).
- [215] W. Koch and M. C. Holthausen: *A Chemist's Guide to Density Functional Theory*, 2nd ed. (Wiley, 2001).

- [216] R. M. Martin: *Electronic Structure: Basic Theory and Practical Methods*, (Cambridge University Press, 2004).
- [217] 常田 貴夫: 密度汎関数法の基礎, (講談社, 2012).
- [218] 藤原 毅夫: 固体電子構造論 : 密度汎関数理論から電子相関まで, (内田老鶴圃, 2015).
- [219] 有田 亮太郎: 多体電子構造論 : 強相関物質の理論設計に向けて, (内田老鶴圃, 2022).
- [220] P. Hohenberg and W. Kohn, Phys. Rev. **136**, B864 (1964).
- [221] W. Kohn and L. J. Sham, Phys. Rev. **140**, A1133 (1965).
- [222] J. P. Perdew and Y. Wang, Phys. Rev. B **45**, 13244 (1992).
- [223] J. P. Perdew, Phys. Rev. B **33**, 8822 (1986).
- [224] J. P. Perdew, Phys. Rev. B **34**, 7406 (1986).
- [225] J. P. Perdew, J. A. Chevary, S. H. Vosko, K. A. Jackson, M. R. Pederson, D. J. Singh, and C. Fiolhais, Phys. Rev. B **46**, 6671 (1992).
- [226] A. D. Becke, Phys. Rev. A **38**, 3098 (1988).
- [227] M. Levy, Proc. Nat. Acad. Sci. **76**, 6062 (1979).
- [228] E. H. Lieb, Int. J. Quantum Chem. **24**, 243 (1983).
- [229] S. H. Vosko, L. Wilk, and M. Nusair, Can. J. Phys. **59**, 1200 (1980).
- [230] D. M. Ceperley and B. J. Alder, Phys. Rev. Lett. **45**, 566 (1980).
- [231] G. Ortiz and P. Ballone, Phys. Rev. B **50**, 1391 (1994).
- [232] Y. Kwon, D. M. Ceperley, and R. M. Martin, Phys. Rev. B **58**, 6800 (1998).
- [233] P. Gori-Giorgi, F. Sacchetti, and G. B. Bachelet, Phys. Rev. B **61**, 7353 (2000).
- [234] M. Rasolt and D. J. W. Geldart, Phys. Rev. B **34**, 1325 (1986).
- [235] J. P. Perdew, S. Kurth, A. c. v. Zupan, and P. Blaha, Phys. Rev. Lett. **82**, 2544 (1999).
- [236] J. Sun, A. Ruzsinszky, and J. P. Perdew, Phys. Rev. Lett. **115**, 036402 (2015).
- [237] V. I. Anisimov, J. Zaanen, and O. K. Andersen, Phys. Rev. B **44**, 943 (1991).
- [238] A. D. Becke, J. Chem. Phys. **98**, 1372 (1993).
- [239] C. Adamo and V. Barone, J. Chem. Phys. **110**, 6158 (1999).
- [240] J. Heyd, G. E. Scuseria, and M. Ernzerhof, J. Chem. Phys. **118**, 8207 (2003).

List of Publications

Papers related to the dissertation

1. R. Oiwa and H. Kusunose,
“Rotation, Electric-Field Responses, and Absolute Enantioselection in Chiral Crystals”,
Physical Review Letters **129**, 116401 (2022),
© 2022 American Physical Society
2. R. Oiwa and H. Kusunose,
“Systematic Analysis Method for Nonlinear Response Tensors”,
Journal of the Physical Society of Japan **91**, 014701 (2022),
© 2022 The Physical Society of Japan
3. H. Kusunose, R. Oiwa, and S. Hayami,
“Complete Multipole Basis Set for Single-Centered Electron Systems”,
Journal of the Physical Society of Japan **89**, 104704 (2020),
© 2020 The Physical Society of Japan

Papers not included in the dissertation

1. S. Hayami, R. Oiwa and H. Kusunose,
“Electric Ferro-Axial Moment as Nanometric Rotator and Source of Longitudinal Spin Current”,
Journal of the Physical Society of Japan **91**, 113702 (2022),
© 2022 The Physical Society of Japan
2. M. Yatsushiro, R. Oiwa, H. Kusunose, and S. Hayami,
“Analysis of model parameter dependences on the second-order nonlinear conductivity in PT-symmetric collinear antiferromagnetic metals with magnetic toroidal moment on zigzag chains”,
Physical Review B **105**, 155157 (2022),
© 2022 American Physical Society
3. R. Oiwa, Y. Yanagi, and H. Kusunose,
“Time-reversal symmetry breaking superconductivity in hole-doped monolayer MoS₂”,
Journal of the Physical Society of Japan **88**, 063703 (2019),
© 2019 The Physical Society of Japan
4. R. Oiwa, Y. Yanagi, and H. Kusunose,
“Theory of superconductivity in hole-doped monolayer MoS₂”,
Physical Review B **98**, 064509 (2018),
© 2018 American Physical Society